André PREUMONT
Université Libre de Bruxelles
Active Structures Laboratory

Vibration Control of Active Structures, An Introduction 3^{rd} Edition

Springer
Berlin Heidelberg New York
Hong Kong London
Milan Paris Tokyo

1

Introduction

1.1 Active versus passive

Consider a precision structure subjected to varying thermal conditions; unless carefully designed, it will distort as a result of the thermal gradients. One way to prevent this is to build the structure from a thermally stable composite material; this is the *passive* approach. An alternative way is to use a set of actuators and sensors connected by a feedback loop; such a structure is *active*. In this case, we exploit the main virtue of feedback, which is to reduce the sensitivity of the output to parameter variations and to attenuate the effect of disturbances within the bandwidth of the control system. Depending on the circumstances, active structures may be cheaper or lighter than passive structures of comparable performances; or they may offer performances that no passive structure could offer, as in the following example.

Until a few years ago, the general belief was that atmospheric turbulence would constitute an important limitation to the resolution of earth based telescopes; this was one of the main reasons for developing the Hubble space telescope. Nowadays, it is possible to correct in real time the disturbances produced by atmospheric turbulence on the optical wave front coming from celestial objects; this allows us to improve the ultimate resolution of the telescope by one order of magnitude, to the limit imposed by diffraction. The correction is achieved by a deformable mirror coupled to a set of actuators (Fig.1.1). A wave front sensor detects the phase difference in the turbulent wave front and the control computer supplies the shape of the deformable mirror which is required to correct this error. *Adaptive optics* has become a standard feature in ground-based astronomy.

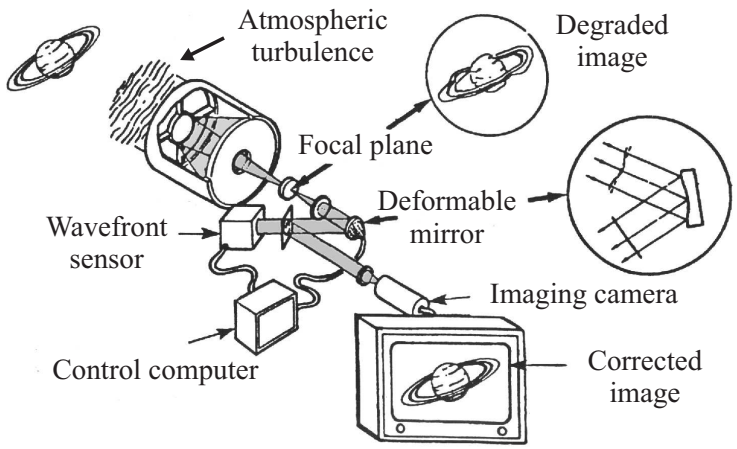

Fig. 1.1. Principle of adaptive optics for the compensation of atmospheric turbulence (by courtesy of G.Rousset-ONERA).

The foregoing example is not the only one where active structures have proved beneficial to astronomy; another example is the primary mirror of large telescopes, which can have a diameter of 8 m or more. Large primary mirrors are very difficult to manufacture and assemble. A passive mirror must be thermally stable and very stiff, in order to keep the right shape in spite of the varying gravity loads during the tracking of a star, and the dynamic loads from the wind. There are two alternatives to that, both active. The first one, adopted on the *Very Large Telescope (VLT)* at *ESO* in Paranal, Chile, consists of having a relatively flexible primary mirror connected at the back to a set of a hundred or so actuators. As in the previous example, the control system uses an image analyzer to evaluate the amplitude of the perturbation of the optical modes; next, the correction is computed to minimize the effect of the perturbation and is applied to the actuators. The influence matrix J between the actuator forces f and the optical mode amplitudes w of the wave front errors can be determined experimentally with the image analyzer:

$$w = Jf \tag{1.1}$$

J is a rectangular matrix, because the number of actuators is larger than the number of optical modes of interest. Once the modal errors w^* have been evaluated, the correcting forces can be calculated from

$$f^* = J^T(JJ^T)^{-1}w^* \tag{1.2}$$

where $J^T(JJ^T)^{-1}$ is the pseudo-inverse of the rectangular matrix J. This is the minimum norm solution to Equ.(1.1) (Problem 1.1).

The second alternative, adopted on the *Keck* observatory at Mauna Kea, Hawaii, consists of using a segmented primary mirror. The potential advantages of such a design are lower weight, lower cost, ease of fabrication and assembly. Each segment has a hexagonal shape and is equipped with three computer controlled degrees of freedom (tilt and piston) and six edge sensors measuring the relative displacements with respect to the neighboring segments; the control system is used to achieve the optical quality of a monolithic mirror (by *cophasing* the segments), to compensate for gravity and wind disturbances, and minimize the impact of the telescope dynamics on the optical performance (Aubrun et al.). Active and adaptive optics will be discussed more deeply in chapter 16.

As a third example, also related to astronomy, consider the future interferometric missions. The aim is to use a number of smaller telescopes as an interferometer to achieve a resolution which could only be achieved with a much larger monolithic telescope. One possible spacecraft architecture for such an interferometric mission is represented in Fig.1.2; it consists of a main truss supporting a set of independently pointing telescopes. The relative positions of the telescopes are monitored by a sophisticated metrology and the optical paths between the individual telescopes and the beam combiner are accurately controlled with optical delay lines, based on the information coming from a wave front sensor. Typically, the distance between the telescopes could be 50 m or more, and the order

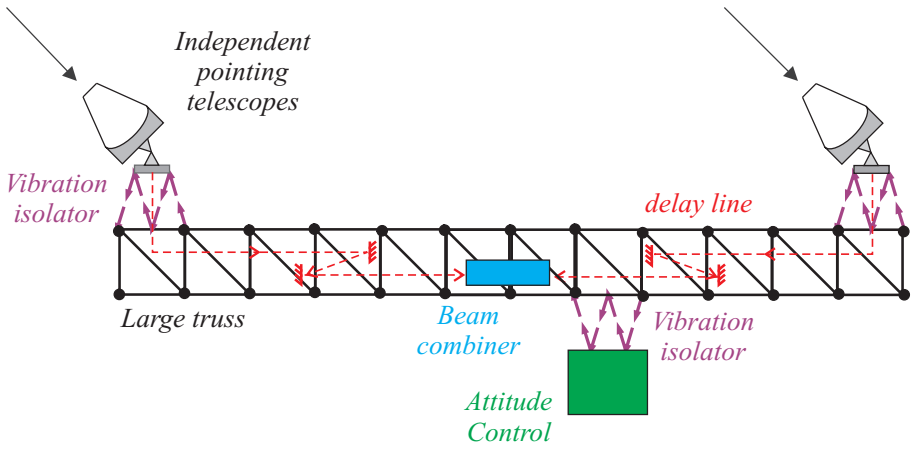

Fig. 1.2. Schematic view of a future interferometric mission.

of magnitude of the error allowed on the optical path length is a few nanometers; the pointing error of the individual telescopes is as low as a few nanoradians (i.e. one order of magnitude better than the Hubble space telescope). Clearly, such stringent geometrical requirements in the harsh space environment cannot be achieved with a precision monolithic structure, but rather by active means as suggested in Fig.1.2. The main requirement on the supporting truss is not *precision* but *stability*, the accuracy of the optical path being taken care of by the wide-band vibration isolation/steering control system of individual telescopes and the optical delay lines (described below). Geometric stability includes thermal stability, vibration damping and prestressing the gaps in deployable structures (this is a critical issue for deployable trusses). In addition to these geometric requirements, this spacecraft would be sent in deep space (e.g. at the *Lagrange point L2*) rather than in low orbit, to ensure maximum sensitivity; this makes the weight issue particularly important.

Another interesting subsystem necessary to achieve the stringent specifications is the six d.o.f. vibration isolator at the interface between the attitude control module and the supporting truss; this isolator allows the low frequency attitude control torque to be transmitted, while filtering out the high frequency disturbances generated by the unbalanced centrifugal forces in the reaction wheels. Another vibration isolator may be used at the interface between the truss and the independent telescopes, possibly combined with the steering of the telescopes. The third component relevant to active control is the optical delay line; it consists of a high precision single degree of freedom translational mechanism supporting a mirror, whose function is to control the optical path length between every telescope and the beam combiner, so that these distances are kept identical to a fraction of the wavelength (e.g. $\lambda/20$).

These examples were concerned mainly with performance. However, as technology develops and with the availability of low cost electronic components, it is likely that there will be a growing number of applications where active solutions will become cheaper than passive ones, for the same level of performance.

The reader should not conclude that *active* will always be better and that a control system can compensate for a bad design. In most cases, a bad design will remain bad, active or not, and an active solution should normally be considered only after all other passive means have been exhausted. One should always bear in mind that feedback control can compensate for external disturbances only in a limited frequency band that

is called the *bandwidth* of the control system. One should never forget that outside the bandwidth, the disturbance is actually amplified by the control system.

1.2 Vibration suppression

Mechanical vibrations span amplitudes from meters (civil engineering) to nanometers (precision engineering). Their detrimental effect on systems may be of various natures:

Failure: vibration-induced structural failure may occur by excessive strain during transient events (e.g. building response to earthquake), by instability due to particular operating conditions (flutter of bridges under wind excitation), or simply by fatigue (mechanical parts in machines).

Comfort: examples where vibrations are detrimental to comfort are numerous: noise and vibration in helicopters, car suspensions, wind-induced sway of buildings.

Operation of precision devices: numerous systems in precision engineering, especially optical systems, put severe restrictions on mechanical vibrations. Precision machine tools, wafer steppers,[1] telescopes are typical examples. The performances of large interferometers such as the VLTI are limited by microvibrations affecting the various parts of the optical path. Lightweight segmented telescopes (space as well as earth-based) will be impossible to build in their final shape with an accuracy of a fraction of the wavelength, because of the various disturbance sources such as the thermal gradient (which dominates the space environment). Such systems will not exist without the capability to control actively the reflector shape.

Vibration reduction can be achieved in many different ways, depending on the problem; the most common are stiffening, damping and isolation. *Stiffening* consists of shifting the resonance frequency of the structure beyond the frequency band of excitation. *Damping* consists of reducing the resonance peaks by dissipating the vibration energy. *Isolation* consists of preventing the propagation of disturbances to sensitive parts of the systems.

[1] *Moore's law* on the number of transistors on an integrated circuit could not hold without a constant improvement of the accuracy of wafer steppers and other precision machines (Taniguchi).

Damping may be achieved *passively*, with fluid dampers, eddy currents, elastomers or hysteretic elements, or by transferring kinetic energy to *Dynamic Vibration Absorbers* (DVA). One can also use transducers as energy converters, to transform vibration energy into electrical energy that is dissipated in electrical networks, or stored (energy harvesting). Recently, *semi-active* devices (also called semi-passive) have become available; they consist of passive devices with controllable properties. The *Magneto-Rheological* (MR) fluid damper is a famous example; piezoelectric transducers with switched electrical networks is another one. Since they behave in a strongly nonlinear way, semi-active devices can transfer energy from one frequency to another, but they are inherently passive and, unlike active devices, cannot destabilize the system; they are also less vulnerable to power failure. When high performance is needed, *active* control can be used; this involves a set of sensors (strain, acceleration, velocity, force,...), a set of actuators (force, inertial, strain,...) and a control algorithm (feedback or feedforward). Active damping is one of the main focuses of this book. The design of an active control system involves many issues such as how to configurate the sensors and actuators, how to secure stability and robustness (e.g. collocated actuator/sensor pairs); the power requirements will often determine the size of the actuators, and the cost of the project.

1.3 Smart materials and structures

An active structure consists of a structure provided with a set of actuators and sensors coupled by a controller; if the bandwidth of the controller includes some vibration modes of the structure, its dynamic response must be considered. If the set of actuators and sensors are located at discrete points of the structure, they can be treated separately. The distinctive feature of *smart* structures is that the actuators and sensors are often distributed, and have a high degree of integration inside the structure, which makes a separate modelling impossible (Fig.1.3). Moreover, in some applications like vibroacoustics, the behaviour of the structure itself is highly coupled with the surrounding medium; this also requires a coupled modelling. From a mechanical point of view, classical structural materials are entirely described by their elastic constants relating stress and strain, and their thermal expansion coefficient relating the strain to the temperature. *Smart materials* are materials where strain can also be generated by different mechanisms involving temperature, electric field or magnetic field,

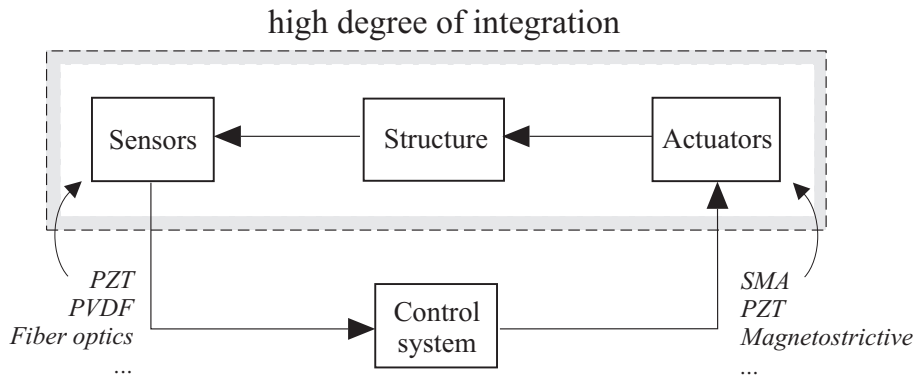

Fig. 1.3. Smart structure.

etc... as a result of some coupling in their constitutive equations. The most celebrated smart materials are briefly described below:

- *Shape Memory Alloys (SMA)* allow one to recover up to 5 % strain from the phase change induced by temperature. Although two-way applications are possible after education, SMA are best suited to one-way tasks such as deployment. In any case, they can be used only at low frequency and for low precision applications, mainly because of the difficulty of cooling. Fatigue under thermal cycling is also a problem. The best known SMA is called *NITINOL*; SMA are little used in active vibration control, and will not be discussed in this book.[2]
- *Piezoelectric materials* have a recoverable strain of 0.1 % under electric field; they can be used as actuators as well as sensors. There are two broad classes of piezoelectric materials used in vibration control: ceramics and polymers. The piezopolymers are used mostly as sensors, because they require extremely high voltages and they have a limited control authority; the best known is the *polyvinylidene fluoride* ($PVDF$ or PVF_2). Piezoceramics are used extensively as actuators and sensors, for a wide range of frequency including ultrasonic applications; they are well suited for high precision in the nanometer range ($1nm = 10^{-9}m$). The best known piezoceramic is the *Lead Zirconate Titanate (PZT)*; PZT patches can be glued or co-fired on the supporting structure.
- *Magnetostrictive materials* have a recoverable strain of 0.15 % under magnetic field; the maximum response is obtained when the material

[2] The superelastic behavior of SMA may be exploited to achieve damping, for low frequency and low cycle applications, such as earthquake protection.

is subjected to compressive loads. Magnetostrictive actuators can be used as load carrying elements (in compression alone) and they have a long lifetime. They can also be used in high precision applications. The best known is the *TERFENOL-D*; it can be an alternative to PZT in some applications (sonar).

- *Magneto-rheological (MR)* fluids consist of viscous fluids containing micron-sized particles of magnetic material. When the fluid is subjected to a magnetic field, the particles create columnar structures requiring a minimum shear stress to initiate the flow. This effect is reversible and very fast (response time of the order of millisecond). Some fluids exhibit the same behavior under electrical field; they are called *electro-rheological (ER)* fluids; however, their performances (limited by the electric field breakdown) are currently inferior to MR fluids. MR and ER fluids are used in semi-active devices.

This brief list of commercially available smart materials is just a flavor of what is to come: *phase change materials* are currently under development and are likely to become available in a few years time; they will offer a recoverable strain of the order of 1 % under an electric or magnetic field, one order of magnitude more than the piezoceramics. *Electroactive polymers* are also slowly emerging for large strain low stiffness applications.

The range of available devices to measure position, velocity, acceleration and strain is extremely wide, and there are more to come, particularly in optomechanics. Displacements can be measured with inductive, capacitive and optical means (laser interferometer); the latter two have a resolution in the nanometer range. Piezoelectric accelerometers are very popular but they cannot measure a d.c. component. Strain can be measured with strain gages, piezoceramics, piezopolymers and fiber optics. The latter can be embedded in a structure and give a global average measure of the deformation; they offer a great potential for health monitoring as well. Piezopolymers can be shaped to react only to a limited set of vibration modes (modal filters).

1.4 Control strategies

There are two radically different approaches to disturbance rejection: feedback and feedforward. Although this text is entirely devoted to feedback control, it is important to point out the salient features of both approaches, in order to enable the user to select the most appropriate one for a given application.

1.4.1 Feedback

The principle of feedback is represented in Fig.1.4; the output y of the system is compared to the reference input r, and the error signal, $e = r - y$, is passed into a compensator $H(s)$ and applied to the system $G(s)$. The design problem consists of finding the appropriate compensator $H(s)$ such that the closed-loop system is stable and behaves in the appropriate manner.

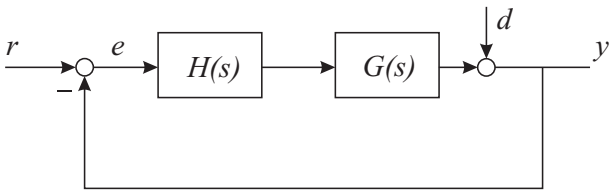

Fig. 1.4. Principle of feedback control.

In the control of lightly damped structures, feedback control is used for two distinct and somewhat complementary purposes: *active damping* and *model based* feedback.

The objective of active damping is to reduce the effect of the resonant peaks on the response of the structure. From

$$\frac{y(s)}{d(s)} = \frac{1}{1+GH} \tag{1.3}$$

(Problem 1.2), this requires $GH \gg 1$ near the resonances. Active damping can generally be achieved with moderate gains; another nice property is that it can be achieved without a model of the structure, and with guaranteed stability, provided that the actuator and sensor are collocated and have perfect dynamics. Of course actuators and sensors always have finite dynamics and any active damping system has a finite bandwidth.

The control objectives can be more ambitious, and we may wish to keep a control variable y (a position, or the pointing of an antenna) to a desired value r in spite of external disturbances d in some frequency range. From the previous formula and

$$F(s) = \frac{y(s)}{r(s)} = \frac{GH}{1+GH} \tag{1.4}$$

we readily see that this requires large values of GH in the frequency range where $y \simeq r$ is sought. $GH \gg 1$ implies that the closed-loop transfer

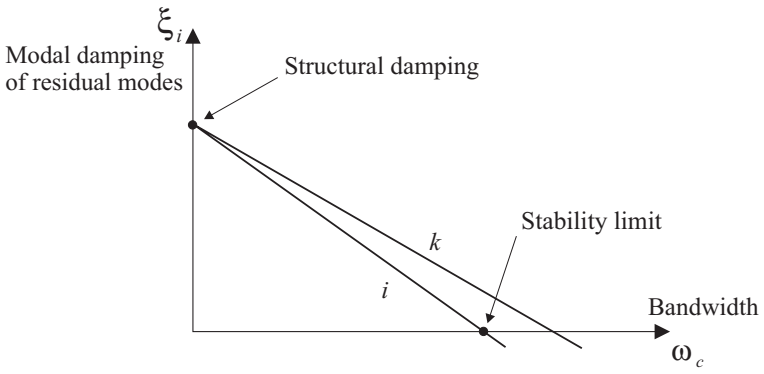

Fig. 1.5. Effect of the control bandwidth on the net damping of the residual modes.

function $F(s)$ is close to 1, which means that the output y tracks the input r accurately. From Equ.(1.3), this also ensures disturbance rejection within the bandwidth of the control system. In general, to achieve this, we need a more elaborate strategy involving a mathematical model of the system which, at best, can only be a low-dimensional approximation of the actual system $G(s)$. There are many techniques available to find the appropriate compensator, and only the simplest and the best established will be reviewed in this text. They all have a number of common features:

- The bandwidth ω_c of the control system is limited by the accuracy of the model; there is always some destabilization of the flexible modes outside ω_c (residual modes). The phenomenon whereby the net damping of the residual modes actually decreases when the bandwidth increases is known as *spillover* (Fig.1.5).
- The disturbance rejection within the bandwidth of the control system is always compensated by an amplification of the disturbances outside the bandwidth.
- When implemented digitally, the sampling frequency ω_s must always be two orders of magnitude larger than ω_c to preserve reasonably the behaviour of the continuous system. This puts some hardware restrictions on the bandwidth of the control system.

1.4.2 Feedforward

When a signal correlated to the disturbance is available, feedforward adaptive filtering constitutes an attractive alternative to feedback for disturbance rejection; it was originally developed for noise control (Nelson &

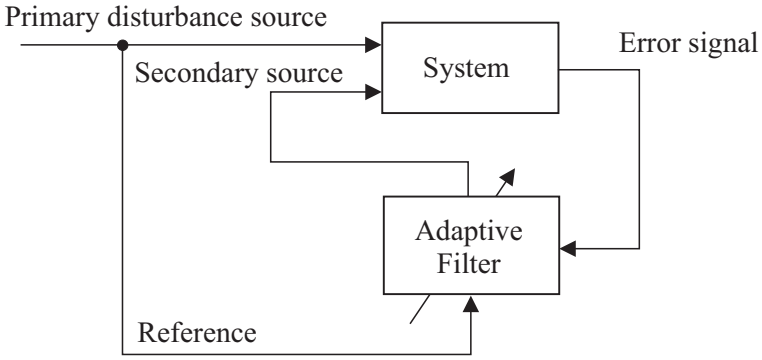

Fig. 1.6. Principle of feedforward control.

Elliott), but it is very efficient for vibration control too (Fuller et al.). Its principle is explained in Fig.1.6. The method relies on the availability of a reference signal correlated to the primary disturbance; this signal is passed through an adaptive filter, the output of which is applied to the system by secondary sources. The filter coefficients are adapted in such a way that the error signal at one or several critical points is minimized. The idea is to produce a secondary disturbance such that it cancels the effect of the primary disturbance at the location of the error sensor. Of course, there is no guarantee that the global response is also reduced at other locations and, unless the response is dominated by a single mode, there are places where the response can be amplified; the method can therefore be considered as a local one, in contrast to feedback which is global. Unlike active damping which can only attenuate the disturbances near the resonances, feedforward works for any frequency and attempts to cancel the disturbance completely by generating a secondary signal of opposite phase.

The method does not need a model of the system, but the adaption procedure relies on the measured impulse response. The approach works better for narrow-band disturbances, but wide-band applications have also been reported. Because it is less sensitive to phase lag than feedback, feedforward control can be used at higher frequency (a good rule of thumb is $\omega_c \simeq \omega_s/10$); this is why it has been so successful in acoustics.

The main limitation of feedforward adaptive filtering is the availability of a reference signal correlated to the disturbance. There are many applications where such a signal can be readily available from a sensor located on the propagation path of the perturbation. For disturbances induced by rotating machinery, an impulse train generated by the rotation

Type of control	Advantages	Disadvantages
Feedback		
Active damping	• no model needed • guaranteed stability when collocated	• effective only near resonances
Model based (LQG,H_∞...)	• global method • attenuates all disturbances within ω_c	• limited bandwidth ($\omega_c \ll \omega_s$) • disturbances outside ω_c are amplified • spillover
Feedforward		
Adaptive filtering of reference (*x-filtered LMS*)	• no model necessary • wider bandwidth ($\omega_c \simeq \omega_s/10$) • works better for narrow-band disturb.	• reference needed • local method (response may be amplified in some part of the system) • large amount of real time computations

Table 1.1. Comparison of feedback and feedforward control strategies.

of the main shaft can be used as reference. Table 1.1 summarizes the main features of the two approaches.

1.5 The various steps of the design

The various steps of the design of a controlled structure are shown in Fig.1.7. The starting point is a mechanical system, some performance objectives (e.g. position accuracy) and a specification of the disturbances applied to it; the controller cannot be designed without some knowledge of the disturbance applied to the system. If the frequency distribution of the energy of the disturbance (i.e. the power spectral density) is known, the open-loop performances can be evaluated and the need for an active control system can be assessed (see next section). If an active system is required, its bandwidth can be roughly specified from Equ.(1.3). The next step consists of selecting the proper type and location for a set of sensors to monitor the behavior of the system, and actuators to control

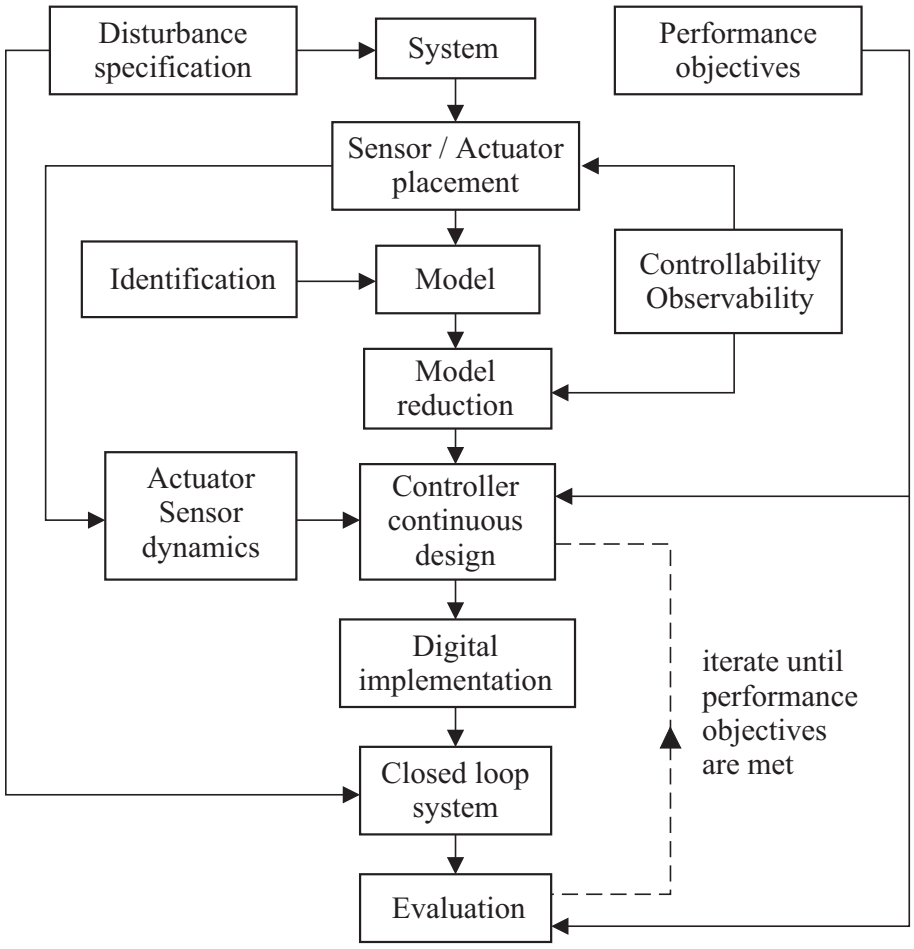

Fig. 1.7. The various steps of the design.

it. The concept of controllability measures the capability of an actuator to interfere with the states of the system. Once the actuators and sensors have been selected, a model of the structure is developed, usually with finite elements; it can be improved by identification if experimental transfer functions are available. Such models generally involve too many degrees of freedom to be directly useful for design purposes; they must be reduced to produce a control design model involving only a few degrees of freedom, usually the vibration modes of the system, which carry the most important information about the system behavior. At this point, if the actuators and sensors can be considered as perfect (in the frequency band of interest), they can be ignored in the model; their effect on the

control system performance will be tested after the design has been completed. If, on the contrary, the dynamics of the actuators and sensors may significantly affect the behavior of the system, they must be included in the model before the controller design. Even though most controllers are implemented in a digital manner, nowadays, there are good reasons to carry out a continuous design and transform the continuous controller into a digital one with an appropriate technique. This approach works well when the sampling frequency is two orders of magnitude faster than the bandwidth of the control system, as is generally the case in structural control.

1.6 Plant description, error and control budget

Consider the block diagram of (Fig.1.8), in which the plant consists of the structure and its actuator and sensor. w is the disturbance applied to the structure, z is the controlled variable or performance metrics (that one wants to keep as close as possible to 0), u is the control input and y is the sensor output (they are all assumed scalar for simplicity). $H(s)$ is the feedback control law, expressed in the Laplace domain (s is the Laplace variable). We define the open-loop transfer functions :

$G_{zw}(s)$: between w and z
$G_{zu}(s)$: between u and z
$G_{yw}(s)$: between w and y
$G_{yu}(s)$: between u and y

From the definition of the open-loop transfer functions,

$$y = G_{yw}w + G_{yu}Hy \tag{1.5}$$

or

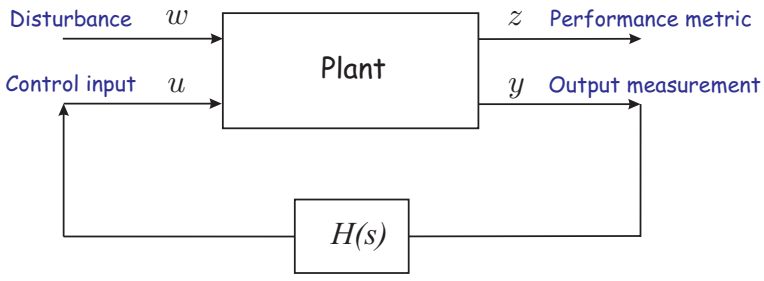

Fig. 1.8. Block diagram of the control system.

$$y = (I - G_{yu}H)^{-1}G_{yw}w \tag{1.6}$$

It follows that

$$u = Hy = H(I - G_{yu}H)^{-1}G_{yw}w = T_{uw}w \tag{1.7}$$

On the other hand

$$z = G_{zw}w + G_{zu}u \tag{1.8}$$

Combining the two foregoing equations, one finds the closed-loop transmissibility between the disturbance w and the control metrics z :

$$z = T_{zw}w = [G_{zw} + G_{zu}H(I - G_{yu}H)^{-1}G_{yw}]w \tag{1.9}$$

The frequency content of the disturbance w is usually described by its *Power Spectral Density* (PSD), $\Phi_w(\omega)$ which describes the frequency distribution of the mean-square (MS) value

$$\sigma_w^2 = \int_0^\infty \Phi_w(\omega)d\omega \tag{1.10}$$

[the unit of Φ_w is readily obtained from this equation; it is expressed in units of w squared per (rad/s)]. From(1.9), the PSD of the control metric z is given by :

$$\Phi_z(\omega) = |T_{zw}|^2\Phi_w(\omega) \tag{1.11}$$

$\Phi_z(\omega)$ gives the frequency distribution of the mean-square value of the performance metric. Even more interesting for design is the *cumulative* MS response, defined by the integral of the PSD in the frequency range $[\omega, \infty[$

$$\sigma_z^2(\omega) = \int_\omega^\infty \Phi_z(\nu)d\nu = \int_\omega^\infty |T_{zw}|^2\Phi_w(\nu)d\nu \tag{1.12}$$

It is a monotonously decreasing function of frequency and describes the contribution of all the frequencies above ω to the mean-square value of z. $\sigma_z(\omega)$ is expressed in the same units as the performance metric z and $\sigma_z(0)$ is the global RMS response; a typical plot is shown in Fig.1.9 for an hypothetical system with 4 modes. For lightly damped structures, the diagram exhibits steps at the natural frequencies of the modes and the magnitude of the steps gives the contribution of each mode to the error budget, in the same units as the performance metric; it is very helpful to identify the critical modes in a design, at which the effort should be

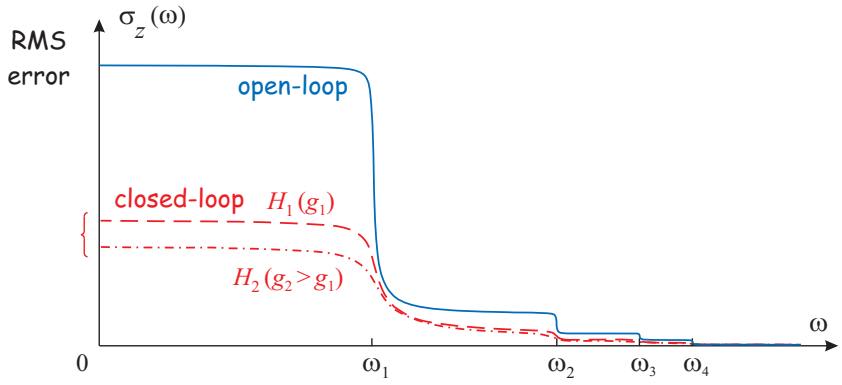

Fig. 1.9. Error budget distribution in open-loop and in closed-loop for increasing gains.

targeted. This diagram can be used to assess the control laws and compare different actuator and sensor configurations. In a similar way, the control budget can be assessed from

$$\sigma_u^2(\omega) = \int_\omega^\infty \Phi_u(\nu)d\nu = \int_\omega^\infty |T_{uw}|^2 \Phi_w(\nu)d\nu \tag{1.13}$$

$\sigma_u(\omega)$ describes how the RMS control input is distributed over the various modes of the structure and plays a critical role in the actuator design.

Clearly, the frequency content of the disturbance w, described by $\Phi_w(\omega)$, is essential in the evaluation of the error and control budgets and it is very difficult, even risky, to attempt to design a control system without prior information on the disturbance.

1.7 Readership and Organization of the book

Structural control and smart structures belong to the general field of *Mechatronics*; they consist of a mixture of mechanical and electrical engineering, structural mechanics, control engineering, material science and computer science. This book has been written primarily for structural engineers willing to acquire some background in structural control, but it will also interest control engineers involved in flexible structures. It has been assumed that the reader is familiar with structural dynamics and has some basic knowledge of linear system theory, including Laplace transform, root locus, Bode plots, Nyquist plots, etc... Readers who are not familiar with these concepts are advised to read a basic text on linear

system theory (e.g. Cannon, Franklin et al.). Some elementary background in signal processing is also assumed.

Chapter 2 recalls briefly some concepts of structural dynamics; chapter 3 to 5 consider the transduction mechanisms, the piezoelectric materials and structures and the damping via passive networks. Chapter 6 and 7 consider collocated (and dual) control systems and their use in active damping. Chapter 8 is devoted to vibration isolation. Chapter 9 to 13 cover classical topics in control: state space modelling, frequency domain, optimal control, controllability and observability, and stability. Various structural control applications (active damping, position control of a flexible structure, vibroacoustics) are covered in chapter 14; chapter 15 is devoted to cable-structures and chapter 16 to the wavefront control of large optical telescopes. Finally, chapter 17 is devoted to semi-active control. Each chapter is supplemented by a set of problems; it is assumed that the reader is familiar with *MATLAB-SIMULINK* or some equivalent computer aided control engineering software.

Chapters 1 to 9 plus part of Chapter 10 and some applications of chapter 14 can constitute a one semester graduate course in structural control.

1.8 References

AUBRUN, J.N., LORELL, K.R., HAVAS & T.W., HENNINGER, W.C. Performance Analysis of the Segment Alignment Control System for the Ten-Meter Telescope, *Automatica*, Vol.24, No 4, 437-453, 1988.

CANNON, R.H. *Dynamics of Physical Systems*, McGraw-Hill, 1967.

FRANKLIN, G.F., POWELL, J.D. & EMAMI-NAEINI, A. *Feedback Control of Dynamic Systems.* Addison-Wesley, 1986.

FULLER, C.R., ELLIOTT, S.J. & NELSON, P.A. *Active Control of Vibration*, Academic Press, 1996.

GANDHI, M.V. & THOMPSON, B.S. *Smart Materials and Structures,* Chapman & Hall, 1992.

NELSON, P.A. & ELLIOTT, S.J. *Active Control of Sound,* Academic Press, 1992.

TANIGUCHI, N. Current Status in, and Future Trends of, Ultraprecision Machining and Ultrafine Materials Processing, *CIRP Annals*, Vol.32, No 2, 573-582, 1983.

UCHINO, K. *Ferroelectric Devices*, Marcel Dekker, 2000.

General literature on control of flexible structures

CLARK, R.L., SAUNDERS, W.R. & GIBBS, G.P. *Adaptive Structures, Dynamics and Control*, Wiley, 1998.
GAWRONSKI, W.K. *Dynamics and Control of Structures - A Modal Approach*, Springer, 1998.
GAWRONSKI, W.K. *Advanced Structural Dynamics and Active Control of Structures*, Springer, 2004.
HYLAND, D.C., JUNKINS, J.L. & LONGMAN, R.W. Active control technology for large space structures, *J. of Guidance, Vol.16, No 5, 801-821, Sept.-Oct.1993.*
INMAN, D.J. *Vibration, with Control, Measurement, and Stability.* Prentice-Hall, 1989.
INMAN, D.J. *Vibration with Control*, Wiley 2006.
JANOCHA, H. (Editor), *Adaptronics and Smart Structures (Basics, Materials, Design and Applications)*, Springer, 1999.
JOHSI, S.M. *Control of Large Flexible Space Structures,* Lecture Notes in Control and Information Sciences, Vol.131, Springer-Verlag, 1989.
JUNKINS, J.L. (Editor) *Mechanics and Control of Large Flexible Structures,* AIAA Progress in Astronautics and Aeronautics, Vol.129, 1990.
JUNKINS, J.L. & KIM, Y. *Introduction to Dynamics and Control of Flexible Structures,* AIAA Education Series, 1993.
MEIROVITCH, L. *Dynamics and Control of Structures*, Wiley, 1990.
MIU, D.K. *Mechatronics - Electromechanics and Contromechanics*, Springer-Verlag, 1993.
PREUMONT, A. *Mechatronics, Dynamics of Electromechanical and Piezoelectric Systems*, Springer, 2006.
PREUMONT, A. & SETO, K. *Active Control of Structures*, Wiley, 2008.
SKELTON, R.E. *Dynamic System Control - Linear System Analysis and Synthesis,* Wiley, 1988.
SPARKS, D.W. Jr & JUANG, J.N. Survey of experiments and experimental facilities for control of flexible structures, *AIAA J.of Guidance, Vol.15, No 4, 801-816, July-August 1992.*

1.9 Problems

P.1.1 *Consider the underdeterminate system of equations*

$$Jx = w$$

Show that the minimum norm solution, i.e. the solution of the minimization problem

$$\min_x (x^T x) \qquad \text{such that} \qquad Jx = w$$

is

$$x = J^+ w = J^T (JJ^T)^{-1} w$$

J^+ *is called the pseudo-inverse of* J. *[hint: Use Lagrange multipliers to remove the equality constraint.]*

P.1.2 *Consider the feedback control system of Fig.1.4. Show that the transfer functions from the input* r *and the disturbance* d *to the output* y *are respectively*

$$\frac{y(s)}{r(s)} = \frac{GH}{1+GH} \qquad \frac{y(s)}{d(s)} = \frac{1}{1+GH}$$

P.1.3 *Based on your own experience, describe one application in which you feel an active structure may outclass a passive one; outline the system and suggest a configuration for the actuators and sensors.*

2

Some concepts in structural dynamics

2.1 Introduction

This chapter is not intended to be a substitute for a course in structural dynamics, which is part of the prerequisites to read this book. The goal of this chapter is twofold: *(i)* recalling some of the notations which will be used throughout this book, and *(ii)* insisting on some aspects which are particularly important when dealing with *controlled* structures and which may otherwise be overlooked. As an example, the structural dynamic analysts are seldom interested in antiresonance frequencies which play a capital role in structural control.

2.2 Equation of motion of a discrete system

Consider the system with three point masses represented in Fig.2.1. The equations of motion can be established by considering the free body diagrams of the three masses and applying Newton's law; one easily gets:

$$M\ddot{x}_1 + k(x_1 - x_2) + c(\dot{x}_1 - \dot{x}_2) = f$$

$$m\ddot{x}_2 + k(2x_2 - x_1 - x_3) + c(2\dot{x}_2 - \dot{x}_1 - \dot{x}_3) = 0$$

$$m\ddot{x}_3 + k(x_3 - x_2) + c(\dot{x}_3 - \dot{x}_2) = 0$$

or, in matrix form,

$$\begin{pmatrix} M & 0 & 0 \\ 0 & m & 0 \\ 0 & 0 & m \end{pmatrix} \begin{pmatrix} \ddot{x}_1 \\ \ddot{x}_2 \\ \ddot{x}_3 \end{pmatrix} + \begin{pmatrix} c & -c & 0 \\ -c & 2c & -c \\ 0 & -c & c \end{pmatrix} \begin{pmatrix} \dot{x}_1 \\ \dot{x}_2 \\ \dot{x}_3 \end{pmatrix} + \begin{pmatrix} k & -k & 0 \\ -k & 2k & -k \\ 0 & -k & k \end{pmatrix} \begin{pmatrix} x_1 \\ x_2 \\ x_3 \end{pmatrix} = \begin{pmatrix} f \\ 0 \\ 0 \end{pmatrix} \tag{2.1}$$

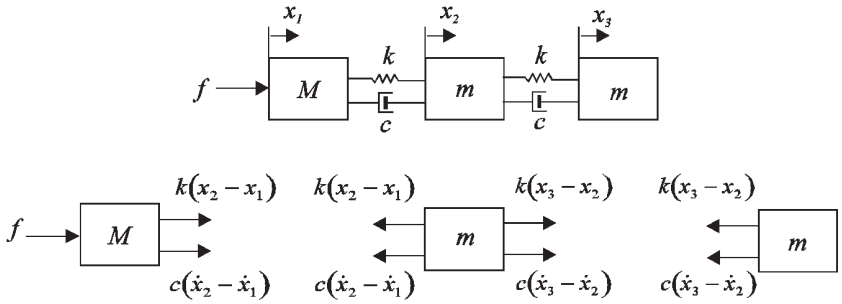

Fig. 2.1. Three mass system and its free body diagram.

The general form of the equation of motion governing the dynamic equilibrium between the external, elastic, inertia and damping forces acting on a non-gyroscopic, discrete, flexible structure with a finite number n of degrees of freedom (d.o.f.) is

$$M\ddot{x} + C\dot{x} + Kx = f \tag{2.2}$$

where x and f are the vectors of generalized displacements (translations and rotations) and forces (point forces and torques) and M, K and C are respectively the mass, stiffness and damping matrices; they are symmetric and semi positive definite. M and K arise from the discretization of the structure, usually with finite elements. A lumped mass system such as that of Fig.2.1 has a diagonal mass matrix. The finite element method usually leads to non-diagonal (consistent) mass matrices, but a diagonal mass matrix often provides an acceptable representation of the inertia in the structure (Problem 2.2).

The damping matrix C represents the various dissipation mechanisms in the structure, which are usually poorly known. To compensate for this lack of knowledge, it is customary to make assumptions on its form. One of the most popular hypotheses is the *Rayleigh damping*:

$$C = \alpha M + \beta K \tag{2.3}$$

The coefficients α and β are selected to fit the structure under consideration.

2.3 Vibration modes

Consider the free response of a undamped (conservative) system of order n. It is governed by

$$M\ddot{x} + Kx = 0 \tag{2.4}$$

If one tries a solution of the form $x = \phi_i \, e^{j\omega_i t}$, ϕ_i and ω_i must satisfy the eigenvalue problem

$$(K - \omega_i^2 M)\phi_i = 0 \tag{2.5}$$

Because M and K are symmetric, K is positive semi definite and M is positive definite, the eigenvalue ω_i^2 must be real and non negative. ω_i is the natural frequency and ϕ_i is the corresponding mode shape; the number of modes is equal to the number of degrees of freedom, n. Note that Equ.(2.5) defines only the shape, but not the amplitude of the mode which can be scaled arbitrarily. The modes are usually ordered by increasing frequencies ($\omega_1 \leq \omega_2 \leq \omega_3 \leq ...$). From Equ.(2.5), one sees that if the structure is released from initial conditions $x(0) = \phi_i$ and $\dot{x}(0) = 0$, it oscillates at the frequency ω_i according to $x(t) = \phi_i \cos \omega_i t$, always keeping the shape of mode i.

Left multiplying Equ.(2.5) by ϕ_j^T, one gets the scalar equation

$$\phi_j^T K \phi_i = \omega_i^2 \phi_j^T M \phi_i$$

and, upon permuting i and j, one gets similarly,

$$\phi_i^T K \phi_j = \omega_j^2 \phi_i^T M \phi_j$$

Substracting these equations, taking into account that a scalar is equal to its transpose, and that K and M are symmetric, one gets

$$0 = (\omega_i^2 - \omega_j^2)\phi_j^T M \phi_i$$

which shows that the mode shapes corresponding to distinct natural frequencies are orthogonal with respect to the mass matrix.

$$\phi_j^T M \phi_i = 0 \quad (\omega_i \neq \omega_j)$$

It follows from the foregoing equations that the mode shapes are also orthogonal with respect to the stiffness matrix. The orthogonality conditions are often written as

$$\phi_i^T M \phi_j = \mu_i \, \delta_{ij} \tag{2.6}$$

$$\phi_i^T K \phi_j = \mu_i \, \omega_i^2 \, \delta_{ij} \tag{2.7}$$

where δ_{ij} is the Kronecker delta ($\delta_{ij} = 1$ if $i = j$, $\delta_{ij} = 0$ if $i \neq j$), μ_i is the *modal mass* (also called generalized mass) of mode i. Since the mode shapes can be scaled arbitrarily, it is usual to normalize them in such a way that $\mu_i = 1$. If one defines the matrix of the mode shapes $\Phi = (\phi_1, \phi_2, ..., \phi_n)$, the orthogonality relationships read

$$\Phi^T M \Phi = diag(\mu_i) \tag{2.8}$$

$$\Phi^T K \Phi = diag(\mu_i \omega_i^2) \tag{2.9}$$

To demonstrate the orthogonality conditions, we have used the fact that the natural frequencies were distinct. If several modes have the same natural frequency (as often occurs in practice because of symmetry), they form a subspace of dimension equal to the multiplicity of the eigenvalue. Any vector in this subspace is a solution of the eigenvalue problem, and it is always possible to find a set of vectors such that the orthogonality conditions are satisfied. A rigid body mode is such that there is no strain energy associated with it ($\phi_i^T K \phi_i = 0$). It can be demonstrated that this implies that $K\phi_i = 0$; the rigid body modes can therefore be regarded as solutions of the eigenvalue problem (2.5) with $\omega_i = 0$.

2.4 Modal decomposition

2.4.1 Structure without rigid body modes

Let us perform a change of variables from physical coordinates x to modal coordinates according to

$$x = \Phi z \tag{2.10}$$

where z is the vector of modal amplitudes. Substituting into Equ.(2.2), we get

$$M\Phi\ddot{z} + C\Phi\dot{z} + K\Phi z = f$$

Left multiplying by Φ^T and using the orthogonality relationships (2.8) and (2.9), we obtain

$$diag(\mu_i)\ddot{z} + \Phi^T C \Phi \dot{z} + diag(\mu_i \omega_i^2) z = \Phi^T f \tag{2.11}$$

If the matrix $\Phi^T C \Phi$ is diagonal, the damping is said *classical* or *normal*. In this case, the modal fraction of critical damping ξ_i (in short *modal damping*) is defined by

$$\Phi^T C \Phi = diag(2\xi_i \mu_i \omega_i) \tag{2.12}$$

One can readily check that the Rayleigh damping (2.3) complies with this condition and that the corresponding modal damping ratios are

$$\xi_i = \frac{1}{2}(\frac{\alpha}{\omega_i} + \beta\omega_i) \tag{2.13}$$

The two free parameters α and β can be selected in order to match the modal damping of two modes. Note that the Rayleigh damping tends to overestimate the damping of the high frequency modes.

Under condition (2.12), the modal equations are decoupled and Equ.(2.11) can be rewritten

$$\ddot{z} + 2\xi\,\Omega\,\dot{z} + \Omega^2 z = \mu^{-1}\Phi^T f \tag{2.14}$$

with the notations

$$\begin{aligned} \xi &= diag(\xi_i) \\ \Omega &= diag(\omega_i) \\ \mu &= diag(\mu_i) \end{aligned} \tag{2.15}$$

The following values of the modal damping ratio can be regarded as typical: satellites and space structures are generally very lightly damped ($\xi \simeq 0.001 - 0.005$), because of the extensive use of fiber reinforced composites, the absence of aerodynamic damping, and the low strain level. Mechanical engineering applications (steel structures, piping,...) are in the range of $\xi \simeq 0.01 - 0.02$; most dissipation takes place in the joints, and the damping increases with the strain level. For civil engineering applications, $\xi \simeq 0.05$ is typical and, when radiation damping through the ground is involved, it may reach $\xi \simeq 0.20$, depending on the local soil conditions. The assumption of classical damping is often justified for light damping, but it is questionable when the damping is large, as in problems involving soil-structure interaction. Lightly damped structures are usually easier to model, but more difficult to control, because their poles are located very near the imaginary axis and they can be destabilized very easily.

If one accepts the assumption of classical damping, the only difference between Equ.(2.2) and (2.14) lies in the change of coordinates (2.10). However, in physical coordinates, the number of degrees of freedom of a discretized model of the form (2.2) is usually large, especially if the geometry is complicated, because of the difficulty of accurately representing the stiffness of the structure. This number of degrees of freedom is unnecessarily large to represent the structural response in a limited bandwidth.

If a structure is excited by a band-limited excitation, its response is dominated by the modes whose natural frequencies belong to the bandwidth of the excitation, and the integration of Equ.(2.14) can often be restricted to these modes. The number of degrees of freedom contributing effectively to the response is therefore reduced drastically in modal coordinates.

2.4.2 Dynamic flexibility matrix

Consider the steady state harmonic response of Equ.(2.2) to a vector excitation $f = Fe^{j\omega t}$. The response is also harmonic, $x = Xe^{j\omega t}$, and the amplitude of F and X are related by

$$X = [-\omega^2 M + j\omega C + K]^{-1} F = G(\omega) F \tag{2.16}$$

Where the matrix $G(\omega)$ is called the *dynamic flexibility matrix* ; it is a dynamic generalization of the static flexibility matrix, $G(0) = K^{-1}$. The modal expansion of $G(\omega)$ can be obtained by transforming (2.16) into modal coordinates $x = \Phi z$ as we did earlier. The modal response is also harmonic, $z = Ze^{j\omega t}$ and one finds easily that

$$Z = diag\{\frac{1}{\mu_i(\omega_i^2 + 2j\xi_i\omega_i\omega - \omega^2)}\}\,\Phi^T F$$

leading to

$$X = \Phi Z = \Phi\, diag\{\frac{1}{\mu_i(\omega_i^2 + 2j\xi_i\omega_i\omega - \omega^2)}\}\,\Phi^T F$$

Comparing with (2.16), one finds the modal expansion of the dynamic flexibility matrix:

$$G(\omega) = [-\omega^2 M + j\omega C + K]^{-1} = \sum_{i=1}^{n} \frac{\phi_i \phi_i^T}{\mu_i(\omega_i^2 + 2j\xi_i\omega_i\omega - \omega^2)} \tag{2.17}$$

where the sum extends to all the modes. $G_{lk}(\omega)$ expresses the complex amplitude of the structural response of d.o.f. l when a unit harmonic force $e^{j\omega t}$ is applied at d.o.f. k. $G(\omega)$ can be rewritten

$$G(\omega) = \sum_{i=1}^{n} \frac{\phi_i \phi_i^T}{\mu_i \omega_i^2} D_i(\omega) \tag{2.18}$$

where

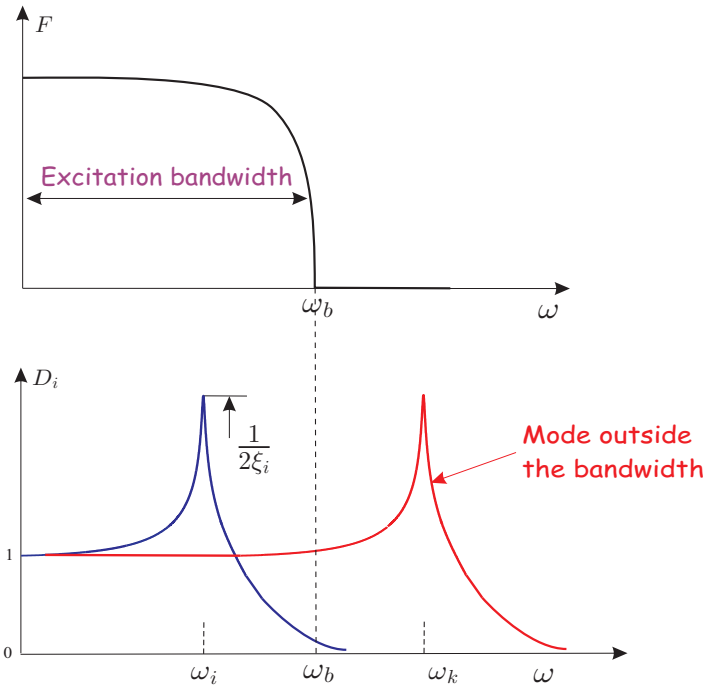

Fig. 2.2. Fourier spectrum of the excitation F with a limited frequency content $\omega < \omega_b$ and dynamic amplification D_i of mode i such that $\omega_i < \omega_b$ and $\omega_k \gg \omega_b$.

$$D_i(\omega) = \frac{1}{1 - \omega^2/\omega_i^2 + 2j\xi_i\omega/\omega_i} \tag{2.19}$$

is the *dynamic amplification factor* of mode i. $D_i(\omega)$ is equal to 1 at $\omega = 0$, it exhibits large values in the vicinity of ω_i, $|D_i(\omega_i)| = (2\xi_i)^{-1}$, and then decreases beyond ω_i (Fig.2.2).

According to the definition of $G(\omega)$ the Fourier transform of the response $X(\omega)$ is related to the Fourier transform of the excitation $F(\omega)$ by

$$X(\omega) = G(\omega)F(\omega)$$

This equation means that all the frequency components work independently, and if the excitation has no energy at one frequency, there is no energy in the response at that frequency. From Fig.2.2, one sees that when the excitation has a limited bandwidth, $\omega < \omega_b$, the contribution of all the high frequency modes (i.e. such that $\omega_k \gg \omega_b$) to $G(\omega)$ can be evaluated by assuming $D_k(\omega) \simeq 1$. As a result, if $\omega_m > \omega_b$,

$$G(\omega) \simeq \sum_{i=1}^{m} \frac{\phi_i \phi_i^T}{\mu_i \omega_i^2} D_i(\omega) + \sum_{i=m+1}^{n} \frac{\phi_i \phi_i^T}{\mu_i \omega_i^2} \tag{2.20}$$

This approximation is valid for $\omega < \omega_m$. The first term in the right hand side is the contribution of all the modes which respond dynamically and the second term is a quasi-static correction for the high frequency modes. Taking into account that

$$G(0) = K^{-1} = \sum_{i=1}^{n} \frac{\phi_i \phi_i^T}{\mu_i \omega_i^2} \tag{2.21}$$

$G(\omega)$ can be rewritten in terms of the low frequency modes only:

$$G(\omega) \simeq \sum_{i=1}^{m} \frac{\phi_i \phi_i^T}{\mu_i \omega_i^2} D_i(\omega) + K^{-1} - \sum_{i=1}^{m} \frac{\phi_i \phi_i^T}{\mu_i \omega_i^2} \tag{2.22}$$

The quasi-static correction of the high frequency modes is often called the *residual mode*, denoted by R. Unlike all the terms involving $D_i(\omega)$ which reduce to 0 as $\omega \to \infty$, R is independent of the frequency and introduces a *feedthrough* (constant) component in the transfer matrix. We will shortly see that R has a strong influence on the location of the transmission zeros and that neglecting it may lead to substantial errors in the prediction of the performance of the control system.

2.4.3 Structure with rigid body modes

The approximation (2.22) applies only at low frequency, $\omega < \omega_m$. If the structure has r rigid body modes, the first sum can be split into rigid and flexible modes; however, the residual mode cannot be used any more, because K^{-1} no longer exists. This problem can be solved in the following way. The displacements are partitioned into their rigid and flexible contributions according to

$$x = x_r + x_e = \Phi_r z_r + \Phi_e z_e \tag{2.23}$$

where Φ_r and Φ_e are the matrices whose columns are the rigid body modes and the flexible modes, respectively. Assuming no damping, to make things formally simpler, and taking into account that the rigid body modes satisfy $K\Phi_r = 0$, we obtain the equation of motion

$$M\Phi_r \ddot{z}_r + M\Phi_e \ddot{z}_e + K\Phi_e z_e = f \tag{2.24}$$

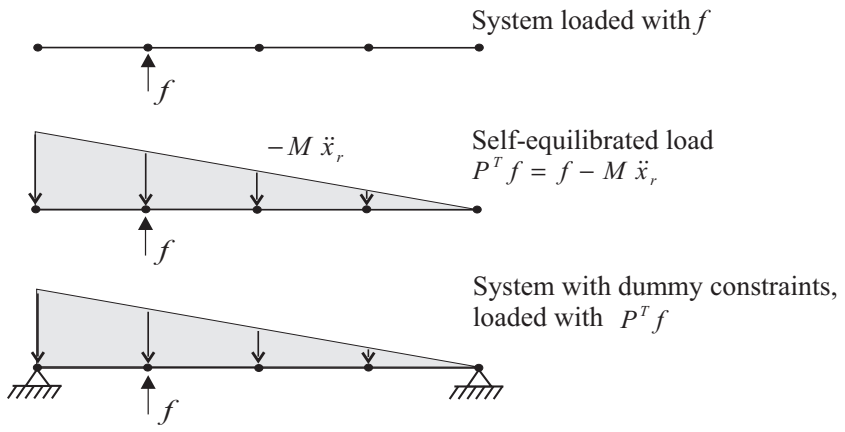

Fig. 2.3. Structure with rigid body modes.

Left multiplying by Φ_r^T and using the orthogonality relations (2.6) and (2.7), we see that the rigid body modes are governed by

$$\Phi_r^T M \Phi_r \, \ddot{z}_r = \Phi_r^T f$$

or

$$\ddot{z}_r = \mu_r^{-1} \Phi_r^T f \tag{2.25}$$

Substituting this result into Equ.(2.24), we get

$$M\Phi_e \ddot{z}_e + K\Phi_e z_e = f - M\Phi_r \ddot{z}_r$$

$$= f - M\Phi_r \mu_r^{-1} \Phi_r^T f = (I - M\Phi_r \mu_r^{-1} \Phi_r^T) f$$

or

$$M\Phi_e \ddot{z}_e + K\Phi_e z_e = P^T f \tag{2.26}$$

where we have defined the projection matrix

$$P = I - \Phi_r \mu_r^{-1} \Phi_r^T M \tag{2.27}$$

such that $P^T f$ is orthogonal to the rigid body modes. In fact, we can easily check that

$$P\Phi_r = 0 \tag{2.28}$$

$$P\Phi_e = \Phi_e \tag{2.29}$$

P can therefore be regarded as a filter which leaves unchanged the flexible modes and eliminates the rigid body modes.

If we follow the same procedure as in the foregoing section, we need to evaluate the elastic contribution of the static deflection, which is the solution of

$$Kx_e = P^T f \tag{2.30}$$

Since $K\Phi_r = 0$, the solution may contain an arbitrary contribution from the rigid body modes. On the other hand, $P^T f = f - M\ddot{x}_r$ is the superposition of the external forces and the inertia forces associated with the motion as a rigid body; it is self-equilibrated, because it is orthogonal to the rigid body modes. Since the system is in equilibrium as a rigid body, a particular solution of Equ.(2.30) can be obtained by adding *dummy constraints* to remove the rigid body modes (Fig.2.3). The modified system is statically determinate and its stiffness matrix can be inverted. If we denote by G_{iso} the flexibility matrix of the modified system, the general solution of (2.30) is

$$x_e = G_{iso}P^T f + \Phi_r \gamma$$

where γ is a vector of arbitrary constants. The contribution of the rigid body modes can be eliminated with the projection matrix P, leading to

$$x_e = PG_{iso}P^T f \tag{2.31}$$

$PG_{iso}P^T$ is the pseudo-static flexibility matrix of the flexible modes. On the other hand, left multiplying Equ.(2.24) by Φ_e^T, we get

$$\Phi_e^T M \Phi_e \ddot{z}_e + \Phi_e^T K \Phi_e z_e = \Phi_e^T f$$

where the diagonal matrix $\Phi_e^T K \Phi_e$ is regular. It follows that the pseudo-static deflection can be written alternatively

$$x_e = \Phi_e z_e = \Phi_e (\Phi_e^T K \Phi_e)^{-1} \Phi_e^T f \tag{2.32}$$

Comparing with Equ.(2.31), we get

$$PG_{iso}P^T = \Phi_e (\Phi_e^T K \Phi_e)^{-1} \Phi_e^T = \sum_{r+1}^{n} \frac{\phi_i \phi_i^T}{\mu_i \omega_i^2} \tag{2.33}$$

This equation is identical to Equ.(2.20) when there are no rigid body modes. From this result, we can extend Equ.(2.22) to systems with rigid body modes:

$$G(\omega) \simeq \sum_{i=1}^{r} \frac{\phi_i \phi_i^T}{-\mu_i \omega^2} + \sum_{i=r+1}^{m} \frac{\phi_i \phi_i^T}{\mu_i (\omega_i^2 - \omega^2 + 2j\xi_i \omega_i \omega)} + R \tag{2.34}$$

where the contribution from the residual mode is

$$R = \sum_{m+1}^{n} \frac{\phi_i \phi_i^T}{\mu_i \omega_i^2} = P G_{iso} P^T - \sum_{r+1}^{m} \frac{\phi_i \phi_i^T}{\mu_i \omega_i^2} \tag{2.35}$$

Note that G_{iso} is the flexibility matrix of the system obtained by adding dummy constraints to remove the rigid body modes. Obviously, this can be achieved in many different ways and it may look surprising that they all lead to the same result (2.35). In fact, different boundary conditions lead to different displacements under the self-equilibrated load $P^T f$, but they differ only by a contribution of the rigid body modes, which is destroyed by the projection matrix P, leading to the same $P G_{iso} P^T$. Let us illustrate the procedure with an example.

2.4.4 Example

Consider the system of three identical masses of Fig.2.4. There is one rigid body mode and two flexible ones:

$$\Phi = (\Phi_r, \Phi_e) = \begin{pmatrix} 1 & 1 & 1 \\ 1 & 0 & -2 \\ 1 & -1 & 1 \end{pmatrix}$$

and

$$\Phi^T M \Phi = diag(3, 2, 6) \qquad \Phi^T K \Phi = k.diag(0, 2, 18)$$

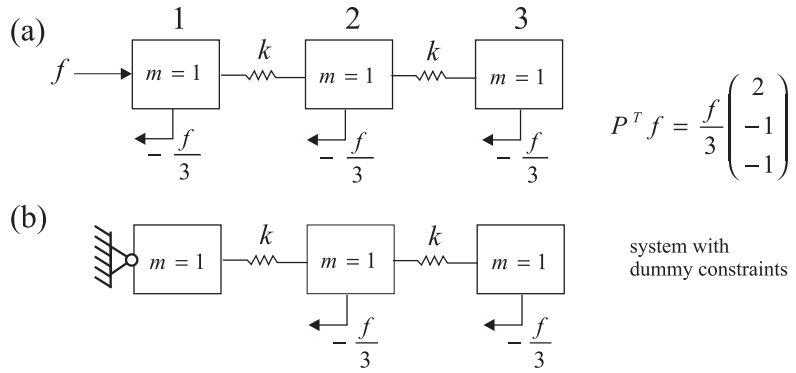

Fig. 2.4. Three mass system: (a) self-equilibrated forces associated with a force f applied to mass 1; (b) dummy constraints.

From Equ.(2.27), the projection matrix is

$$P = \begin{pmatrix} 1 & 0 & 0 \\ 0 & 1 & 0 \\ 0 & 0 & 1 \end{pmatrix} - \begin{pmatrix} 1 \\ 1 \\ 1 \end{pmatrix} . \frac{1}{3} . (1,\ 1,\ 1) = \begin{pmatrix} 1 & 0 & 0 \\ 0 & 1 & 0 \\ 0 & 0 & 1 \end{pmatrix} - \frac{1}{3} \begin{pmatrix} 1 & 1 & 1 \\ 1 & 1 & 1 \\ 1 & 1 & 1 \end{pmatrix}$$

or

$$P = \frac{1}{3} \begin{pmatrix} 2 & -1 & -1 \\ -1 & 2 & -1 \\ -1 & -1 & 2 \end{pmatrix}$$

We can readily check that

$$P\Phi = P(\Phi_r, \Phi_e) = (0, \Phi_e)$$

and the self-equilibrated loads associated with a force f applied to mass 1 is, Fig.2.4.a

$$P^T f = \frac{1}{3} \begin{pmatrix} 2 & -1 & -1 \\ -1 & 2 & -1 \\ -1 & -1 & 2 \end{pmatrix} \begin{pmatrix} f \\ 0 \\ 0 \end{pmatrix} = \begin{pmatrix} 2/3 \\ -1/3 \\ -1/3 \end{pmatrix} f$$

If we impose the statically determinate constraint on mass 1, Fig.2.4.b, the resulting flexibility matrix is

$$G_{iso} = \frac{1}{k} \begin{pmatrix} 0 & 0 & 0 \\ 0 & 1 & 1 \\ 0 & 1 & 2 \end{pmatrix}$$

leading to

$$PG_{iso}P^T = \frac{1}{9k} \begin{pmatrix} 5 & -1 & -4 \\ -1 & 2 & -1 \\ -4 & -1 & 5 \end{pmatrix}$$

The reader can easily check that other dummy constraints would lead to the same pseudo-static flexibility matrix (Problem 2.3).

2.5 Collocated control system

A collocated control system is a control system where the actuator and the sensor are attached to the same degree of freedom. It is not sufficient to be attached to the same location, but they must also be *dual*, that is a force actuator must be associated with a translation sensor (measuring

displacement, velocity or acceleration), and a torque actuator with a rotation sensor (measuring an angle or an angular velocity), in such a way that the product of the actuator signal and the sensor signal represents the energy (power) exchange between the structure and the control system. Such systems enjoy very interesting properties. The open-loop Frequency Response Function (FRF) of a collocated control system corresponds to a diagonal component of the dynamic flexibility matrix. If the actuator and sensor are attached to d.o.f. k, the open-loop FRF reads

$$G_{kk}(\omega) = \sum_{i=1}^{m} \frac{\phi_i^2(k)}{\mu_i \omega_i^2} D_i(\omega) + R_{kk} \tag{2.36}$$

If one assumes that the system is undamped, the FRF is purely real

$$G_{kk}(\omega) = \sum_{i=1}^{m} \frac{\phi_i^2(k)}{\mu_i (\omega_i^2 - \omega^2)} + R_{kk} \tag{2.37}$$

All the residues are positive (square of the modal amplitude) and, as a result, $G_{kk}(\omega)$ is a monotonously increasing function of ω, which behaves as illustrated in Fig.2.5. The amplitude of the FRF goes from $-\infty$ at the resonance frequencies ω_i (corresponding to a pair of imaginary poles at $s = \pm j\omega_i$ in the open-loop transfer function) to $+\infty$ at the next resonance frequency ω_{i+1}. Since the function is continuous, in every interval, there is a frequency z_i such that $\omega_i < z_i < \omega_{i+1}$ where the amplitude of the

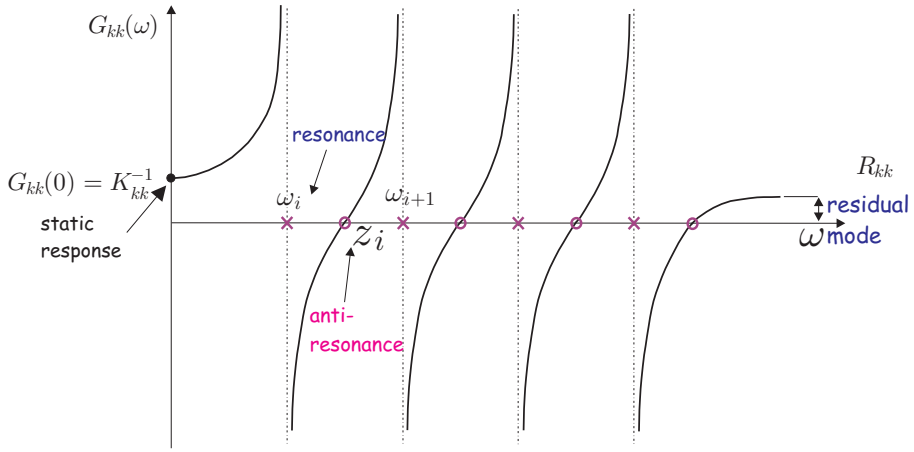

Fig. 2.5. Open-loop FRF of an undamped structure with a collocated actuator/sensor pair (no rigid body modes).

FRF vanishes. In structural dynamics, such frequencies are called *anti-resonances*; they correspond to purely imaginary zeros at $\pm jz_i$, in the open-loop transfer function. Thus, *undamped collocated control systems have alternating poles and zeros on the imaginary axis.* The pole / zero pattern is that of Fig.2.6.a. For a lightly damped structure, the poles and zeros are just moved a little in the left-half plane, but they are still *interlacing*, Fig.2.6.b.

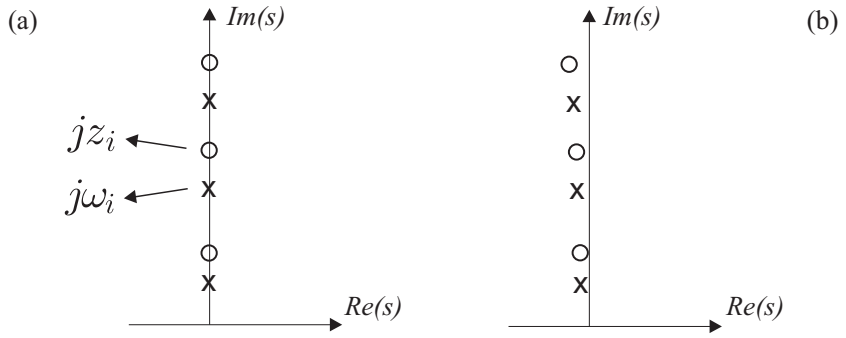

Fig. 2.6. Pole/Zero pattern of a structure with collocated (dual) actuator and sensor; (a) undamped; (b) lightly damped (only the upper half of the complex plane is shown, the diagram is symmetrical with respect to the real axis).

If the undamped structure is excited harmonically by the actuator at the frequency of the transmission zero, z_i, the amplitude of the response of the collocated sensor vanishes. This means that the structure oscillates at the frequency z_i according to the shape shown in dotted line on Fig.2.7.b. We will establish in the next section that this shape, and the frequency z_i, are actually a mode shape and a natural frequency of the system obtained by constraining the d.o.f. on which the control system acts. We know from control theory that the open-loop zeros are asymptotic values of the closed-loop poles, when the feedback gain goes to infinity.

The natural frequencies of the constrained system depend on the d.o.f. where the constraint has been added (this is indeed well known in control theory that the open-loop poles are independent of the actuator and sensor configuration while the open-loop zeros do depend on it). However, from the foregoing discussion, for every actuator/sensor configuration, there will be one and only one zero between two consecutive poles, and the interlacing property applies for any location of the collocated pair.

Referring once again to Fig.2.5, one easily sees that neglecting the residual mode in the modelling amounts to translating the FRF diagram

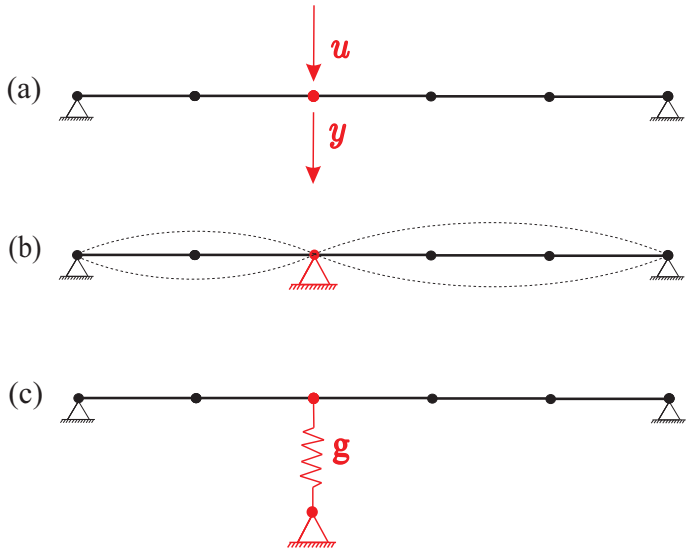

Fig. 2.7. (a) Structure with collocated actuator and sensor; (b) structure with additional constraint; (c) structure with additional stiffness along the controlled d.o.f.

vertically in such a way that its high frequency asymptote becomes tangent to the frequency axis. This produces a shift in the location of the transmission zeros to the right, and the last one even moves to infinity as the feedthrough (constant) component R_{kk} disappears from the FRF. Thus, neglecting the residual modes tends to overestimate the frequency of the transmission zeros. As we shall see shortly, the closed-loop poles which remain at finite distance move on loops joining the open-loop poles to the open-loop zeros; therefore, altering the open-loop pole/zero pattern has a direct impact on the closed-loop poles.

The open-loop transfer function of a undamped structure with a collocated actuator/sensor pair can be written

$$G(s) = G_0 \frac{\prod_i (s^2/z_i^2 + 1)}{\prod_j (s^2/\omega_j^2 + 1)} \qquad (\omega_i < z_i < \omega_{i+1}) \tag{2.38}$$

For a lightly damped structure, it reads

$$G(s) = G_0 \frac{\prod_i (s^2/z_i^2 + 2\xi_i s/z_i + 1)}{\prod_j (s^2/\omega_j^2 + 2\xi_j s/\omega_j + 1)} \tag{2.39}$$

The corresponding Bode and Nyquist plots are represented in Fig 2.8. Every imaginary pole at $\pm j\omega_i$ introduces a 180^0 phase lag and every

imaginary zero at $\pm jz_i$ a 180^0 phase lead. In this way, the phase diagram is always contained between 0 and -180^0, as a consequence of the interlacing property. For the same reason, the Nyquist diagram consists of a set of nearly circles (one per mode), all contained in the third and fourth quadrants. Thus, the entire curve $G(\omega)$ is below the real axis (the diameter of every circle is proportional to ξ_i^{-1}).

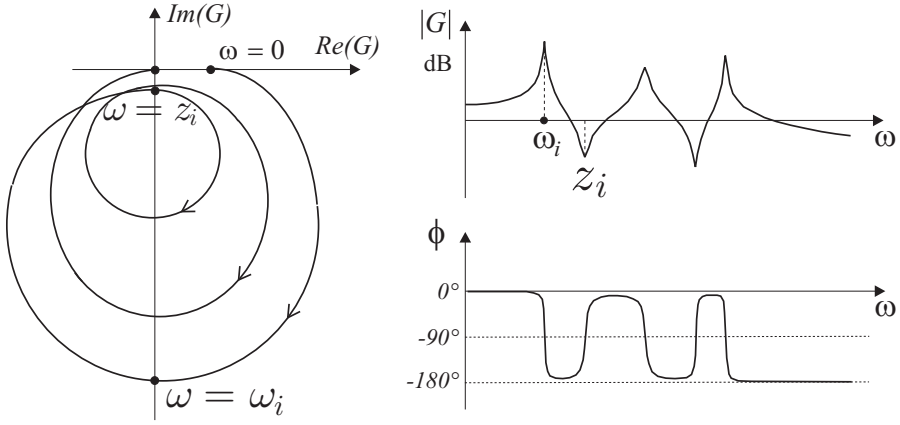

Fig. 2.8. Nyquist diagram and Bode plots of a lightly damped structure with collocated actuator and sensor.

2.5.1 Transmission zeros and constrained system

We now establish that the transmission zeros of the undamped system are the poles (natural frequencies) of the constrained system. Consider the undamped structure of Fig.2.7.a (a displacement sensor is assumed for simplicity). The governing equations are

Structure:

$$M\ddot{x} + Kx = b\,u \tag{2.40}$$

Output sensor:

$$y = b^T x \tag{2.41}$$

u is the actuator input (scalar) and y is the sensor output (also scalar). The fact that the same vector b appears in the two equations is due to collocation. For a stationary harmonic input at the actuator, $u = u_0 e^{j\omega_0 t}$; the response is harmonic, $x = x_0 e^{j\omega_0 t}$, and the amplitude vector x_0 is solution of

$$(K - \omega_0^2 M)x_0 = b\,u_0 \tag{2.42}$$

The sensor output is also harmonic, $y = y_0 e^{j\omega_0 t}$ and the output amplitude is given by

$$y_0 = b^T x_0 = b^T (K - \omega_0^2 M)^{-1} b\,u_0 \tag{2.43}$$

Thus, the transmission zeros (antiresonance frequencies) ω_0 are solutions of

$$b^T (K - \omega_0^2 M)^{-1} b = 0 \tag{2.44}$$

Now, consider the system with the additional stiffness g along the same d.o.f. as the actuator/sensor, Fig 2.7.c. The stiffness matrix of the modified system is $K + gbb^T$. The natural frequencies of the modified system are solutions of the eigenvalue problem

$$[K + gbb^T - \omega^2 M]\phi = 0 \tag{2.45}$$

For all g the solution (ω, ϕ) of the eigenvalue problem is such that

$$(K - \omega^2 M)\phi + gbb^T\phi = 0 \tag{2.46}$$

or

$$b^T\phi = -b^T (K - \omega^2 M)^{-1} gbb^T\phi \tag{2.47}$$

Since $b^T\phi$ is a scalar, this implies that

$$b^T (K - \omega^2 M)^{-1} b = -\frac{1}{g} \tag{2.48}$$

Taking the limit for $g \to \infty$, one sees that the eigenvalues ω satisfy

$$b^T (K - \omega^2 M)^{-1} b = 0 \tag{2.49}$$

which is identical to (2.44). Thus, $\omega = \omega_0$; the imaginary zeros of the undamped collocated system, solutions of (2.44), are the poles of the constrained system (2.45) at the limit, when the stiffness g added along the actuation d.o.f. increases to ∞:

$$\lim_{g\to\infty} [(K + gbb^T) - \omega_0^2 M]x_0 = 0 \tag{2.50}$$

This is equivalent to placing a kinematic constraint along the control d.o.f.

2.6 Continuous structures

Continuous structures are distributed parameter systems which are governed by partial differential equations. Various discretization techniques, such as the Rayleigh-Ritz method, or finite elements, allow us to approximate the partial differential equation by a finite set of ordinary differential equations. In this section, we illustrate some of the features of distributed parameter systems with continuous beams. This example will be frequently used in the subsequent chapters.

The plane transverse vibration of a beam is governed by the following partial differential equation

$$(EIw'')'' + m\ddot{w} = p \tag{2.51}$$

This equation is based on the Euler-Bernoulli assumptions that the neutral axis undergoes no extension and that the cross section remains perpendicular to the neutral axis (no shear deformation). EI is the bending stiffness, m is the mass per unit length and p the distributed external load per unit length. If the beam is uniform, the free vibration is governed by

$$w^{IV} + \frac{m}{EI}\ddot{w} = 0 \tag{2.52}$$

The boundary conditions depend on the support configuration: a simple support implies $w = 0$ and $w'' = 0$ (no displacement, no bending moment); for a clamped end, we have $w = 0$ and $w' = 0$ (no displacement, no rotation); a free end corresponds to $w'' = 0$ and $w''' = 0$ (no bending moment, no shear), etc...

A harmonic solution of the form $w(x,t) = \phi(x)\,\mathrm{e}^{j\omega t}$ can be obtained if $\phi(x)$ and ω satisfy

$$\frac{\mathrm{d}^4\phi}{\mathrm{d}x^4} - \frac{m}{EI}\omega^2\phi = 0 \tag{2.53}$$

with the appropriate boundary conditions. This equation defines a eigenvalue problem; the solution consists of the natural frequencies ω_i (infinite in number) and the corresponding mode shapes $\phi_i(x)$. The eigenvalues are tabulated for various boundary conditions in textbooks on mechanical vibrations (e.g. Geradin & Rixen, 1993, p.187). For the pinned-pinned case, the natural frequencies and mode shapes are

$$\omega_n^2 = (n\pi)^4 \frac{EI}{ml^4} \tag{2.54}$$

$$\phi_n(x) = \sin \frac{n\pi x}{l} \tag{2.55}$$

Just as for discrete systems, the mode shapes are orthogonal with respect to the mass and stiffness distribution:

$$\int_0^l m\, \phi_i(x)\phi_j(x)\, dx = \mu_i \delta_{ij} \tag{2.56}$$

$$\int_0^l EI\, \phi_i''(x)\phi_j''(x)\, dx = \mu_i \omega_i^2 \delta_{ij} \tag{2.57}$$

The generalized mass corresponding to Equ.(2.55) is $\mu_n = ml/2$. As with discrete structures, the frequency response function between a point force actuator at x_a and a displacement sensor at x_s is

$$G(\omega) = \sum_{i=1}^{\infty} \frac{\phi_i(x_a)\phi_i(x_s)}{\mu_i(\omega_i^2 - \omega^2 + 2j\xi_i\omega_i\omega)} \tag{2.58}$$

where the sum extends to infinity. Exactly as for discrete systems, the expansion can be limited to a finite set of modes, the high frequency modes being included in a quasi-static correction as in Equ.(2.34) (Problem 2.5).

2.7 Guyan reduction

As already mentioned, the size of a discretized model obtained by finite elements is essentially governed by the representation of the stiffness of the structure. For complicated geometries, it may become very large, especially with automated mesh generators. Before solving the eigenvalue problem (2.5), it may be advisable to reduce the size of the model by condensing the degrees of freedom with little or no inertia and which are not excited by external forces, nor involved in the control. The degrees of freedom to be condensed, denoted x_2 in what follows, are often referred to as *slaves*; those kept in the reduced model are called *masters* and are denoted x_1.

To begin with, consider the undamped forced vibration of a structure where the slaves x_2 are not excited and have no inertia; the governing equation is

$$\begin{pmatrix} M_{11} & 0 \\ 0 & 0 \end{pmatrix} \begin{pmatrix} \ddot{x}_1 \\ \ddot{x}_2 \end{pmatrix} + \begin{pmatrix} K_{11} & K_{12} \\ K_{21} & K_{22} \end{pmatrix} \begin{pmatrix} x_1 \\ x_2 \end{pmatrix} = \begin{pmatrix} f_1 \\ 0 \end{pmatrix} \tag{2.59}$$

or

$$M_{11}\ddot{x}_1 + K_{11}x_1 + K_{12}x_2 = f_1 \tag{2.60}$$

$$K_{21}x_1 + K_{22}x_2 = 0 \tag{2.61}$$

According to the second equation, the slaves x_2 are completely determined by the masters x_1:

$$x_2 = -K_{22}^{-1}K_{21}x_1 \tag{2.62}$$

Substituting into Equ.(2.60), we find the reduced equation

$$M_{11}\ddot{x}_1 + (K_{11} - K_{12}K_{22}^{-1}K_{21})x_1 = f_1 \tag{2.63}$$

which involves only x_1. Note that in this case, the reduced equation has been obtained without approximation.

The idea in the so-called *Guyan reduction* is to assume that the master-slave relationship (2.62) applies even if the degrees of freedom x_2 have some inertia (i.e. when the sub-matrix $M_{22} \neq 0$) or applied forces. Thus, one *assumes* the following transformation

$$x = \begin{pmatrix} x_1 \\ x_2 \end{pmatrix} = \begin{pmatrix} I \\ -K_{22}^{-1}K_{21} \end{pmatrix} x_1 = Lx_1 \tag{2.64}$$

The reduced mass and stiffness matrices are obtained by substituting the above transformation into the kinetic and strain energy:

$$\mathcal{T} = \frac{1}{2}\dot{x}^T M\dot{x} = \frac{1}{2}\dot{x}_1^T L^T ML\dot{x}_1 = \frac{1}{2}\dot{x}_1^T \hat{M}\dot{x}_1$$

$$\mathcal{U} = \frac{1}{2}x^T Kx = \frac{1}{2}x_1^T L^T KLx_1 = \frac{1}{2}x_1^T \hat{K}x_1$$

with

$$\hat{M} = L^T ML \qquad \hat{K} = L^T KL \tag{2.65}$$

The second equation produces $\hat{K} = K_{11} - K_{12}K_{22}^{-1}K_{21}$ as in Equ.(2.63). If external loads are applied to x_2, the reduced loads are obtained by equating the virtual work

$$\delta x^T f = \delta x_1^T L^T f = \delta x_1^T \hat{f}_1$$

or

$$\hat{f}_1 = L^T f = f_1 - K_{12}K_{22}^{-1}f_2 \tag{2.66}$$

Finally, the reduced equation of motion reads

$$\hat{M}\ddot{x}_1 + \hat{K}x_1 = \hat{f}_1 \tag{2.67}$$

Usually, it is not necessary to consider the damping matrix in the reduction, because it is rarely known explicitly at this stage. The Guyan reduction can be performed automatically in commercial finite element packages, the selection of masters and slaves being made by the user. In the selection process the following should be kept in mind:

- The degrees of freedom without inertia or applied load can be condensed without affecting the accuracy.
- Translational degrees of freedom carry more information than rotational ones. In selecting the masters, preference should be given to translations, especially if large modal amplitudes are expected (Problem 2.7).
- It can be demonstrated that the error in the mode shape ϕ_i associated with the Guyan reduction is a increasing function of the ratio

$$\frac{\omega_i^2}{\nu_1^2}$$

where ω_i is the natural frequency of the mode and ν_1 is the first natural frequency of the constrained system, where all the degrees of freedom x_1 (masters) have been blocked [ν_1 is the smallest solution of $\det(K_{22} - \nu^2 M_{22}) = 0$]. Therefore, the quality of a Guyan reduction is strongly related to the natural frequencies of the constrained system and ν_1 should be kept far above the frequency band ω_b where the model is expected to be accurate. If this is not the case, the model reduction can be improved as follows.

2.8 Craig-Bampton reduction

Consider the finite element model

$$\begin{pmatrix} M_{11} & M_{12} \\ M_{21} & M_{22} \end{pmatrix} \begin{pmatrix} \ddot{x}_1 \\ \ddot{x}_2 \end{pmatrix} + \begin{pmatrix} K_{11} & K_{12} \\ K_{21} & K_{22} \end{pmatrix} \begin{pmatrix} x_1 \\ x_2 \end{pmatrix} = \begin{pmatrix} f_1 \\ 0 \end{pmatrix} \tag{2.68}$$

where the degrees of freedom have been partitioned into the masters x_1 and the slaves x_2. The masters include all the d.o.f. with a specific interest in the problem: those where disturbance and control loads are applied, where sensors are located and where the performance is evaluated (controlled d.o.f.). The slaves include all the other d.o.f. which have no particular interest in the control problem and are ready for elimination.

The *Craig-Bampton reduction* is conducted in two steps. First, a Guyan reduction is performed according to the static relationship (2.62). In a second step, the constrained system is considered:

$$M_{22}\ddot{x}_2 + K_{22}x_2 = 0 \tag{2.69}$$

(obtained by setting $x_1 = 0$ in the foregoing equation). Let us assume that the eigen modes of this system constitute the column of the matrix Ψ_2, and that they are normalized according to $\Psi_2^T M_{22}\Psi_2 = I$. We then perform the change of coordinates

$$\begin{pmatrix} x_1 \\ x_2 \end{pmatrix} = \begin{pmatrix} I & 0 \\ -K_{22}^{-1}K_{21} & \Psi_2 \end{pmatrix} \begin{pmatrix} x_1 \\ \alpha \end{pmatrix} = T \begin{pmatrix} x_1 \\ \alpha \end{pmatrix} \tag{2.70}$$

Comparing with (2.64), one sees that the solution has been enriched with a set of fixed boundary modes of modal amplitude α. Using the transformation matrix T, the mass and stiffness matrices are obtained as in the previous section:

$$\hat{M} = T^T M T \qquad\qquad \hat{K} = T^T K T \tag{2.71}$$

leading to

$$\begin{pmatrix} \hat{M}_{11} & \hat{M}_{12} \\ \hat{M}_{12} & I \end{pmatrix} \begin{pmatrix} \ddot{x}_1 \\ \ddot{\alpha} \end{pmatrix} + \begin{pmatrix} \hat{K}_{11} & 0 \\ 0 & \Omega^2 \end{pmatrix} \begin{pmatrix} x_1 \\ \alpha \end{pmatrix} = \begin{pmatrix} f_1 \\ 0 \end{pmatrix} \tag{2.72}$$

In this equation, the stiffness matrix is block diagonal, with $\hat{K}_{11} = K_{11} - K_{12}K_{22}^{-1}K_{21}$ being the Guyan stiffness matrix and $\Omega^2 = \Psi_2^T K_{22}\Psi_2$ being a diagonal matrix with entries equal to the square of the natural frequencies of the fixed boundary modes. Similarly, $\hat{M}_{11} = M_{11} - M_{12}K_{22}^{-1}K_{21} - K_{12}K_{22}^{-1}M_{21} + K_{12}K_{22}^{-1}M_{22}K_{22}^{-1}K_{21}$ is the Guyan mass matrix [the same as that given by (2.65)]. $\hat{K}_{11}$ and $\hat{M}_{11}$ are fully populated but do not depend on the set of constrained modes Ψ_2. The off-diagonal term of the mass matrix is given by $\hat{M}_{12} = (M_{12} - K_{12}K_{22}^{-1}M_{22})\Psi_2$. Since all the external loads are applied to the master d.o.f., the right hand side of this equation is unchanged by the transformation. The foregoing equation may be used with an increasing number of constrained modes (increasing the size of α), until the model provides an appropriate representation of the system in the requested frequency band.

2.9 References

BATHE, K.J. & WILSON, E.L. *Numerical Methods in Finite Element Analysis*, Prentice-Hall, 1976.
CANNON, R.H. *Dynamics of Physical Systems*, McGraw-Hill, 1967.
CLOUGH, R.W. & PENZIEN, J. *Dynamics of Structures*, McGraw-Hill, 1975.
CRAIG, R.R. *Structural Dynamics*, Wiley, 1981.
CRAIG, R.R., BAMPTON, M.C.C. Coupling of Substructures for Dynamic Analyses, *AIAA Journal*, Vol.6(7), 1313-1319, 1968.
GAWRONSKI, W.K. *Advanced Structural Dynamics and Active Control of Structures*, Springer, 2004.
GERADIN, M. & RIXEN, D. *Mechanical Vibrations, Theory and Application to Structural Dynamics*, Wiley, 1993.
HUGHES, P.C. Attitude dynamics of three-axis stabilized satellite with a large flexible solar array, *J. Astronautical Sciences, Vol.20, 166-189, Nov.-Dec. 1972.*
HUGHES, P.C. Dynamics of flexible space vehicles with active attitude control, *Celestial Mechanics Journal, Vol.9, 21-39, March 1974.*
HUGHES, T.J.R. *The Finite Element Method, Linear Static and Dynamic Finite Element Analysis*, Prentice-Hall, 1987.
INMAN, D.J. *Vibration, with Control, Measurement, and Stability.* Prentice-Hall, 1989.
MEIROVITCH, L. *Computational Methods in Structural Dynamics*, Sijthoff & Noordhoff, 1980.
MODI, V.J. Attitude dynamics of satellites with flexible appendages - A brief review. *AIAA J. Spacecraft and Rockets*, Vol.11, 743-751, 1974.
ZIENKIEWICZ, O.C., & TAYLOR, R.L. *The Finite Element Method*, Fourth edition (2 vol.), McGraw-Hill, 1989.

2.10 Problems

P.2.1 *Using a finite element program, discretize a simply supported uniform beam with an increasing number of elements (4,8,etc...). Compare the natural frequencies with those obtained with the continuous beam theory. Observe that the finite elements tend to overestimate the natural frequencies. Why is that so?*

P.2.2 *Using the same stiffness matrix as in the previous example and a diagonal mass matrix obtained by lumping the mass of every element at the nodes (the entries of the mass matrix for all translational degrees of freedom are ml/n_E, where n_E is the number of elements; no inertia is attributed to the rotations), compute the natural frequencies. Compare the results with those obtained with a consistent mass matrix in Problem 2.1. Notice that using a diagonal mass matrix usually tends to underestimate the natural frequencies.*

P.2.3 *Consider the three mass system of section 2.4.4. Show that changing the dummy constraint to mass 2 does not change the pseudo-static flexibility matrix $PG_{iso}P^T$.*

P.2.4 *Consider a simply supported beam with the following properties: $l = 1m$, $m = 1kg/m$, $EI = 10.266\ 10^{-3}Nm^2$. It is excited by a point force at $x_a = l/4$.*

(a) Assuming that a displacement sensor is located at $x_s = l/4$ (collocated) and that the system is undamped, plot the transfer function for an increasing number of modes, with and without quasi-static correction for the high-frequency modes. Comment on the variation of the zeros with the number of modes and on the absence of mode 4.

Note: To evaluate the quasi-static contribution of the high-frequency modes, it is useful to recall that the static displacement at $x = \xi$ created by a unit force applied at $x = a$ on a simply supported beam is

$$\delta(\xi, a) = \frac{(l-a)\xi}{6lEI}[a(2l-a) - \xi^2] \quad (\xi \leq a)$$

$$\delta(\xi, a) = \frac{a(l-\xi)}{6lEI}[\xi(2l-\xi) - a^2] \quad (\xi > a)$$

The symmetric operator $\delta(\xi, a)$ is often called "flexibility kernel" or Green's function.

(b) Including three modes and the quasi-static correction, draw the Nyquist and Bode plots and locate the poles and zeros in the complex plane for a uniform modal damping of $\xi_i = 0.01$ and $\xi_i = 0.03$.

(c) Do the same as (b) when the sensor location is $x_s = 3l/4$. Notice that the interlacing property of the poles and zeros no longer holds.

P.2.5 *Consider the modal expansion of the transfer function (2.58) and assume that the low frequency amplitude $G(0)$ is available, either from static calculations or from experiments at low frequency. Show that $G(\omega)$ can be approximated by the truncated expansion*

$$G(\omega) = G(0) + \sum_{i=1}^{m} \frac{\phi_i(x_a)\phi_i(x_s)}{\mu_i \omega_i^2} \frac{(\omega^2 - 2j\xi_i\omega_i\omega)}{(\omega_i^2 - \omega^2 + 2j\xi_i\omega_i\omega)}$$

P.2.6 *Show that the impulse response matrix of a damped structure with rigid body modes reads*

$$g(\tau) = \left[\sum_{i=1}^{r} \frac{\phi_i \phi_i^T}{\mu_i} \tau + \sum_{r+1}^{n} \frac{\phi_i \phi_i^T}{\mu_i \omega_{di}} \mathrm{e}^{-\xi_i \omega_i \tau} \sin \omega_{di} \tau \right] \mathbf{1}(\tau)$$

where $\omega_{di} = \omega_i \sqrt{1 - \xi_i^2}$ and $\mathbf{1}(\tau)$ is the Heaviside step function.

P.2.7 *Consider a uniform beam clamped at one end and free at the other end; it is discretized with six finite elements of equal size. The twelve degrees of freedom are numbered w_1, θ_1 to w_6, θ_6 starting from the clamped end. We perform various Guyan reductions in which we select x_1 according to:*
(a) all w_i, θ_i (12 degrees of freedom, no reduction);
(b) all w_i (6 d.o.f.);
(c) all θ_i (6 d.o.f.);
(d) $w_2, \theta_2, w_4, \theta_4, w_6, \theta_6$ (6 d.o.f.);
(e) w_2, w_4, w_6 (3 d.o.f.);
(f) $\theta_2, \theta_4, \theta_6$ (3 d.o.f.);
For each case, compute the natural frequency ω_i of the first three modes and the first natural frequency ν_1 of the constrained system. Compare the roles of the translations and rotations.

P.2.8 *Consider a spacecraft consisting of a rigid main body to which one or several flexible appendages are attached. Assume that there is at least one axis about which the attitude motion is uncoupled from the other axes. Let θ be the (small) angle of rotation about this axis and J be the moment of inertia (of the main body plus the appendages). Show that the equations of motion read*

$$J\ddot{\theta} - \sum_{i=1}^{m} \Gamma_i \ddot{z}_i = T_0$$

$$\mu_i \ddot{z}_i + \mu_i \Omega_i^2 z_i - \Gamma_i \ddot{\theta} = 0 \qquad i = 1, ..., m$$

where T_0 is the torque applied to the main body, μ_i and Ω_i are the modal masses and the natural frequencies of the constrained modes of the flexible appendages and Γ_i are the modal participation factors of the flexible modes [i.e. Γ_i is the work done on mode i of the flexible appendages by the inertia forces associated with a unit angular acceleration of the main body] (Hughes, 1974). [Hint: Decompose the motion into the rigid body mode and the components of the constrained flexible modes, express the kinetic energy and the strain energy, write the Lagrangian in the form

$$L = T - V = \frac{1}{2} J \dot{\theta}^2 - \sum_i \Gamma_i \dot{z}_i \dot{\theta} + \frac{1}{2} \sum_i \mu_i \dot{z}_i^2 - \frac{1}{2} \sum_i \mu_i \Omega_i^2 z_i$$

and write the Lagrange equations.]

3

Electromagnetic and piezoelectric transducers

3.1 Introduction

The transducers are critical in active structures technology; they can play the role of actuator, sensor, or simply energy converter, depending on the applications. In many applications, the actuators are the most critical part of the system; however, the sensors become very important in precision engineering where sub-micron amplitudes must be detected.

Two broad categories of actuators can be distinguished: "grounded" and "structure borne" actuators. The former react on a fixed support; they include torque motors, force motors (electrodynamic shakers) or tendons. The second category, also called "space realizable", include jets, reaction wheels, control moment gyros, proof-mass actuators, active members (capable of both structural functions and generating active control forces), piezo strips, etc... Active members and all actuating devices involving only internal, self-equilibrating forces, cannot influence the rigid body motion of a structure.

This chapter begins with a description of the voice-coil transducer and its application to the proof-mass actuator and the geophone (absolute velocity sensor). Follows a brief discussion of the single axis gyrostabilizer. The remaining of the chapter is devoted to the piezoelectric materials and the constitutive equations of a discrete piezoelectric transducer. Integrating piezoelectric elements in beams, plates and trusses will be considered in the following chapter.

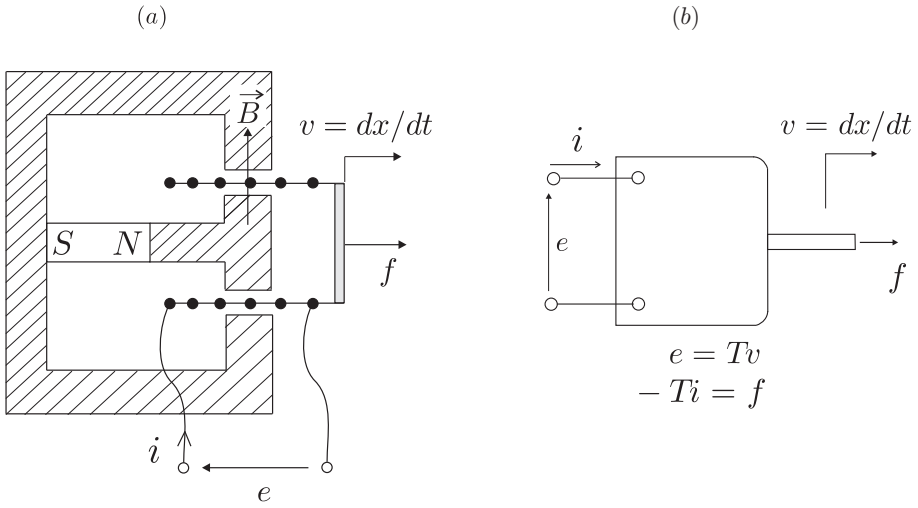

Fig. 3.1. Voice-coil transducer: (a) Physical principle. (b) Symbolic representation.

3.2 Voice coil transducer

A voice coil transducer is an energy transformer which converts electrical power into mechanical power and vice versa. The system consists of a permanent magnet (Fig.3.1) which produces a uniform magnetic flux density B normal to the gap, and a coil which is free to move axially within the gap. Let v be the velocity of the coil, f the external force acting to maintain the coil in equilibrium against the electromagnetic forces, e the voltage difference across the coil and i the current into the coil. In this ideal transducer, we neglect the electrical resistance and the self inductance of the coil, as well as its mass and damping (if necessary, these can be handled by adding R and L to the electrical circuit of the coil, or a mass and damper to its mechanical model). The *voice coil* actuator is one of the most popular actuators in mechatronics (e.g. it is used in electromagnetic loudspeakers), but it is also used as sensor in geophones.

The first constitutive equation of the voice coil transducer follows from Faraday's law:

$$e = 2\pi nrBv = Tv \tag{3.1}$$

where

$$T = 2\pi nrB \tag{3.2}$$

is the *transducer constant*, equal to the product of the length of the coil exposed to the magnetic flux, $2\pi nr$, and the magnetic flux density B. The

second equation follows from the Lorentz force law: The external force f required to *balance* the total force of the magnetic field on n turns of the conductor is

$$f = -i\,2\pi nrB = -Ti \tag{3.3}$$

where T is again the transducer constant (3.2). Equation (3.1) and (3.3) are the constitutive equations of the voice coil transducer. Notice that the transducer constant T appearing in Faraday's law (3.1), expressed in $volt.sec/m$, is the same as that appearing in the Lorentz force (3.3), expressed in N/Amp.

The total power delivered to the moving-coil transducer is equal to the sum of the electric power, ei, and the mechanical power, fv. Combining with (3.1) and (3.3), one gets

$$ei + fv = Tvi - Tiv = 0 \tag{3.4}$$

Thus, at any time, there is an equilibrium between the electrical power absorbed by the device and the mechanical power delivered (and vice versa). The moving-coil transducer cannot store energy, and behaves as a perfect electromechanical converter. In practice, however, the transfer is never perfect due to eddy currents, flux leakage and magnetic hysteresis, leading to slightly different values of T in (3.1) and (3.3).

3.2.1 Proof-mass actuator

A proof-mass actuator (Fig.3.2) is an inertial actuator which is used in various applications of vibration control. A reaction mass m is connected to the support structure by a spring k, a damper c and a force actuator f which can be either magnetic or hydraulic. In the electromagnetic actuator discussed here, the force actuator consists of a voice coil transducer of constant T excited by a current generator i; the spring is achieved with membranes which also guide the linear motion of the moving mass. The system is readily modelled as in Fig.3.2.a. Combining the equation of a single d.o.f. oscillator with the Lorentz force law (3.3), one finds

$$m\ddot{x} + c\dot{x} + kx = Ti \tag{3.5}$$

or, in the Laplace domain,

$$x = \frac{Ti}{ms^2 + cs + k} \tag{3.6}$$

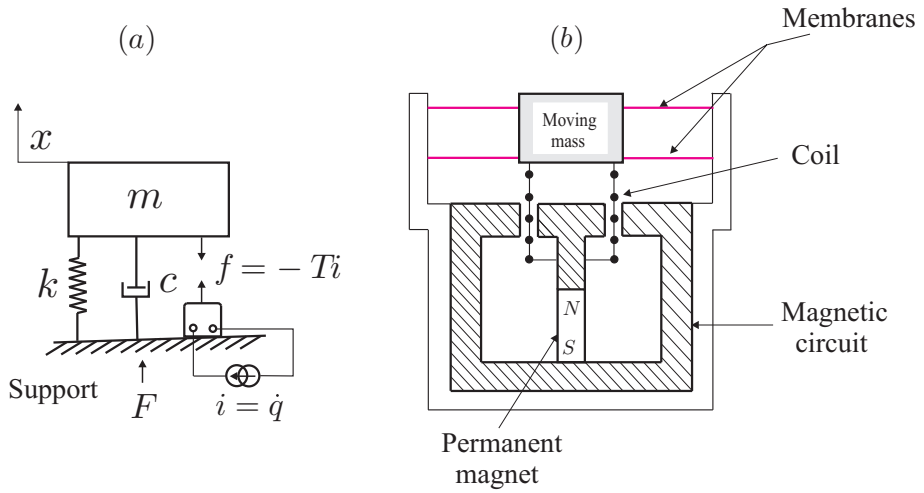

Fig. 3.2. Proof-mass actuator (a) model assuming a current generator; (b) conceptual design of an electrodynamic actuator based on a voice coil transducer.

(s is the Laplace variable). The total force applied to the support is equal and opposite to that applied to the mass:

$$F = -ms^2x = \frac{-ms^2Ti}{ms^2 + cs + k} \tag{3.7}$$

It follows that the transfer function between the total force F and the current i applied to the coil is

$$\frac{F}{i} = \frac{-s^2T}{s^2 + 2\xi_p\omega_p s + \omega_p^2} \tag{3.8}$$

where T is the transducer constant (in N/Amp), $\omega_p = (k/m)^{1/2}$ is the natural frequency of the spring-mass system and ξ_p is the damping ratio, which in practice is fairly high, typically 20 % or more. [1] The Bode plots of (3.8) are shown in Fig.3.3; one sees that the system behaves like a high-pass filter with a high frequency asymptote equal to the transducer constant T; above some critical frequency $\omega_c \simeq 2\omega_p$, the proof-mass actuator can be regarded as an *ideal force generator*. It has no authority over the rigid body modes and the operation at low frequency requires a large stroke, which is technically difficult. Medium to high frequency actuators (40 Hz and more) are relatively easy to obtain with low cost components (loudspeaker technology).

[1] the negative sign is irrelevant.

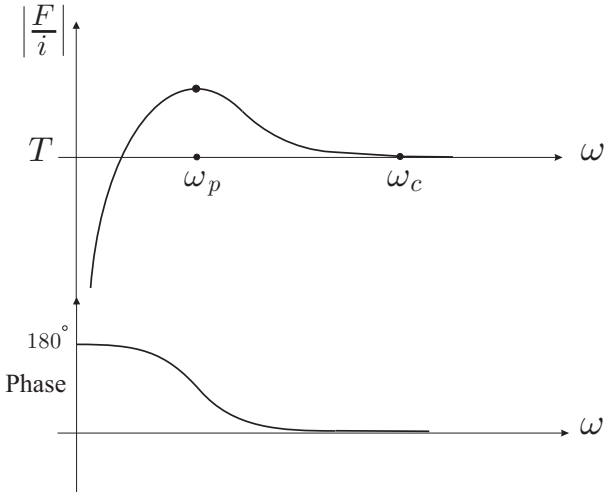

Fig. 3.3. Bode plot F/i of an electrodynamic proof-mass actuator.

If the current source is replaced by a voltage source (Fig.3.4), the modelling is slightly more complicated and combines the mechanical equation (3.5) and an electrical equation which is readily derived from Faraday's law:

$$T\dot{x} + L\frac{di}{dt} + Ri = E(t) \tag{3.9}$$

where L is the inductance and R is the resistance of the electrical circuit.

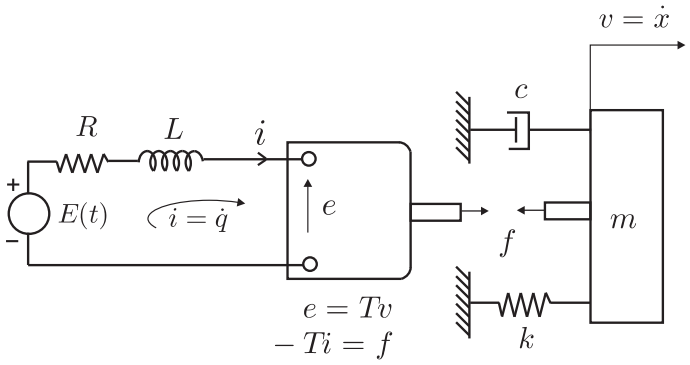

Fig. 3.4. Model of a proof mass actuator with a voltage source.

3.2.2 Geophone

The geophone is a transducer which behaves like an *absolute velocity sensor* above some cut-off frequency which depends on its mechanical construction. The system of Fig.3.2.a is readily transformed into a geophone by using the voltage e as the sensor output (Fig.3.5). If x_0 is the displace-

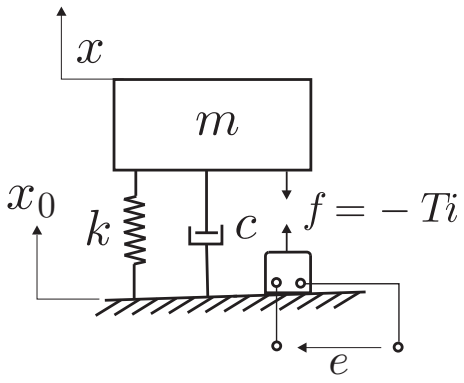

Fig. 3.5. Model of a geophone based on a voice coil transducer.

ment of the support and if the voice coil is open ($i = 0$), the governing equations are

$$m\ddot{x} + c(\dot{x} - \dot{x}_0) + k(x - x_0) = 0$$
$$T(\dot{x} - \dot{x}_0) = e$$

combining these equations, one readily finds that

$$x - x_0 = \frac{-ms^2 x_0}{ms^2 + cs + k}$$
$$e = Ts(x - x_0) = \frac{-s^2 T}{s^2 + (c/m)s + k/m}\, sx_0$$
$$\frac{e}{\dot{x}_0} = \frac{-s^2 T}{s^2 + 2\xi_p \omega_p s + \omega_p^2} \tag{3.10}$$

Thus, there is a perfect *duality* between a proof-mass actuator used with a current source and a geophone (connected to an infinite resistor); above the corner frequency, the gain of the geophone is equal to the transducer constant T. Designing geophones with very low corner frequency is in general difficult, especially if their orientation with respect to the gravity vector is variable; active geophones where the corner frequency is lowered electronically may constitute a good alternative option.

3.3 General electromechanical transducer

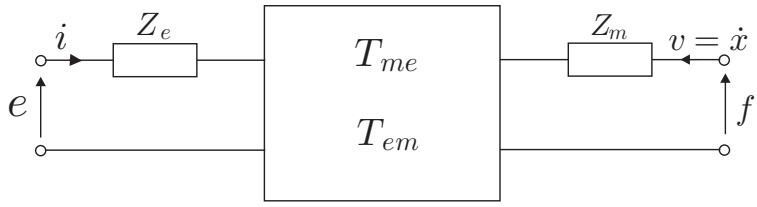

Fig. 3.6. Electrical analog representation of an electromechanical transducer.

3.3.1 Constitutive equations

The constitutive behavior of a wide class of electromechanical transducers can be modelled as in Fig.3.6, where the central box represents the conversion mechanism between electrical energy and mechanical energy, and vice versa. In Laplace form, the constitutive equations read

$$e = Z_e i + T_{em} v \tag{3.11}$$

$$f = T_{me} i + Z_m v \tag{3.12}$$

where e is the Laplace transform of the input voltage across the electrical terminals, i the input current, f the force applied to the mechanical terminals, and v the velocity of the mechanical part. Z_e is the blocked electrical impedance, measured for $v = 0$; T_{em} is the transduction coefficient representing the electromotive force (voltage) appearing in the electrical circuit per unit velocity in the mechanical part (in *volt.sec/m*). T_{me} is the transduction coefficient representing the force acting on the mechanical terminals to balance the electromagnetic force induced per unit current input on the electrical side (in *N/Amp*), and Z_m is the mechanical impedance, measured when the electrical side is open ($i = 0$). As an example, it is easy to check that the proof-mass with voltage source (Fig.3.4) can be written in this form with $Z_e = Ls+R$, $Z_m = ms+c+k/s$, $T_{em} = T$ and $T_{me} = -T$. The same representation applies also to the piezoelectric transducer analyzed below.

In absence of external force ($f = 0$), v can be eliminated between the two foregoing equations, leading to

$$e = (Z_e - \frac{T_{em} T_{me}}{Z_m}) i$$

$-T_{em}T_{me}/Z_m$ is called the *motional impedance*. The total driving point electrical impedance is the sum of the blocked and the motional impedances.

3.3.2 Self-sensing

Equation (3.11) shows that the voltage drop across the electrical terminals of any electromechanical transducer is the sum of a contribution proportional to the current applied and a contribution proportional to the velocity of the mechanical terminals. Thus, if $Z_e i$ can be measured and subtracted from e, a signal proportional to the velocity is obtained. This suggests the bridge structure of Fig.3.7. The bridge equations are as follows: for the branch containing the transducer,

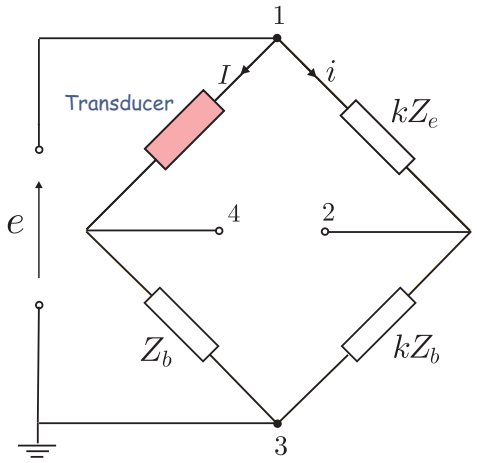

Fig. 3.7. Bridge circuit for self-sensing actuation.

$$e = Z_e I + T_{em} v + Z_b I$$

$$I = \frac{1}{Z_e + Z_b}(e - T_{em} v)$$

$$V_4 = Z_b I = \frac{Z_b}{Z_e + Z_b}(e - T_{em} v)$$

For the other branch,

$$e = kZ_e i + kZ_b i$$

$$V_2 = kZ_b i = \frac{Z_b}{Z_e + Z_b}\, e$$

and the bridge output

$$V_4 - V_2 = \left(\frac{-Z_b\, T_{em}}{Z_e + Z_b}\right) v \tag{3.13}$$

is indeed a linear function of the velocity v of the mechanical terminals. Note, however, that $-Z_b\, T_{em}/(Z_e + Z_b)$ acts as a filter; the bridge impedance Z_b must be adapted to the transducer impedance Z_e to avoid amplitude distortion and phase shift between the output voltage $V_4 - V_2$ and the transducer velocity in the frequency band of interest.

3.4 Reaction wheels and gyrostabilizers

These devices are torque actuators normally used in attitude control of satellites. They have authority over the rigid body modes as well as the flexible modes. A *reaction wheel* consists of a rotating wheel whose axis is fixed with respect to the spacecraft; a torque is generated by increasing or decreasing the angular velocity. If the angular velocity exceeds the specification, the wheel must be unloaded, using another type of actuator (jets or magnetic).

In *control moment gyros (CMG)*, the rotating wheel is mounted on gimbals, and the gimbal torques are used as control inputs. The principle of a one-axis gyrostabilizer is described in Fig.3.7. Rotating the gimbal about the x axis with an angular velocity $\dot{\theta}_x$ produces torques:

$$T_y = J_z \Omega \dot{\theta}_x \cos\theta_x \tag{3.14}$$

$$T_z = J_z \Omega \dot{\theta}_x \sin\theta_x \tag{3.15}$$

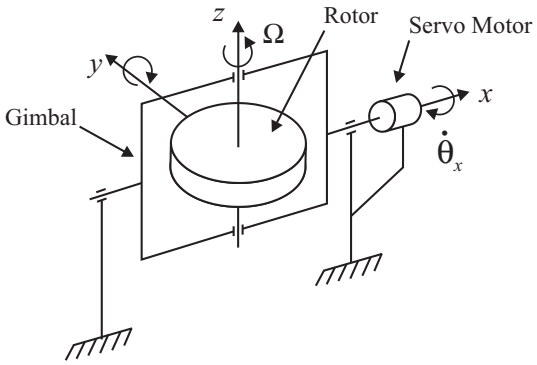

Fig. 3.8. One-axis gyrostabilizer.

where $J_z\Omega$ is the angular momentum along the z axis, and θ_x is the deviation of the rotor axis with respect to the vertical. The servo motor on the gimbal axis is velocity controlled. The angle θ_x is measured also, and a small gain feedback maintains the axis of the rotor in the vertical position (for a deeper discussion of the use of *CMG* in attitude control, see Jacot & Liska).

3.5 Smart materials

Piezoelectric materials belong to the so-called *smart materials*, or *multifunctional materials*, which have the ability to respond significantly to stimuli of different physical natures. Figure 3.9 lists various effects that are observed in materials in response to various inputs: mechanical, electrical, magnetic, thermal, light. The coupling between the physical fields of different types is expressed by the non-diagonal cells in the figure; if its magnitude is sufficient, the coupling can be used to build discrete or distributed transducers of various types, which can be used as sensors, actuators, or even integrated in structures with various degrees of tailoring and complexity (e.g. as fibers), to make them controllable or responsive

Input \ Output	Strain	Electric charge	Magnetic flux	Temperature	Light
Stress	Elasticity	Piezo-electricity	Magneto-striction		Photo-elasticity
Electric field	Piezo-electricity	Permittivity			Electro-optic effect
Magnetic field	Magneto-striction	Magneto-electric effect	Permeability		Magneto-optic
Heat	Thermal expansion	Pyro-electricity		Specific heat	
Light	Photostriction	Photo-voltaic effect			Refractive index

Fig. 3.9. Stimulus-response relations indicating various effects in materials. The smart materials correspond to the non-diagonal cells.

to their environment (e.g. for shape morphing, precision shape control, damage detection, dynamic response alleviation,...).

3.6 Piezoelectric transducer

The piezoelectric effect was discovered by Pierre and Jacques Curie in 1880. The direct piezoelectric effect consists in the ability of certain crystalline materials to generate an electrical charge in proportion to an externally applied force; the direct effect is used in force transducers. According to the inverse piezoelectric effect, an electric field parallel to the direction of polarization induces an expansion of the material. The piezoelectric effect is anisotropic; it can be exhibited only by materials whose crystal structure has no center of symmetry; this is the case for some ceramics below a certain temperature called the *Curie temperature*; in this phase, the crystal has built-in electric dipoles, but the dipoles are randomly orientated and the net electric dipole on a macroscopic scale is zero. During the poling process, when the crystal is cooled in the presence of a high electric field, the dipoles tend to align, leading to an electric dipole on a macroscopic scale. After cooling and removing of the poling field, the dipoles cannot return to their original position; they remain aligned along the poling direction and the material body becomes permanently piezoelectric, with the ability to convert mechanical energy to electrical energy and vice versa; this property will be lost if the temperature exceeds the Curie temperature or if the transducer is subjected to an excessive electric field in the direction opposed to the poling field.

The most popular piezoelectric materials are *Lead-Zirconate-Titanate (PZT)* which is a ceramic, and *Polyvinylidene fluoride (PVDF)* which is a polymer. In addition to the piezoelectric effect, piezoelectric materials exhibit a *pyroelectric* effect, according to which electric charges are generated when the material is subjected to temperature; this effect is used to produce heat detectors; it will not be discussed here.

In this section, we consider a transducer made of a one-dimensional piezoelectric material of constitutive equations (we use the notations of the IEEE Standard on Piezoelectricity)

$$D = \varepsilon^T E + d_{33} T \tag{3.16}$$

$$S = d_{33} E + s^E T \tag{3.17}$$

where D is the electric displacement (charge per unit area, expressed in $Coulomb/m^2$), E the electric field (V/m), T the stress (N/m^2) and S the strain. ε^T is the dielectric constant (permittivity) under constant stress, s^E is the compliance when the electric field is constant (inverse of the Young's modulus) and d_{33} is the piezoelectric constant, expressed in m/V or $Coulomb/Newton$; the reason for the subscript 33 is that, by convention, index 3 is always aligned to the poling direction of the material, and we assume that the electric field is parallel to the poling direction. More complicated situations will be considered later. Note that the same constant d_{33} appears in (3.16) and (3.17).

In the absence of external force, a transducer subjected to a voltage with the same polarity as that during poling produces an elongation, and a voltage opposed to that during poling makes it shrink (inverse piezoelectric effect). In (3.17), this amounts to a positive d_{33}. Conversely (direct piezoelectric effect), if we consider a transducer with open electrodes ($D = 0$), according to (3.16), $E = -(d_{33}/\varepsilon^T)T$, which means that a traction stress will produce a voltage with polarity opposed to that during poling, and a compressive stress will produce a voltage with the same polarity as that during poling.

3.6.1 Constitutive relations of a discrete transducer

Equations (3.16) and (3.17) can be written in a matrix form

$$\begin{Bmatrix} D \\ S \end{Bmatrix} = \begin{bmatrix} \varepsilon^T & d_{33} \\ d_{33} & s^E \end{bmatrix} \begin{Bmatrix} E \\ T \end{Bmatrix} \tag{3.18}$$

where (E, T) are the independent variables and (D, S) are the dependent variables. If (E, S) are taken as the independent variables, they can be rewritten

$$D = \frac{d_{33}}{s^E} S + \varepsilon^T \left(1 - \frac{{d_{33}}^2}{s^E \varepsilon^T}\right) E$$

$$T = \frac{1}{s^E} S - \frac{d_{33}}{s^E} E$$

or

$$\begin{Bmatrix} D \\ T \end{Bmatrix} = \begin{bmatrix} \varepsilon^T(1-k^2) & e_{33} \\ -e_{33} & c^E \end{bmatrix} \begin{Bmatrix} E \\ S \end{Bmatrix} \tag{3.19}$$

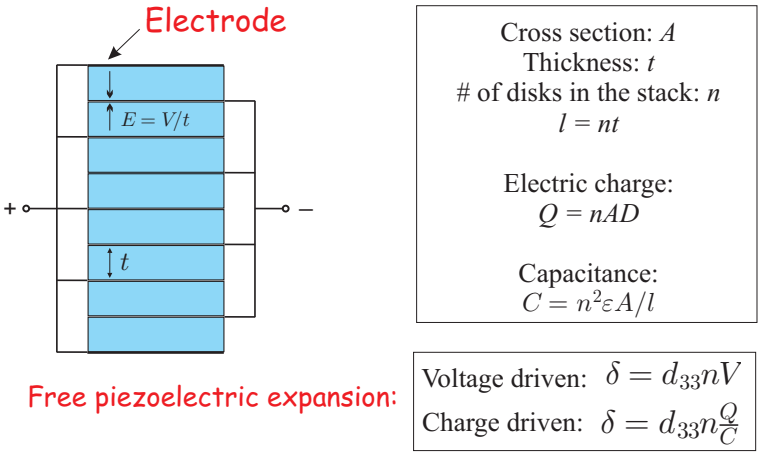

Fig. 3.10. Piezoelectric linear transducer.

where $c^E = 1/s^E$ is the Young's modulus under $E = 0$ (short circuited electrodes), in N/m^2 (Pa); $e_{33} = d_{33}/s^E$, product of d_{33} by the Young modulus, is the constant relating the electric displacement to the strain for short-circuited electrodes (in $Coulomb/m^2$), and also that relating the compressive stress to the electric field when the transducer is blocked $(S = 0)$.

$$k^2 = \frac{{d_{33}}^2}{s^E \varepsilon^T} = \frac{{e_{33}}^2}{c^E \varepsilon^T} \tag{3.20}$$

k is called the *electromechanical coupling factor* of the material; it measures the efficiency of the conversion of mechanical energy into electrical energy, and vice versa, as discussed below. From (3.19), we note that $\varepsilon^T(1 - k^2)$ is the dielectric constant under zero strain.

If one assumes that all the electrical and mechanical quantities are uniformly distributed in a linear transducer formed by a stack of n disks of thickness t and cross section A (Fig.3.10), the global constitutive equations of the transducer are obtained by integrating Equ.(3.18) or (3.19) over the volume of the transducer; one easily finds

$$\begin{Bmatrix} Q \\ \Delta \end{Bmatrix} = \begin{bmatrix} C & nd_{33} \\ nd_{33} & 1/K_a \end{bmatrix} \begin{Bmatrix} V \\ f \end{Bmatrix} \tag{3.21}$$

or

$$\begin{Bmatrix} Q \\ f \end{Bmatrix} = \begin{bmatrix} C(1-k^2) & nd_{33}K_a \\ -nd_{33}K_a & K_a \end{bmatrix} \begin{Bmatrix} V \\ \Delta \end{Bmatrix} \tag{3.22}$$

where $Q = nAD$ is the total electric charge on the electrodes of the transducer, $\Delta = Sl$ is the total extension ($l = nt$ is the length of the transducer), $f = AT$ is the total force and V the voltage applied between the electrodes of the transducer, resulting in an electric field $E = V/t = nV/l$. $C = \varepsilon^T An^2/l$ is the capacitance of the transducer with no external load ($f = 0$), $K_a = A/s^E l$ is the stiffness with short-circuited electrodes ($V = 0$). Note that the electromechanical coupling factor can be written alternatively

$$k^2 = \frac{{d_{33}}^2}{s^E \varepsilon^T} = \frac{n^2 {d_{33}}^2 K_a}{C} \tag{3.23}$$

Equation (3.21) can be inverted

$$\begin{Bmatrix} V \\ f \end{Bmatrix} = \frac{K_a}{C(1-k^2)} \begin{bmatrix} 1/K_a & -nd_{33} \\ -nd_{33} & C \end{bmatrix} \begin{Bmatrix} Q \\ \Delta \end{Bmatrix} \tag{3.24}$$

from which we can see that the stiffness with open electrodes ($Q = 0$) is $K_a/(1-k^2)$ and the capacitance for a fixed geometry ($\Delta = 0$) is $C(1-k^2)$. Note that typical values of k are in the range $0.3 - 0.7$; for large k, the stiffness changes significantly with the electrical boundary conditions, and similarly the capacitance depends on the mechanical boundary conditions.

Next, let us write the total stored electromechanical energy and coenergy functions.[2] Consider the discrete piezoelectric transducer of Fig.3.11;

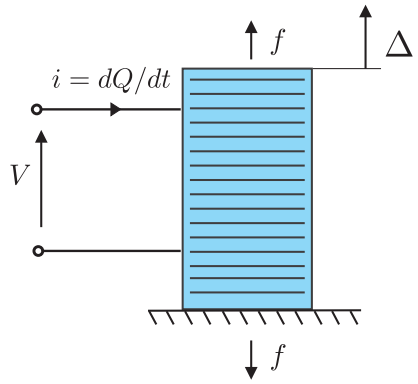

Fig. 3.11. Discrete Piezoelectric transducer.

[2] Energy and coenergy functions are needed in connection with energy formulations such as Hamilton principle, Lagrange equations or finite elements.

the total power delivered to the transducer is the sum of the electric power, Vi and the mechanical power, $f\dot{\Delta}$. The net work on the transducer is

$$dW = Vidt + f\dot{\Delta}dt = VdQ + fd\Delta \tag{3.25}$$

For a conservative element, this work is converted into stored energy, dW_e, and the total stored energy, $W_e(\Delta, Q)$ can be obtained by integrating (3.25) from the reference state to the state (Δ, Q).[3] Upon differentiating $W_e(\Delta, Q)$,

$$dW_e(\Delta, Q) = \frac{\partial W_e}{\partial \Delta}d\Delta + \frac{\partial W_e}{\partial Q}dQ \tag{3.26}$$

and, comparing with (3.25), we recover the constitutive equations

$$f = \frac{\partial W_e}{\partial \Delta} \qquad\qquad V = \frac{\partial W_e}{\partial Q} \tag{3.27}$$

Substituting f and V from (3.24) into (3.25), one gets

$$dW_e = VdQ + fd\Delta$$

$$= \frac{Q\,dQ}{C(1-k^2)} - \frac{nd_{33}K_a}{C(1-k^2)}(\Delta\,dQ + Q\,d\Delta) + \frac{K_a}{1-k^2}\Delta\,d\Delta$$

which is the total differential of

$$W_e(\Delta, Q) = \frac{Q^2}{2C(1-k^2)} - \frac{nd_{33}K_a}{C(1-k^2)}Q\Delta + \frac{K_a}{1-k^2}\frac{\Delta^2}{2} \tag{3.28}$$

This is the analytical expression of the stored electromechanical energy for the discrete piezoelectric transducer. Equations (3.27) recover the constitutive equations (3.24). The first term on the right hand side of (3.28) is the electrical energy stored in the capacitance $C(1-k^2)$ (corresponding to a fixed geometry, $\triangle = 0$); the third term is the elastic strain energy stored in a spring of stiffness $K_a/(1-k^2)$ (corresponding to open electrodes, $Q = 0$); the second term is the piezoelectric energy.

The electromechanical energy function uses Δ and Q as independent state variables. A *coenergy* function using Δ and V as independent variables can be defined by the *Legendre transformation*

$$W_e^*(\Delta, V) = VQ - W_e(\Delta, Q) \tag{3.29}$$

[3] Since the system is conservative, the integration can be done along any path leading from $(0, 0)$ to (Δ, Q).

The total differential of the coenergy is

$$dW_e^* = Q\,dV + V\,dQ - \frac{\partial W_e}{\partial \Delta} d\Delta - \frac{\partial W_e}{\partial Q} dQ$$

$$dW_e^* = Q\,dV - f\,d\Delta \tag{3.30}$$

where Equ.(3.27) have been used. It follows that

$$Q = \frac{\partial W_e^*}{\partial V} \qquad \text{and} \qquad f = -\frac{\partial W_e^*}{\partial \Delta} \tag{3.31}$$

Introducing the constitutive equations (3.22) into (3.30),

$$dW_e^* = \left[C(1-k^2)V + nd_{33}K_a\Delta\right] dV + (nd_{33}K_aV - K_a\Delta)\, d\Delta$$

$$= C(1-k^2)V\,dV + nd_{33}K_a\,(\Delta dV + V\,d\Delta) - K_a\Delta\,d\Delta$$

which is the total differential of

$$W_e^*(\Delta, V) = C(1-k^2)\frac{V^2}{2} + nd_{33}K_aV\Delta - K_a\frac{\Delta^2}{2} \tag{3.32}$$

This is the analytical form of the coenergy function for the discrete piezoelectric transducer. The first term on the right hand side of (3.32) is recognized as the electrical coenergy in the capacitance $C(1-k^2)$ (corresponding to a fixed geometry, $\Delta = 0$); the third is the strain energy stored in a spring of stiffness K_a (corresponding to short-circuited electrodes, $V = 0$). The second term of (3.32) is the piezoelectric coenergy; using the fact that the uniform electric field is $E = nV/l$ and the uniform strain is $S = \Delta/l$, it can be rewritten

$$\int_\Omega Se_{33}E\,d\Omega \tag{3.33}$$

where the integral extends to the volume Ω of the transducer.

The analytical form (3.28) of the electromechanical energy, together with the constitutive equations (3.27) can be regarded as an alternative definition of a discrete piezoelectric transducer, and similarly for the analytical expression of the coenergy (3.32) and the constitutive equations (3.31).

3.6.2 Interpretation of k^2

Consider a piezoelectric transducer subjected to the following mechanical cycle: first, it is loaded with a force F with short-circuited electrodes; the resulting extension is

$$\Delta_1 = \frac{F}{K_a}$$

where $K_a = A/(s^E l)$ is the stiffness with short-circuited electrodes. The energy stored in the system is

$$W_1 = \int_0^{\Delta_1} f\, dx = \frac{F\Delta_1}{2} = \frac{F^2}{2K_a}$$

At this point, the electrodes are open and the transducer is unloaded according to a path of slope $K_a/(1-k^2)$, corresponding to the new electrical boundary conditions,

$$\Delta_2 = \frac{F(1-k^2)}{K_a}$$

The energy recovered in this way is

$$W_2 = \int_0^{\Delta_2} f\, dx = \frac{F\Delta_2}{2} = \frac{F^2(1-k^2)}{2K_a}$$

leaving $W_1 - W_2$ stored in the transducer. The ratio between the remaining stored energy and the initial stored energy is

$$\frac{W_1 - W_2}{W_1} = k^2$$

Similarly, consider the following electrical cycle: first, a voltage V is applied to the transducer which is mechanically unconstrained ($f = 0$). The electric charges appearing on the electrodes are

$$Q_1 = CV$$

where $C = \varepsilon^T A n^2/l$ is the unconstrained capacitance, and the energy stored in the transducer is

$$W_1 = \int_0^{Q_1} v\, dq = \frac{VQ_1}{2} = \frac{CV^2}{2}$$

At this point, the transducer is blocked mechanically and electrically unloaded from V to 0. The electrical charges are removed according to

$$Q_2 = C(1 - k^2)V$$

where the capacitance for fixed geometry has been used. The energy recovered in this way is

$$W_2 = \int_0^{Q_2} v\, dq = \frac{C(1 - k^2)V^2}{2}$$

leaving $W_1 - W_2$ stored in the transducer. Here again, the ratio between the remaining stored energy and the initial stored energy is

$$\frac{W_1 - W_2}{W_1} = k^2$$

Although the foregoing relationships provide a clear physical interpretation of the electromechanical coupling factor, they do not bring a practical way of measuring k^2; the experimental determination of k^2 is often based on impedance (or admittance) measurements.

3.6.3 Admittance of the piezoelectric transducer

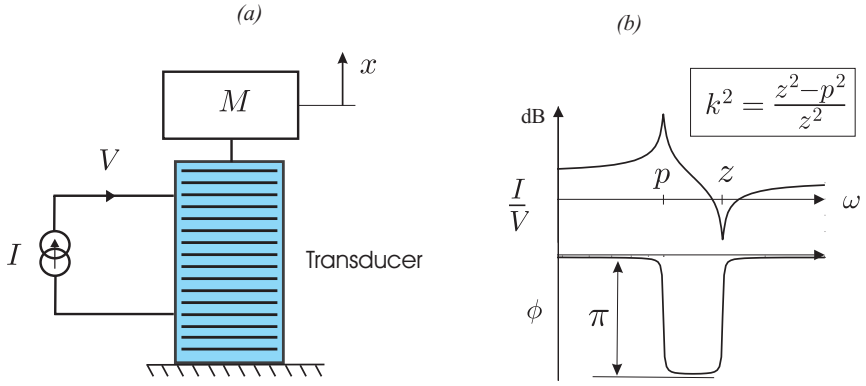

Fig. 3.12. (a) Elementary dynamical model of the piezoelectric transducer. (b) Typical admittance FRF of the transducer, in the vicinity of its natural frequency.

Consider the system of Fig.3.12, where the piezoelectric transducer is assumed massless and is connected to a mass M. The force acting on the mass is the negative of that acting on the transducer, $f = -M\ddot{x}$; using (3.22),

$$\begin{Bmatrix} Q \\ -M\ddot{x} \end{Bmatrix} = \begin{bmatrix} C(1 - k^2) & nd_{33}K_a \\ -nd_{33}K_a & K_a \end{bmatrix} \begin{Bmatrix} V \\ x \end{Bmatrix} \tag{3.34}$$

From the second equation, one gets (in Laplace form)

$$x = \frac{nd_{33}K_a}{Ms^2 + K_a}$$

and, substituting in the first one and using (3.23), one finds

$$\frac{Q}{V} = C(1-k^2)\left[\frac{Ms^2 + K_a/(1-k^2)}{Ms^2 + K_a}\right] \tag{3.35}$$

It follows that the admittance reads:

$$\frac{I}{V} = \frac{sQ}{V} = sC(1-k^2)\frac{s^2+z^2}{s^2+p^2} \tag{3.36}$$

where the poles and zeros are respectively

$$p^2 = \frac{K_a}{M} \qquad \text{and} \qquad z^2 = \frac{K_a/(1-k^2)}{M} \tag{3.37}$$

p is the natural frequency with short-circuited electrodes ($V = 0$) and z is the natural frequency with open electrodes ($I = 0$). From the previous equation one sees that

$$\frac{z^2 - p^2}{z^2} = k^2 \tag{3.38}$$

which constitutes a practical way to determine the electromechanical coupling factor from the poles and zeros of admittance (or impedance) FRF measurements (Fig.3.12.b).

3.7 References

CADY, W.G. *Piezoelectricity: an Introduction to the Theory and Applications of Electromechanical Phenomena in Crystals*, McGrawHill, 1946.
CRANDALL, S.H., KARNOPP, D.C., KURTZ, E.F, Jr., PRIDMORE-BROWN, D.C. *Dynamics of Mechanical and Electromechanical Systems*, McGraw-Hill, N-Y, 1968.
DE BOER, E., Theory of Motional Feedback, *IRE Transactions on Audio*, 15-21, Jan.-Feb., 1961.
HUNT, F.V. *Electroacoustics: The Analysis of Transduction, and its Historical Background*, Harvard Monographs in Applied Science, No 5, 1954. Reprinted, Acoustical Society of America, 1982.
IEEE Standard on Piezoelectricity. (ANSI/IEEE Std 176-1987).

JACOT, A.D. & LISKA, D.J. Control moment gyros in attitude control, *AIAA J. of Spacecraft and Rockets*, Vol.3, No 9, 1313-1320, Sept. 1966.
Philips Application Book on Piezoelectric Ceramics, (J. Van Randeraat & R.E. Setterington, Edts), Mullard Limited, London, 1974.
Physik Intrumente catalogue, Products for Micropositioning (*PI* GmbH).
PRATT, J., FLATAU, A. Development and analysis of self-sensing magnetostrictive actuator design, SPIE Smart Materials and Structures Conference, Vol.1917, 1993.
PREUMONT, A. *Mechatronics, Dynamics of Electromechanical and Piezoelectric Systems*, Springer, 2006.
ROSEN, C.A. Ceramic transformers and filters, Proc. Electronic Component Symposium, p.205-211 (1956).
UCHINO, K. *Ferroelectric Devices*, Marcel Dekker, 2000.
WOODSON, H.H., MELCHER, J.R. *Electromechanical Dynamics, Part I: Discrete Systems*, Wiley, 1968.

3.8 Problems

P.3.1 *Consider the piezoelectric linear transducer of Fig.3.10; assuming that all the electrical and mechanical quantities are uniformly distributed, show that the constitutive equations of the transducer, Equ.(3.22) can be derived from those of the material, Equ.(3.19).*
P.3.2 *A piezoelectric transducer supporting an inertial mass M (Fig.3.12.a) can be used as an accelerometer. Assuming that the transducer is placed on a surface subjected to an acceleration* $\ddot{x}_0$ *and that it is connected to a charge amplifier enforcing the electrical boundary conditions* $V = 0$*, establish the relationship between the the support acceleration and the electric charge* Q*. Discuss the conditions under which this system can be used to measure* $\ddot{x}_0$ *(some damping may be introduced in the system by assuming a mechanical behavior* $f = (K_a + cs)\Delta$ *instead of* $f = K_a\Delta$*).*
P.3.3 *Draw the cycle diagrams* (f, Δ) *and* (V, Q) *of the physical interpretations of the electromechanical coupling factor* k^2*, in section 3.6.2.*
P.3.4 *Represent the discrete piezoelectric transducer (3.24) in the electrical analog form of Fig.3.6.*

4

Piezoelectric beam, plate and truss

4.1 Piezoelectric material

4.1.1 Constitutive relations

The constitutive equations of a general piezoelectric material are

$$T_{ij} = c^E_{ijkl} S_{kl} - e_{kij} E_k \tag{4.1}$$

$$D_i = e_{ikl} S_{kl} + \varepsilon^S_{ik} E_k \tag{4.2}$$

where T_{ij} and S_{kl} are the components of the stress and strain tensors, respectively, c^E_{ijkl} are the elastic constants under constant electric field (Hooke's tensor), e_{ikl} the piezoelectric constants (in $Coulomb/m^2$) and ε^S_{ij} the dielectric constant under constant strain. These formulae use classical tensor notations, where all indices $i, j, k, l = 1, 2, 3$, and there is a summation on all repeated indices. The above equations are a generalization of (3.19), with S_{kl} and E_j as independent variables; they can be written alternatively with T_{kl} and E_j as independent variables:

$$S_{ij} = s^E_{ijkl} T_{kl} + d_{kij} E_k \tag{4.3}$$

$$D_i = d_{ikl} T_{kl} + \varepsilon^T_{ik} E_k \tag{4.4}$$

where s^E_{ijkl} is the tensor of compliance under constant electric field, d_{ikl} the piezoelectric constants (in $Coulomb/Newton$) and ε^T_{ik} the dielectric constant under constant stress. The difference between the properties under constant stress and under constant strain has been stressed earlier. As an alternative to the above tensor notations, it is customary to use the engineering vector notations

$$T = \begin{Bmatrix} T_{11} \\ T_{22} \\ T_{33} \\ T_{23} \\ T_{31} \\ T_{12} \end{Bmatrix} \qquad S = \begin{Bmatrix} S_{11} \\ S_{22} \\ S_{33} \\ 2S_{23} \\ 2S_{31} \\ 2S_{12} \end{Bmatrix} \tag{4.5}$$

With these notations, Equ.(4.1) (4.2) can be written in matrix form

$$\begin{aligned} \{T\} &= [c]\{S\} - [e]\{E\} \\ \{D\} &= [e]^T\{S\} + [\varepsilon]\{E\} \end{aligned} \tag{4.6}$$

and (4.3), (4.4),

$$\begin{aligned} \{S\} &= [s]\{T\} + [d]\{E\} \\ \{D\} &= [d]^T\{T\} + [\varepsilon]\{E\} \end{aligned} \tag{4.7}$$

where the superscript T stands for the transposed; the other superscripts have been omitted, but can be guessed from the equation itself. Assuming that the coordinate system coincides with the orthotropy axes of the material and that the direction of polarization coincides with direction 3, the explicit form of (4.7) is:

Actuation :

$$\begin{Bmatrix} S_{11} \\ S_{22} \\ S_{33} \\ 2S_{23} \\ 2S_{31} \\ 2S_{12} \end{Bmatrix} = \begin{bmatrix} s_{11} & s_{12} & s_{13} & 0 & 0 & 0 \\ s_{12} & s_{22} & s_{23} & 0 & 0 & 0 \\ s_{13} & s_{23} & s_{33} & 0 & 0 & 0 \\ 0 & 0 & 0 & s_{44} & 0 & 0 \\ 0 & 0 & 0 & 0 & s_{55} & 0 \\ 0 & 0 & 0 & 0 & 0 & s_{66} \end{bmatrix} \begin{Bmatrix} T_{11} \\ T_{22} \\ T_{33} \\ T_{23} \\ T_{31} \\ T_{12} \end{Bmatrix} + \begin{bmatrix} 0 & 0 & d_{31} \\ 0 & 0 & d_{32} \\ 0 & 0 & d_{33} \\ 0 & d_{24} & 0 \\ d_{15} & 0 & 0 \\ 0 & 0 & 0 \end{bmatrix} \begin{Bmatrix} E_1 \\ E_2 \\ E_3 \end{Bmatrix} \tag{4.8}$$

Sensing :

$$\begin{Bmatrix} D_1 \\ D_2 \\ D_3 \end{Bmatrix} = \begin{bmatrix} 0 & 0 & 0 & 0 & d_{15} & 0 \\ 0 & 0 & 0 & d_{24} & 0 & 0 \\ d_{31} & d_{32} & d_{33} & 0 & 0 & 0 \end{bmatrix} \begin{Bmatrix} T_{11} \\ T_{22} \\ T_{33} \\ T_{23} \\ T_{31} \\ T_{12} \end{Bmatrix} + \begin{bmatrix} \varepsilon_{11} & 0 & 0 \\ 0 & \varepsilon_{22} & 0 \\ 0 & 0 & \varepsilon_{33} \end{bmatrix} \begin{Bmatrix} E_1 \\ E_2 \\ E_3 \end{Bmatrix} \tag{4.9}$$

Typical values of the piezoelectric constants for piezoceramics (PZT) and piezopolymers (PVDF) are given Table 3.1. Examining the actuator equation (4.8), we note that when an electric field E_3 is applied parallel to the direction of polarization, an extension is observed along the same direction; its amplitude is governed by the piezoelectric coefficient d_{33}. Similarly, a shrinkage is observed along the directions 1 and 2 perpendicular to the electric field, the amplitude of which is controlled by d_{31} and d_{32}, respectively (shrinkage, because d_{31} and d_{32} are negative). Piezoceramics have an isotropic behaviour in the plane, $d_{31} = d_{32}$; on the contrary, when PVDF is polarized under stress, its piezoelectric properties are highly anisotropic, with $d_{31} \sim 5d_{32}$. Equation (4.8) also indicates that an electric field E_1 normal to the direction of polarization 3 produces a shear deformation S_{13}, controlled by the piezoelectric constant d_{15} (similarly, a shear deformation S_{23} occurs if an electric field E_2 is applied; it is controlled by d_{24}). An interesting feature of this type of actuation is that d_{15} is the largest of all piezoelectric coefficients (500 $10^{-12}C/N$ for PZT). The various modes of operation associated with the piezoelectric coefficients d_{33}, d_{31} and d_{15} are illustrated in Fig.4.1.

4.1.2 Coenergy density function

With an approach parallel to that of the discrete transducer, the total stored energy density in a unit volume of material is the sum of the mechanical work and the electrical work,

$$dW_e(S, D) = \{dS\}^T\{T\} + \{dD\}^T\{E\} \tag{4.10}$$

[compare with (3.25)]. For a conservative system, $W_e(S, D)$ can be obtained by integrating (4.10) from the reference state to the state (S, D); since the system is conservative, the integration can be done along any path from $(0, 0)$ to (S, D). Upon differentiating $W_e(S, D)$ and comparing with (4.10) we recover the constitutive equations

$$\{T\} = \left\{\frac{\partial W_e}{\partial S}\right\} \qquad \text{and} \qquad \{E\} = \left\{\frac{\partial W_e}{\partial D}\right\} \tag{4.11}$$

which are the distributed counterparts of (3.27). The *coenergy density function* is defined by the Legendre transformation

$$W_e^*(S, E) = \{E\}^T\{D\} - W_e(S, D) \tag{4.12}$$

[compare with (3.29)]. The total differential is

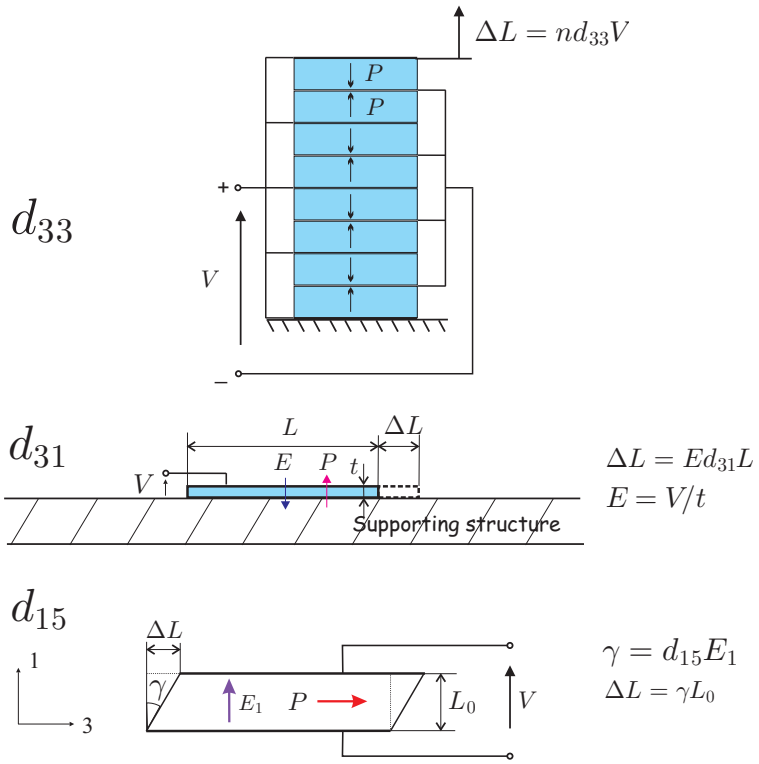

Fig. 4.1. Actuation modes of piezoelectric actuators. P indicates the direction of polarization.

$$dW_e^* = \{dE\}^T\{D\} + \{E\}^T\{dD\} - \{dS\}^T\left\{\frac{\partial W_e}{\partial S}\right\} - \{dD\}^T\left\{\frac{\partial W_e}{\partial D}\right\}$$
$$= \{dE\}^T\{D\} - \{dS\}^T\{T\} \tag{4.13}$$

where (4.11) have been used. It follows that

$$\{D\} = \left\{\frac{\partial W_e^*}{\partial E}\right\} \qquad \text{and} \qquad \{T\} = -\left\{\frac{\partial W_e^*}{\partial S}\right\} \tag{4.14}$$

Substituting (4.6) into (4.13),

$$dW_e^* = \{dE\}^T[e]^T\{S\} + \{dE\}^T[\varepsilon]\{E\} - \{dS\}^T[c]\{S\} + \{dS\}^T[e]\{E\} \tag{4.15}$$

which is the total differential of

$$W_e^*(S,E) = \frac{1}{2}\{E\}^T[\varepsilon]\{E\} + \{S\}^T[e]\{E\} - \frac{1}{2}\{S\}^T[c]\{S\} \tag{4.16}$$

Material properties	PZT	PVDF
Piezoelectric constants		
$d_{33}(10^{-12}C/N$ or $m/V)$	300	-25
$d_{31}(10^{-12}C/N$ or $m/V)$	-150	*uni-axial*: $d_{31} = 15$ $d_{32} = 3$ *bi-axial*: $d_{31} = d_{32} = 3$
$d_{15}(10^{-12}C/N$ or $m/V)$	500	0
$e_{31} = d_{31}/s^E(C/m^2)$	-7.5	0.025
Electromechanical coupling factor		
k_{33}	0.7	
k_{31}	0.3	~ 0.1
k_{15}	0.7	
Dielectric constant $\varepsilon^T/\varepsilon_0$ $(\varepsilon_0 = 8.85\ 10^{-12}F/m)$	1800	10
Max. Electric field (V/mm)	2000	$5\ 10^5$
Max. operating (Curie) T° $(^\circ C)$	$80^\circ - 150^\circ$	90°
Density (Kg/m^3)	7600	1800
Young's modulus $1/s^E$ (GPa)	50	2.5
Maximum stress (MPa)		
Traction	80	200
Compression	600	200
Maximum strain	Brittle	50 %

Table 4.1. Typical properties of piezoelectric materials.

[compare with (3.32)]. The first term in the right hand side is the electrical coenergy stored in the dielectric material (ε is the matrix of permittivity under constant strain); the third term is the strain energy stored in the elastic material (c is the matrix of elastic constants under constant electric field); the second term is the piezoelectric coenergy, which generalizes (3.33) in three dimensions. Taking the partial derivatives (4.14), one recovers the constitutive equations (4.6). In that sense, the analytical form of the coenergy density function, (4.16) together with (4.14), can be seen as an alternative definition of the linear piezoelectricity. In the literature,

$$H(S, E) = -W_e^*(S, E) \tag{4.17}$$

is known as the *electric enthalpy density.*

4.2 Hamilton's principle

According to Hamilton's principle, the variational indicator

$$\text{V.I.} = \int_{t_1}^{t_2} [\delta(T^* + W_e^*) + \delta W_{nc}] dt = 0 \tag{4.18}$$

is stationary for all admissible (virtual) variations δu_i and δE_i of the path between the two fixed configurations at t_1 and t_2.

$$T^* = \frac{1}{2} \int_\Omega \varrho \{\dot{u}\}^T \{\dot{u}\} d\Omega \tag{4.19}$$

is the kinetic (co)energy (ϱ is the density) and

$$W_e^* = \frac{1}{2} \int_\Omega \left(\{E\}^T [\varepsilon] \{E\} + 2\{S\}^T [e] \{E\} - \{S\}^T [c] \{S\} \right) d\Omega \tag{4.20}$$

has been defined in the previous section. $T^* + W_e^*$ is the Lagrangian and δW_{nc} is the virtual work of nonconservative external forces and applied currents.

4.3 Piezoelectric beam actuator

Consider the piezoelectric beam of Fig.4.2; it is covered with a single piezoelectric layer of uniform thickness h_p, polarized along the z axis; the supporting structure is acting as electrode on one side and there is an electrode of variable width $b_p(x)$ on the other side. The voltage difference between the electrodes is controlled, so that the part of the piezoelectric material located between the electrodes is subjected to an electric field E_3 parallel to the polarization (note that the piezoelectric material which is not covered by the electrode on both sides is useless as active material). We denote by $w(x,t)$ the transverse displacements of the beam; according to the Euler-Bernoulli assumption, the stress and strain fields are uniaxial, along Ox; the axial strain S_1 is related to the curvature w'' by

$$S_1 = -zw'' \tag{4.21}$$

where z is the distance to the neutral axis. We also assume that the piezoelectric layer is thin enough, so that E_3 is constant across the thickness.

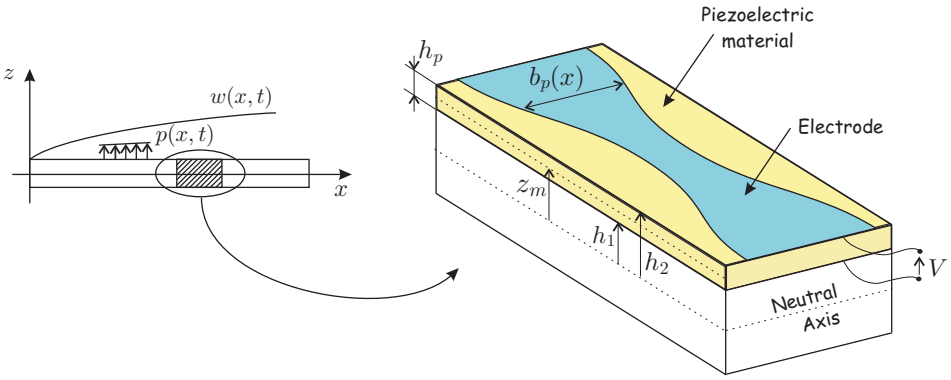

Fig. 4.2. Piezoelectric beam covered by a single piezoelectric layer with an electrode profile of width $b_p(x)$.

4.3.1 Hamilton's principle

The kinetic coenergy reads

$$T^* = \frac{1}{2}\int_0^l \varrho A \dot{w}^2 dx \tag{4.22}$$

where A is the cross-section of the beam. Both the electric field and the strain vectors have a single non-zero component, respectively E_3 and S_1; the coenergy function (4.20) is therefore

$$W_e^* = \frac{1}{2}\int_0^l dx \int_A \left(\varepsilon_{33} E_3^2 + 2 S_1 e_{31} E_3 - c_{11} S_1^2\right) dA \tag{4.23}$$

and, combining with (4.21),

$$W_e^* = \frac{1}{2}\int_0^l dx \int_A \left(\varepsilon_{33} E_3^2 - 2w'' z e_{31} E_3 - c_{11} w''^2 z^2\right) dA \tag{4.24}$$

The first contribution to W_e^* is restricted to the piezoelectric part of the beam under the electrode area; the integral over the cross section can be written $\varepsilon_{33} E_3^2 b_p h_p$. The second contribution is also restricted to the piezoelectric layer; taking into account that

$$\int_A z dA = \int_{h_1}^{h_2} b_p \, z \, dz = b_p h_p z_m$$

where z_m is the distance between the mid-plane of the piezoelectric layer and the neutral axis (Fig.4.2), it can be written $-2w'' e_{31} E_3 b_p h_p z_m$. The

third term in W_e^* can be rewritten by introducing the bending stiffness (we give up the classical notation EI familiar to structural engineers to avoid confusion)

$$\mathcal{D} = \int_A c_{11} z^2 dA \tag{4.25}$$

Thus, W_e^* reads

$$W_e^* = \frac{1}{2} \int_0^l \left(\varepsilon_{33} E_3^2 b_p h_p - 2w'' e_{31} E_3 b_p h_p z_m - \mathcal{D} w''^2 \right) dx$$

Next, we can apply Hamilton's principle, recalling that only the vertical displacement is subject to virtual changes, δw, since the electric potential is fixed (voltage control). Integrating by part the kinetic energy with respect to time and taking into account that $\delta w(x, t_1) = \delta w(x, t_2) = 0$,

$$\int_{t_1}^{t_2} \delta T^* dt = \int_{t_1}^{t_2} dt \int_0^l \varrho A \dot{w}\, \delta \dot{w}\, dx = - \int_{t_1}^{t_2} dt \int_0^l \varrho A \ddot{w}\, \delta w\, dx$$

Similarly,

$$\delta W_e^* = \int_0^l [-\delta w'' \left(e_{31} E_3 b_p h_p z_m \right) - \mathcal{D} w'' \delta w''] dx$$

and, integrating by part twice with respect to x,

$$\delta W_e^* = - \left(e_{31} E_3 b_p h_p z_m \right) \delta w' \Big]_0^l + \left(e_{31} E_3 b_p h_p z_m \right)' \delta w \Big]_0^l - \int_0^l \left(e_{31} E_3 b_p h_p z_m \right)'' \delta w\, dx$$

$$- \mathcal{D} w'' \delta w' \Big]_0^l + \left(\mathcal{D} w'' \right)' \delta w \Big]_0^l - \int_0^l \left(\mathcal{D} w'' \right)'' \delta w\, dx$$

The virtual work of nonconservative forces is

$$\delta W_{nc} = \int_0^l p(x,t) \delta w\, dx$$

where $p(x,t)$ is the distributed transverse load applied to the beam. Introducing in Hamilton's principle (4.18), one gets that

$$\text{V.I.} = \int_{t_1}^{t_2} dt \int_0^l \left[-\varrho A \ddot{w} - \left(e_{31} E_3 b_p h_p z_m \right)'' - \left(\mathcal{D} w'' \right)'' + p \right] \delta w\, dx$$

$$- \left[\left(e_{31} E_3 b_p h_p z_m + \mathcal{D} w'' \right) \delta w' \right]_0^l + \left[\{ \left(e_{31} E_3 b_p h_p z_m \right)' + \left(\mathcal{D} w'' \right)' \} \delta w \right]_0^l = 0$$

for all admissible variations δw compatible with the kinematics of the system (i.e. boundary conditions); let us discuss this equation.

4.3.2 Piezoelectric loads

It follows from the previous equation that the differential equation governing the problem is

$$\varrho A\ddot{w} + \left(\mathcal{D}w''\right)'' = p - \left(e_{31}E_3 b_p h_p z_m\right)'' \tag{4.26}$$

If one takes into account that only b_p depends on the spatial variable x and that $E_3 h_p = V$, the voltage applied between the electrodes of the piezoelectric layer, it becomes

$$\varrho A\ddot{w} + \left(\mathcal{D}w''\right)'' = p - e_{31}V z_m {b_p}''(x) \tag{4.27}$$

This equation indicates that the effect of the piezoelectric layer is equivalent to a *distributed load proportional to the second derivative of the width of the electrode.*

Examining the remaining terms, one must also have

$$\begin{gathered}\left(e_{31}E_3 b_p h_p z_m + \mathcal{D}w''\right)\delta w' = 0 \\ \left[\left(e_{31}E_3 b_p h_p z_m\right)' + \left(\mathcal{D}w''\right)'\right]\delta w = 0 \quad \text{at } x = 0 \text{ and } x = l\end{gathered} \tag{4.28}$$

The first condition states that at an end where the rotation is free (where a virtual rotation is allowed, $\delta w' \neq 0$), one must have

$$e_{31}V b_p z_m + \mathcal{D}w'' = 0 \tag{4.29}$$

This means that the effect of the piezoelectric layer is that of a *bending moment proportional to the width of the electrode.* Similarly, the second condition states that at an end where the displacement is free (where a virtual displacement is allowed, $\delta w \neq 0$), one must have

$$e_{31}V b_p' z_m + \left(\mathcal{D}w''\right)' = 0 \tag{4.30}$$

$\left(\mathcal{D}w''\right)'$ represents the transverse shear force along the beam in classical beam theory, and step changes of the shear distribution occur where point loads are applied. This means that the effect of a change of slope b_p' in the width of the electrode is equivalent to a *point force proportional to change of the first derivative of the electrode width.* One should always keep in mind that the piezoelectric loading consists of internal forces which are always *self-equilibrated.*

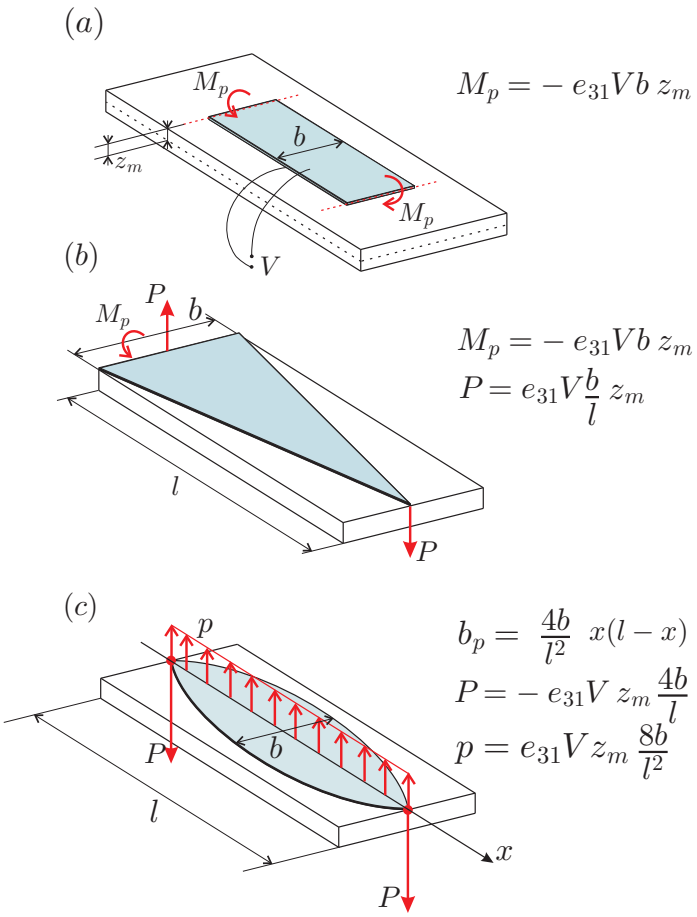

Fig. 4.3. Examples of electrode shapes and corresponding piezoelectric loading: (a) rectangular electrode, (b) triangular electrode, (c) parabolic electrode. The piezoelectric loading is always self-equilibrated.

Figure 4.3 shows a few examples of electrode shapes and the corresponding piezoelectric loading. A rectangular electrode (Fig.4.3.a) is equivalent to a pair of bending moments M_p applied at the ends of the electrode. A triangular electrode (Fig.4.3.b) is equivalent to a pair of point forces P and a bending moment M_p; note that if the beam is clamped on the left side, the corresponding loads will be taken by the support, and the only remaining force is the point load at the right end. A parabolic electrode (Fig.4.3.c) is equivalent to a uniform distributed load p and a pair of point forces P at the ends.

As another example, consider the electrode shape of Fig.4.4. It consists of a rectangular part of length l_1, followed by a part with constant slope, of length l_2. According to the foregoing discussion, this is equivalent to bending moments M_1 and M_2 at the extremities of the electrodes, and point forces P at the location where there is a sudden change in the first derivative $b^{'}(x)$. Once again, the piezoelectric loading is self-equilibrated.

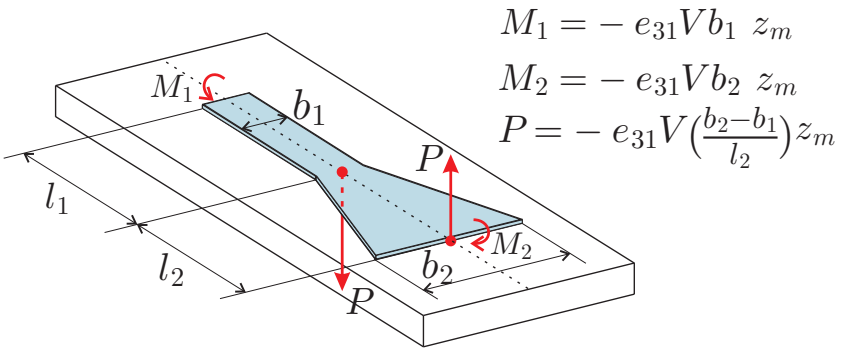

Fig. 4.4. Self-equilibrated equivalent piezoelectric loading for an electrode with a sudden change in $b'_p(x)$.

4.4 Laminar sensor

4.4.1 Current and charge amplifiers

When used in sensing mode, a piezoelectric transducer is coupled to an operational amplifier (Fig.4.5.a) to form either a current amplifier (Fig.4.5.b), or a charge amplifier (Fig.4.5.c). An operational amplifier is an active electrical circuit working as a high gain linear voltage amplifier with infinite input resistance (so that the input currents i_- and i_+ are essentially zero), and zero output resistance, so that the output voltage e_0 is essentially proportional to the voltage difference $e_+ - e_-$; the open loop gain A is usually very high, which means that the allowable input voltage is very small (millivolt). As a result, when the electrodes of a piezoelectric transducer are connected to an operational amplifier, they can be regarded as short-circuited and the electric field through the piezo can be considered as $E_3 = 0$. Then, it follows from the constitutive

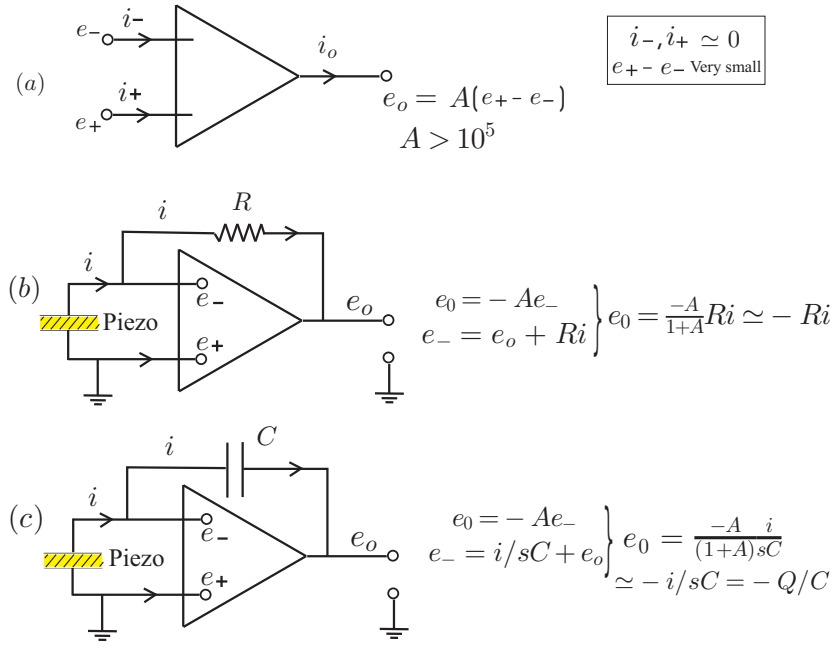

Fig. 4.5. (a) Operational amplifier, (b) Current amplifier, (c) Charge amplifier.

equation (4.2) that the electric displacement is proportional to the strain

$$D_3 = e_{31} S_1 \tag{4.31}$$

4.4.2 Distributed sensor output

If one assumes that the piezoelectric sensor is thin with respect to the beam, the strain can be regarded as uniform over its thickness, $S_1 = -z_m w''$, and $E_3 = 0$ is enforced by the charge amplifier; integrating over the electrode area (Fig.4.2), one gets

$$Q = \int D_3 dA = -\int_a^b b_p(x) z_m e_{31} w'' dx = -z_m e_{31} \int_a^b b_p(x) w'' dx \tag{4.32}$$

with a constant polarization profile e_{31}. It is assumed that the sensor extends from $x = a$ to $x = b$ along the beam. Thus, the amount of electric charge is proportional to the *weighted average of the curvature*, the weighing function being the width of the electrode. For an electrode with constant width,

$$Q = -z_m e_{31} b_p [w^{'}(b) - w^{'}(a)] \tag{4.33}$$

The sensor output is proportional to the *difference of slopes* (i.e. rotations) at the extremities of the sensor strip. We note that this result is dual of that of Fig.4.3.a, where the piezoelectric transducer is used in actuation mode.

Equation (4.32) can be integrated by parts, twice, leading to

$$\int_a^b w^{''} b_p(x) dx = w^{'} b_p \Big]_a^b - w b_p^{'} \Big]_a^b + \int_a^b w\, b^{''} dx \tag{4.34}$$

If, as an example, one considers the case of a cantilever beam clamped at $x = 0$ and covered with a piezoelectric strip and an electrode of triangular shape extending over the whole length as in Fig.4.3.b ($a = 0$ and $b = l$), $w(0) = w^{'}(0) = 0$ (cantilever beam) and $b_p^{''} = 0$, $b_p(l) = 0$, $b_p^{'} = -b_p(0)/l$ (triangular electrode). Substituting into the foregoing equations, one gets

$$Q = -z_m e_{31} \frac{b_p(0)}{l} w(l) \;\sim\; w(l) \tag{4.35}$$

Thus, the output signal is proportional to the *tip displacement* of the cantilever beam. Once again, this result is dual of that obtained in actuation mode (the piezoelectric loading is a point force at the tip). Similarly, if one considers a parabolic electrode as in Fig.4.3.c and if the beam is such that $w(0) = w(l) = 0$ (this includes pinned-pinned, pinned-clamped, etc), we have $b_p(0) = b_p(l) = 0$ and $b_p^{''}(x) = -8b/l^2$ and, substituting into (4.34),

$$Q = z_m e_{31} \frac{8b}{l^2} \int_0^l w(x) dx \;\sim\; \int_0^l w(x) dx \tag{4.36}$$

Thus, the output signal is proportional to the *volume displacement*, which is, once again, dual of the uniform distributed load in actuation mode. All the above results are based on the beam theory which is essentially one-dimensional; their accuracy in practical applications will depend very much on the relevance of these assumptions for the applications concerned. This issue is important in applications, especially in collocated control systems.

4.4.3 Charge amplifier dynamics

According to Fig.4.5.c, the output voltage is proportional to the amount of electric charge generated on the electrode; the amplifier gain is fixed by the capacitance C. This relation is correct at frequencies beyond some

corner frequency depending on the amplifier construction, but does not apply statically (near $\omega = 0$). If a refined model of the charge amplifier is required, this behavior can be represented by adding a second order high-pass filter

$$F(s) = \frac{s^2}{s^2 + 2\xi_c\omega_c s + \omega_c^2} \tag{4.37}$$

with appropriate parameters ω_c and ξ_c. For frequencies well above the corner frequency ω_c, $F(s)$ behaves like a unit gain.

4.5 Spatial modal filters

4.5.1 Modal actuator

According to (4.27), a piezoelectric layer with an electrode of width $b_p(x)$ is equivalent to a distributed transverse load proportional to $b_p''(x)$. Let

$$w(x,t) = \sum_i z_i(t)\phi_i(x) \tag{4.38}$$

be the modal expansion of the transverse displacements, where $z_i(t)$ are the modal amplitudes, and $\phi_i(x)$ the mode shapes, solutions of the eigenvalue problem

$$\left[\mathcal{D}\phi_i''(x)\right]'' - \omega_i^2 \varrho A \phi_i = 0 \tag{4.39}$$

They satisfy the orthogonality conditions

$$\int_0^l \varrho A\, \phi_i(x)\phi_j(x)dx = \mu_i\delta_{ij} \tag{4.40}$$

$$\int_0^l \mathcal{D}\, \phi_i''(x)\phi_j''(x)dx = \mu_i\omega_i^2\delta_{ij} \tag{4.41}$$

where μ_i is the modal mass, ω_i the natural frequency of mode i, and δ_{ij} is the Kronecker delta ($\delta_{ij} = 1$ if $i = j$, $\delta_{ij} = 0$ if $i \neq j$). Substituting (4.38) into (4.27) (assuming $p = 0$), one gets

$$\varrho A \sum_i \ddot{z}_i\phi_i + \sum_i z_i(\mathcal{D}\phi_i'')'' = -e_{31}Vb_p''z_m$$

or using (4.39),

$$\varrho A \sum_i \ddot{z}_i \phi_i + \varrho A \sum_i z_i \omega_i^2 \phi_i = -e_{31} V b_p^{''} z_m$$

where the sums extend over all modes. Upon multiplying by $\phi_k(x)$, integrating over the length of the beam, and using the orthogonality condition (4.40), one finds easily the equation governing the modal amplitude z_k:

$$\mu_k(\ddot{z_k} + \omega_k^2 z_k) = -e_{31} V z_m \int_0^l b_p^{''}(x)\phi_k(x)dx \tag{4.42}$$

The right hand side is the modal force p_k applied by the piezoelectric strip to mode k. From the first orthogonality condition (4.40), it is readily seen that if the electrode profile is chosen in such a way that

$$b_p^{''} \ \sim \ \varrho A \phi_l(x) \tag{4.43}$$

all the modal forces p_k vanish, except p_l:

$$p_k \ \sim \ -e_{31} V z_m \int_0^l \varrho A \phi_l \phi_k dx \ \sim \ -e_{31} V z_m \mu_l \delta_{kl} \tag{4.44}$$

such an electrode profile will excite only mode l; it constitutes a *modal actuator* (for mode l).

4.5.2 Modal sensor

Similarly, if the piezoelectric layer is used as a sensor, the electric charge appearing on the sensor is given by (4.32). Introducing the modal expansion (4.38),

$$Q = -z_m e_{31} \sum_i z_i(t) \int_0^l b_p(x)\phi_i^{''}(x)dx \tag{4.45}$$

Comparing this equation with the second orthogonality conditions (4.41), one sees that any specific mode can be made unobservable by choosing the electrode profile in such a way that the integral vanishes. If the electrode profile is chosen according to

$$b_p(x) \ \sim \ \mathcal{D}\phi_l^{''}(x) \tag{4.46}$$

(proportional to the distribution of the bending moment of mode l), the output charge becomes

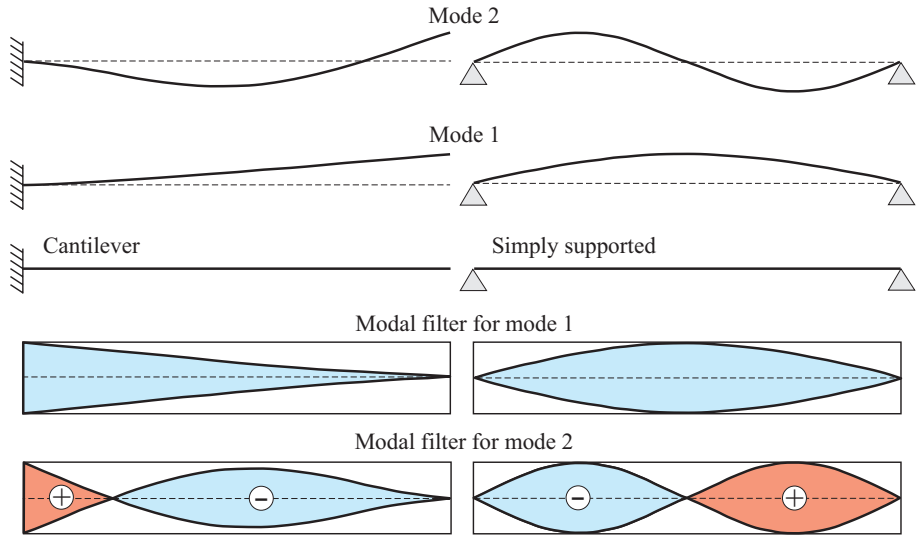

Fig. 4.6. Electrode profile of modal filters for the first two modes of a uniform beam for various boundary conditions: left: cantilever, right: simply supported.

$$Q \sim -z_m e_{31} \mu_l \omega_l^2 z_l(t) \tag{4.47}$$

It contains only a contribution from mode l. This electrode profile constitutes a *modal sensor*. Note that, for a uniform beam, (4.39) implies that the mode shapes satisfy $\phi_i^{IV}(x) \sim \phi_i(x)$. It follows that the electrode profile of a modal sensor also satisfies that of a modal actuator: from (4.46),

$$b_p''(x) \sim \phi_l^{IV}(x) \sim \phi_l(x) \tag{4.48}$$

which satisfies (4.43). Figure 4.6 illustrates the electrode profile of modal filters used for a uniform beam with various boundary conditions; the change of sign indicates a change in polarity of the piezoelectric strip, which is equivalent to negative values of $b_p(x)$. As an alternative, the part of the sensor with negative polarity can be bonded on the opposite side of the beam, with the same polarity. The reader will notice that the electrode shape of the simply supported beam is the same as the mode shape itself, while for the cantilever beam, the electrode shape is that of the mode shape of a beam clamped at the opposite end.

Modal filters constitute an attractive option for *spillover* alleviation, because they allow one to minimize the controllability and observability of a known set of modes. In practical applications, however, the beam

approximation often provides fairly poor modal filters, because the piezoelectric layer reacts as an orthotropic material rather than a unidirectional one (Preumont et al., 2003).

4.6 Active beam with collocated actuator-sensor

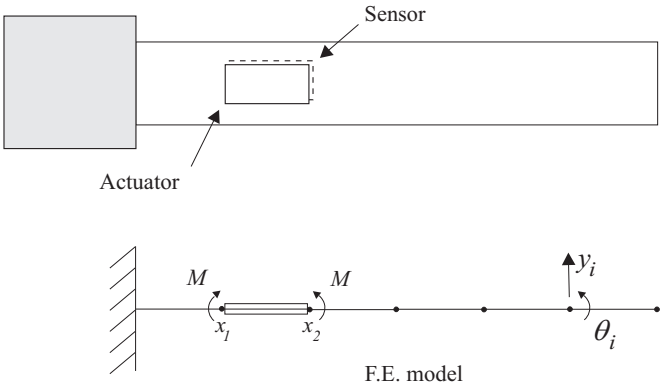

Fig. 4.7. Active cantilever beam with collocated piezoelectric actuator and sensor. Every node has 2 d.o.f. (y_i and θ_i)

Consider a beam provided with a pair of rectangular piezoelectric actuator and sensor (Fig.4.7). The two patches do not have to be of the same size, nor have the same material properties, but they are collocated in the sense of the Euler-Bernoulli beam theory, which means that they extend over the same length along the beam. The system can, for example, be modelled by finite elements; the mesh is such that there is a node at both ends of the piezo patches (each node has two degrees of freedom, one translation y_i and one rotation θ_i). We seek the open-loop FRF between the voltage $V(t)$ applied to the actuator, and the output voltage $v_0(t)$ of the sensor (assumed to be connected to a charge amplifier).

4.6.1 Frequency response function

According to Fig.4.3.a, the rectangular piezoelectric actuator is equivalent to a pair of torques M with opposite signs and proportional to V:

$$M = -e_{31} z_m b_p V = g_a V \tag{4.49}$$

where g_a is the actuator gain which can be computed from the actuator size and the material properties. In the general form of the equation of motion, the external force vector in a FE model is

$$f = bM = bg_aV \tag{4.50}$$

where the influence vector b has the form $b^T = (..,0,-1,0,1,...)$; the only non-zero components correspond to the rotational degrees of freedom of the nodes located at $x = x_1$ and $x = x_2$ in the model. In modal coordinates, the system dynamics is governed by a set of independent second order equations

$$\ddot{z}_k + 2\xi_k\omega_k\dot{z}_k + \omega_k^2 z_k = \frac{\phi_k^T f}{\mu_k} = \frac{p_k}{\mu_k} \tag{4.51}$$

where ω_k is the natural frequency of mode k, ξ_k the modal damping ratio and μ_k the modal mass. Using the Laplace variable s, we can write it alternatively as

$$z_k = \frac{p_k}{\mu_k(s^2 + 2\xi_k\omega_k s + \omega_k^2)} \tag{4.52}$$

The modal forces p_k represent the work of the external loading on the various mode shapes:

$$p_k = \phi_k^T f = \phi_k^T b g_a V = g_a V \Delta\theta_k^a \tag{4.53}$$

where $\Delta\theta_k^a = \phi_k^T b$ is the relative rotation [difference of slope $w'(x_2) - w'(x_1)$] between the extremities of the actuator, for mode k. Similarly, according to (4.33), the sensor output is also proportional to the difference of slopes, that is the relative rotation of the extremities of the sensor, $\triangle\theta^s$. In modal coordinates,

$$v_0 = g_s\Delta\theta^s = g_s\sum_i z_i\Delta\theta_i^s \tag{4.54}$$

where g_s is the sensor gain, depending on the sensor size, material properties and on the charge amplifier gain (which converts the electric charge into voltage), and $\Delta\theta_i^s$ are the modal components of the relative rotation between the extremities of the sensor. Note that if the sensor and the actuator extend over the same length of the beam, they can be considered as *collocated* in the sense of the Euler-Bernoulli beam theory, and

$$\Delta\theta_i^s = \Delta\theta_i^a = \Delta\theta_i \tag{4.55}$$

Combining the foregoing equations, one easily gets the transfer function between the actuator voltage V and the sensor output v_0; the FRF follows by substituting $s = j\omega$.

$$\frac{v_0}{V} = G(\omega) = g_a g_s \sum_{i=1}^{n} \frac{\Delta\theta_i^2}{\mu_i \left(\omega_i^2 - \omega^2 + 2j\xi_i\omega_i\omega\right)} \tag{4.56}$$

4.6.2 Pole-zero pattern

For an undamped system, the FRF is purely real:

$$\frac{v_0}{V} = G(\omega) = g_a g_s \sum_{i=1}^{n} \frac{\Delta\theta_i^2}{\mu_i \left(\omega_i^2 - \omega^2\right)} \tag{4.57}$$

All the residues of the modal expansion are positive and $G(\omega)$ is an increasing function of ω similar to that represented in Fig.2.5; the pole-zero pattern is that of Fig.2.6.a. As explained in chapter 2, for a lightly damped structure, the poles and zeros are slightly moved to the left half plane as in Fig.2.6.b. The position of the zeros in the complex plane depends on the position of the actuator/sensor pair along the beam, while the poles do not. The Bode and Nyquist plots of such a system are always similar to those of Fig.2.8. Once again, this *interlacing* property of the poles and

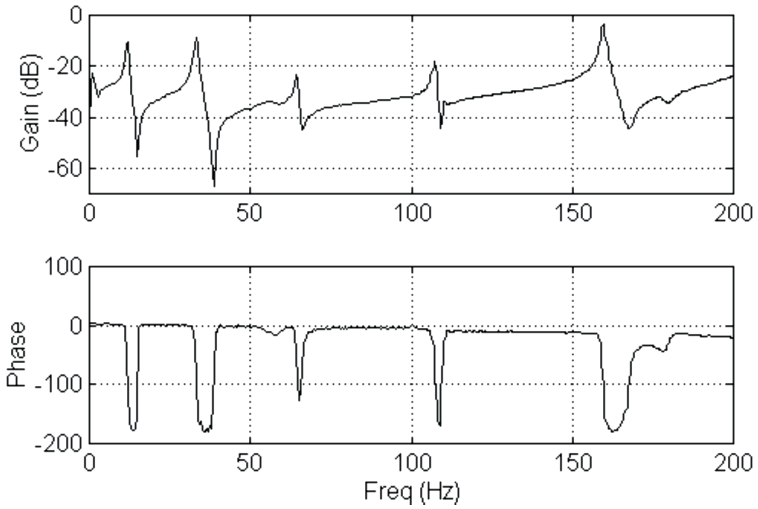

Fig. 4.8. Experimental open-loop FRF $G(\omega)$ of a piezoelectric beam similar to that of Fig.4.7.

zeros is of fundamental importance in control system design for lightly damped vibrating systems, because it is possible to find a fixed controller with guaranteed stability, irrespective to changes in the mass and stiffness distribution of the system.

Figure 4.8 shows typical experimental results obtained with a system similar to that of Fig.4.6. Observe that $G(\omega)$ does not exhibit any roll-off (decay) at high frequency; this indicates a *feedthrough* component in the system, which is not apparent from the modal expansion (4.56) (according to which the high frequency behavior is as ω^{-2}). It will become clearer when we consider the modal truncation. [1]

4.6.3 Modal truncation

Let us now examine the modal truncation of (4.56) which normally includes all the modes of the system (a finite number n with a discrete model, or infinite if one looks at the system as a distributed one). Obviously, if one wants an accurate model in some frequency band $[0, \omega_c]$, all the modes (with significant residues) which belong to this frequency band must be included in the truncated expansion, but the high frequency modes cannot be completely ignored. To analyze this, one rewrites (4.56)

$$G(\omega) = g_a g_s \sum_{i=1}^{n} \frac{\Delta\theta_i^2}{\mu_i \omega_i^2} . D_i(\omega) \tag{4.58}$$

where

$$D_i(\omega) = \sum_{i=1}^{n} \frac{1}{1 - \omega^2/\omega_i^2 + 2j\xi_i\omega/\omega_i} \tag{4.59}$$

is the *dynamic amplification* of mode i. For any mode with a natural frequency ω_i substantially larger than ω_c, on see from Fig.2.2 that $D_i(\omega) \simeq 1$ within $[0, \omega_c]$ and the sum (4.58) may be replaced by

$$G(\omega) = g_a g_s \sum_{i=1}^{m} \frac{\Delta\theta_i^2}{\mu_i \omega_i^2} . D_i(\omega) + g_a g_s \sum_{i=m+1}^{n} \frac{\Delta\theta_i^2}{\mu_i \omega_i^2} \tag{4.60}$$

where m has been selected in such a way that $\omega_m \gg \omega_c$. This equation recognizes the fact that, at low frequency, the high frequency modes respond in a *quasi-static* manner. The sum over the high frequency modes can be eliminated by noting that the static gain satisfies

[1] Another observation is that a small linear shift appears in the phase diagram, due to the fact that these results have been obtained digitally (the sampling is responsible for a small delay in the system).

$$G(0) = g_a g_s \sum_{i=1}^{n} \frac{\Delta\theta_i^2}{\mu_i \omega_i^2} \tag{4.61}$$

leading to

$$G(\omega) = g_a g_s \sum_{i=1}^{m} \frac{\Delta\theta_i^2}{\mu_i \omega_i^2}.D_i(\omega) + [G(0) - g_a g_s \sum_{i=1}^{m} \frac{\Delta\theta_i^2}{\mu_i \omega_i^2}] \tag{4.62}$$

The term between brackets, independent of ω, which corresponds to the high frequency modes is often called the *residual mode*. This equation can be written alternatively

$$G(\omega) = G(0) + g_a g_s \sum_{i=1}^{m} \frac{\Delta\theta_i^2}{\mu_i \omega_i^2}.[D_i(\omega) - 1]$$

or

$$G(\omega) = G(0) + g_a g_s \sum_{i=1}^{m} \frac{\Delta\theta_i^2}{\mu_i \omega_i^2} \frac{(\omega^2 - 2j\xi_i\omega_i\omega)}{(\omega_i^2 - \omega^2 + 2j\xi_i\omega_i\omega)} \tag{4.63}$$

The feedthrough component observed in Fig.4.8 is clearly apparent in (4.62). Note that the above equations require the static gain $G(0)$, but do not require the knowledge of the high frequency modes.

It is important to emphasize the fact that the quasi-static correction has a significant impact on the open-loop zeros of $G(\omega)$, and consequently on the performance of the control system. Referring to Fig.2.5, it is clear that neglecting the residual mode (quasi-static correction) amounts to shifting the diagram $G(\omega)$ along the vertical axis; this operation alters the location of the zeros which are at the crossing of $G(\omega)$ with the horizontal axis. Including the quasi-static correction tends to bring the zeros closer to the poles which, in general, tends to reduce the performance of the control system. Thus, it is a fairly general statement to say that *neglecting the residual mode (high frequency dynamics) tends to overestimate the performance of the control system*. Finally, note that since the piezoelectric loads are self-equilibrated, they would not affect the rigid body modes if there were any.

4.7 Admittance of a beam with a piezoelectric patch

Let us consider a beam provided with a single piezoelectric patch and establish the analytical expression of the admittance FRF, or equivalently of the *dynamic capacitance*. Assuming a rectangular patch of length l

(from x_1 to x_2), width b_p, thickness t, and distant z_m from the mid-plane of the beam, applying a voltage V generates a pair of self-equilibrated moments $M = -e_{31} b_p z_m V$. As in the previous section, the response of mode i is governed by (assuming no damping)

$$\mu_i \ddot{z}_i + \mu_i \omega_i^2 z_i = M \Delta\theta_i \tag{4.64}$$

or

$$z_i = -e_{31} b_p z_m V \frac{\Delta\theta_i}{\mu_i (s^2 + \omega_i^2)} \tag{4.65}$$

where $\Delta\theta_i = \phi_i'(x_2) - \phi_i'(x_1)$ is the difference of slope of mode i at the ends of the patch. The beam deflection is

$$w = \sum_{i=1}^{n} z_i \phi_i(x) = -e_{31} b_p z_m V \sum_{i=1}^{n} \frac{\Delta\theta_i \phi_i(x)}{\mu_i (s^2 + \omega_i^2)} \tag{4.66}$$

In the previous section, the charge amplifier cancelled the electric field across the sensor. Here, we must use the second constitutive equation of a unidirectional piezoelectric material

$$D = \varepsilon^T (1 - k^2) E + e_{31} S \tag{4.67}$$

with the electric field $E = V/t$; it is assumed that $t << z_m$ and that the strain level is uniform across the thickness of the patch, leading to $S = -z_m w''$ according to the Bernoulli assumption. The electric charge is obtained by integrating over the area of the electrode

$$Q = \int_A D \, dA = \int_A \varepsilon^T (1 - k^2) \frac{V}{t} dA - e_{31} z_m b_p \int_{x_1}^{x_2} w'' dx$$

$$Q = (1 - k^2) CV - e_{31} z_m b_p [w'(x_2) - w'(x_1)]$$

Thus,

$$\frac{Q}{(1 - k^2) CV} = 1 + \frac{(e_{31} z_m b_p)^2}{(1 - k^2) C} \sum_{i=1}^{n} \frac{\Delta\theta_i^2}{\mu_i (s^2 + \omega_i^2)} \tag{4.68}$$

or, after using (3.20) and $C = \varepsilon^T b_p l / t$

$$\frac{Q}{(1 - k^2) CV} = 1 + \frac{k^2}{1 - k^2} \sum_{i=1}^{n} \frac{c^E b_p t z_m^2 \Delta\theta_i^2}{l \, \mu_i \omega_i^2} \frac{1}{1 + s^2/\omega_i^2} \tag{4.69}$$

If one notes that the average strain in the piezo patch is $\bar{S} = -z_m \Delta\theta / l$ and $b_p l t$ is the volume of the patch, the strain energy in the patch when the structure vibrates according to mode i can be written approximately

$$W_e \simeq \frac{\bar{S}^2.c^E.b_p lt}{2} = \frac{c^E z_m^2 \Delta\theta_i^2 b_p t}{2l} \tag{4.70}$$

Since $\mu_i\omega_i^2/2$ is the total strain energy in the beam when it vibrates according to mode i, the residues in the modal expansion represent the *fraction of modal strain energy* in the piezo patch, for mode i:

$$\nu_i = \frac{c^E b_p t z_m^2 \Delta\theta_i^2}{l\,\mu_i\omega_i^2} = \{\frac{\text{Strain energy in the piezo patch}}{\text{Strain energy in the beam}}\}_i \tag{4.71}$$

and the relation between Q and V reads finally

$$\frac{Q}{(1-k^2)CV} = 1 + \frac{k^2}{1-k^2}\sum_{i=1}^{n}\frac{\nu_i}{1+s^2/\omega_i^2} \tag{4.72}$$

or equivalently, the dynamic capacitance reads

$$\frac{Q}{V} = C(1-k^2)[1+\sum_{i=1}^{n}\frac{K_i^2}{1+s^2/\omega_i^2}] \tag{4.73}$$

where

$$K_i^2 = \frac{k^2\nu_i}{1-k^2} \tag{4.74}$$

is known as the *effective electromechanical coupling factor* for mode i. $C(1-k^2)$ is the blocked capacitance of the piezo. The static capacitance (at $\omega = 0$) is given by

$$C_{\text{stat}} = \{\frac{Q}{V}\}_{\omega=0} = C(1-k^2)(1+\sum_{i=1}^{n}K_i^2) \tag{4.75}$$

The poles of the FRF are the natural frequencies ω_i of the beam with short-circuited electrodes, while the zeros correspond to the natural frequencies Ω_i with open electrodes ($Q = 0$). Typically, Ω_i is very close to ω_i, so that in the vicinity of $\omega = \Omega_i$, the modal expansion is dominated by the contribution of mode i. It follows that Ω_i satisfies the equation

$$1 + \frac{K_i^2}{1-\Omega_i^2/\omega_i^2} \simeq 0 \tag{4.76}$$

or

$$K_i^2 \simeq \frac{\Omega_i^2 - \omega_i^2}{\omega_i^2} \tag{4.77}$$

Thus, the effective electromechanical coupling factor of all modes can be evaluated from a single admittance FRF test (the poles of which are ω_i and the zeros are Ω_i). The foregoing formula is an extension of (3.38).[2]

Formula (4.73) can be written alternatively

$$\frac{Q}{V} = C_{\text{stat}} \cdot \frac{\prod(1 + s^2/\Omega_i^2)}{\prod(1 + s^2/\omega_j^2)} \tag{4.78}$$

4.8 Piezoelectric laminate

In the first part of this chapter, the partial differential equation governing the dynamics of a piezoelectric beam, and the equivalent piezoelectric loads were established from Hamilton's principle. A similar approach can be used for piezoelectric laminates, but it is lengthy and cumbersome. The analytical expression for the equivalent piezoelectric loads and the sensor output can be obtained alternatively, as in the classical analysis of laminate composites, by using the appropriate constitutive equations; this is essentially the approach followed by (C.K. Lee, 1990).

4.8.1 Two dimensional constitutive equations

Consider a two dimensional piezoelectric laminate in a plane (x, y): the poling direction z is normal to the laminate and the electric field is also applied along z. In the piezoelectric orthotropy axes, the constitutive equations (4.1) (4.2) read

$$\{T\} = [c]\{S\} - \begin{Bmatrix} e_{31} \\ e_{32} \\ 0 \end{Bmatrix} E_3 \tag{4.79}$$

$$D_3 = \{e_{31}\ e_{32}\ 0\}\{S\} + \varepsilon E_3 \tag{4.80}$$

where

$$\{T\} = \begin{Bmatrix} T_{11} \\ T_{22} \\ T_{12} \end{Bmatrix} \qquad \{S\} = \begin{Bmatrix} S_{11} \\ S_{22} \\ 2S_{12} \end{Bmatrix} = \begin{Bmatrix} \partial u/\partial x \\ \partial v/\partial y \\ \partial u/\partial y + \partial v/\partial x \end{Bmatrix} \tag{4.81}$$

[2] the presence of ω_i instead of Ω_i at the denominator of (4.77) is insignificant in practice.

are the stress and strain vector, respectively, $[c]$ is the matrix of elastic constants under constant electric field, E_3 is the component of the electric field along z, D_3 is the z component of the electric displacement and ε the dielectric constant under constant strain (ε^S).

4.8.2 Kirchhoff theory

Following the Kirchhoff theory (e.g. Agarwal and Broutman, 1990), we assume that a line originally straight and normal to the midplane remains so in the deformed state. This is equivalent to neglecting the shear deformations S_{23} and S_{31}. If the midplane undergoes a displacement u_0 , v_0 , w_0 , a point located on the same normal at a distance z from the midplane undergoes the displacements (Fig.4.9)

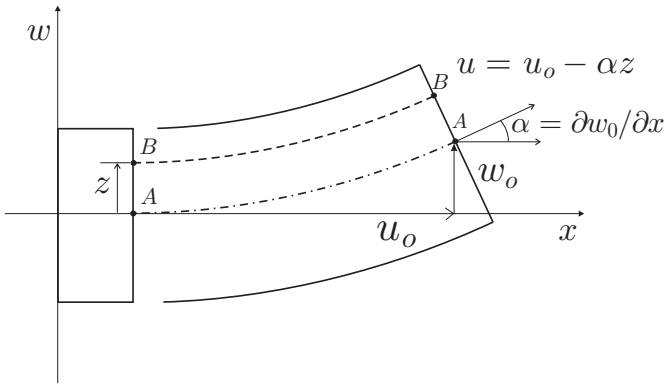

Fig. 4.9. Kinematics of a Kirchhoff plate.

$$\begin{aligned} u &= u_0 - z\frac{\partial w_0}{\partial x} \\ v &= v_0 - z\frac{\partial w_0}{\partial y} \\ w &= w_0 \end{aligned} \tag{4.82}$$

The corresponding strains are

$$\{S\} = \{S^0\} + z\{\kappa\} \tag{4.83}$$

where

$$\{S^0\} = \begin{Bmatrix} S^0_{11} \\ S^0_{22} \\ 2S^0_{12} \end{Bmatrix} = \begin{Bmatrix} \partial u_0/\partial x \\ \partial v_0/\partial y \\ \partial u_0/\partial y + \partial v_0/\partial x \end{Bmatrix} \tag{4.84}$$

are the midplane strains and

$$\{\kappa\} = \begin{Bmatrix} \kappa_{11} \\ \kappa_{22} \\ \kappa_{12} \end{Bmatrix} = - \begin{Bmatrix} \partial^2 w_0/\partial x^2 \\ \partial^2 w_0/\partial y^2 \\ 2\partial^2 w_0/\partial x \partial y \end{Bmatrix} \tag{4.85}$$

are the curvatures (the third component represents twisting). The stresses in the laminate vary from layer to layer (because of varying stiffness properties) and it is convenient to integrate over the thickness to obtain an equivalent system of forces and moments acting on the cross sections:

$$\{N\} = \int_{-h/2}^{h/2} \{T\} dz \qquad \{M\} = \int_{-h/2}^{h/2} \{T\} z \, dz \tag{4.86}$$

The positive direction of the resultant forces and moments is given in Fig.4.10. $\{N\}$ and $\{M\}$ are respectively a force per unit length, and a moment per unit length.

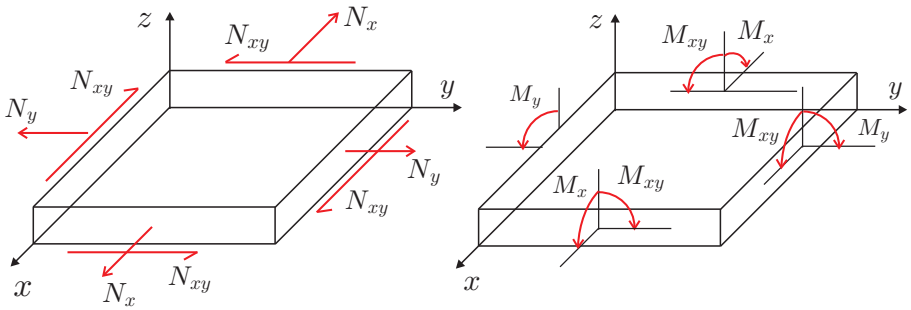

Fig. 4.10. Resultant forces and moments.

4.8.3 Stiffness matrix of a multi-layer elastic laminate

Before analyzing a piezoelectric laminate, let us recall the stiffness matrix of a multi-layer elastic laminate (Fig.4.11). If $[c]_k$ represents the stiffness matrix of the material of layer k, expressed in global coordinates, the constitutive equation within layer k is

$$\{T\} = [c]_k\{S\} = [c]_k\{S^0\} + z[c]_k\{\kappa\} \tag{4.87}$$

Upon integrating over the thickness of the laminate, one gets

$$\begin{Bmatrix} N \\ M \end{Bmatrix} = \begin{bmatrix} A & B \\ B & D \end{bmatrix} \begin{Bmatrix} S^0 \\ \kappa \end{Bmatrix} \tag{4.88}$$

with

$$\begin{aligned} A &= \sum_{k=1}^{n} [c]_k (h_k - h_{k-1}) \\ B &= \frac{1}{2} \sum_{k=1}^{n} [c]_k (h_k^2 - h_{k-1}^2) \\ D &= \frac{1}{3} \sum_{k=1}^{n} [c]_k (h_k^3 - h_{k-1}^3) \end{aligned} \tag{4.89}$$

where the sum extends over all the layers of the laminate; this is a classical result in laminate composites. A is the extensional stiffness matrix relating the in-plane resultant forces to the midplane strains; D is the bending stiffness matrix relating the moments to the curvatures, and B is the coupling stiffness matrix, which introduces coupling between bending and extension in a laminated plate; from (4.89), it is readily seen that B vanishes if the laminate is symmetric, because two symmetric layers contribute equally, but with opposite signs to the sum.

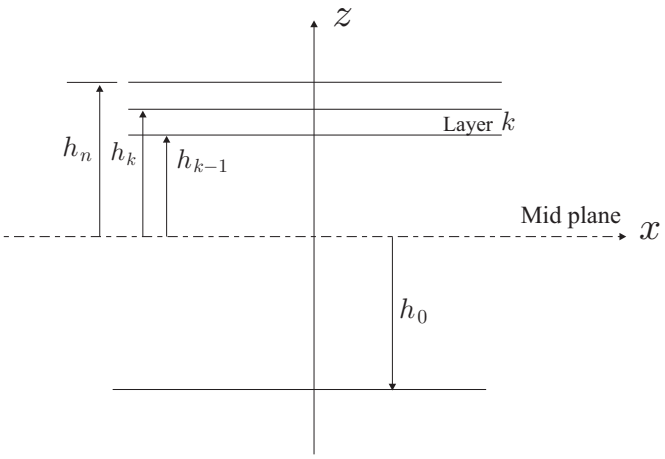

Fig. 4.11. Geometry of a multilayered laminate.

4.8.4 Multi-layer laminate with a piezoelectric layer

Next, consider a multi-layer laminate with a single piezoelectric layer (Fig.4.12); the constitutive equations of the piezoelectric layer are (4.79) and (4.80). Upon integrating over the thickness of the laminate as in the previous section, assuming that the global axes coincide with orthotropy axes of the piezoelectric layer, one gets

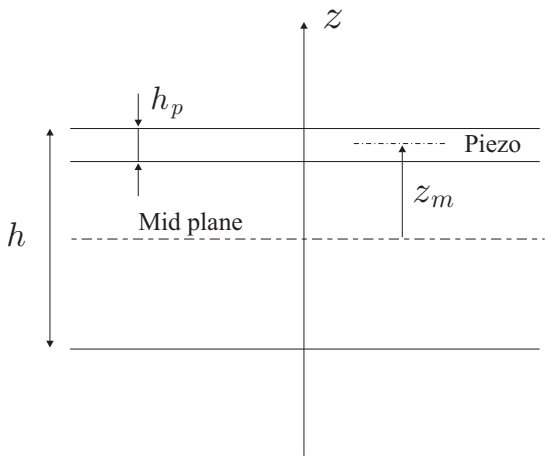

Fig. 4.12. Piezoelectric layer.

$$\begin{Bmatrix} N \\ M \end{Bmatrix} = \begin{bmatrix} A & B \\ B & D \end{bmatrix} \begin{Bmatrix} S^0 \\ \kappa \end{Bmatrix} + \begin{bmatrix} I_3 \\ z_m I_3 \end{bmatrix} \begin{Bmatrix} e_{31} \\ e_{32} \\ 0 \end{Bmatrix} V \tag{4.90}$$

$$D_3 = \{e_{31}\ e_{32}\ 0\}[I_3\ \ z_m I_3] \begin{Bmatrix} S^0 \\ \kappa \end{Bmatrix} - \varepsilon\, V/h_p \tag{4.91}$$

where V is the difference of potential between the electrodes of the piezoelectric layer ($E_3 = -V/h_p$), h_p the thickness of the piezoelectric layer, z_m the distance between the midplane of the piezoelectric layer and the midplane of the laminated; I_3 is the unity matrix of rank 3 and A,B,D are given by (4.89), including the piezoelectric layer.[3] In writing (4.91), it has been assumed that the thickness of the piezoelectric layer is small with respect to that of the laminate, so that the strain can be regarded as uniform across its thickness.

[3] The piezoelectric layer contributes to A, B and D with the stiffness properties under constant electric field.

4.8.5 Equivalent piezoelectric loads

If there is no external load, $\{N\}$ and $\{M\}$ vanish and (4.90) can be rewritten

$$\begin{bmatrix} A & B \\ B & D \end{bmatrix} \begin{Bmatrix} S^0 \\ \kappa \end{Bmatrix} = - \begin{bmatrix} I_3 \\ z_m I_3 \end{bmatrix} \begin{Bmatrix} e_{31} \\ e_{32} \\ 0 \end{Bmatrix} V \tag{4.92}$$

The right hand side represents the equivalent piezoelectric loads. If the material is isotropic, $e_{31} = e_{32}$, and the equivalent piezoelectric loads are *hydrostatic* (i.e. they are independent of the orientation of the facet within the part covered by the electrode). Overall, they consist of an *in-plane force normal to the contour of the electrode, and a constant moment acting on the contour of the electrode* (Fig.4.13); the force per unit length and moment per unit length are respectively

$$N_p = -e_{31} V \qquad\qquad M_p = -e_{31} z_m V \tag{4.93}$$

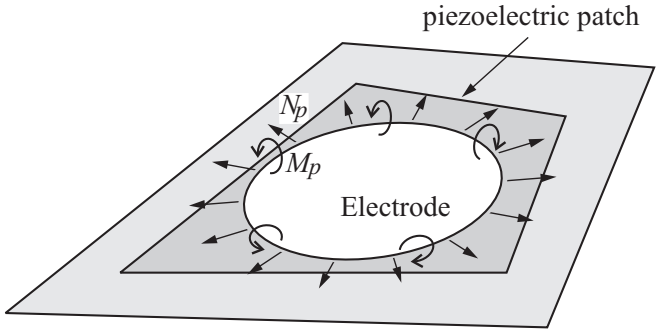

Fig. 4.13. Equivalent piezoelectric loads (per unit length) for an isotropic piezoelectric actuator: $N_p = -e_{31} V$, $M_p = -e_{31} z_m V$.

4.8.6 Sensor output

On the other hand, if the piezoelectric layer is used as a sensor and if its electrodes are connected to a charge amplifier which enforces $V \sim 0$, the sensor equation (4.91) becomes

$$D_3 = \{e_{31}\ e_{32}\ 0\}[I_3\ \ z_m I_3] \left\{ \begin{matrix} S^0 \\ \kappa \end{matrix} \right\} \tag{4.94}$$

Upon substituting the midplane strains and curvature from (4.84-85), and integrating over the electrode area, one gets

$$Q = \int_\Omega D_3 d\Omega = \int_\Omega \left[e_{31} \frac{\partial u_0}{\partial x} + e_{32} \frac{\partial v_0}{\partial y} - z_m \left(e_{31} \frac{\partial^2 w}{\partial x^2} + e_{32} \frac{\partial^2 w}{\partial y^2} \right) \right] d\Omega \tag{4.95}$$

The integral extends over the electrode area (the part of the piezo not covered by the electrode does not contribute to the signal). The first part of the integral is the contribution of the *membrane strains*, while the second is due to *bending*.

If the piezoelectric properties are isotropic ($e_{31} = e_{32}$), the surface integral can be further transformed into a contour integral using the divergence theorem; the previous equation is rewritten

$$\begin{aligned} Q &= e_{31} \int_\Omega \text{div } \vec{u}_0 \ d\Omega - e_{31} z_m \int_\Omega \text{div. } \vec{\text{grad}}\, w \ d\Omega \\ &= e_{31} \int_C \vec{n}.\vec{u}_0 \, dl - e_{31} z_m \int_C \vec{n}.\ \vec{\text{grad}}\, w \ dl \end{aligned}$$

where $\vec{n}$ is the outward normal to the contour of the electrode in its plane. Alternatively,

$$Q = e_{31} \int_C (\vec{u}_0.\vec{n} - z_m \frac{\partial w}{\partial \vec{n}}) dl \tag{4.96}$$

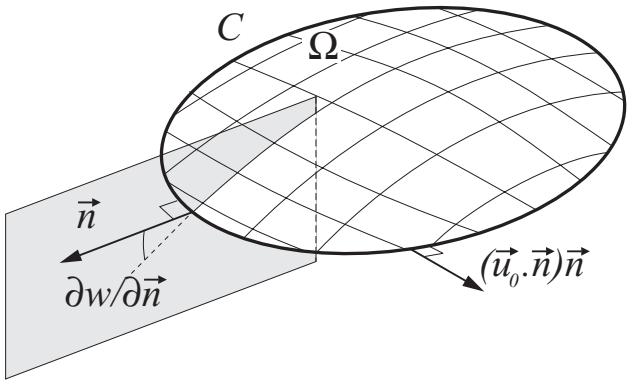

Fig. 4.14. Contributions to the sensor output for an isotropic piezoelectric layer. Ω is the electrode area.

This integral extends over the contour of the electrode (Fig.4.14); the first contribution is the component of the mid-plane, *in-plane displacement normal to the contour* and the second one is associated with the *slope along the contour*.
Once again, the duality between the equivalent piezoelectric loads generated by the transducer used as actuator, and the sensor output when the transducer is connected to a charge amplifier must be pointed out.

4.8.7 Beam model vs. plate model

In this chapter, we have analyzed successively the piezoelectric beam according to the assumption of Euler-Bernoulli, and piezoelectric laminate according to Kirchhoff's assumption. The corresponding piezoelectric loads have been illustrated in Fig.4.3 and 4.13, respectively; the sensor output, when the transducer is used in sensing mode, can be deduced by *duality*: *a bending moment normal to the contour in actuation mode corresponds to the slope along the contour in sensing mode, and the in-plane force normal to the contour in actuation mode corresponds to the in-plane displacement normal to the contour in sensing mode*. Figure 4.15 illustrates the equivalent piezoelectric loads according to both theories for a rectangular isotropic piezoceramic patch acting on a structure extending along one dimension: according to the beam theory, the equivalent piezoelectric loads consist of a pair of torques applied to the ends of the electrode (Fig.4.15.a), while according to the laminate theory, the torque

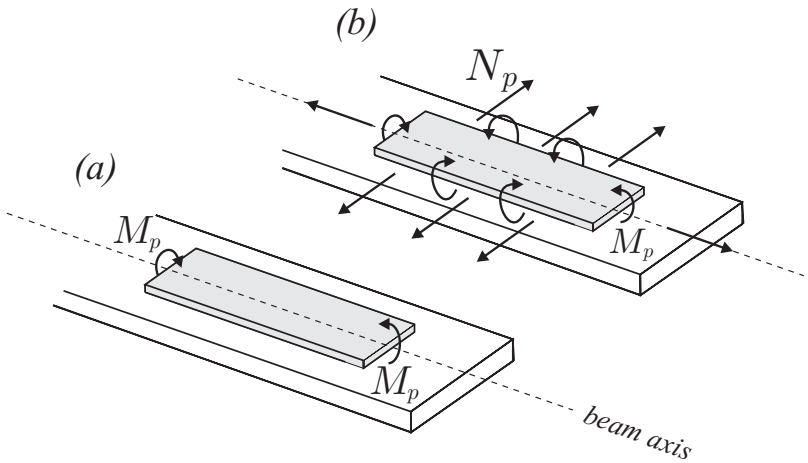

Fig. 4.15. Equivalent piezoelectric loads of a rectangular piezoelectric patch bonded on a beam: (a) beam theory, (b) laminate theory.

is applied along the whole contour of the electrode and it is supplemented by an in-plane force N_p normal to the contour (Fig.4.15.b). If the structure extends dominantly along one axis, and if one is interested in the structural response *far away* from the actuator (e.g. tip displacement), it is reasonable to think that the piezoelectric loads of the beam theory are indeed the dominant ones. However, in active vibration control, one is often interested in configurations where the dual actuator and sensor are close to being *collocated*, to warrant alternating poles and zeros in the open-loop FRF, for a wide frequency range (the perfectly dual and collocated case was considered in section 4.6); in this case, it turns out that the contributions to the piezoelectric loading and to the sensor output which are ignored in the beam theory are significant, and neglecting them usually leads to substantial errors in the open-loop zeros of the control system. This important issue will be addressed again in later chapters.

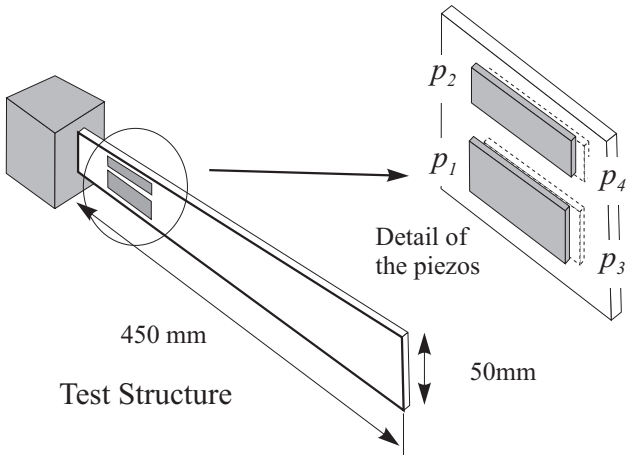

Fig. 4.16. Cantilever plate with piezoceramics.

To illustrate how a beam model and a plate model can be different for nearly collocated systems, consider the cantilever plate of Fig.4.16; the steel plate is 0.5 mm thick and 4 piezoceramic strips of 250 μm thickness are bounded symmetrically as indicated in the figure. The size of the piezos is respectively 55 $mm \times 25$ mm for p_1 and p_3, and 55 $mm \times 12.5$ mm for p_2 and p_4. p_1 is used as actuator while the sensor is taken successively as p_2, p_3 and p_4. Since they cover the same extension along the beam, the various sensor locations cannot be distinguished in the sense of the Euler-Bernoulli beam theory (except for the sign or a constant factor,

because p_2 and p_4 are on opposite sides and the size of p_3 is twice that of p_2 and p_4) and they should lead to the same transfer function. This is

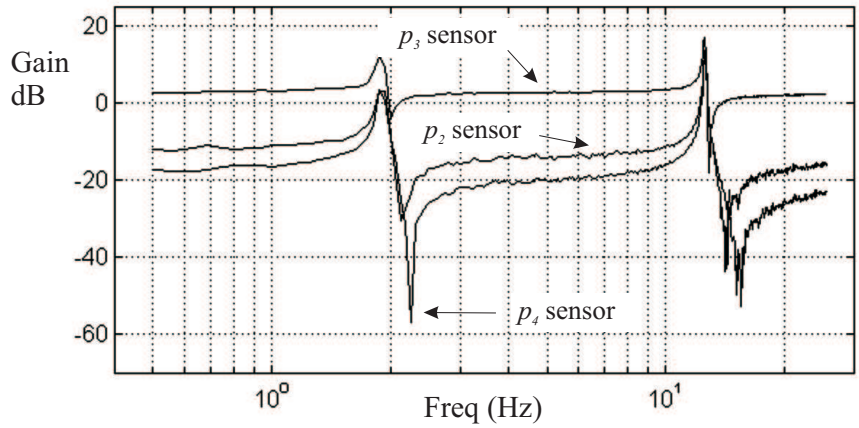

Fig. 4.17. Cantilever plate with piezoceramics; experimental FRF for the three sensor configurations of Fig.4.16.

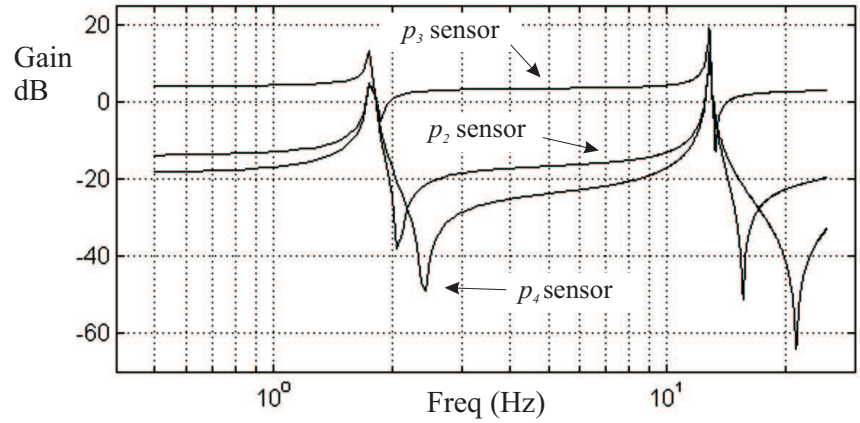

Fig. 4.18. Cantilever plate with piezoceramics; Numerical (finite elements) FRF for the three sensor configurations of Fig.4.16.

not the case in practice, as we can see in the experimental results shown in Fig.4.17. We see that the transmission zeros vary significantly from one configuration to the other. In fact, because of the nearness of the actuator

to the sensor, and the small thickness of the plate, the membrane strains play an important role in the transmission of the strain from the actuator to the sensor and are responsible for the differences between the three sensor configurations. Figure 4.18 show computed FRF based on the plate theory using Mindlin-type finite elements (Piefort, 2001); one sees that the FRF curves behave in a way similar to the experimental ones and that the plate theory accounts for the experimental results. We shall see later that, because the closed-loop poles are located on branches going from the open-loop poles to the open-loop zeros, overestimating the spacing between the poles and the zeros leads to overestimating the closed-loop performances of the system.

A deeper discussion of the finite element formulation of multi-layer piezoelectric shells can be found in (Benjeddou, 2000, Garcia Lage et al., 2004, Heyliger et al, 1996, Piefort, 2001) and the literature quoted in these papers. The newly available PZT fibers (with interdigitated electrodes or not), which are usually supplied in a soft polymer cladding, seem to be particularly difficult to model accurately, due to the stiffness discrepancy between the supporting structure, the PZT fibers and the soft polymer interface; this is the subject of on-going research.

4.8.8 Additional remarks

1. Experiments conducted on a cantilever beam excited by a PZT patch on one side and covered with an isotropic PVDF film on the other side, with an electrode shaped as a modal filter for the first mode according to the theory of modal sensors developed in section 4.5, have revealed significant discrepancies between the measured FRF and that predicted by the beam theory; however, the FRF could be predicted quite accurately by the laminated plate theory (Preumont et al., 2003).

2. For beams, modal filtering has been achieved by shaping the width of the electrode. This concept cannot be directly transposed to plates. Spatial filtering of two-dimensional structures will be examined in Chapter 14.

4.9 Active truss

Figure 4.19 shows a truss structure where some of the bars have been replaced by active struts; each of them consists of a piezoelectric linear actuator colinear with a force transducer. Such an active truss can be used

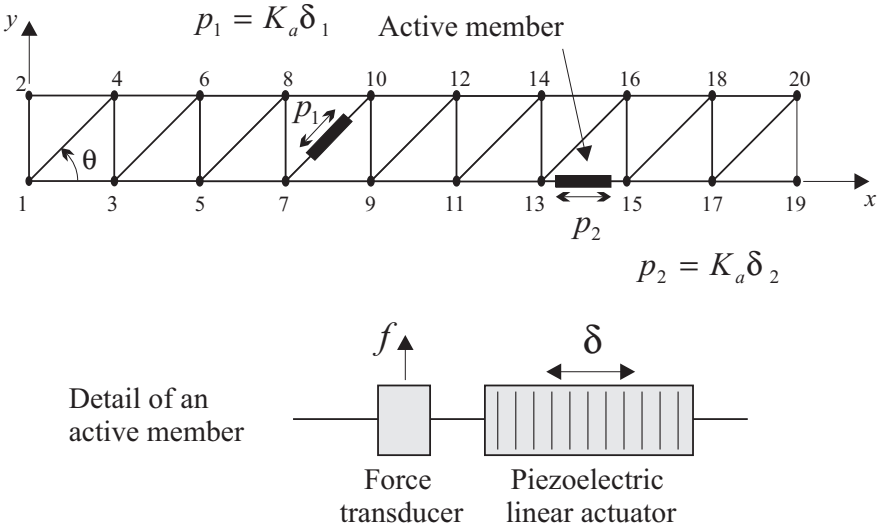

Fig. 4.19. Active truss. The active struts consist of a piezoelectric linear actuator with a force sensor.

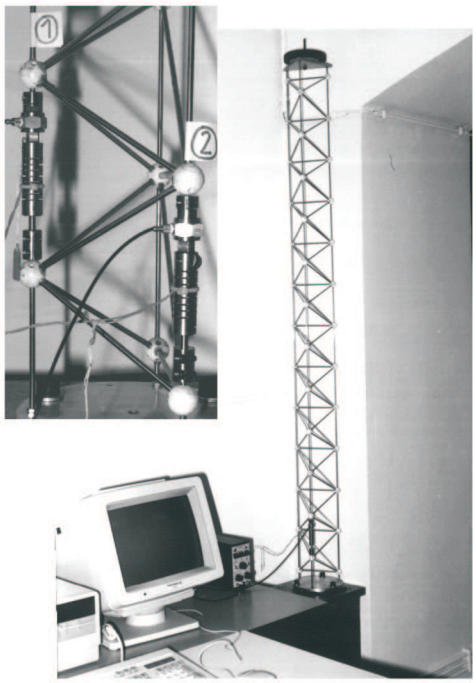

Fig. 4.20. ULB Active truss (1988).

for vibration attenuation, or to improve the dimensional stability under thermal gradients. If the stiffness of the active struts matches that of the other bars in the truss, the passive behaviour of the truss is basically unchanged. Fig.4.20 shows an example of active truss equipped with two active struts (built in the late 80's).

Consider a structure with a single discrete piezoelectric transducer (Fig.4.21); the transducer is governed by Equ.(3.22)

$$\begin{Bmatrix} Q \\ f \end{Bmatrix} = \begin{bmatrix} C(1-k^2) & nd_{33}K_a \\ -nd_{33}K_a & K_a \end{bmatrix} \begin{Bmatrix} V \\ b^T x \end{Bmatrix} \tag{4.97}$$

where $\Delta = b^T x$ is the relative displacement at the extremities of the transducer. The dynamics of the structure is governed by

$$M\ddot{x} + K^* x = -bf \tag{4.98}$$

where K^* is the stiffness matrix of the structure without the transducer and b is the influence vector of the transducer in the global coordinate system of the structure. The non-zero components of b are the direction cosines of the active bar (Problem 4.5). The minus sign on the right hand side of the previous equation comes from the fact that the force acting on the structure is opposed to that acting on the transducer. Note that the same vector b appears in both equations because the relative displacement is measured along the direction of f.

Substituting f from the constitutive equation into the second equation, one finds

$$M\ddot{x} + Kx = bK_a\delta \tag{4.99}$$

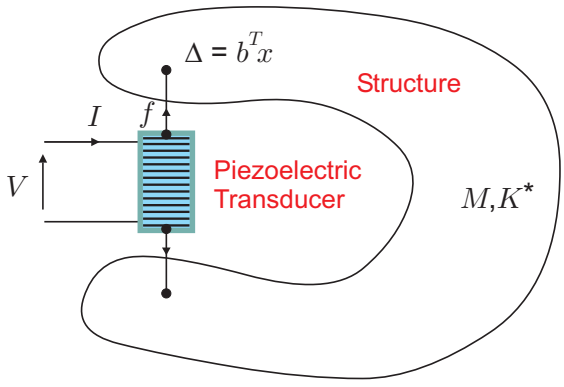

Fig. 4.21. Structure with a piezoelectric transducer.

where $K = K^* + bb^T K_a$ is the global stiffness matrix of the structure including the piezoelectric transducer in short-circuited conditions (which contributes for $bb^T K_a$); $\delta = nd_{33}V$ is the *free expansion* of the transducer induced by a voltage V; $K_a\delta$ is the equivalent piezoelectric loading: the effect of the piezoelectric transducer on the structure consists of a pair of *self-equilibrating* forces applied axially to the ends of the transducer; as for thermal loads, their magnitude is equal to the product of the stiffness of the transducer (in short-circuited conditions) by the unconstrained piezoelectric expansion; this is known as the *thermal analogy*.

Let ϕ_i be the normal modes, solutions of the eigenvalue problem

$$(K - \omega_i^2 M)\phi_i = 0 \tag{4.100}$$

They satisfy the usual orthogonality conditions

$$\phi_i^T M \phi_j = \mu_i \delta_{ij} \tag{4.101}$$

$$\phi_i^T K \phi_j = \mu_i \omega_i^2 \delta_{ij} \tag{4.102}$$

where ω_i is the natural frequency when the transducer is short-circuited. If the global displacements are expanded into modal coordinates,

$$x = \sum_i z_i \phi_i \tag{4.103}$$

where z_i are the modal amplitudes, (4.99) is easily transformed into

$$\mu_i(\ddot{z}_i + \omega_i^2 z_i) = \phi_i^T b K_a \delta \tag{4.104}$$

Upon taking the Laplace transform, one easily gets

$$x = \sum_{i=1}^{n} \frac{\phi_i \phi_i^T}{\mu_i(\omega_i^2 + s^2)} b K_a \delta \tag{4.105}$$

and the transducer extension

$$\Delta = b^T x = \sum_{i=1}^{n} \frac{K_a (b^T \phi_i)^2}{\mu_i \omega_i^2 (1 + s^2/\omega_i^2)}\, \delta \tag{4.106}$$

From Equ.(4.102), $\mu_i\omega_i^2/2$ is clearly the strain energy in the structure when it vibrates according to mode i, and $K_a(b^T\phi_i)^2/2$ represents the strain energy in the transducer when the structure vibrates according to mode i. Thus, the ratio

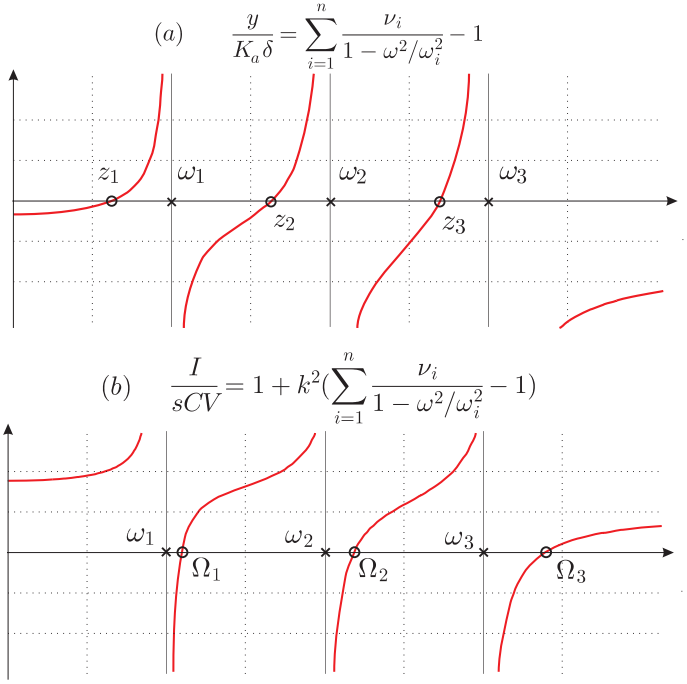

Fig. 4.22. (a) Open-loop FRF of the active strut mounted in the structure (undamped). (b) Admittance of the transducer mounted in the structure.

$$\nu_i = \frac{K_a(b^T\phi_i)^2}{\mu_i\omega_i^2} \tag{4.107}$$

is readily interpreted as the *fraction of modal strain energy* in the transducer for mode i. With this notation, the previous equation is rewritten

$$\Delta = b^T x = \sum_{i=1}^{n} \frac{\nu_i}{(1+s^2/\omega_i^2)}\,\delta \tag{4.108}$$

4.9.1 Open-loop transfer function

From the second constitutive equation (4.97), one readily establish the open-loop transfer function between the free expansion δ of the transducer (proportional to the applied voltage) and the force f in the active strut

$$\frac{f}{\delta} = K_a[\sum_{i=1}^{n} \frac{\nu_i}{(1+s^2/\omega_i^2)} - 1] \tag{4.109}$$

All the residues being positive, there will be alternating poles and zeros along the imaginary axis. Note the presence of a feedthrough in the transfer function. Figure 4.22.a shows the open-loop FRF in the undamped case; as expected the poles at $\pm j\omega_i$ are interlaced with the zeros at $\pm z_i$. As usual, the transfer function can be truncated after m modes:

$$\frac{f}{\delta} = K_a[\sum_{i=1}^{m} \frac{\nu_i}{(1+s^2/\omega_i^2)} + \sum_{i=m+1}^{n} \nu_i - 1] \tag{4.110}$$

4.9.2 Admittance function

According to the first constitutive equation (4.97),

$$Q = C(1-k^2)V + nd_{33}K_a b^T x$$

Using (4.108),

$$Q = C(1-k^2)V + n^2 d_{33}^2 K_a \sum_{i=1}^{n} \frac{\nu_i}{(1+s^2/\omega_i^2)} V \tag{4.111}$$

and, taking into account (3.23), one finds the dynamic capacitance

$$\frac{Q}{V} = C(1-k^2)[1 + \frac{k^2}{1-k^2} \sum_{i=1}^{n} \frac{\nu_i}{(1+s^2/\omega_i^2)}] \tag{4.112}$$

(the admittance is related to the dynamic capacitance by $I/V = sQ/V$),

$$\frac{Q}{V} = C(1-k^2)[1 + \sum_{i=1}^{n} \frac{K_i^2}{(1+s^2/\omega_i^2)}] \tag{4.113}$$

where

$$K_i^2 = \frac{k^2 \nu_i}{1-k^2} \tag{4.114}$$

is once again the effective electromechanical coupling factor for mode i. This equation is identical to (4.73). The corresponding FRF is represented in Fig.4.22(b). The zeros of the admittance (or the dynamic capacitance) function correspond to the natural frequencies Ω_i with open electrodes and equations (4.77) and (4.78) apply also for this configuration,

$$K_i^2 \simeq \frac{\Omega_i^2 - \omega_i^2}{\omega_i^2} \tag{4.115}$$

$$\frac{Q}{V} = C_{\text{stat}} \cdot \frac{\prod_{i=1}^{n}(1+s^2/\Omega_i^2)}{\prod_{j=1}^{n}(1+s^2/\omega_j^2)} \tag{4.116}$$

4.10 Finite element formulation

The finite element formulation of a piezoelectric continuum can be derived from Hamilton's principle (section 4.2). The Lagrangian of a structure involving a finite number of discrete piezoelectric transducers can be written in the general form

$$L = T^* + W_e^* = \frac{1}{2}\dot{x}^T M\dot{x} - \frac{1}{2}x^T K_{xx}x + \frac{1}{2}\phi^T C_{\phi\phi}\phi + \phi^T K_{\phi x}x \quad (4.117)$$

In this equation, M is the mass matrix, K_{xx} is the stiffness matrix (including the mechanical part of the transducers with short circuited electrical boundary conditions), $C_{\phi\phi}$ is the matrix of capacitance of the transducers (for fixed displacements) and $K_{\phi x}$ is the coupling matrix of piezoelectric properties, relating the mechanical and electrical variables.

The resulting dynamic equations read

$$M\ddot{x} + K_{xx}x - K_{\phi x}^T\phi = f \quad (4.118)$$

$$K_{\phi x}x + C_{\phi\phi}\phi = Q \quad (4.119)$$

where Q is the vector of electric charges appearing on the electrodes. For voltage driven electrodes, the electric potential ϕ is controlled and Equ.(4.118) can be rewritten (assuming no external load, $f = 0$)

$$M\ddot{x} + K_{xx}x = K_{\phi x}^T\phi \quad (4.120)$$

where the right hand side represents the self-equilibrated piezoelectric loads associated with the voltage distribution ϕ. Note that the dynamics of the system with short-circuited electrodes ($\phi = 0$) is the same as if there were no piezoelectric electromechanical coupling.

Conversely, open electrodes correspond to a charge condition $Q = 0$; in this case, one can substitute ϕ from Equ.(4.119) into Equ.(4.118)

$$M\ddot{x} + (K_{xx} + K_{\phi x}^T C_{\phi\phi}^{-1} K_{\phi x})x = f \quad (4.121)$$

This equation shows that the piezoelectric coupling tends to increase the global stiffness of the system if the electrodes are left open. The natural frequencies of the system with open electrodes are larger than those with short-circuited electrodes, as we have discussed extensively earlier in this chapter. If the electrodes are connected to a passive electrical network, the relationship between ϕ and Q is fixed by the network, as discussed in the following chapter.

4.11 References

AGARWAL, B.D., BROUTMAN, L.J. *Analysis and Performance of Fiber Composites*, Wiley, 2nd Ed., 1990.

ALLIK, H., HUGHES T.J.R. Finite Element method for piezoelectric vibration, *Int. J. for Numerical Methods in Engineering*, Vol.2, 151-157, 1970.

BENJEDDOU, A. Advances in piezoelectric finite element modeling of adaptive structural element: a survey, *Computers and Structures*, 76, 347-363, 2000.

BURKE, S.E., HUBBARD, J.E. Active vibration control of a simply supported beam using spatially distributed actuator. *IEEE Control Systems Magazine*, August, 25-30, 1987.

CADY, W.G. *Piezoelectricity: an Introduction to the Theory and Applications of Electromechanical Phenomena in Crystals*, McGrawHill, 1946.

CRAWLEY, E.F., LAZARUS, K.B. Induced strain actuation of isotropic and anisotropic plates, *AIAA Journal*, Vol.29, No 6, pp.944-951, 1991.

DE MARNEFFE, B. *Active and Passive Vibration Isolation and Damping via Shunted Transducers*, Ph.D. Thesis, Active Structures Laboratory, ULB, Dec. 2007.

DIMITRIADIS, E.K., FULLER, C.R., ROGERS, C.A. Piezoelectric actuators for distributed vibration excitation of thin plates, *Trans. ASME, J. of Vibration and Acoustics*, Vol.113, pp.100-107, January 1991.

EER NISSE, E.P. Variational method for electrostatic vibration analysis, *IEEE Trans. on Sonics and Ultrasonics*, Vol. SU-14, No 4, 153-160 October 1967.

GARCIA LAGE, R., MOTA SOARES, C.M., MOTA SOARES, C.A., REDDY, J.N. Layerwise partial mixed finite element analysis of magneto-electro-elastic plates, *Computers an Structures*, 82, 1293-1301, 2004.

HEYLIGER, P., PEI, K.C., SARAVANOS, D. Layerwise mechanics and finite element model for laminated piezoelectric shells, *AIAA Journal*, Vol.34, No 11, 2353-2360, November 1996.

HWANG, W.-S., PARK, H.C. Finite element modeling of piezoelectric sensors and actuators, *AIAA Journal*, Vol.31, No 5, pp.930-937, May 1993.

LEE, C.-K. Theory of laminated piezoelectric plates for the design of distributed sensors/actuators - Part I: Governing equations and reciprocal relationships, *J. of Acoustical Society of America*, Vol 87, No 3, 1144-1158, March 1990.

LEE, C.-K., CHIANG, W.-W., O'SULLIVAN, T.C. Piezoelectric modal sensor/actuator pairs for critical active damping vibration control, *J. of Acoustical Society of America*, Vol 90, No 1, 374-384, July 1991.
LEE, C.-K., MOON, F.C. Modal sensors/actuators, *Trans. ASME, J. of Applied Mechanics*, Vol.57, pp.434-441, June 1990.
LERCH, R. Simulation of piezoelectric devices by two and three dimensional finite elements, *IEEE Transactions on Ultrasonics, Ferroelectrics, and Frequency Control*, Vol 37, No 3, May 1990.
PIEFORT, V. *Finite element modelling of piezoelectric active structures*, PhD Thesis, Université Libre de Bruxelles, Active Structures Laboratory, 2001.
PREUMONT, A., FRANÇOIS, A., DE MAN, P., PIEFORT, V. Spatial filters in structural control, *Journal of Sound and Vibration*, 265, 61-79, 2003.
PREUMONT, A. *Mechatronics, Dynamics of Electromechanical and Piezoelectric Systems*, Springer, 2006.
TIERSTEN, H.F. Hamilton's principle for linear piezoelectric media, *Proceedings of the IEEE*, 1523-1524, August 1967.

4.12 Problems

P.4.1 *Consider a simply supported beam with collocated piezoelectric d_{31} rectangular actuator and sensor extending longitudinally from $x = a$ to $x = b$. Using the results of section 2.6, show that the expression $\Delta\theta_i$ appearing at the numerator of Equ.(4.56) can be written analytically*

$$\Delta\theta_i = 2\frac{i\pi}{l}\{\sin\frac{i\pi}{l}(\frac{a+b}{2}).\sin\frac{i\pi}{l}(\frac{a-b}{2})\}$$

P.4.2 *From the result of the previous problem, sketch the actuator (and the sensor) which maximizes the response of mode 1, mode 2 and mode 3, respectively.*

P.4.3 *Consider the active cantilever beam of transfer function (4.56). Assuming that $G(0)$ is available from static calculations or from an experiment at low frequency, show that the truncated modal expansion including a quasi-static correction can be written*

$$G(\omega) = G(0) + g_a g_s \sum_{i=1}^{m} \frac{\Delta\theta_i^2}{\mu_i\omega_i^2}\frac{(\omega^2 - 2j\xi_i\omega_i\omega)}{(\omega_i^2 - \omega^2 + 2j\xi_i\omega_i\omega)}$$

P.4.4 *Consider a free-free beam covered with a piezoelectric layer with the various electrodes profiles of Fig.4.23. For each of them, sketch the equivalent piezoelectric loading.*

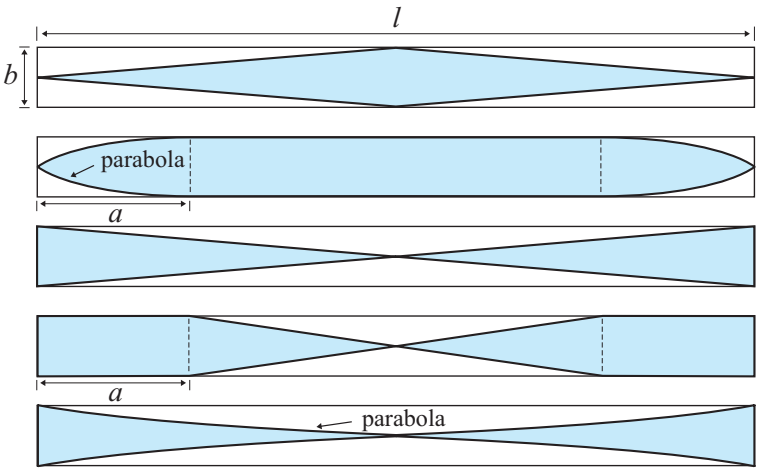

Fig. 4.23. Free-free beam covered with a piezoelectric layer with various electrode profiles.

P.4.5 *Consider the active truss of Fig.4.19.*
(a) *For each active strut, write the influence vector b of the piezoelectric loads in global coordinates.*
(b) *Assuming small displacements, check that the projection of the differential displacements of the end nodes of the active struts are given by* $b^T x$ *where b is the result of* (a).
P.4.6 *Consider a nine bay planar truss similar to that of Fig.4.19. Each bay is square with one diagonal; all the bars have the same cross section. For the following boundary conditions, use a finite element program to calculate the first three flexible modes of the truss. Suggest two reasonable locations of an active strut to control these modes.*
(a) Free-free boundary conditions.
(b) Clamped-free boundary conditions.
[Hint: Use the modal fraction of strain energy ν_i *as index in the selection of the active strut location.]*
P.4.7 *Consider a general piezoelectric structure governed by Equ.(4.118-119) (assume* $f = 0$*). Write the general form of the admittance matrix* Y*:*

$sQ = Y\phi$. Compare it to Equ.(4.113) and interpret the meaning of the various terms.

5

Passive damping with piezoelectric transducers

5.1 Introduction

In this chapter, we examine the basics of the passive damping with shunted piezoelectric transducers. We have seen in the previous chapters that a flexible structure (assumed undamped) with embedded piezoelectric transducers (Fig.5.1) is characterized by an admittance function of the form

$$\frac{I}{V} = \frac{sQ}{V} = s.C_{\text{stat}}.\frac{\prod_{i=1}^{n}(1+s^2/\Omega_i^2)}{\prod_{j=1}^{n}(1+s^2/\omega_j^2)} \tag{5.1}$$

or alternatively

$$\frac{I}{V} = \frac{sQ}{V} = sC(1-k^2)[1+\sum_{i=1}^{n}\frac{K_i^2}{1+s^2/\omega_i^2}] \tag{5.2}$$

where $C(1-k^2)$ is the blocked capacitance[1] of the transducer and K_i^2 are the modal effective electromechanical coupling factors

$$K_i^2 = \frac{k^2\nu_i}{1-k^2} = \frac{\Omega_i^2-\omega_i^2}{\omega_i^2} \tag{5.3}$$

with ω_i being the natural frequencies of the structure when the piezoelectric transducer has short-circuited electrodes and Ω_i when the electrodes are open. It is assumed that the structure has well separated modes, and that the transducer produces only a minor perturbation to the original structure: the mode shapes are not affected significantly by the electrical boundary conditions and ω_i and Ω_i are very close to each other.

[1] comparing the two foregoing equations, one finds that the static capacitance reads $C_{\text{stat}} = C(1-k^2)(1+\sum K_i^2)$.

According to the foregoing formula, there are two contributions to K_i^2:

(i) the electromechanical coupling factor k^2 which is a material property. If the material is used in the extension (d_{33}) mode, the value k_{33} should be used, and if it is used in shear mode (d_{13}), k_{13} applies. Refer to Table 4.1 for typical values (note that k_{13} is significantly smaller than k_{33}).

(ii) the modal fraction of strain energy ν_i which depends on the size as well as the location of the transducer inside the structure. It varies from mode to mode. The transducer should be located where the strain energy is large for the targeted mode(s).

Note that the definition (5.3) of K_i^2 does not imply that $K_i^2 = k^2$ if $\nu_i = 1$. The classical definition is $K_i^2 = (\Omega_i^2 - \omega_i^2)/\Omega_i^2$ but, Ω_i and ω_i are in general very close and the difference is insignificant in most cases.

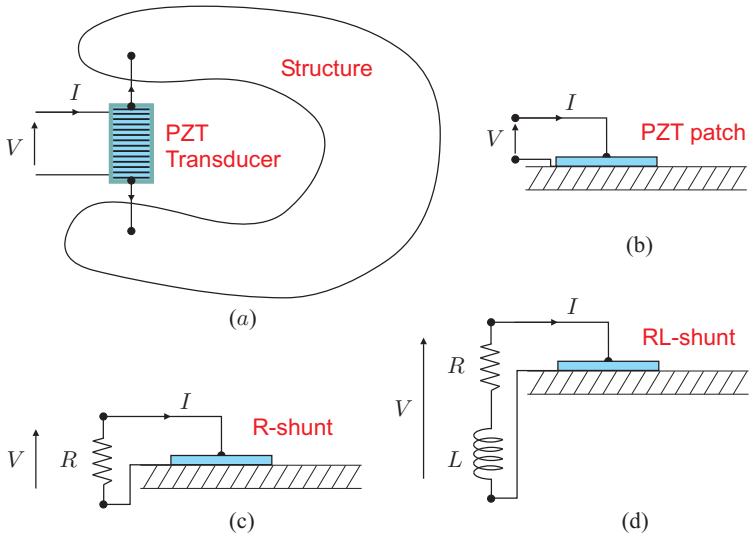

Fig. 5.1. Structure with a shunted piezoelectric transducer (a) in d_{33} mode (b) in d_{31} mode (c) R shunt (d) RL shunt.

5.2 Resistive shunting

Using the same positive signs for V and I as for the structure (Fig.5.1.c), the admittance of the shunt is $I/V = -1/R$. The characteristic equation of the system is obtained by equating it to the admittance of the structure:

$$-\frac{1}{R} = sC(1-k^2)[1+\sum_{i=1}^{n}\frac{K_i^2}{1+s^2/\omega_i^2}] \tag{5.4}$$

or

$$-\frac{1}{sRC(1-k^2)} = 1+\sum_{i=1}^{n}\frac{K_i^2\omega_i^2}{s^2+\omega_i^2} \tag{5.5}$$

In the vicinity of $\pm j\omega_i$, the sum is dominated by the contribution of mode i and the other terms can be neglected; defining $\gamma = [RC(1-k^2)]^{-1}$, the equation may be simplified as

$$-\frac{\gamma}{s} = 1+\frac{K_i^2\omega_i^2}{s^2+\omega_i^2}$$

which in turn can be rewritten

$$1+\gamma\frac{s^2+\omega_i^2}{s(s^2+\Omega_i^2)} = 0 \tag{5.6}$$

This form of the characteristic equation is that of a root locus in auto-

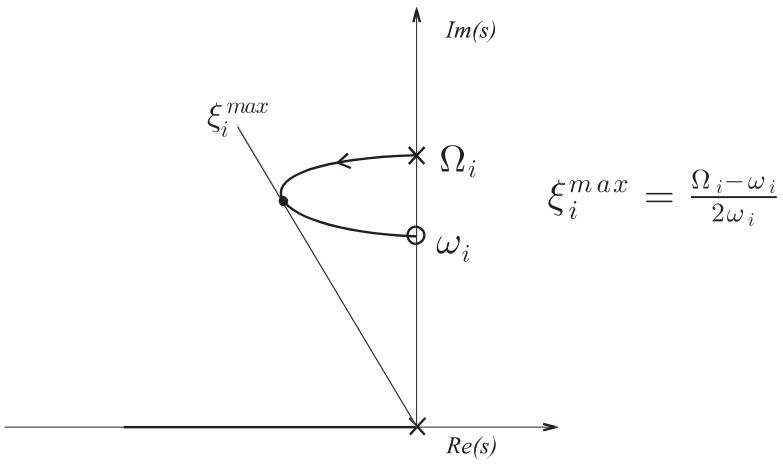

Fig. 5.2. Resistive shunt. Evolution of the poles of the system as $\gamma = [RC(1-k^2)]^{-1}$ goes from 0 to ∞ (the diagram is symmetrical with respect to the real axis, only the upper half is shown).

matic control (Fig.5.2);[2] where the parameter γ acts as the feedback gain in classical root locus plots; for $\gamma = 0$ ($R = \infty$), the poles are $\pm j\Omega_i$, corresponding to the natural frequency of the system with open electrodes. The

[2] This root locus will be met many times in the following chapters.

system is undamped. As the resistance decreases (γ increases), the poles move to the left and some damping appears in the system; the maximum damping is achieved for $\gamma = \Omega_i\sqrt{\Omega_i/\omega_i} \simeq \Omega_i$ and is (Problem 5.1)

$$\xi_i^{\max} = \frac{\Omega_i - \omega_i}{2\omega_i} \simeq \frac{\Omega_i^2 - \omega_i^2}{4\omega_i^2} = \frac{K_i^2}{4} \tag{5.7}$$

5.3 Inductive shunting

We proceed in the same way as for the R-shunt (Fig.5.1.d); the admittance of the shunt is now $I/V = -1/(R + Ls)$. The characteristic equation is therefore

$$-\frac{1}{R+Ls} = sC(1-k^2)[1 + \sum_{i=1}^{n} \frac{K_i^2}{1 + s^2/\omega_i^2}] \tag{5.8}$$

or

$$-\frac{1}{(R+Ls)sC(1-k^2)} = 1 + \sum_{i=1}^{n} \frac{K_i^2\omega_i^2}{s^2+\omega_i^2} \tag{5.9}$$

Once again, in the vicinity of $\pm j\omega_i$, the sum is dominated by the contribution of modi i and the equation is simplified as

$$-\frac{1}{(R+Ls)sC(1-k^2)} = 1 + \frac{K_i^2\omega_i^2}{s^2+\omega_i^2} \tag{5.10}$$

Defining the electrical frequency

$$\omega_e^2 = \frac{1}{LC(1-k^2)} \tag{5.11}$$

and the electrical damping

$$2\xi_e\omega_e = \frac{R}{L} \tag{5.12}$$

it is rewritten

$$-\frac{\omega_e^2}{2\xi_e\omega_e s + s^2} = 1 + \frac{K_i^2\omega_i^2}{s^2+\omega_i^2} = \frac{s^2+\Omega_i^2}{s^2+\omega_i^2} \tag{5.13}$$

or

$$s^4 + 2\xi_e\omega_e s^3 + (\Omega_i^2 + \omega_e^2)s^2 + 2\Omega_i^2\xi_e\omega_e s + \omega_i^2\omega_e^2 = 0 \tag{5.14}$$

This can be rewritten in a root locus form

$$1 + 2\xi_e\omega_e \frac{s(s^2+\Omega_i^2)}{s^4 + (\Omega_i^2+\omega_e^2)s^2 + \omega_i^2\omega_e^2} = 0 \tag{5.15}$$

In this formulation, $2\xi_e\omega_e$ plays the role of the gain in a classical root locus. Note that, for large R, the poles tend to $\pm j\Omega_i$, as expected. For $R = 0$ (i.e. $\xi_e = 0$), they are the solutions p_1 and p_2 of the characteristic equation $s^4 + (\Omega_i^2 + \omega_e^2)s^2 + \omega_i^2\omega_e^2 = 0$ which accounts for the classical double peak of resonant dampers, with p_1 above $j\Omega_i$ and p_2 below $j\omega_i$. Figure 5.3 shows the root locus for a fixed value of ω_i/Ω_i and various values of the electrical tuning, expressed by the ratio

$$\alpha_e = \frac{\omega_e\omega_i}{\Omega_i^2} \tag{5.16}$$

The locus consists of two loops, starting respectively from p_1 and p_2; one of them goes to $j\Omega_i$ and the other goes to the real axis, near $-\Omega_i$. If $\alpha_e > 1$ (Fig.5.3.a), the upper loop starting from p_1 goes to the real axis, and that starting from p_2 goes to $j\Omega_i$, and the upper pole is always more heavily damped than the lower one (note that, if $\omega_e \to \infty$, $p_1 \to \infty$ and $p_2 \to j\omega_i$; the lower branch of the root locus becomes that of the resistive shunting). The opposite situation occurs if $\alpha_e < 1$ (Fig.5.3.b): the upper loop goes from p_1 to $j\Omega_i$ and the lower one goes from p_2 to the real axis; the lower pole is always more heavily damped. If $\alpha_e = 1$ (Fig.5.3.c), the two poles are always equally damped until the two branches touch each other in Q. This double root is achieved for

$$\alpha_e = \frac{\omega_e\omega_i}{\Omega_i^2} = 1 \qquad , \qquad \xi_e^2 = 1 - \frac{\omega_i^2}{\Omega_i^2} \simeq K_i^2 \tag{5.17}$$

This can be regarded as the optimum tuning of the inductive shunting. The corresponding eigenvalues satisfy

$$s^2 + \Omega_i^2 + \Omega_i(\frac{\Omega_i^2}{\omega_i^2} - 1)^{1/2}s = 0 \tag{5.18}$$

For various values of ω_i/Ω_i (or K_i), the optimum poles at Q move along a circle of radius Ω_i (Fig.5.3.d). The corresponding damping ratio can be obtained easily by identifying the previous equation with the classical form of the damped oscillator, $s^2 + 2\xi_i\Omega_i s + \Omega_i^2 = 0$, leading to

$$\xi_i = \frac{1}{2}(\frac{\Omega_i^2}{\omega_i^2} - 1)^{1/2} = \frac{K_i}{2} = \frac{1}{2}(\frac{k^2\nu_i}{1-k^2})^{1/2} \tag{5.19}$$

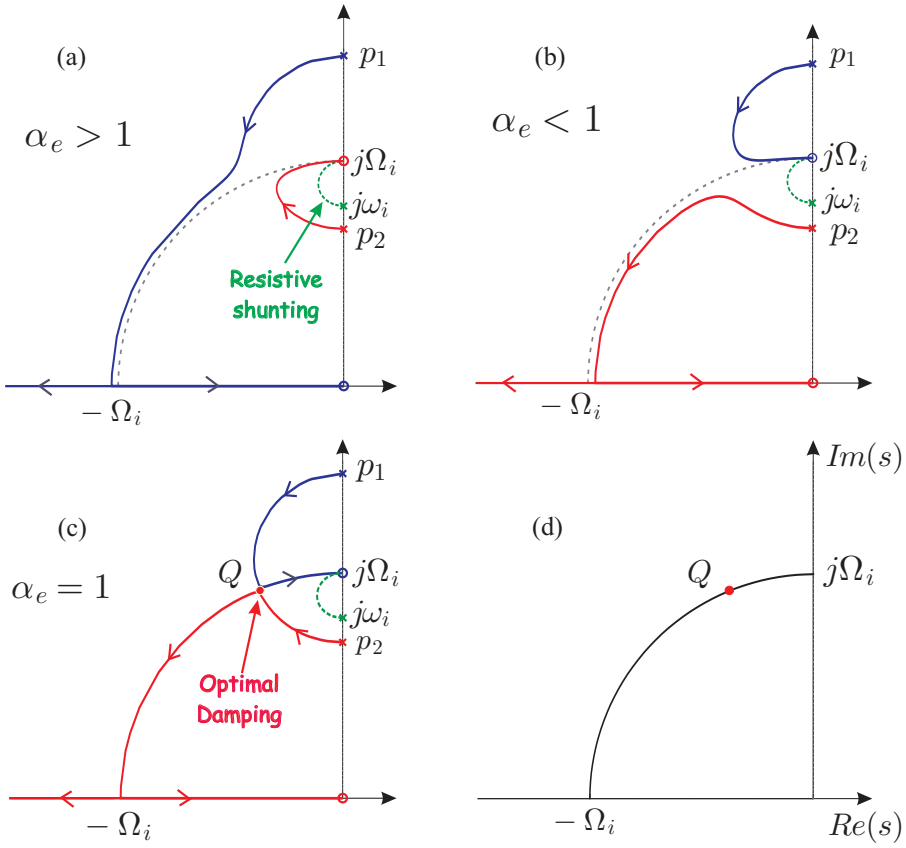

Fig. 5.3. Root locus plot for inductive shunting (only the upper half is shown). The optimum damping at Q is achieved for $\alpha_e = 1$ and $\xi_e = K_i^2$; the maximum modal damping is $\xi_i \simeq K_i/2$.

This value is significantly higher than that achieved with purely resistive shunting [it is exactly the square-root of (5.7)]. Note, however, that it is much more sensitive to the tuning of the electrical parameters on the targeted modes. This is illustrated in Fig.5.4, which displays the evolution of the damping ratio ξ_i when the actual natural frequency ω_i' moves away from the nominal frequency ω_i for which the shunt has been optimized (the damping ratio associated with p_1 and p_2 is plotted in dotted lines; the ratio ω_i'/Ω_i' is kept constant in all cases). One sees that the performance of the inductive shunting drops rapidly below that of the resistive shunting when the de-tuning increases. Note that, for low frequency modes, the optimum inductance value can be very large; such large inductors can be

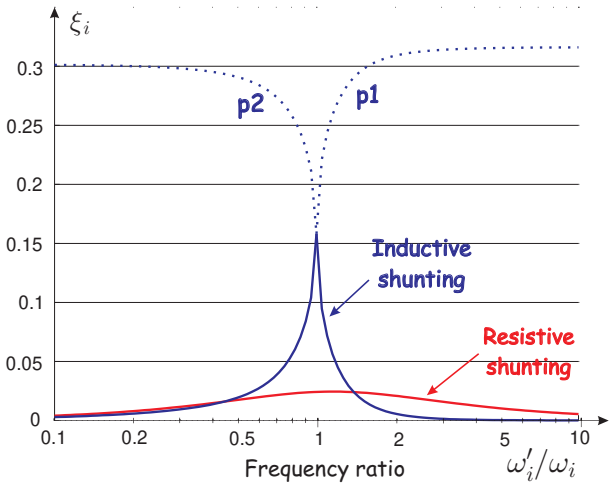

Fig. 5.4. Evolution of the damping ratio of the inductive and resistive shunting with the de-tuning of the structural mode. ω_i is the natural frequency for which the shunt has been optimized, ω_i' is the actual value ($k = 0.5$, $\nu_i = 0.3$).

synthesized electronically. The multimodal passive damping via resonant shunt has been investigated by (Hollkamp, 1994).

All the dissipation mechanisms considered in this chapter are based on linear time-invariant filters. Recently, promising alternative nonlinear methods based on state switching have been proposed. The transducer is connected to a solid-state switch device which discharges periodically the piezoelectric element on a small inductor, producing a voltage inversion (Guyomar & Richard, 2005).

5.4 References

DAVIS, C.L., LESIEUTRE, G.A. A modal strain energy approach to the prediction of resistivity shunted piezoceramic damping, *Journal of Sound and Vibration*, **184** (1), 129-139, 1995.

DE MARNEFFE, B. *Active and Passive Vibration Isolation and Damping via Shunted Transducers*, Ph.D. Thesis, Active Structures Laboratory, ULB, Dec. 2007.

EDBERG, D.L., BICOS, A.S., FECHTER, J.S. On piezoelectric energy conversion for electronic passive damping enhancement, Proceedings of *Damping'91*, San Diego, 1991.

FORWARD, R.L. Electronic damping of vibrations in optical structures, *Journal of Applied Optics*, **18**, 690-697, March, 1979.

FORWARD, R.L. Electromechanical transducer-coupled mechanical structure with negative capacitance compensation circuit. US Patent 4,158,787, June 1979.
GUYOMAR, D., RICHARD, C. Non-linear and hysteretic processing of piezoelement: Application to vibration control, wave control and energy harvesting, *Int. Journal of Applied Electromagnetics and Mechanics*, 21, 193-207, 2005.
HAGOOD, N.W., von FLOTOW, A. Damping of structural vibrations with piezoelectric materials and passive electrical networks, *Journal of Sound and Vibration* **146**(2), 243-268, 1991.
HOLLKAMP, J.J. Multimodal passive vibration suppression with piezoelectric materials and resonant shunts, *J. Intell. Material Syst. Structures*, Vol.5, Jan.1994.
MOHEIMANI, S.O.R. A survey of recent innovations in vibration damping and control using shunted piezoelectric transducers, *IEEE Transactions on Control Systems Technology*, Vol.11, No 4, 482-494, July 2003.
PREUMONT, A. *Mechatronics, Dynamics of Electromechanical and Piezoelectric Systems*, Springer, 2006.

5.5 Problems

P.5.1 *Show that the maximum damping achievable with a resistive shunt is given by Equ.(5.7). [Hint: The use of a symbolic calculation software is recommended.]*

P.5.2 *Consider a beam equipped with a rectangular piezoelectric transducer extending from a to b, and a collocated actuator-sensor pair at l (Fig.5.5). The natural frequencies and the mode shapes with short-circuited electrodes are respectively ω_k and $\phi_k(x)$. This system is intended to be equipped with various forms of shunt damping or energy harvesting devices. The input-output relationship of this system can be written in the form*

$$\begin{Bmatrix} w \\ i \end{Bmatrix} = \begin{bmatrix} G_{11}(s) & G_{12}(s) \\ G_{21}(s) & G_{22}(s) \end{bmatrix} \begin{Bmatrix} f \\ V \end{Bmatrix}$$

Write the analytical form of the various transfer functions $G_{kj}(s)$ involved in this expression.

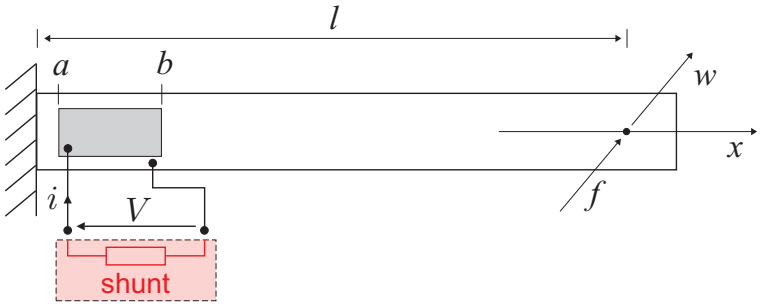

Fig. 5.5. Beam equipped with a piezoelectric transducer extending from a to b, and a collocated actuator sensor pair.

6

Collocated versus non-collocated control

6.1 Introduction

In the foregoing chapters, we have seen that the use of collocated actuator and sensor pairs, for a lightly damped flexible structure, always leads to alternating poles and zeros near the imaginary axis, Fig.6.1.a. In this chapter, using the root locus technique, we show that this property guarantees the asymptotic stability of a wide class of single-input single-output (*SISO*) control systems, even if the system parameters are subject to large perturbations. This is because the root locus plot keeps the same general shape, and remains entirely within the left half plane when the system parameters are changed from their nominal values. Such a control system is said to be *robust* with respect to stability. The use of collocated actuator/sensor pairs is recommended whenever it is possible.

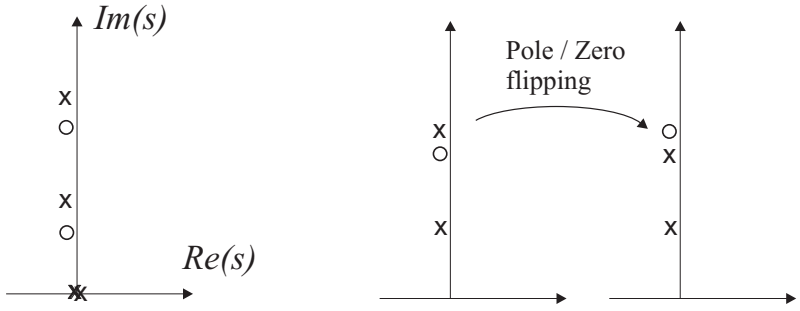

Fig. 6.1. (a) Alternating pole-zero pattern of a lightly damped flexible structure with collocated actuator and sensor. (b) Pole-zero flipping for a non-collocated system.

This interlacing property of the poles and zeros no longer holds for a non-collocated control, and the root locus plot may experience severe alterations for small parameter changes. This is especially true when the sequence of poles and zeros along the imaginary axis is reversed as in Fig.6.1.b. This situation is called a *pole-zero flipping*. It is responsible for a phase uncertainty of 360^0, and the only protection against instability is provided by the *damping* (systems which are prone to such a huge phase uncertainty can only be *gain-stabilized*).

6.2 Pole-zero flipping

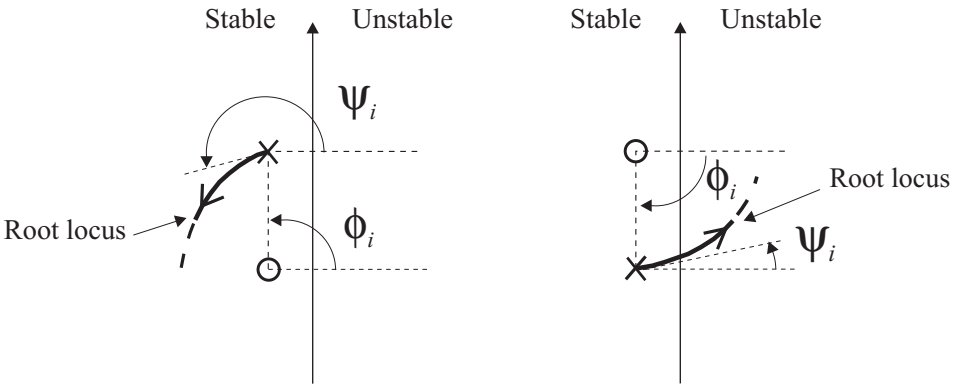

Fig. 6.2. Detail of a root locus showing the effect of the pole-zero flipping on the departure angle from a pole. Since the contribution of the far away poles and zeros is unchanged, that of the pole and the nearby zero, $\phi_i - \psi_i$ must also remain unchanged.

Recall that the root locus shows, in a graphical form, the evolution of the poles of the closed-loop system as a function of the scalar gain g applied to the compensator. The open-loop transfer function GH includes the structure, the compensator, and possibly the actuator and sensor dynamics, if necessary. The root locus is the locus of the solution s of the closed-loop characteristic equation $1 + gGH(s) = 0$ when the real parameter g goes from zero to infinity. If the open-loop transfer function is written

$$GH(s) = k\frac{\prod_{i=1}^{m}(s - z_i)}{\prod_{i=1}^{n}(s - p_i)} \tag{6.1}$$

the locus goes from the poles p_i (for $g = 0$) to the zeros z_i (as $g \to \infty$) of the open-loop system, and any point P on the locus is such that

$$\sum_{i=1}^{m} \phi_i - \sum_{i=1}^{n} \psi_i = 180^0 + l\,360^0 \tag{6.2}$$

where ϕ_i are the phase angles of the vectors $\vec{a_i}$ joining the zeros z_i to P and ψ_i are the phase angles of the vector $\vec{b_i}$ joining the poles p_i to P (see Fig.6.8). Since $n \geq m$, there are $n - m$ branches of the locus going asymptotically to infinity as g increases.

Consider the departure angle from a pole and the arrival angle at the zero when they experience a pole-zero flipping; since the contribution of the far away poles and zeros remains essentially unchanged, the difference $\phi_i - \psi_i$ must remain constant after flipping. As a result, a nice stabilizing loop before flipping is converted into a destabilizing one after flipping (Fig.6.2). If the system has some damping, the control system is still able to operate with a small gain after flipping.

Since the root locus technique does not distinguish between the system and the compensator, the pole-zero flipping may occur in two different ways:

- There are compensator zeros near system poles (this is called a *notch filter*). If the actual poles of the system are different from those assumed in the compensator design, the notch filter may become inefficient (if the pole moves away from the zero), or worse, a pole-zero flipping may occur. This is why notch filters have to be used with extreme care. As we shall see in later chapters, notch filters are generated by optimum feedback compensators and this may lead to serious robustness questions if the parameter uncertainty is large.
- Some actuator/sensor configurations may produce pole-zero flipping within the system alone, for small parameter changes. These situations are often associated with a pole-zero (near) cancellation due to a deficiency in the controllability or the observability of the system (typically, when the actuator or the sensor is close to a nodal point in the mode shapes). In some cases, however, especially if the damping is extremely light, instability may occur. No pole-zero flipping can occur within the structure if the actuator and sensor are collocated. The following sections provide examples illustrating these points.

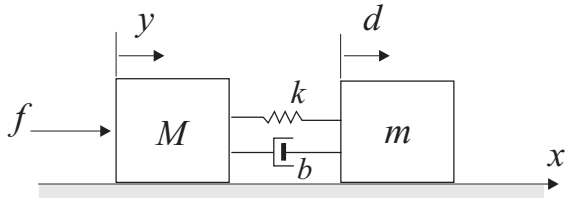

Fig. 6.3. Two-mass problem.

6.3 The two-mass problem

Consider the two-mass problem of Fig.6.3. The system has a rigid body mode along the x axis; it is controlled by a force f applied to the main body M. A flexible appendage m is connected to the main body by a spring k and a damper b. First, a position control system will be designed, using a sensor placed on the main body (collocated); a sensor attached to the flexible appendage will be considered in the next section.

With f representing the control torque and y and d being the attitude angles, this problem is representative of the single-axis attitude control of a satellite, with M representing the main body, and the other inertia representing either a flexible appendage like a solar panel (in which case the sensor can be on the main body, i.e. collocated), or a scientific instrument like a telescope which must be accurately pointed towards a target (now the sensor has to be part of the secondary structure; i.e. non-collocated). A more elaborate single-axis model of a spacecraft is considered in Problem 2.8.

The system equations are :

$$M\ddot{y} + (\dot{y} - \dot{d})b + (y - d)k = f \tag{6.3}$$

$$m\ddot{d} + (\dot{d} - \dot{y})b + (d - y)k = 0 \tag{6.4}$$

With the notations

$$\omega_o^2 = k/m, \quad \mu = m/M, \quad 2\xi\omega_o = b/m \tag{6.5}$$

the transfer functions between the input force f and y and d are respectively :

$$G_1(s) = \frac{Y(s)}{F(s)} = \frac{s^2 + 2\xi\omega_o s + \omega_o^2}{Ms^2\left[s^2 + (1+\mu)\left(2\xi\omega_o s + \omega_o^2\right)\right]} \tag{6.6}$$

$$G_2(s) = \frac{D(s)}{F(s)} = \frac{2\xi\omega_0 s + \omega_0^2}{Ms^2\left[s^2 + (1+\mu)\left(2\xi\omega_o s + \omega_o^2\right)\right]} \tag{6.7}$$

$$G_2(s) \simeq \frac{\omega_0^2}{Ms^2\left[s^2 + (1+\mu)\left(2\xi\omega_o s + \omega_o^2\right)\right]} \tag{6.8}$$

Approximation (6.8) recognizes the fact that, for low damping ($\xi \ll 1$), the far away zero will not influence the closed-loop response. There are two poles near the imaginary axis. In $G_1(s)$, which refers to the collocated sensor, there are two zeros also near the imaginary axis, at $(-\xi\omega_0 \pm j\omega_0)$. As observed earlier, these zeros are identical to the poles of the modified system where the main body has been blocked (i.e. constrained mode of the flexible appendage). When the mass ratio μ is small, the polynomials in the numerator and denominator are almost equal, and there is a pole-zero cancellation.

6.3.1 Collocated control

Let us consider a *lead compensator*

$$H(s) = g\frac{Ts+1}{\alpha Ts+1} \qquad (\alpha < 1) \tag{6.9}$$

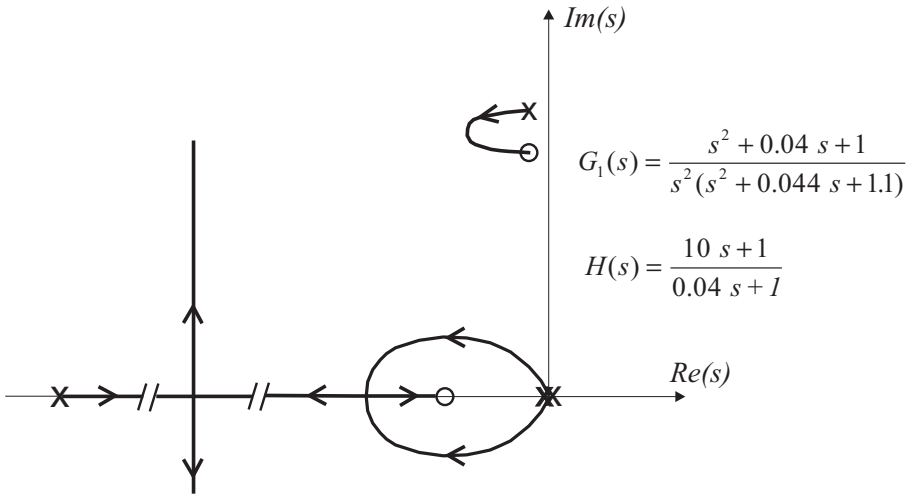

Fig. 6.4. Two-mass problem, root locus plot for the collocated control with a lead compensator (the plot is symmetrical with respect to the real axis, only the upper part is shown).

It includes one pole and one zero located on the negative real axis; the pole is to the left of the zero. Figure 6.4 shows a typical root locus plot for the collocated case when $\omega_0 = 1$, $M = 1$, $\xi = 0.02$ and $\mu = 0.1$. The parameters of the compensator are $T = 10$ and $\alpha = 0.004$. Since there are two more poles than zeros ($n - m = 2$), the root locus has two asymptotes at $\pm 90^0$. One observes that the system is stable for every value of the gain, and that the bandwidth of the control system can be a substantial part of ω_0. The lead compensator *always* increases the damping of the flexible mode.

If there are not one, but several flexible modes, there are as many pole-zero pairs and the number of poles in excess of zeros remains the same ($n - m = 2$ in this case), so that the angles of the asymptotes remain $\pm 90^0$ and the root locus never leaves the stable region. The lead compensator increases the damping ratio of *all* the flexible modes, but especially those having their natural frequency between the pole and the zero of the compensator. Of course, we have assumed that the sensor and the actuator have perfect dynamics; if this is not the case, the foregoing conclusions may be considerably modified, especially for large gains.

6.3.2 Non-collocated control

Figure 6.5 shows the root locus plot for the lead compensator applied to the non-collocated open-loop system characterized by the transfer function $G_2(s)$, Equ.(6.7), with the following numerical data: $\omega_0 = 1$, $M = 1$, $\mu = 0.1$, $\xi = 0.02$. The excess number of poles is in this case $n - m = 3$ so

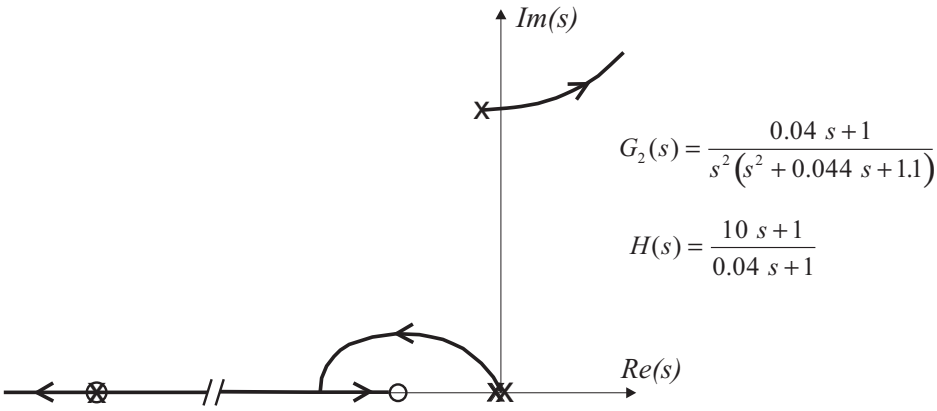

Fig. 6.5. Two-mass problem, root locus plot for the non-collocated control with a lead compensator.

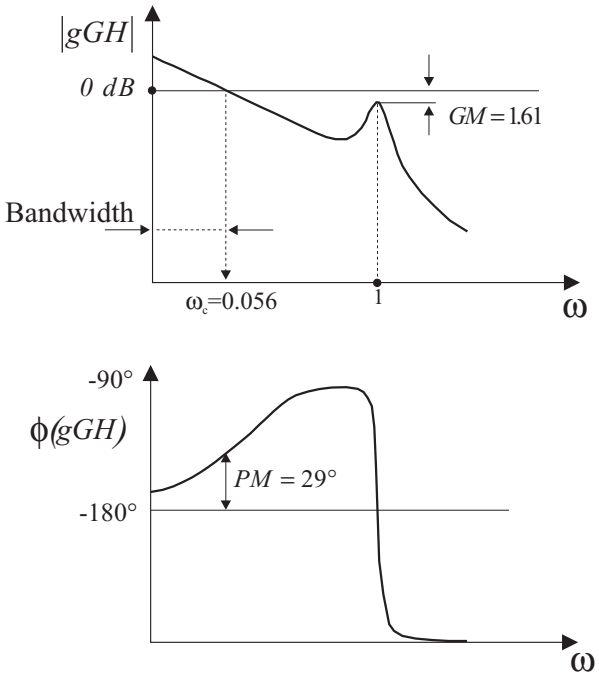

Fig. 6.6. Two-mass problem, Bode plots of the non-collocated control for g = 0.003.

that, for large gains, the flexible modes are heading towards the asymptotes at $\pm 60^0$, in the right half plane. For a gain $g = 0.003$, the closed-loop poles are located at $-0.0136 \pm 0.0505j$ and $-0.0084 \pm 1.0467j$ (these locations are not shown in Fig.6.5 for clarity: the poles of the rigid body mode are close to the origin and those of the flexible mode are located between the open-loop poles and the imaginary axis). The corresponding Bode plots are shown in Fig.6.6; the phase and gain margins are indicated. One observes that even with this small bandwidth (crossover frequency $\omega_c = 0.056$), the gain margin is extremely small. A slightly lower value of the damping ratio would make the closed-loop system unstable (Problem 6.1).

6.4 Notch filter

A classical way of alleviating the effect of the flexible modes in non-collocated control is to supplement the lead compensator with a notch filter with two zeros located near the flexible poles:

$$H(s) = g \cdot \frac{Ts+1}{\alpha Ts+1} \cdot \frac{s^2/\omega_1^2+1}{(s/a+1)^2} \tag{6.10}$$

The zeros of the notch filter, at $s = \pm j\omega_1$, are selected right below the flexible poles. The double pole at $-a$ aims at keeping the compensator proper (i.e. the degree of the numerator not larger than that of the denominator); it can, for example, be selected far enough along the negative real axis. The corresponding root locus is represented in Fig.6.7.a for $\omega_1 = 0.9$ and $a = 10$. This compensator allows a larger bandwidth than the lead compensator alone (Problem 6.2).

To be effective, a notch filter must be closely tuned to the flexible mode that we want to attenuate. However, as we already mentioned, the notch filter suffers from a lack of robustness and should not be used if the uncertainty in the system properties is large. To illustrate this, Fig.6.7.b shows a detail of the root locus near the notch, when the natural frequency of the system is smaller than expected (in the example, ω_0 is reduced from 1 rad/s to 0.8 rad/s; the other data are identical to that of Fig.6.5, while the notch filter is kept the same (being implemented in the computer, the notch filter is not subject to parameter uncertainty). The rest of the root locus is only slightly affected by the change.

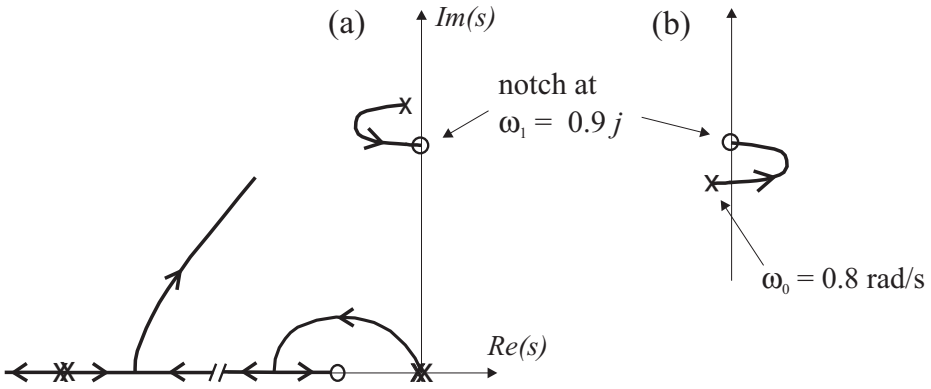

Fig. 6.7. Two-mass problem, non-collocated control; (a) Lead compensator plus notch filter (b) Detail of the root locus near the notch for off-nominal open-loop system (ω_0 reduced from 1 to 0.8).

Because the open-loop poles of the flexible mode move from above to below the zero of the notch filter (from $\pm j$ to $\pm 0.8j$ with the zeros at $\pm 0.9j$ in the example), there is a pole-zero flipping, with the consequence that the branch of the root locus connecting the pole to the zero

rapidly becomes unstable. This example emphasizes the fact that notch filters should be used with extreme care, especially for systems where the uncertainty is large (Problem 6.3).

6.5 Effect of pole-zero flipping on the Bode plots

From Equ.(6.1),

$$GH(j\omega) = k\frac{\prod_{i=1}^{m}(j\omega - z_i)}{\prod_{i=1}^{n}(j\omega - p_i)} \tag{6.11}$$

the phase of $GH(j\omega)$ for a specific value $j\omega$ is given by

$$\sum_{i=1}^{m}\phi_i - \sum_{i=1}^{n}\psi_i \tag{6.12}$$

where ϕ_i is the phase angle of the vector $\vec{a_i}$ joining the zero z_i to $j\omega$ and ψ_i is the phase angle of the vector $\vec{b_i}$ joining the pole p_i to $j\omega$ (Fig.6.8). Accordingly, an imaginary zero at $j\omega_0$ produces a phase lead of 180^0 for $\omega > \omega_0$ and an imaginary pole produces similarly a phase lag of 180^0. Therefore, a pole-zero flipping near the imaginary axis produces a phase uncertainty of 360^0 in the frequency range between the pole and the zero. It appears that the only way the closed-loop stability can be guaranteed in the vicinity of a pole-zero flipping is to have the open-loop system *gain-stabilized* (i.e. such that $|gHG| < 1$) in that frequency range.

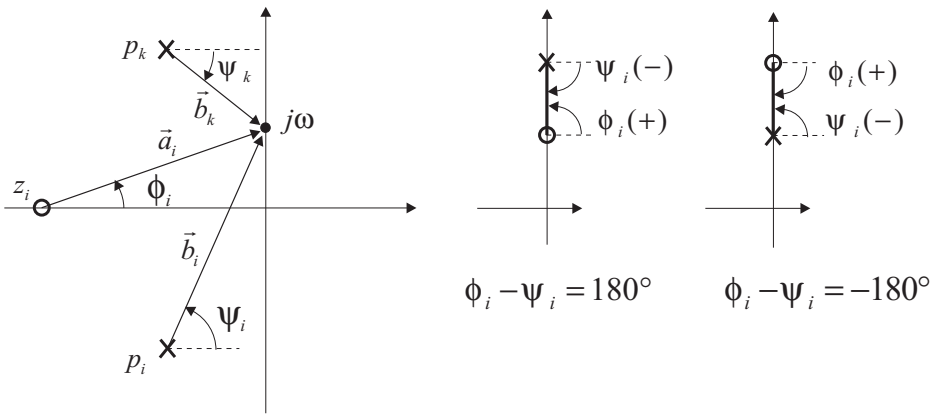

Fig. 6.8. Effect of the pole-zero flipping on the phase diagram.

6.6 Nearly collocated control system

In many cases, the actuator and sensor pair are close to each other without being strictly collocated. This situation is examined here.

Fig. 6.9. Structure with nearly collocated actuator/sensor pair.

Consider the undamped system of Fig.6.9 where the actuator input u is applied at a and the sensor y is located at s. The open-loop FRF of the system is given by

$$G(\omega) = \frac{y}{u} = \sum_{i=1}^{n} \frac{\phi_i(a)\phi_i(s)}{\mu_i(\omega_i^2 - \omega^2)} \tag{6.13}$$

where $\phi_i(a)$ and $\phi_i(s)$ are the modal amplitudes at the actuator and the sensor locations, respectively (the sum includes all the normal modes in this case). The residues of (6.13) are no longer guaranteed to be positive; however, if the actuator location a is close to the sensor location s, the modal amplitudes $\phi_i(a)$ and $\phi_i(s)$ will be close to each other, at least for the low frequency modes, and the corresponding residues will again be positive. The following result can be established in this case : *If two neighboring modes are such that their residues* $\phi_i(a)\phi_i(s)$ *and* $\phi_{i+1}(a)\phi_{i+1}(s)$ *have the same sign, there is always an imaginary zero between the two poles* (Martin, 1978).

Since $G(\omega)$ is continuous between ω_i and ω_{i+1}, this result will be established if one proves that the sign of $G(\omega)$ near ω_i is opposite to that near ω_{i+1}. At $\omega = \omega_i + \delta\omega$, $G(\omega)$ is dominated by the contribution of mode i and its sign is

$$sign[\frac{\phi_i(a)\phi_i(s)}{\omega_i^2 - \omega^2}] = -sign[\phi_i(a)\phi_i(s)] \tag{6.14}$$

At $\omega = \omega_{i+1} - \delta\omega$, $G(\omega)$ is dominated by the contribution of mode $i+1$ and its sign is

$$sign[\frac{\phi_{i+1}(a)\phi_{i+1}(s)}{\omega_{i+1}^2 - \omega^2}] = sign[\phi_{i+1}(a)\phi_{i+1}(s)] \tag{6.15}$$

Thus, if the two residues have the same sign, the sign of $G(\omega)$ near ω_{i+1}^- is opposite to that near ω_i^+. By continuity, $G(\omega)$ must vanishes somewhere in between, at z_i such that $\omega_i^+ < z_i < \omega_{i+1}^-$. Note, however, that when the residues of the expansion (6.13) are not all positive, there is no guarantee that $G(\omega)$ is an increasing function of ω, and one can find situations where there are more than one zero between two neighboring poles.

6.7 Non-collocated control systems

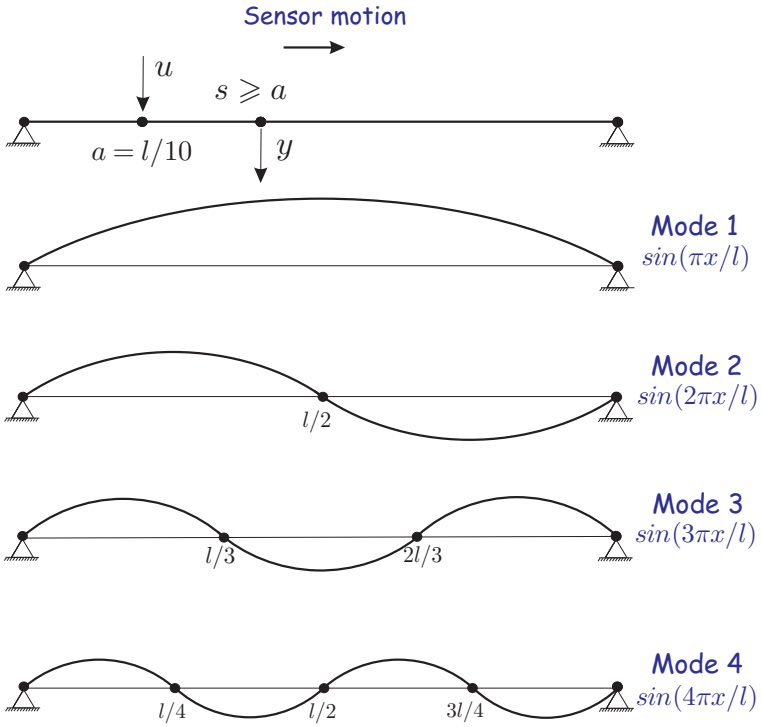

Fig. 6.10. Uniform beam with non-collocated actuator/sensor pair. Mode shapes 1 to 4.

Since the low frequency modes vary slowly in space, the sign of $\phi_i(a)\phi_i(s)$ tend to be positive for low frequency modes when the actuator and sensor are close to each other, and the interlacing of the poles and zeros is maintained at low frequency. This is illustrated in the following example: Consider a simply supported uniform beam of mass per unit

length m and bending stiffness EI. The natural frequencies and mode shapes are respectively

$$\omega_i^2 = (i\pi)^4 \frac{EI}{ml^4} \tag{6.16}$$

and

$$\phi_i(x) = \sin \frac{i\pi x}{l} \tag{6.17}$$

(the generalized mass is $\mu_i = ml/2$). Note that the natural frequency increases as the square of the mode order. We assume that a force actuator is placed at $a = 0.1\,l$ and we examine the evolution of the open-loop zeros as a displacement sensor is moved to the right from $s = a$ (collocated), towards the end of the beam (Fig 6.10).

The evolution of the open-loop zeros with the sensor location along the beam is shown in Fig 6.11; the plot shows the ratio z_i/ω_1, so that the open-loop poles (independent of the actuator/sensor configuration) are at 1, 4, 9, 25, etc.... For $s = a = 0.1\,l$, the open-loop zeros are represented by ∘; they alternate with the poles. Another position of the actuator/sensor

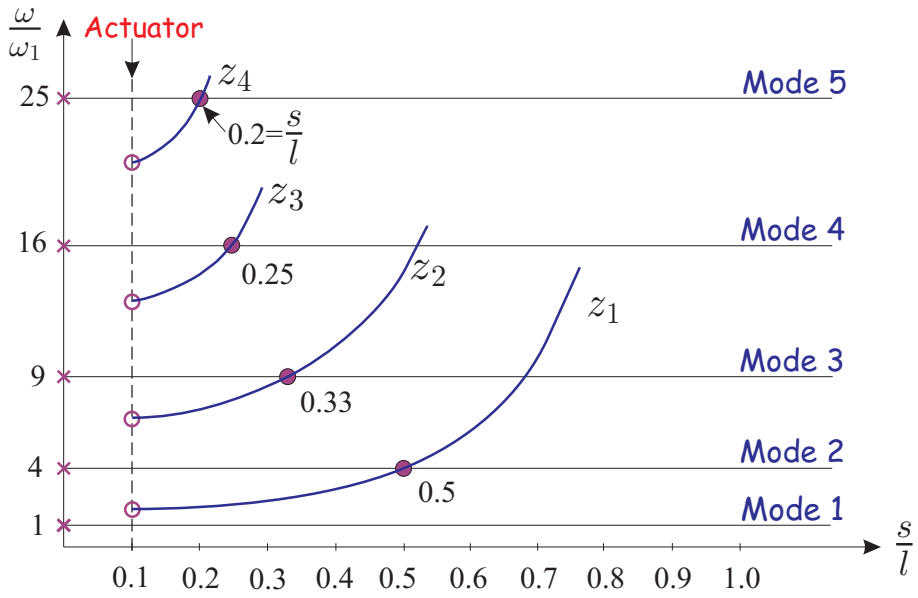

Fig. 6.11. Evolution of the imaginary zeros when the sensor moves away from the actuator along a simply supported beam (the actuator is at $0.1\,l$). The abscissa is the sensor location, the ordinate is the frequency of the transmission zero.

pair along the beam would lead to a different position of the zeros, but always alternating with the poles.

As the sensor is displaced from the actuator, $s > a$, the zeros tend to increase in magnitude as shown in Fig.6.11, but the low frequency ones still alternate. When $s = 0.2\,l$, z_4 becomes equal to ω_5 and there is no zero any longer between ω_4 and ω_5 when s exceeds $0.2\,l$. Thus, a pole/zero flipping occurs. Similarly, z_3 flips with ω_4 for $s = l/4$, z_2 flips with ω_3 for $s = l/3$ and z_1 flips with ω_2 for $s = l/2$. Examining the mode shapes, one notices that the pole-zero flipping always occurs at a node of one of the mode shapes, and this corresponds to a change of sign in $\phi_i(a)\phi_i(s)$, as discussed above.

This simple example confirms the behavior of the pole/zero pattern for nearly collocated control systems: the poles and zeros are still interlacing at low frequency, but not at higher frequency, and the frequency where the interlacing stops decreases as the distance between the actuator and sensor increases. A more accurate analysis (Spector & Flashner, 1989; Miu, 1993) shows that:

For structures such as bars in extension, shafts in torsion or simply connected spring-mass systems (non dispersive), when the sensor is displaced from the actuator, the zeros migrate along the imaginary axis towards infinity. The imaginary zeros are the resonance frequencies of the two substructures formed by constraining the structure at the actuator and sensor (this generalizes the result of chapter 2).

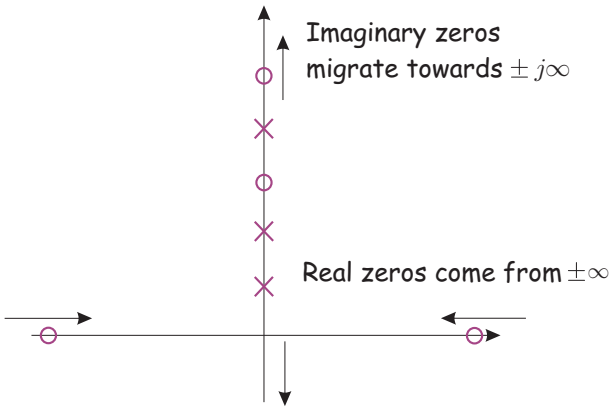

Fig. 6.12. Evolution of the zeros of a beam when the sensor moves away from the actuator. Every pair of imaginary zeros which disappears at infinity reappears on the real axis.

For beams with specific boundary conditions, the imaginary zeros still migrate along the imaginary axis, but every pair of zeros that disappears at infinity reappears symmetrically at infinity on the real axis and moves towards the origin (Fig 6.12). Systems with right half plane zeros are called *non-minimum phase*. Thus, non collocated control systems are always non-minimum phase, but this does not cause difficulties if the right half plane zeros lie well outside the desired bandwidth of the closed-loop system. When they interfere with the bandwidth, they put severe restrictions on the control system, by reducing significantly the phase margin; this point will be discussed later in chapter 10.

6.8 The role of damping

To conclude this chapter, we would like to insist on the role of the damping for non-collocated control systems. We have seen that the imaginary zeros provide the necessary phase lead to compensate the undesirable phase lag caused by the poles. Whenever a flexible pole is not associated with a zero, it produces a net phase lag of 180^0. According to the stability criterion, the amplitude of the open-loop transfer function must satisfy $|gGH| < 1$ whenever the phase lag exceeds 180^0. Since the amplitude of gGH in the roll-off region is dominated by the resonant peaks of G, it is clear that the damping of the flexible modes is essential for non-collocated systems (Problem 6.1).

Damping augmentation can be achieved by passive as well as active means. For spacecraft applications, the former often use constrained layers of high damping elastomers placed at appropriate locations in the structure (e.g. Johnson 1981 or Ikegami, 1986). More varied ways are regularly used in civil engineering applications, such as tuned-mass dampers, tuned liquid dampers, chain dampers, etc... Active damping is the subject of next chapter.

6.9 References

CANNON, R.H. & ROSENTHAL, D.E. Experiment in control of flexible structures with noncolocated sensors and actuators. *AIAA Journal of Guidance*, Vol. 7, No 5, Sept-Oct., 546-553, 1984.

FRANKLIN, G.F., POWELL, J.D. & EMAMI-NAEINI, A. *Feedback Control of Dynamic Systems.* Addison-Wesley, 1986.

GEVARTER, W.B. Basic relations for control of flexible vehicles. *AIAA Journal*, Vol.8,No 4, April, 666-672, 1970.
HUGHES, P.C. & ABDEL-RAHMAN, T.M. Stability of proportional plus derivative plus integral control of flexible spacecraft, *AIAA J. Guidance and Control*, Vol.2, No 6, 499-503, Nov.-Dec. 1979.
IKEGAMI, R. & JOHNSON, D.W. The design of viscoelastic passive damping treatments for satellite equipment support structures, Proceedings of DAMPING'86, AFWAL-TR-86-3059, 1986.
JOHNSON, C.D., KIENHOLZ, D.A. & ROGERS, L.C. Finite element prediction of damping in beams with constrained viscoelastic layers, *Shock and Vibration Bulletin*, No 51, 78-81, May 1981.
MARTIN, G.D. *On the Control of Flexible Mechanical Systems*. Ph.D. Dissertation, Stanford University, 1978.
MIU, D.K. Physical interpretation of transfer function zeros for simple control systems with mechanical flexibilities. *ASME J. Dynamic Systems Measurement and Control*, Vol.113, September, 419-424, 1991.
SPECTOR, V.A. & FLASHNER, H. Sensitivity of structural models for noncollocated control systems. *ASME J. Dynamic Systems Measurement and Control*, Vol.111, No 4, December, 646-655, 1989.
SPECTOR, V.A. & FLASHNER, H. Modeling and design implications of noncollocated control in flexible systems. *ASME J. Dynamic Systems Measurement and Control*, Vol.112, June, 186-193, 1990.

6.10 Problems

P.6.1 *Consider the lead compensator for the non-collocated control of the two-mass system.*

(a) Determine the value of the damping ratio ξ which would reduce the gain margin to zero.

(b) What would be the gain margin if $\xi = 0.04$ instead of $\xi = 0.02$.

P.6.2 *Consider the lead compensator plus notch filter for the non-collocated control of the two-mass system (section 6.4). Draw the corresponding Bode plots. Select a reasonable value of the gain g and compare the bandwidth, the gain and phase margins with those of the lead compensator of Fig.6.6.*

P.6.3 *(a) Repeat the previous problem when the frequency of the appendage is lower than that of the notch filter (ω_0 =0.8 rad/sec); compare the Bode plots and comment on the role of the damping.*

(*b*) *Same as* (a) *with the frequency of the appendage moving away from the notch filter* (ω_0 =*1.1 rad/sec). Comment on the importance of tuning the notch filter.*

P.6.4 *Consider the PD regulator*

$$H(s) = g(Ts + 1)$$

applied to the open-loop structure

$$G(s) = \sum_{i=1}^{\infty} \frac{\phi_i(a)\phi_i(s)}{s^2 + \omega_i^2}$$

Assuming that the modes are well separated, show that, for small gain g*, the closed-loop damping ratio of mode* i *is*

$$\xi_i = gT \frac{\phi_i(a)\phi_i(s)}{2\omega_i}$$

Conclude on the stability condition (Gevarter, 1970).

[*Hint: Use a perturbation method,* $s = \omega_i[-\xi + j(1 + \delta)]$ *in the vicinity of* $j\omega_i$*, and write the closed-loop characteristic equation.*]

P.6.5 *Consider a simply supported uniform beam with a point force actuator and a displacement sensor. Based on the result of the previous problem, sketch a non-collocated actuator and sensor configuration such that a PD regulator is stabilizing for the first three modes.*

P.6.6 *Consider a system of* n *identical masses* M *simply connected with* $n + 1$ *springs of stiffness* k*; assume that a point force is applied on mass* i *and a displacement sensor is connected to mass* $j(> i)$*. Show that the zeros of the transfer function are the resonance frequencies of the two substructures (from 1 to* i *and from* $j + 1$ *to* n *), formed by constraining the masses* i *and* j *(Miu, 1991).*

P.6.7 *Consider the non-collocated control of the two-mass problem [the system transfer function is given by Equ.(6.7)] with* $M = 1$*. For various values of the mass ratio* $\mu = 0.1, 0.01, 0.001$*, assuming a lead compensator (6.9), draw a diagram of the bandwidth of the control system,* ω_c/ω_0 *as a function of the damping ratio* ξ *for the limit of stability* ($GM = 0$).

7

Active damping with collocated system

7.1 Introduction

The use of collocated (and dual) actuator and sensor pairs, for a lightly damped flexible structure, always leads to alternating poles and zeros near the imaginary axis, Fig.7.1. In this chapter, we use this interlacing property to develop Single Input-Single Output (SISO) active damping schemes with guaranteed stability. By active damping, we mean that the primary objective of the controller is simply to increase the negative real part of the system poles, while maintaining the natural frequencies essentially unchanged. This simply attenuates the resonance peak in the dynamic amplification (Fig 7.2). Recall that the relationship between the damping ratio ξ and the angle ϕ with respect to the imaginary axis is $\sin\phi = \xi$, and that the dynamic amplification at resonance is $1/2\xi$. Note that for typical damping values encountered in practice, the values of ϕ are very close to 0; this is why in most of the root locus plots shown in

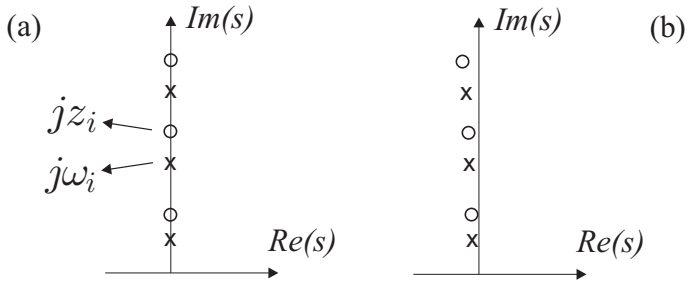

Fig. 7.1. Pole/Zero pattern of a structure with collocated (dual) actuator and sensor; (a) undamped; (b) lightly damped.

this chapter, different scales are used for the real and the imaginary axes, leading to a distortion of the angles.

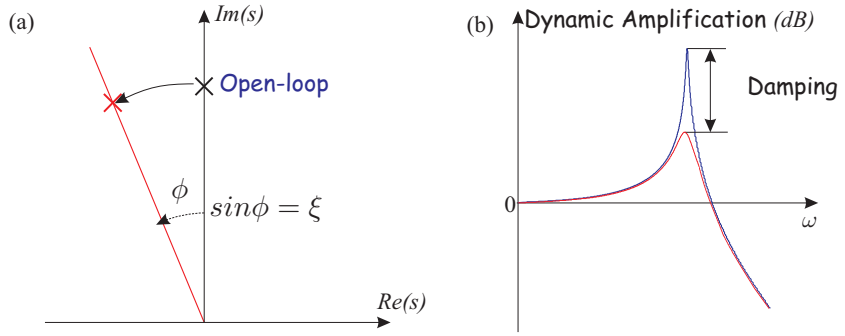

Fig. 7.2. Role of damping (a) System poles. (b) Dynamic amplification ($1/2\xi$).

Active damping requires relatively little control effort; this is why it is also called *Low Authority Control* (LAC), by contrast with other control strategies which fully relocate the closed-loop poles (natural frequency and damping) and are called *High Authority control* (HAC).

A remarkable feature of the LAC controllers discussed here is that the control law requires very little knowledge of the system (at most the knowledge of the natural frequencies). However, guaranteed stability does not mean guaranteed performances; good performance does require information on the system as well as on the disturbance applied to it, for appropriate actuator/sensor placement, actuator sizing, sensor selection and controller tuning. Actuator placement means good controllability of the dominant modes (note that, for collocated systems, controllability and observability go together, because the actuator and the sensor are collocated); this will be reflected by well separated poles and zeros, leading to wide loops in the root-locus plots.

In order to keep the formal complexity to a minimum, we assume no structural damping and perfect actuator and sensor dynamics throughout most of this chapter. The impact of the actuator and sensor dynamics on stability, and the beneficial effect of passive damping is discussed at the end.

7.2 Lead control

Consider a undamped structure with a collocated, dual actuator/sensor pair. We assume that the open-loop FRF $G(\omega)$ does not have any feedthrough (constant) component, so that $G(\omega)$ decays at high frequency as s^{-2}; the *roll-off* (high frequency decay rate) is -40 *dB/decade* in this case.

The open-loop transfer function of such a system, expressed in modal coordinates, reads

$$G(s) = \sum_{i=1}^{n} \frac{(b^T \phi_i)^2}{\mu_i (s^2 + \omega_i^2)} \tag{7.1}$$

where $b^T \phi_i$ is the modal amplitude at the actuator/sensor location. This corresponds, typically, to a point force actuator collocated with a displacement sensor, or a torque actuator collocated with an angular sensor. The pole-zero pattern is that of Fig 7.3 (where 3 modes have been assumed); there are two structural poles in excess of zeros, which provide a roll-off rate s^{-2} (a feedthrough component would introduce an additional pair of zeros). This system can be damped with a *lead compensator*:

$$H(s) = g \frac{s+z}{s+p} \qquad (p \gg z) \tag{7.2}$$

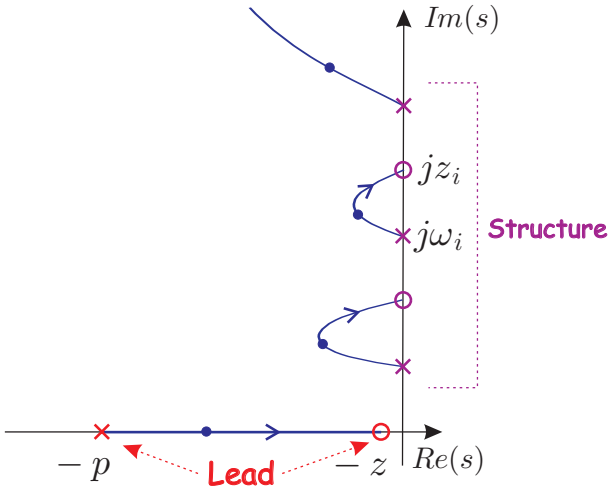

Fig. 7.3. Open-loop pole/zero pattern and root locus of the lead compensator applied to a structure with collocated actuator/sensor (open-loop transfer function with two poles in excess of zeros). Different scales are used on the real and imaginary axes and only the upper half of the plot is shown.

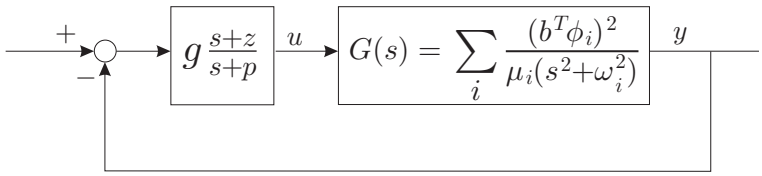

Fig. 7.4. Block diagram of the lead compensator applied to a structure with collocated actuator/sensor (open-loop transfer function $G(s)$ with two poles in excess of zeros).

The block diagram of the control system is shown in Fig 7.4. This controller takes its name from the fact that it produces a phase lead in the frequency band between z and p, bringing active damping to all the modes belonging to $z < \omega_i < p$. Figure 7.3 also shows the root locus of the closed-loop poles when the gain g is varied from 0 to ∞. The closed-loop poles which remain at finite distance start at the open-loop poles for $g = 0$ and eventually go to the open-loop zeros for $g \to \infty$. Since there are two poles more than zeros, two branches go to infinity. The controller does not have any roll-off, but the roll-off of the structure is enough to guarantee *gain stability* at high frequency.

Note that the asymptotic values of the closed-loop poles for large gains being the open-loop zeros z_i, which are the natural frequencies of the constrained system, they are therefore independent of the lead controller parameters z and p. For a structure with well separated modes, the individual loops in the root-locus (Fig 7.3) are to a large extent independent of each other, and the root-locus for a single mode can be drawn from the lead controller and the asymptotic values ω_i and z_i of that mode only (Fig 7.5). The characteristic equation for this simplified system can be written from the pole-zero pattern:

$$1 + \alpha \frac{(s^2 + z_i^2)(s + z)}{(s^2 + \omega_i^2)(s + p)} = 0 \tag{7.3}$$

where α is the variable parameter going from $\alpha = 0$ (open-loop) to infinity. This can be written alternatively

$$1 + \frac{1}{\alpha} \frac{(s^2 + \omega_i^2)(s + p)}{(s^2 + z_i^2)(s + z)} = 0$$

If z and p have been chosen in such a way that $z \ll \omega_i < z_i \ll p$, this can be approximated in the vicinity of $j\omega_i$ by

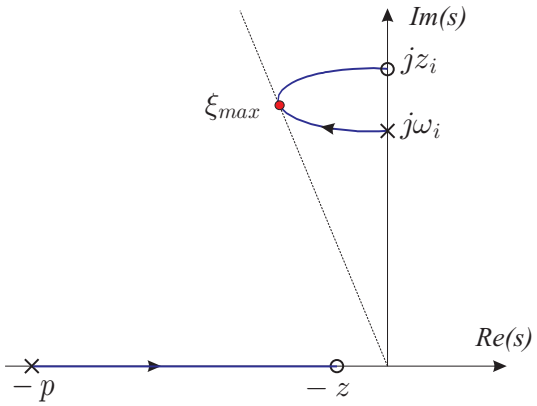

Fig. 7.5. Structure with well separated modes and lead compensator, root-locus of a single mode.

$$1 + \frac{p}{\alpha} \frac{(s^2 + \omega_i^2)}{s(s^2 + z_i^2)} = 0 \tag{7.4}$$

This characteristic equation turns out to be the same as that of the *Integral Force Feedback* (IFF) controller discussed a little later in this chapter, Equ.(7.31); it follows that the maximum achievable modal damping is given by

$$\xi_{max} = \frac{z_i - \omega_i}{2\omega_i} \qquad (\omega_i > z_i/3) \tag{7.5}$$

Note that the maximum achievable damping is controlled by the separation between the open-loop pole ω_i and the nearby zero z_i.

7.3 Direct velocity feedback

The *Direct Velocity Feedback* (DVF) is the particular case of the lead controller as $z \to 0$ and $p \to \infty$. Returning to the the basic equations:

Structure:

$$M\ddot{x} + Kx = bu \tag{7.6}$$

Output (velocity sensor) :

$$y = b^T \dot{x} \tag{7.7}$$

Control :

$$u = -gy \tag{7.8}$$

one finds easily the closed-loop equation

$$M\ddot{x} + gbb^T\dot{x} + Kx = 0 \tag{7.9}$$

Upon transforming into modal coordinates, $x = \Phi x$ and taking into account the orthogonality conditions, one gets

$$diag(\mu_i)\ddot{z} + g\Phi^T bb^T\Phi\,\dot{z} + diag(\mu_i\omega_i^2)z = 0 \tag{7.10}$$

where z is the vector of modal amplitudes. The matrix $\Phi^T bb^T\Phi$ is in general fully populated. For small gains, one may assume that it is diagonally dominant, $\simeq diag(b^T\phi_i)^2$. This assumption leads to a set of decoupled equations. Mode i is governed by

$$\mu_i\ddot{z}_i + g(b^T\phi_i)^2\dot{z}_i + \mu_i\omega_i^2 z_i = 0 \tag{7.11}$$

By analogy with single a d.o.f. oscillator, one finds that the active modal damping ξ_i is given by

$$2\xi_i\mu_i\omega_i = g(b^T\phi_i)^2 \tag{7.12}$$

or

$$\xi_i = \frac{g(b^T\phi_i)^2}{2\mu_i\omega_i} \tag{7.13}$$

Thus, for small gains, the closed-loop poles sensitivity to the gain (i.e. the departure rate from the open-loop poles) is controlled by $(b^T\phi_i)^2$, the square of the modal amplitude at the actuator/sensor location.

Now, let us examine the asymptotic behavior for large gains. For all g, the closed-loop eigenvalue problem (7.9) is

$$(Ms^2 + gbb^T s + K)x = 0 \tag{7.14}$$

Except for the presence of s in the middle term, this equation is close to Equ.(2.45); proceeding as we did in chapter 2, it follows that

$$x = -(K + Ms^2)^{-1}gsbb^T x$$

or

$$b^T x = -gsb^T(K + Ms^2)^{-1}bb^T x \tag{7.15}$$

Since $b^T x$ is a scalar, one must have

$$sb^T(K + Ms^2)^{-1}b = -\frac{1}{g} \tag{7.16}$$

and taking the limit for $g \to \infty$

$$sb^T(K + Ms^2)^{-1}b = 0 \tag{7.17}$$

The solutions of this equation are $s = 0$ and the solutions of (2.49), that are the eigenvalues of the constrained system. The fact that the eigenvalues are purely imaginary, $s = \pm j\omega_0$ stems from the fact that K and M are symmetric and semi-positive definite. Typical root locus plots for a lead controller and a DVF controller are compared in Fig.7.6.

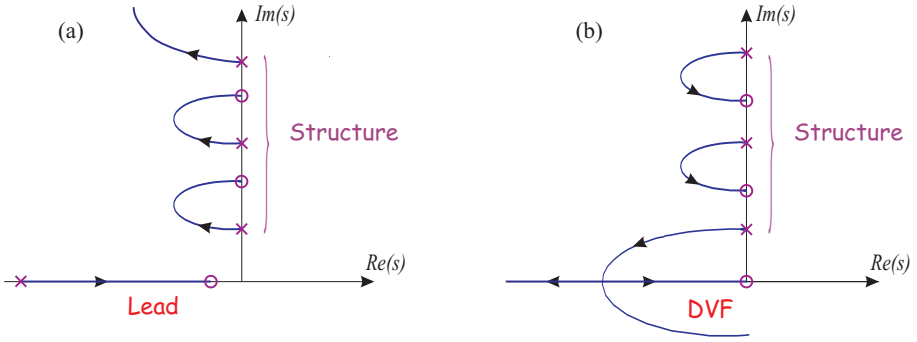

Fig. 7.6. Collocated control system. (a) Root locus for a lead controller. (b) DVF controller.

As for the lead controller, for well separated modes, those which are far enough from the origin can be analyzed independently of each other. In this way, the characteristic equation for mode i is approximated by

$$1 + g\frac{s(s^2 + z_i^2)}{(s^2 + \omega_1^2)(s^2 + \omega_i^2)} = 0$$

(besides the poles at $\pm j\omega_i$ and the zeros at $\pm jz_i$, we include the zero at $s = 0$ and the poles at $\pm j\omega_1$) which in turn, if $\omega_i > z_i \gg \omega_1$, may be approximated by

$$1 + g\frac{s^2 + z_i^2}{s(s^2 + \omega_i^2)} = 0 \tag{7.18}$$

in the vicinity of mode i. This root locus is essentially the same as in the previous section (with z_i appearing in the numerator and ω_i in the denominator), and the formula for the maximum modal damping (7.32) applies

$$\xi_{max} = \frac{\omega_i - z_i}{2z_i} \qquad (z_i > \omega_i/3) \tag{7.19}$$

7.4 Positive Position Feedback (PPF)

There are frequent situations where the open-loop FRF does not exhibit a roll-off of $-40\,dB/decade$ as in the previous section. In fact, a feedthrough component may arise from the truncation of the high frequency dynamics, as in (2.34), or because of the physical nature of the system (e.g. beams or plates covered with collocated piezoelectric patches, Fig.4.8).

In these situations, the degree of the numerator of $G(s)$ is the same as that of the denominator and the open-loop pole-zero pattern has an additional pair of zeros at high frequency. Since the overall degree of the denominator of $H(s)G(s)$ must exceed the degree of the numerator, the controller $H(s)$ must have more poles than zeros. The *Positive Position Feedback* was proposed to solve this problem (Goh & Caughey).

The second-order PPF controller consists of a second order filter

$$H(s) = \frac{-g}{s^2 + 2\xi_f \omega_f s + \omega_f^2} \tag{7.20}$$

where the damping ξ_f is usually rather high (0.5 to 0.7), and the filter frequency ω_f is adapted to target a specific mode. The block diagram of the control system is shown in Fig.7.7; the negative sign in $H(s)$, which produces a positive feedback, is the origin of the name of this controller.

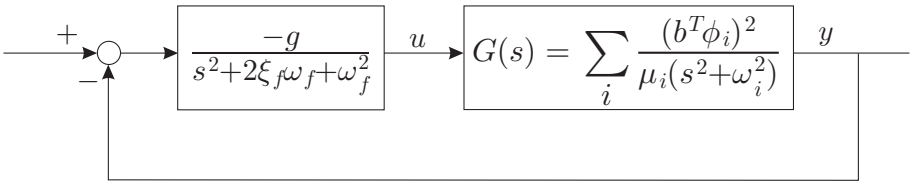

Fig. 7.7. Block diagram of the second-order PPF controller applied to a structure with collocated actuator and sensor (the open-loop transfer function has the same number of poles and zeros).

Figure 7.8 shows typical root loci when the PPF poles are targeted to mode 1 and mode 2, respectively (i.e. ω_f close to ω_1 or ω_2, respectively). One sees that the whole locus is contained in the left half plane, except one branch on the positive real axis, but this part of the locus is reached only for large values of g, which are not used in practice. The stability condition can be established as follows: the characteristic equation of the closed-loop system reads

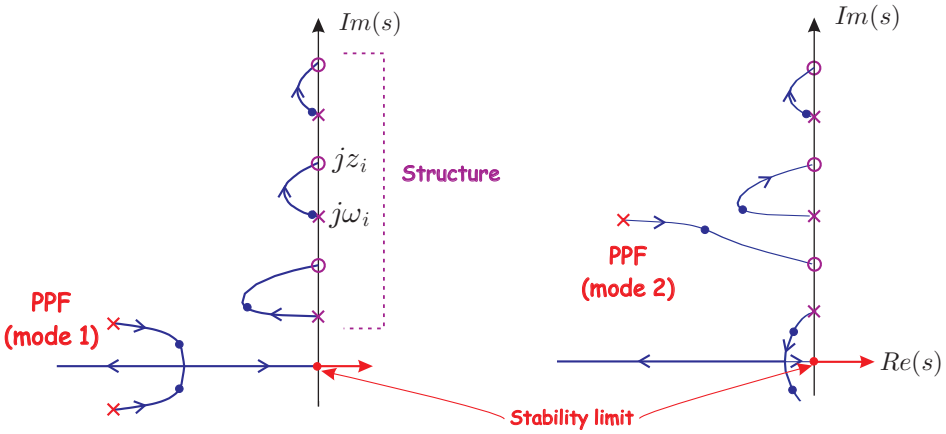

Fig. 7.8. Root locus of the PPF controller applied to a structure with collocated actuator and sensor (the open-loop transfer function has the same number of poles and zeros). (a) Targeted at mode 1. (b) Targeted at mode 2. (For clarity, different scales are used for the real and the imaginary axes.)

$$\psi(s) = 1 + gH(s)G(s) = 1 - \frac{g}{s^2 + 2\xi_f\omega_f s + \omega_f^2}\{\sum_{i=1}^{n} \frac{b^T\phi_i\phi_i^T b}{\mu_i(s^2 + \omega_i{}^2)}\} = 0$$

or

$$\psi(s) = s^2 + 2\xi_f\omega_f s + \omega_f^2 - g\{\sum_{i=1}^{n} \frac{b^T\phi_i\phi_i^T b}{\mu_i(s^2 + \omega_i{}^2)}\} = 0$$

According to the Routh-Hurwitz criterion for stability (see chapter 13), if one of the coefficients of the power expansion of the characteristic equation becomes negative, the system is unstable. It is not possible to write the power expansion $\psi(s)$ explicitly for an arbitrary value of n, however, one can see easily that the constant term (in s^0) is

$$a_n = \psi(0) = \omega_f^2 - g\sum_{i=1}^{n} \frac{b^T\phi_i\phi_i^T b}{\mu_i\omega_i{}^2}$$

In this case, a_n becomes negative when the static loop gain $gG(0)H(0)$ becomes larger than 1. The stability condition is therefore

$$gG(0)H(0) = \frac{g}{\omega_f^2}\{\sum_{i=1}^{n} \frac{b^T\phi_i\phi_i^T b}{\mu_i\omega_i{}^2}\} < 1 \qquad (7.21)$$

Note that it is independent of the structural damping in the system. Since the instability occurs for large gains which are not used in practice,

the PPF can be regarded as unconditionally stable. Unlike the lead controller of the previous section which controls all the modes which belong to $z < \omega_i < p$ and even beyond, the PPF filter must be tuned on the targeted mode (it is therefore essential to know the natural frequency accurately), and the authority on the modes with very different frequencies is substantially reduced. Several PPF filters can be used in parallel, to target several modes simultaneously, but they must be tuned with care, because of the cross coupling between the various loops. An application will be considered in section 14.4.

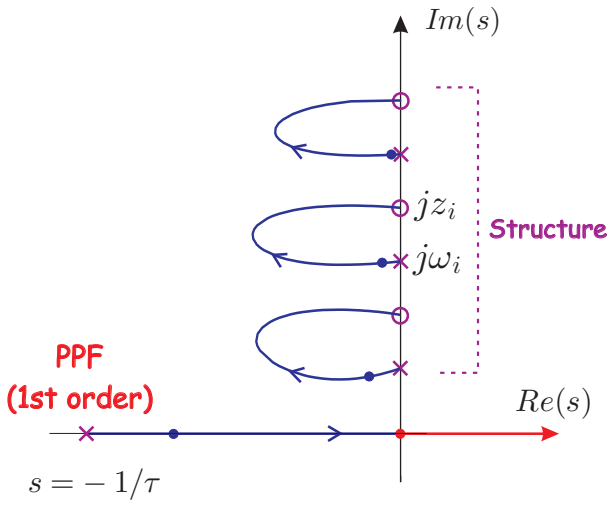

Fig. 7.9. Root locus of the first-order PPF controller (the scale on the real axis has been magnified for clarity).

The following first-order PPF controller is an alternative to the second order controller:

$$H(s) = \frac{-g}{1+\tau s} \tag{7.22}$$

A typical root locus is shown in Fig.7.9. As compared to the second-order controller, this one does not have to be tuned on targeted modes; the roll-off is reduced to $-20\,dB/decade$ instead of $-40\,dB/decade$ with the second order controller. The part of the locus on the real axis also becomes unstable for large gains. Proceeding exactly as we did for the second order controller, one finds easily that the stability condition is, once again, that the static loop gain must be lower than 1:

$$gG(0) < 1 \tag{7.23}$$

Thus the gain margin is $GM = [gG(0)]^{-1}$. The stability condition corresponds to the negative stiffness of the controller overcoming that of the structure. Because of this negative stiffness, the root-locus does not leave the open-loop poles orthogonally to the imaginary axis; this is responsible for larger control efforts, as compared to the other strategies considered before, which may be a serious drawback in applications where the control effort is an important issue.

7.5 Integral Force Feedback(IFF)

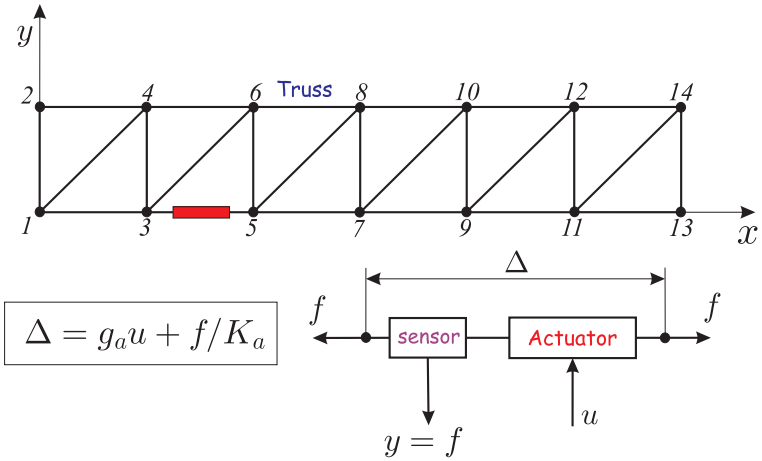

Fig. 7.10. Active truss with an active strut consisting of a displacement actuator and a force sensor. $\delta = g_a u$ is the unconstrained extension of the strut induced by the control u. The passive stiffness of the strut is K_a and f/K_a is the elastic extension. $\Delta = b^T x$ is the total extension of the active strut.

So far, all the collocated system that we have considered exhibit alternating poles and zeros, starting with a pole at low frequency ($\omega_1 < z_1 < \omega_2 < z_2 < \omega_3$....). This corresponds to an important class of actuator/sensor pairs, including (force actuator/displacement or velocity sensor), (torque actuator/angular or angular velocity sensor), (piezoelectric patches used as actuator and sensor). In this section, we discuss an other interlacing pole-zero configuration but starting with a zero ($z_1 < \omega_1 < z_2 < \omega_2$...). This situation arises, typically, in a actuator/sensor pair made of a displacement actuator and a force sensor, such

as that of the piezoelectric active truss of Fig 7.10 already considered considered in section 4.9. The governing equation has been found to be

$$M\ddot{x} + (K^* + bb^T K_a)x = bK_a\delta \tag{7.24}$$

where K^* is the stiffness matrix of the structure without the active strut and $K^* + bb^T K_a$ is the global stiffness matrix, including the active strut. Note that this equation applies to linear actuators of many types, piezoelectric, magnetostrictive, thermal, ball-screw,..., provided that the constitutive equation of the actuator is

$$\Delta = \delta + f/K_a$$

or equivalently

$$y = f = K_a(b^T x - \delta) \tag{7.25}$$

where $\Delta = b^T x$ is the total extension of the active strut, δ its free extension (control), f is the force sensor output, and K_a is the strut stiffness. The open-loop transfer function has been found to be

$$G(s) = \frac{y}{\delta} = K_a[\sum_{i=1}^{m} \frac{\nu_i}{s^2/\omega_i^2 + 1} + \sum_{i=m+1}^{n} \nu_i - 1] \tag{7.26}$$

where the residues ν_i are the fraction of modal strain energy in the active strut. The FRF exhibit alternating poles and zeros on the imaginary axis, beginning with a zero, Fig.7.11.
The feedback control law is in this case a *positive Integral Force Feedback*

$$\delta = \frac{g}{K_a s}\, y \tag{7.27}$$

(the K_a at the denominator is for normalization purpose; y/K_a is the elastic extension of the strut). The block diagram of the system is represented in Fig.7.12. The pole-zero pattern of the system is shown in Fig 7.13. It consists of interlacing pole-zero pairs on the imaginary axis ($z_1 < \omega_1 < z_2 < \omega_2 ...$) and the pole at $s = 0$ from the controller. The root locus plot consists of the negative real axis and a set of loops going from the open-loop poles $\pm j\omega_i$ to the open-loop zeros $\pm jz_i$. All the loops are entirely contained in left half plane, so that the closed-loop system is unconditionally stable, for all values of the gain g. Note also that the root-locus plot does not change significantly if the pole at the origin is moved slightly in the left half plane, to avoid saturation (which is often

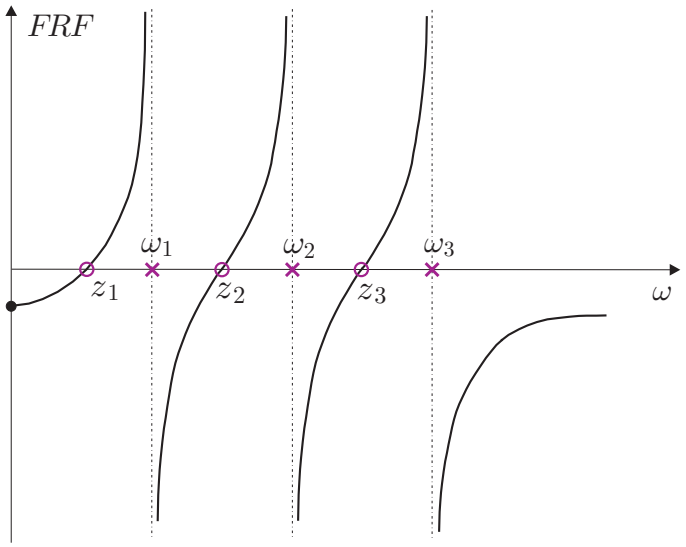

Fig. 7.11. Open-loop FRF of an active truss. The active strut consists of a piezoelectric actuator and a collocated force sensor.

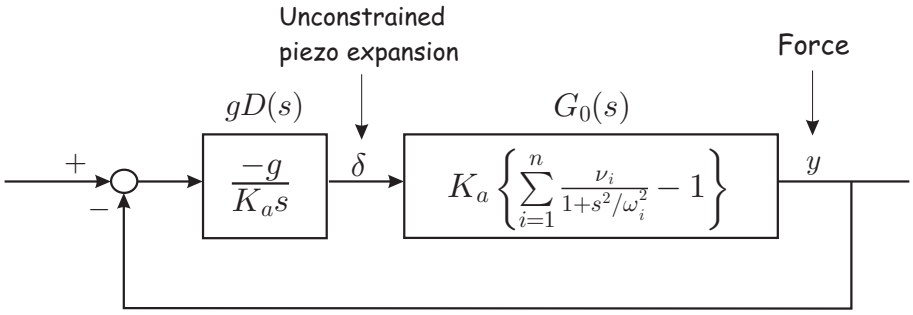

Fig. 7.12. Block diagram of the IFF control.

associated with integral control). In fact, piezoelectric force sensors have a built-in high-pass filter and cannot measure a d.c. component.[1]

Equations (7.25) and (7.27) can be combined, leading to

$$\delta = \frac{g}{s+g} b^T x \tag{7.28}$$

and upon substituting into (7.24), one gets the closed-loop characteristic equation

[1] This issue and the static behavior of the active truss will be reexamined later in this book; see also Problem 7.5.

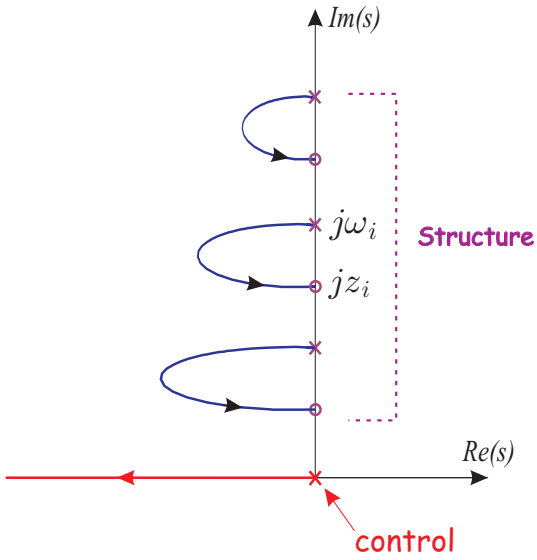

Fig. 7.13. Pole-zero pattern of the active strut and root-locus of the IFF.

$$[Ms^2 + (K^* + bb^T K_a) - bb^T K_a \frac{g}{s+g}]x = 0 \tag{7.29}$$

For $g = 0$, the eigenvalues are indeed the open-loop poles, $\pm j\omega_i$. Asymptotically, for $g \to \infty$, the eigenvalue problem becomes

$$[Ms^2 + K^*]x = 0 \tag{7.30}$$

where K^* is the stiffness matrix of the structure without the active strut. Thus, the open-loop zeros $\pm jz_i$ *are the natural frequencies of the truss after removing the active strut.* This situation should be compared to that discussed earlier (section 2.5.1) in connection with a displacement sensor. In that case, the open-loop zeros were found to be the natural frequencies of the constrained system where the d.o.f. along which the actuator and sensor operate is blocked (i.e. the sensor output is cancelled). In the present case, if the sensor output is zero, the force carried by the active strut vanishes and it can be removed.

For well separated modes, the individual loops in the root-locus of Fig 7.13 are, to a large extent, independent of each other, and the root locus of a single mode can be drawn from the asymptotic values $\pm j\omega_i$ and $\pm jz_i$ only (Fig 7.14.a). The corresponding characteristic equation is [2]

[2] Note the similarity with (7.4) for the lead controller and with (7.18) for the DVF.

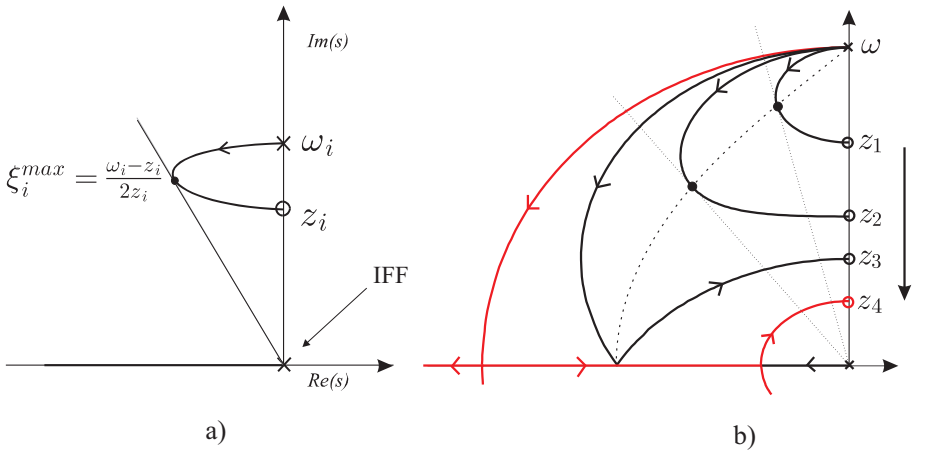

Fig. 7.14. (a) IFF root locus of a single mode. (b) Evolution of the root locus as z_i moves away from ω_i

$$1 + g\frac{(s^2 + z_i^2)}{s(s^2 + \omega_i^2)} = 0 \tag{7.31}$$

The actual root-locus, Fig.7.13, which includes the influence of the other modes, is only slightly different from that of Fig 7.14.a, with the same asymptotic values at $\pm j\omega_i$ and $\pm jz_i$. It can be shown (Problem 7.3) that the maximum modal damping for mode i is given by

$$\xi_i^{max} = \frac{\omega_i - z_i}{2z_i} \qquad (z_i \geq \omega_i/3) \tag{7.32}$$

It is achieved for $g = \omega_i\sqrt{\omega_i/z_i}$ This result applies only for $\xi_i \leq 1$, that is for $z_i \geq \omega_i/3$. For $z_i = \omega_i/3$, the locus touches the real axis as indicated in Fig 7.14.b, and for even larger differences $\omega_i - z_i$, the root locus includes part of the real axis, which means that one can achieve enormous damping values. Equation (7.32) relates clearly the maximum achievable damping and the distance between the pole and the zero. Note, however, that if the system has several modes, there is a single tuning parameter g, and the various loops are travelled at different speeds. As a result, the optimal value of g for one mode will not be optimal for another one, and a compromise must be found.

Equation (7.29) can be transformed into modal coordinates. Using the orthogonality conditions, one finds

$$[diag(\mu_i)s^2 + diag(\mu_i\omega_i^2) - \Phi^T bb^T \Phi K_a \frac{g}{s+g}]z = 0 \tag{7.33}$$

For small g, the equations are nearly decoupled:

$$[s^2 + \omega_i^2 - \nu_i \omega_i^2 \frac{g}{s+g}] z_i = 0 \tag{7.34}$$

after using the definition of ν_i, Equ.(4.107). Since the root locus plot leaves the open-loop pole orthogonally to the imaginary axis, for small gain, one can assume a solution of the form $s = \omega_i(-\xi_i + j)$. Substituting into (7.34), one finds easily

$$\xi_i = \frac{g\nu_i}{2\omega_i} \tag{7.35}$$

Thus, for small gains, the closed-loop poles sensitivity to the gain, i.e. the departure rate from the open-loop poles, is controlled by the fraction of modal strain energy in the active element. This result is very useful for the design of active trusses. The active strut should be located to maximize ν_i for the critical modes of the structure. Note that ν_i is readily available from finite element softwares; an example is analyzed in section 14.2.

In summary, the active strut placement can be made from the inspection of the map of modal strain energy in the finite element model, once the active strut location has been selected, a modal analysis of the truss including the active strut gives the open-loop poles $\pm j\omega_i$, and a modal analysis after removing the active strut gives the open-loop zeros $\pm jz_i$. Then, the root-locus plot can be drawn. The case of a truss involving several active struts controlled in a decentralized manner is examined in section 14.3.

7.6 Duality between the Lead and the IFF controllers

In both cases, if the modes are well separated, they behave essentially independently, and their closed-loop behavior may be analyzed as a single mode, without considering the interaction with the other modes.

7.6.1 Root-locus of a single mode

Figure 7.15 illustrates the duality between the IFF and the Lead controllers. If the pole and the zero of the lead controller (7.2) are such that $z \ll \omega_i < z_i \ll p$, the root-locus plots of every mode turn out to be very similar (Fig.7.15.c and d). The DVF can be looked at as the limit of the Lead controller as $z \to 0$ and $p \to \infty$; however, depending on the situation, the individual loops starting from an open-loop pole may go either to a zero with higher frequency (similar to Fig.7.15.d) or to a zero with lower frequency (similar to Fig.7.15.c).

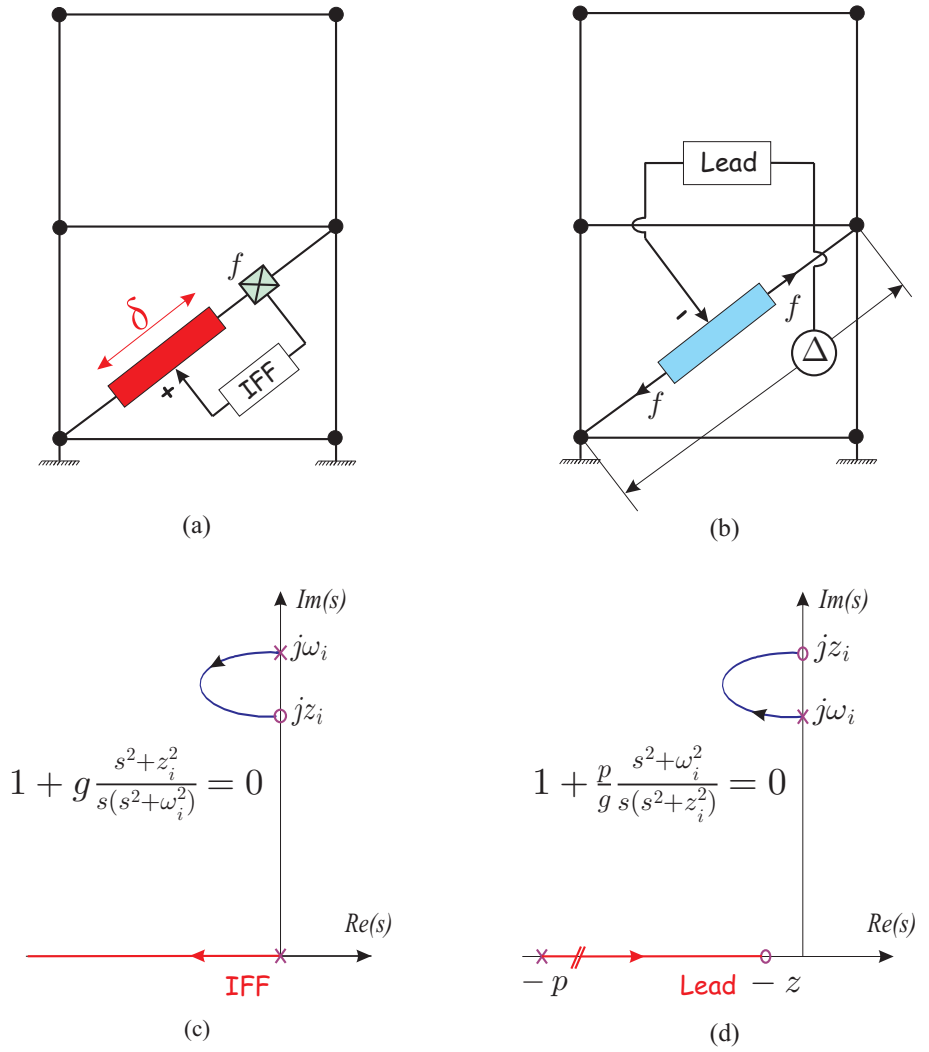

Fig. 7.15. Duality between the IFF and the Lead (DVF) control configurations. (a) IFF architecture with displacement actuator, force sensor and positive integral force feedback. (b) Force actuator and collocated displacement transducer and (negative) Lead controller (DVF is a particular case). (c) IFF control: Root locus for a single mode. (d) Lead control: Root locus for a single mode ($z \ll \omega_i < z_i \ll p$). The loops of the DVF can be approximated by one configuration or the other, depending on the relative value of ω_i and z_i.

7.6.2 Open-loop poles and zeros

For the IFF (Fig.7.15.a), the open-loop poles $j\omega_i$ are the natural frequencies of the structure with the active element working passively (contributing with its own stiffness K_a), while the open-loop zeros, jz_i, are the natural frequencies when the force f in the active strut is zero, that is when the active element is removed. On the contrary, in the control configuration of Fig.7.15.b, the open-loop poles are the natural frequencies when the active element produces no force (same as the zeros in the previous case), and the open-loop zeros are the natural frequencies with the d.o.f. along the actuator blocked ($\Delta = 0$). Note that these are larger than the open-loop poles in the IFF case, because the stiffness K_a of the active strut is finite.

7.7 Actuator and sensor dynamics

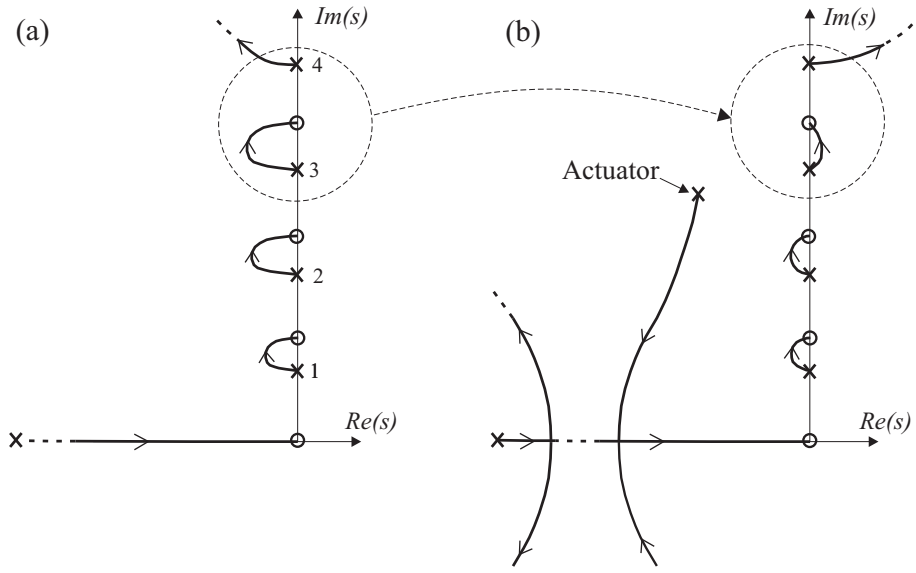

Fig. 7.16. Effect of the actuator dynamics on the Lead compensator. (a) With perfect actuator. (b) Including the actuator dynamics $A(s)$ given by (7.37) (the corner frequency of the actuator is such that $\omega_2 < \omega_a < \omega_3$).

Throughout this chapter, it has been assumed that the actuator and sensor have perfect dynamics. As a result, the active damping algorithms

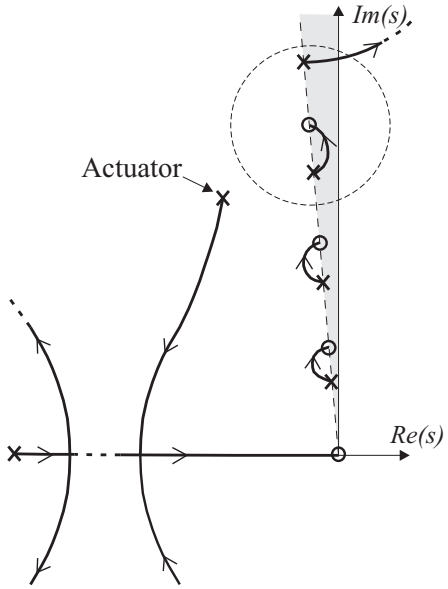

Fig. 7.17. Stabilizing effect of the structural damping on the actuator dynamics.

are stable for all gains g (except the PPF). In practice, however, the open-loop transfer function becomes

$$g\ A(s)\ H(s)\ G_0(s) \tag{7.36}$$

where $A(s)$ includes the sensor, actuator and the digital controller dynamics. The low frequency behavior of the proof-mass actuator and the charge amplifier can both be approximated by a second order high-pass filter such as (3.8). The high frequency behavior of the actuators and sensors can often be represented by a second order low-pass filter

$$A(s) = \frac{\omega_a^2}{s^2 + 2\xi_a\omega_a s + \omega_a^2} \tag{7.37}$$

It is easy to see that the two extra poles of $A(s)$ bring the asymptotes of the root locus inside the right half plane and substantially alter its shape for $\omega > \omega_a$. Figure 7.16 shows the effect of the second order low-pass filter on the root locus plot of the lead compensator (we have assumed $\xi_a = 0.5$ and $\omega_2 < \omega_a < \omega_3$). The active damping is no longer unconditionally stable and always has some destabilizing influence on the modes with natural frequencies beyond ω_a. Fortunately, in practice, the modes of the structure are not exactly on the imaginary axis, because of the structural

damping (Fig.7.17); this allows us to operate the controller with small gains. The control system becomes insensitive to the actuator dynamics if ω_a is far beyond the cross-over frequency of $gH(s)G_0(s)$. The effect of the low frequency dynamics of a proof-mass actuator is left as a problem.

7.8 Decentralized control with collocated pairs

7.8.1 Cross talk

Consider the Multi-Input Multi-output (MIMO) control of a structure with two independent control loops using collocated pairs. The input-output relationship for this system can be written in compact form

$$\begin{pmatrix} y_1 \\ y_2 \\ z \end{pmatrix} = \begin{bmatrix} G_{11} & G_{12} & G_{1w} \\ G_{21} & G_{22} & G_{2w} \\ G_{z1} & G_{z2} & G_{zw} \end{bmatrix} \begin{pmatrix} u_1 \\ u_2 \\ w \end{pmatrix} \tag{7.38}$$

where w is the disturbance and z is the performance metric. One sees that the output y_1 responds to u_2 through G_{12} and y_2 responds to u_1 through G_{21}, respectively. These terms are called *cross-talk*, and are responsible for interactions between the two loops.

7.8.2 Force actuator and displacement sensor

Consider a control system with m collocated force actuator/displacement sensor pairs. The control is governed by the following equations:

Structure:

$$M\ddot{x} + Kx = Bu \tag{7.39}$$

Output:

$$y = B^T x \tag{7.40}$$

where B defines the topology of the actuator/sensor pairs (the size of the vectors u and y is equal to the number m of collocated pairs).

Control:

$$u = -gH(s)y \tag{7.41}$$

where $H(s)$ is a square matrix and g is a scalar parameter (the discussion is not restricted to decentralized control; $H(s)$ is diagonal if the control is decentralized). The closed-loop eigenvalue problem is obtained by combining the three equations above:

$$[Ms^2 + K + gBH(s)B^T]x = 0 \tag{7.42}$$

One can show that the asymptotic values of the finite eigenvalues of this equation as $g \to \infty$ are independent of $H(s)$ (Davison & Wang); therefore, they can be computed with $H(s) = I$:

$$\lim_{g\to\infty}[Ms^2 + K + gBB^T]x = 0 \tag{7.43}$$

The asymptotic solutions of this equation are the transmission zeros of the MIMO system. The matrix gBB^T is the contribution to the global stiffness matrix of a set of springs of stiffness g connected to all the d.o.f. involved in the control. Asymptotically, when $g \to \infty$, the additional springs act as supports restraining the motion along the controlled d.o.f.. Thus, *the transmission zeros are the poles (natural frequencies) of the constrained system where the d.o.f. involved in the control are blocked.* Since all the matrices involved in (7.43) are symmetrical and positive semi-definite, the transmission zeros are purely imaginary; since blocking the controlled d.o.f. reduces the total number of d.o.f. by the number m of control loops, the number of zeros is $2m$ less than the number of poles.

7.8.3 Displacement actuator and force sensor

The equations are in this case:

Structure:

$$M\ddot{x} + Kx = BK_a\delta \tag{7.44}$$

Output:

$$y = K_a(B^T x - \delta) \tag{7.45}$$

Control:

$$\delta = gH(s)y \tag{7.46}$$

where B defines the topology of the active members within the structure, assumed of equal stiffness K_a, $H(s)$ is a square matrix and g is a scalar gain (a positive feedback is assumed as in the IFF controller). The closed-loop eigenvalues are solutions of

$$[Ms^2 + K - gBK_aH(I + gK_aH)^{-1}K_aB^T]x = 0 \tag{7.47}$$

The asymptotic values are respectively, for $g = 0$, the open-loop poles (natural frequencies of the system including the active members) and, for $g \to \infty$,[3] they are solution of

[3] because $\lim_{g\to\infty}(I + gK_aH) \sim gK_aH$

$$(Ms^2 + K - BK_aB^T)x = 0 \tag{7.48}$$

Thus, asymptotically, as $g \to \infty$, the finite eigenvalues coincide with the transmission zeros which are the poles (natural frequencies) of the system where the contribution of the active members to the stiffness matrix has been removed. This result applies in particular for independent IFF loops.

7.9 References

AUBRUN, J.N. Theory of the control of structures by low-authority controllers. *AIAA J. of Guidance, Control and Dynamics*, Vol 3, No 5, Sept-Oct.,444-451, 1980.

BALAS, M.J. Direct velocity feedback control of large space structures. *AIAA J. of Guidance, Control and Dynamics*, Vol 2, No 3, 252-253, 1979.

BAZ, A., POH, S. & FEDOR, J. Independent modal space control with positive position feedback. *Trans. ASME, J. of Dynamic Systems, Measurement, and Control*,Vol.114, No 1,March, 96-103, 1992.

BENHABIB, R.J. IWENS, R.P. & JACKSON, R.L. Stability of large space structure control systems using positivity concepts. *AIAA J. of Guidance, Control and Dynamics*, Vol 4, No 5, 487-494, Sept.-Oct. 1981.

DAVISON, E.J., WANG, S.H. Properties and Calculation of Transmission Zeros of Linear Multivariable Systems, *Automatica*, Vol.10, 643-658, 1974.

DE MARNEFFE, B. *Active an Passive Vibration Isolation and Damping via Shunted Transducers*, Ph.D. Thesis, Active Structures Laboratory, ULB, Dec. 2007.

FANSON, J.L. & CAUGHEY, T.K. Positive position feedback control for large space structures. *AIAA Journal*, Vol.28, No 4,April,717-724, 1990.

FORWARD, R.L. Electronic damping of orthogonal bending modes in a cylindrical mast experiment. *AIAA Journal of Spacecraft*, Vol.18, No 1, Jan.-Feb., 11-17, 1981.

GEVARTER, W.B. Basic relations for control of flexible vehicles. *AIAA Journal*, Vol.8,No 4, April, 666-672, 1970.

GOH, C. & CAUGHEY, T.K. On the stability problem caused by finite actuator dynamics in the control of large space structures, *Int. J. of Control*, Vol.41, No 3, 787-802, 1985.

PREUMONT, A., DUFOUR, J.P. & MALEKIAN, Ch. Active damping by a local force feedback with piezoelectric actuators. *AIAA J. of Guidance, Control and Dynamics*, Vol 15, No 2, March-April, 390-395, 1992.

PREUMONT, A., LOIX, N., MALAISE, D. & LECRENIER, O. Active damping of optical test benches with acceleration feedback, *Machine Vibration*, Vol.2, 119-124, 1993.
PREUMONT, A., ACHKIRE, Y., BOSSENS, F. Active Tendon Control of Large Trusses, *AIAA Journal*, Vol.38, No 3, 493-498, March 2000.
PREUMONT, A., BOSSENS, F. Active tendon control of vibration of truss structures: Theory and experiments, *Journal of Intelligent Material Systems and Structures*, Vol.2, No 11, 91-99, February 2000.
PREUMONT, A., de MARNEFFE, B., KRENK, S., Transmission Zeros in Structural Control with Collocated MIMO Pairs, *AIAA Journal of Guidance, Control and Dynamics*, Vol.31, No 2, 428-431, March-April 2008.
PREUMONT, A., SETO, K. *Active Control of Structures*, Wiley, 2008.
SCHAECHTER, D. Optimal local control of flexible structures, *AIAA J. of Guidance, Control and Dynamics* Vol.4, No 1, 22-26, 1981.
SIM, E., & LEE, S.W. Active vibration control of flexible structures with acceleration or combined feedback. *AIAA J. of Guidance, Control and Dynamics*, Vol.16, No 2, 413-415, 1993.

7.10 Problems

P.7.1 *Compare the following implementations of the Lead and the Direct Velocity Feedback compensators:*

$$H(s) = s$$

$$H(s) = 1 + Ts$$

$$H(s) = \frac{s}{s+a}$$

$$H(s) = \frac{Ts+1}{\alpha Ts+1} \qquad (\alpha < 1)$$

$$H(s) = \frac{\omega_f^2 s}{s^2 + 2\xi_f \omega_f s + \omega_f^2}$$

Discuss the conditions under which these compensators would be applicable for active damping.

P.7.2 *Consider a vibrating structure with a point force actuator collocated with an accelerometer. Consider the two compensators:*

$$H(s) = g/s$$

$$H(s) = \frac{g}{s^2 + 2\xi_f \omega_f s + \omega_f^2}$$

Draw the block diagram of the control system, examine the stability and performance. What would be the effect of the dynamics of a charge amplifier, represented as a second order high-pass filter of corner frequency ω_p *and damping* $\xi_p = 0.7$*, assuming that its corner frequency satisfies* $\omega_p \ll \omega_1$*.*

P.7.3 *Show that the maximum damping achievable in an active truss with the integral force feedback is*

$$\xi_i^{max} = \frac{\omega_i - z_i}{2z_i} \qquad (z_i \geq \omega_i/3)$$

where ω_i *is the natural frequency of the truss including the active strut as a passive element and* z_i *is the natural frequency when the active strut has been removed, and that it is achieved for* $g = \omega_i\sqrt{\omega_i/z_i}$*. [Hint: The use of a symbolic calculation software is recommended.]*

P.7.4 *Consider the plane truss of Fig.4.19; write the influence matrix* B *for the set of active struts depicted on the figure. Check that the topology matrix appearing in the sensor equation is* B^T*.*

P.7.5 *To avoid the saturation associated with integral control, the IFF controller (7.27) may be replaced by*

$$\frac{\delta}{y} = H(s) = \frac{gs}{K_a(s+\beta)^2}$$

where $\beta \ll \omega_1$ *(de Marneffe).*

(a) Compare the root locus and the damping performance of the two controllers.

(b) Show that, on the contrary to (7.27), this control law does not reduce the static stiffness of the structure.

P.7.6 *Consider the seven-story shear frame of Fig.7.18. It is controlled in a decentralized manner with two independent and identical feedback loops. Every actuator* u_i *applies a pair of forces equal and opposite between floor* i *and floor* $i-1$*, while the sensor* $y_i = x_i - x_{i-1}$ *measures the relative displacement between the same floors. The mass, stiffness and* B *matrices are respectively* $M = mI_7$*,*

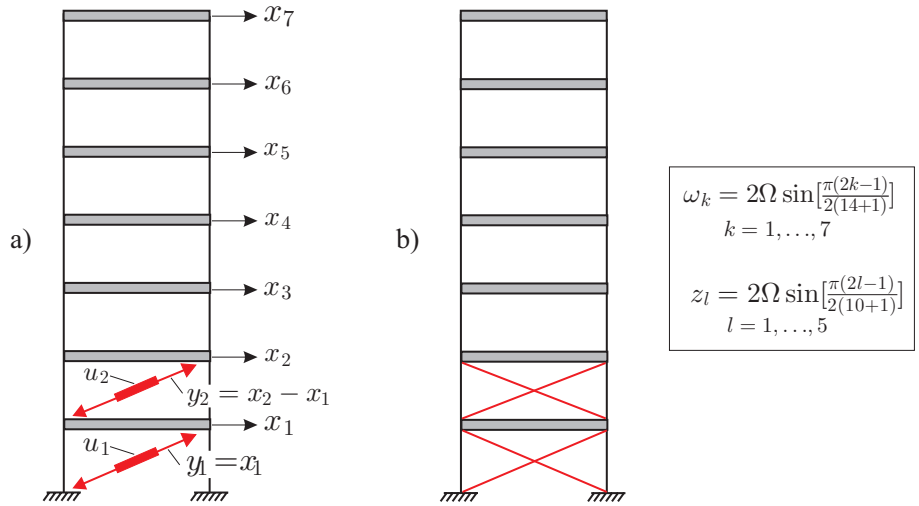

Fig. 7.18. (a) Shear frame with two independent control loops (displacement sensor and force actuator). (b) Configuration corresponding to transmission zeros.

$$K = k \begin{pmatrix} 2 & -1 & 0 & \dots & 0 \\ -1 & 2 & -1 & \dots & 0 \\ 0 & -1 & 2 & \dots & 0 \\ & & \dots & & \\ 0 & 0 & -1 & 2 & -1 \\ 0 & \dots & 0 & -1 & 1 \end{pmatrix}, \quad B = \begin{pmatrix} 1 & -1 \\ 0 & 1 \\ 0 & 0 \\ \vdots & \vdots \\ 0 & 0 \\ 0 & 0 \end{pmatrix} \tag{7.49}$$

(m is the mass and k the stiffness of a single floor). The natural frequency of mode l is given by

$$\omega_l = 2\sqrt{\frac{k}{m}} \sin[\frac{\pi}{2}\frac{(2l-1)}{(2n+1)}] \ , \ l = 1, \cdots, n \tag{7.50}$$

where n is the number of storeys (for the calculations, one can normalize according to $\Omega = \sqrt{k/m} = 1$). Consider the lead compensator

$$H(s) = g\frac{1+Ts}{1+\alpha Ts} \qquad (\alpha < 1) \tag{7.51}$$

and select the parameters T and α to control properly at least the first 3 modes of the system.

(a) Consider a single control loop in the first floor. Compute the transmission zeros, draw the root locus and select a reasonable value of the gain; evaluate the active damping obtained in the 3 targeted modes.

(*b*) *Consider the decentralized control with two independent loops with the same gain. Compute the transmission zeros, draw the root locus and compare it to the previous one; select a reasonable value of the gain and evaluate the active damping obtained for the 3 targeted modes.*

(c) For the single loop controller, evaluate the effect of a band limited actuator by including a low-pass filter (7.37) with a corner frequency $\omega_a = \omega_5$ *and* $\xi_a = 0.7$. *Comment on the feasibility of such a control system.*

P.7.7 *Consider again the seven-story shear frame of Fig.7.18 with one or two active struts in the first two floors; the stiffness* K_a *of the strut is such that* $K_a/k = 5$. *The active struts are equipped with a displacement actuator and a force sensor pair and are controlled in a decentralized manner with the IFF controller:*

$$H(s) = g/s \tag{7.52}$$

(a) Consider a single control loop in the first floor. Compute the open-loop poles and the transmission zeros, draw the root locus and select a reasonable value of the gain; evaluate the active damping obtained in the 3 targeted modes.

(*b*) *Consider the decentralized control with two independent loops with the same gain. Compute the open-loop poles and the transmission zeros, draw the root locus and compare it to the previous one; select a reasonable value of the gain and evaluate the active damping obtained for the 3 targeted modes.*

(c) For the single loop controller, evaluate the effect of a band limited actuator by including a low-pass filter (7.37) with a corner frequency $\omega_a = \omega_5$ *and* $\xi_a = 0.7$. *Comment on the feasibility of such a control system and compare to the previous problem.*

8

Vibration isolation

8.1 Introduction

There are two broad classes of problems in which vibration isolation is necessary: *(i)* Operating equipments generate oscillatory forces which can propagate into the supporting structure (Fig.8.1.a). This situation corresponds to that of an engine in a car. *(ii)* Sensitive equipments may be supported by a structure which vibrates appreciably (Fig.8.1.b); in this case, it is the support motion which constitutes the source of excitation; this situation corresponds to, for example, a telescope in a spacecraft, a wafer stepper or a precision machine tool in a workshop, or a passenger seated in a car.

The disturbance may be either deterministic, such as the unbalance of a motor, or random as in a passenger car riding on a rough road. For deterministic sources of excitation which can be measured, such as

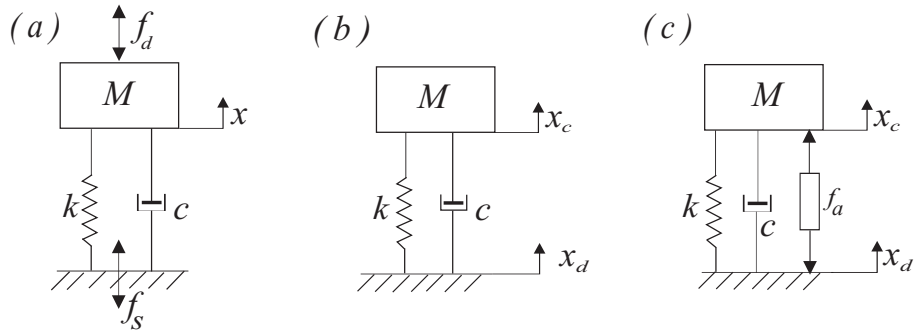

Fig. 8.1. (a) Operating equipment generating a disturbance force f_d. (b) Equipment subjected to a support excitation x_d. (c) Active isolation device.

a rotating unbalance, *feedforward* control can be very effective (see for example chapter 7 of Fuller's book).[1] However, the present chapter is focused on the *feedback* strategies for active isolation; they apply to both deterministic and random disturbances, and they do not need a direct measurement of the disturbance.

Let us begin with the system depicted in Fig.8.1.a, excited by a disturbance force f_d. If the support is fixed, the governing equation is:

$$M\ddot{x} + c\dot{x} + kx = f_d \tag{8.1}$$

The force transmitted to the support is given by

$$f_s = kx + c\dot{x} \tag{8.2}$$

In the Laplace domain,

$$X(s) = \frac{F_d(s)}{M(s^2 + 2\xi\omega_n s + \omega_n^2)} \tag{8.3}$$

$$F_s(s) = M(\omega_n^2 + 2\xi\omega_n s)X(s) \tag{8.4}$$

where $X(s), F_d(s)$ and $F_s(s)$ stand for the Laplace transform of respectively $x(t), f_d(t)$ and $f_s(t)$, and with the usual notations $\omega_n^2 = k/M$ and $2\xi\omega_n = c/M$. The *transmissibility* of the support is defined in this case as the transfer function between the disturbance force f_d applied to the mass and the force f_s transmitted to the support structure; combining the foregoing equations, we get

$$\frac{F_s(s)}{F_d(s)} = \frac{1 + 2\xi s/\omega_n}{1 + 2\xi s/\omega_n + s^2/\omega_n^2} \tag{8.5}$$

Next, consider the second situation illustrated in Fig.8.1.b; the disturbance is the displacement x_d of the supporting structure and the system output is the displacement x_c of the sensitive equipment. Proceeding in a similar way, it is easily established that the transmissibility of this isolation system, defined in this case as the transfer function between the support displacement and the absolute displacement of the mass M, is given by (Problem 8.1)

$$\frac{X_c(s)}{X_d(s)} = \frac{1 + 2\xi s/\omega_n}{1 + 2\xi s/\omega_n + s^2/\omega_n^2} \tag{8.6}$$

[1] In feedforward control, it is not necessary to measure directly the disturbance force, but rather a signal which is correlated to it, such as the rotation velocity, if the disturbance results from a rotating unbalance.

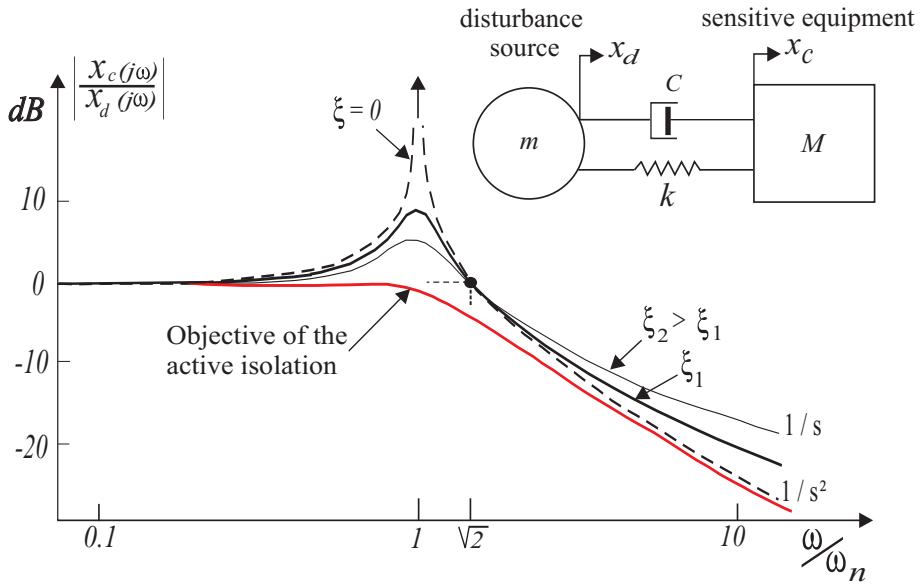

Fig. 8.2. Transmissibility of the passive isolator for various values of the damping ratio ξ. The performance objectives of active isolation are a high frequency decay like s^{-2} together with no overshoot at resonance.

which is identical to the previous one; the two isolation problems can therefore be treated in parallel. The amplitude of the corresponding FRF, for $s = j\omega$, is represented in Fig.8.2 for various values of the damping ratio ξ. We observe that: *(i)* All the curves are larger than 1 for $\omega < \sqrt{2}\ \omega_n$ and become smaller than 1 for $\omega > \sqrt{2}\ \omega_n$. Thus the critical frequency $\sqrt{2}\ \omega_n$ separates the domains of amplification and attenuation of the isolator. *(ii)* When $\xi = 0$, the high frequency decay rate is s^{-2}, that is -40 *dB/decade*, while very large amplitudes occur near the corner frequency ω_n (the natural frequency of the spring-mass system).

Figure 8.2 illustrates the trade-off in passive isolator design: large damping is desirable at low frequency to reduce the resonant peak while low damping is needed at high frequency to maximize the isolation. One may already observe that if the disturbance is generated by a rotating unbalance of a motor, there is an obvious benefit to use a damper with variable damping characteristics which can be adjusted according to the rotation velocity: high when $\omega < \sqrt{2}\omega_n$ and low when $\omega > \sqrt{2}\omega_n$. Such variable (*adaptive*) devices will be discussed in chapter 17. Figure 8.2 also shows the target of an *active* isolation system which combines a decay rate of -40 *dB/decade* with no overshoot at resonance. Before addressing

the active isolation, the following section discusses one way of improving the high frequency isolation in a passive way.

8.2 Relaxation isolator

In the *relaxation* isolator, the viscous damper c is replaced by a Maxwell unit consisting of a damper c and a spring k_1 in series (Fig.8.3.a). The governing equations are

$$M\ddot{x} + k(x - x_0) + c(\dot{x} - \dot{x}_1) = 0 \tag{8.7}$$

$$c(\dot{x} - \dot{x}_1) = k_1(x_1 - x_0) \tag{8.8}$$

or, in matrix form using the Laplace variable s,

$$\begin{bmatrix} Ms^2 + cs + k & -cs \\ -cs & k_1 + cs \end{bmatrix} \begin{Bmatrix} x \\ x_1 \end{Bmatrix} = \begin{Bmatrix} k \\ k_1 \end{Bmatrix} x_0 \tag{8.9}$$

It follows that the transmissibility reads

$$\frac{x}{x_0} = \frac{(k_1 + cs)k + k_1 cs}{(Ms^2 + cs + k)(k_1 + cs) - c^2 s^2} = \frac{(k_1 + cs)k + k_1 cs}{(Ms^2 + k)(k_1 + cs) + k_1 cs} \tag{8.10}$$

One sees that the asymptotic decay rate for large frequencies is in s^{-2}, that is -40 *dB/decade*. Physically, this corresponds to the fact that, at high frequency, the viscous damper tends to be blocked, and the system

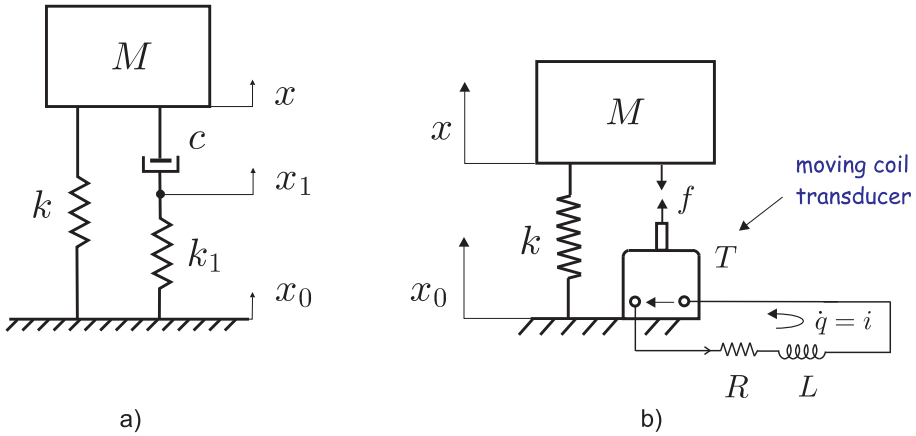

Fig. 8.3. (a) Relaxation isolator. (b) Electromagnetic realization.

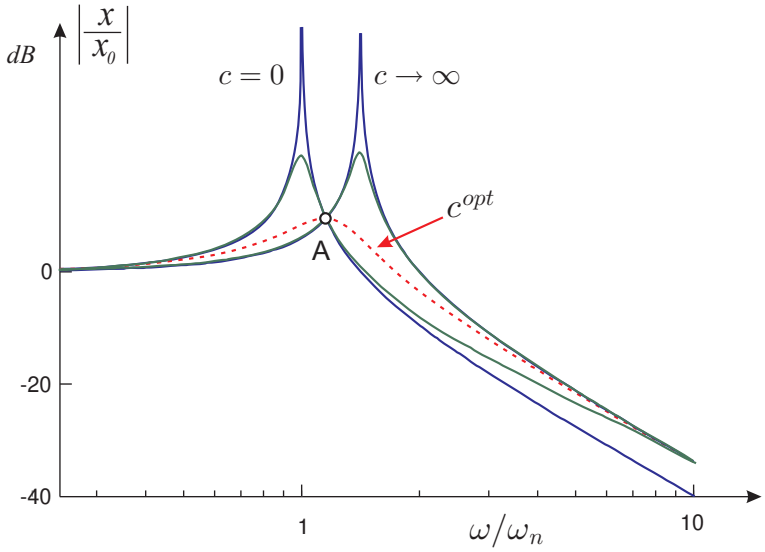

Fig. 8.4. Transmissibility of the relaxation oscillator for fixed values of k and k_1 and various values of c. The first peak corresponds to $\omega = \omega_n$; the second one corresponds to $\omega = \Omega_n$. All the curves cross each other at A and have an asymptotic decay rate of -40 *dB/decade*. The curve corresponding to c_{opt} is nearly maximum at A.

behaves like a undamped isolator with two springs acting in parallel. Figure 8.4 compares the transmissibility curves for given values of k and k_1 and various values of c. For $c = 0$, the relaxation isolator behaves like an undamped isolator of natural frequency $\omega_n = (k/M)^{1/2}$. Likewise, for $c \to \infty$, it behaves like an undamped isolator of frequency $\Omega_n = [(k + k_1)/M]^{1/2}$. In between, the poles of the system are solution of the characteristic equation

$$(Ms^2 + k)(k_1 + cs) + k_1 cs = (Ms^2 + k)k_1 + cs(Ms^2 + k + k_1) = 0$$

which can be rewritten in root locus form

$$1 + \frac{k_1}{c} \frac{s^2 + \omega_n^2}{s(s^2 + \Omega_n^2)} = 0 \tag{8.11}$$

It is very similar to (7.31); it is represented in Fig.8.5 when c varies from 0 to ∞; using the results of section 7.5, the maximum damping ratio is achieved for

$$\frac{k_1}{c} = \frac{\Omega_n^{3/2}}{\omega_n^{1/2}} \tag{8.12}$$

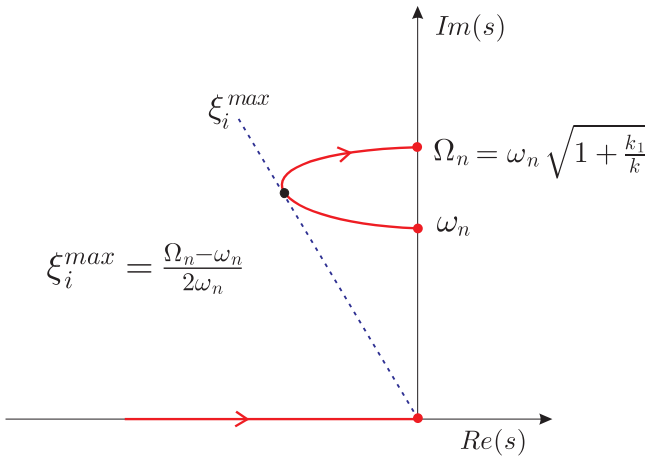

Fig. 8.5. Root locus of the solutions of Equ.(8.11) as c goes from zero to infinity. The maximum damping is achieved for $k_1/c = \Omega_n^{3/2}\omega_n^{-1/2}$.

and the corresponding damper constant is

$$c_{opt} = \frac{k_1}{\Omega_n}(\frac{\omega_n}{\Omega_n})^{1/2} = \frac{k_1}{\Omega_n}(1 + \frac{k_1}{k})^{-1/4} = \frac{k_1}{\omega_n}(1 + \frac{k_1}{k})^{-3/4} \tag{8.13}$$

The transmissibility corresponding to c_{opt} is also represented in Fig.8.4; it is nearly maximum at A.

8.2.1 Electromagnetic realization

The principle of the relaxation isolator is simple and it can be realized with viscoelastic materials. However, it may be difficult to integrate in the system, and also to achieve thermal stability. In some circumstances, especially when thermal stability is critical, it may be more convenient to achieve the same effect through an electromechanical converter which consists of a voice coil transducer, an inductor L and a resistor R.

A voice coil transducer is an energy converter transforming mechanical energy into electrical energy and vice-versa; its constitutive equations are given by Equ.(3.1) to (3.3).

Referring to Fig.8.3.b, the governing equations of the system are

$$M\ddot{x} + k(x - x_0) - Ti = 0 \tag{8.14}$$

$$L\frac{di}{dt} + T(\dot{x} - \dot{x}_0) + Ri = 0 \tag{8.15}$$

where T is the transducer constant; in matrix form, using the Laplace variable,

$$\begin{bmatrix} Ms^2+k & -T \\ Ts & Ls+R \end{bmatrix} \begin{Bmatrix} x \\ i \end{Bmatrix} = \begin{Bmatrix} k \\ Ts \end{Bmatrix} x_0 \tag{8.16}$$

It follows that the transmissibility reads

$$\frac{x}{x_0} = \frac{(Ls+R)k + T^2 s}{(Ms^2+k)(Ls+R) + T^2 s} \tag{8.17}$$

Comparing with Equ.(8.10), one sees that the electromechanical isolator behaves exactly like a relaxation isolator provided that

$$\frac{Ls+R}{T^2} = \frac{cs+k_1}{k_1 c} \tag{8.18}$$

or

$$k_1 = \frac{T^2}{L} \qquad c = \frac{T^2}{R} \tag{8.19}$$

These are the two relationships between the three parameters T, L and R so that the transmissibility of the electromechanical system of Fig.8.3.b is the same as that of Fig.8.3.a.

8.3 Active isolation

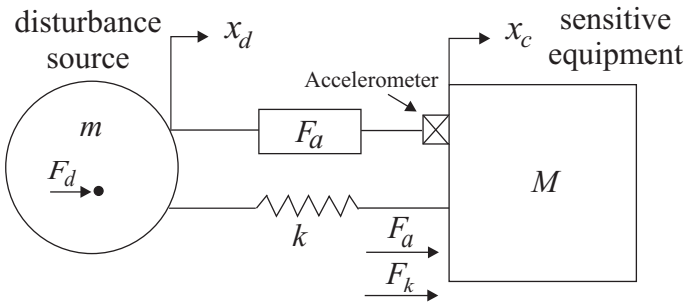

Fig. 8.6. Single-axis active isolator.

Consider the single-axis isolator connecting a disturbance source m to a payload M (Fig.8.6). It consists of a soft spring k in parallel with a force actuator f_a; the objective is to isolate the motion x_c of the payload M

from the motion x_d of m due to the disturbance load f_d. The governing equations are

$$M\ddot{x}_c + k(x_c - x_d) = f_a \tag{8.20}$$

$$m\ddot{x}_d + k(x_d - x_c) = f_d - f_a \tag{8.21}$$

or, in matrix form using the Laplace variable s,

$$\begin{bmatrix} Ms^2 + k & -k \\ -k & ms^2 + k \end{bmatrix} \begin{Bmatrix} X_c \\ X_d \end{Bmatrix} = \begin{Bmatrix} F_a \\ F_d - F_a \end{Bmatrix} \tag{8.22}$$

Upon inverting this equation, one gets

$$X_c = \frac{kF_d}{s^2[Mms^2 + (M+m)k]} + \frac{mF_a}{Mms^2 + (M+m)k} \tag{8.23}$$

The first term of this expression describes the payload response to the disturbance load while the second term is the payload response to the actuator. If an accelerometer or a geophone is attached to the payload, measuring the absolute acceleration $\ddot{x}_c$ or the absolute velocity $\dot{x}_c$, the open-loop transfer function is

$$G(s) = \frac{s^2 X_c}{F_a} = \frac{ms^2}{Mms^2 + (M+m)k} \tag{8.24}$$

Consider the closed-loop response to a general feedback law based on the absolute velocity $\dot{x}_c$:

$$F_a = -H(s)sX_c(s) \tag{8.25}$$

Introducing this into (8.22), one gets

$$\begin{bmatrix} Ms^2 + H(s)s + k & -k \\ -k - H(s)s & ms^2 + k \end{bmatrix} \begin{Bmatrix} X_c \\ X_d \end{Bmatrix} = \begin{Bmatrix} 0 \\ F_d \end{Bmatrix} \tag{8.26}$$

Upon considering the first line of this equation, one finds easily that the closed-loop transmissibility is

$$\frac{X_c}{X_d} = \frac{k}{Ms^2 + H(s)s + k} \tag{8.27}$$

8.3.1 Sky-hook damper

Equation (8.27) shows the influence of the feedback control law on the transmissibility; it shows that a simple velocity feedback, $H(s) = g$ leads to the transmissibility

$$\frac{X_c}{X_d} = \frac{k}{Ms^2 + gs + k} = \frac{1}{s^2/\omega_n^2 + gs/k + 1} \tag{8.28}$$

which complies with the objectives of active isolation stated in Fig.8.2, because the asymptotic decay rate is in s^{-2} (i.e. -40 *dB/decade*) and the overshoot at resonance may be controlled by adjusting the gain g of the controller to achieve critical damping. This control law is called *sky-hook*, because the control force $f_a = -g\dot{x}_c$ is identical to that of a viscous damper of constant g attached to the payload and a fixed point in space (the sky), Fig.8.7.

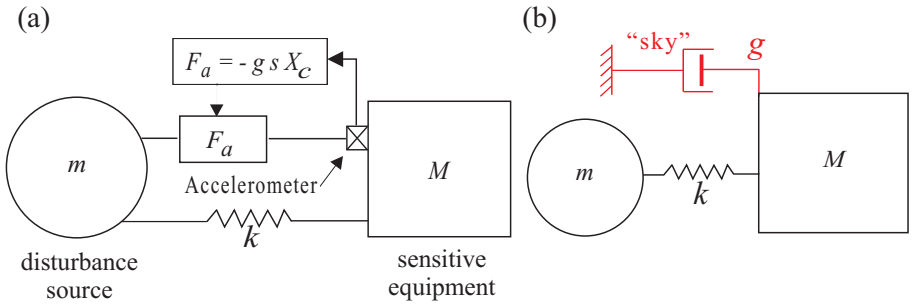

Fig. 8.7. (a) Isolator with absolute velocity feedback. (b) Equivalent *sky-hook* damper.

The open-loop transfer function between the input force f_a and the output acceleration $\ddot{x}_c$ is given by (8.24); it has a pair of imaginary poles at

$$p_i = \pm j\sqrt{\frac{(M+m)k}{Mm}} \tag{8.29}$$

and a pair of zeros at the origin. The root-locus of the sky-hook is shown in Fig.8.8; it is entirely contained in the left-half plane, which means that the sky-hook damper is unconditionally stable (infinite gain margin).

8.3.2 Integral Force feedback

We have just seen that the sky-hook damper based on the absolute velocity of the payload is unconditionally stable for a rigid body. However,

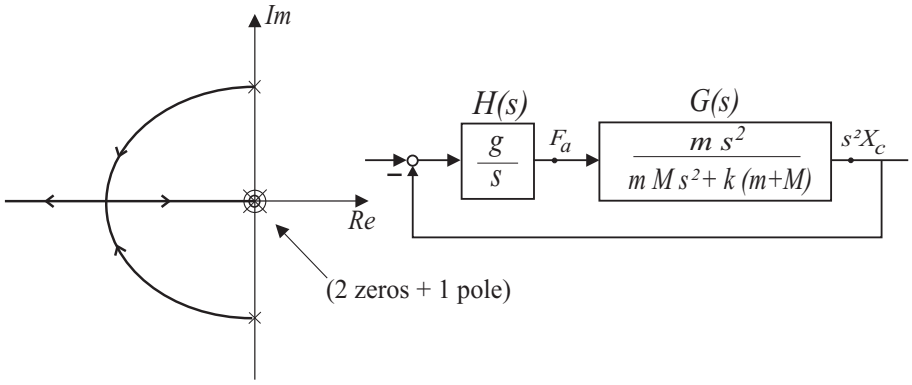

Fig. 8.8. Root-locus of the *sky-hook* damper.

this is no longer true if the payload cannot be regarded as a rigid body, situation which is frequently met in space applications. Since the absolute acceleration of a rigid body is proportional to the force applied to it, $F = M\ddot{x}_c$, the acceleration feedback of Fig.8.7 may be replaced by a force feedback as shown in Fig.8.9. Note that, besides the advantage of achieving alternating poles and zeros discussed here, a force sensor may be more sensitive than an accelerometer in low frequency applications; for example, a force sensor with a sensitivity of $10^{-3}N$ is common place; for a mass M of 1000 kg (e.g. a space telescope), this corresponds to an acceleration of $10^{-6}m/s^2$; such a sensitivity is more difficult to achieve. Force sensing is especially attractive in micro-gravity where one does not have to consider the dead loads of a structure. The open-loop transfer function is, in this case

$$G(s) = \frac{F}{F_a} = \frac{Mms^2}{Mms^2 + (M+m)k} \tag{8.30}$$

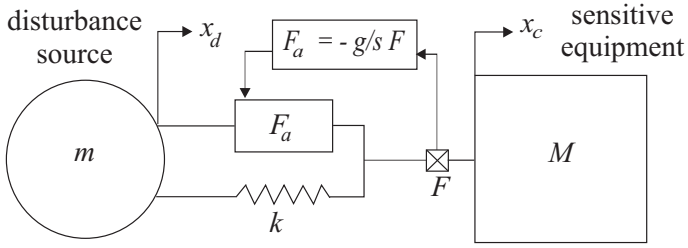

Fig. 8.9. Sky-hook based on a force sensor (F is taken positive when it is acting in the direction of x_c on mass M).

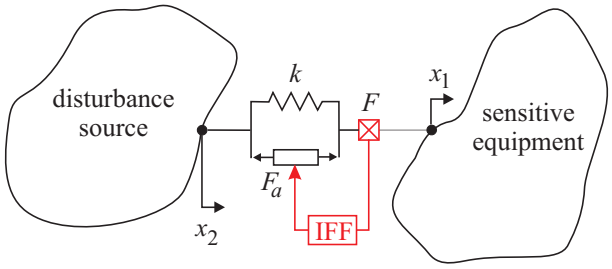

Fig. 8.10. Arbitrary flexible structures connected by a single-axis isolator with force feedback.

which has the same pole/zero pattern and the same root-locus as Fig.8.8. However, when the payload is flexible, the force applied and the acceleration are no longer proportional and the pole/zero pattern may differ significantly. It can be observed that the feedback based on the acceleration still leads to alternating poles and zeros in the open-loop transfer function when the flexible modes are significantly above the suspension mode, but they do not alternate any more when the flexible modes interact with the suspension mode. On the contrary, *if two arbitrary undamped flexible bodies are connected by a single-axis isolator with force feedback, the poles and zeros of the open-loop transfer function F/F_a always alternate on the imaginary axis* (Fig.8.10).

This result is not obvious, because the actuator F_a and the sensor F, if collocated, are not *dual* as requested for alternating poles and zeros (as emphasized in previous chapters); it can be demonstrated as follows: The system with input F_a and output the relative displacement between the two bodies, $\Delta x = x_1 - x_2$ is collocated and *dual*; therefore, the FRF (which is purely real in the undamped case) exhibits alternating poles and zeros (full line in Fig.8.11). On the other hand, the control force F_a, the relative displacement Δx and the output (total) force F are related by

$$F = k\Delta x - F_a \tag{8.31}$$

(in this equation, F is assumed positive in traction while F_a is positive when it tends to separate the two bodies). It follows that the FRF F/F_a and $\Delta X/F_a$ are related by

$$\frac{F}{F_a} = \frac{k\Delta X}{F_a} - 1 \tag{8.32}$$

This equation states that the FRF with force sensor, F/F_a, can be obtained from that with relative displacement sensor, $k\Delta X/F_a$ by a simple

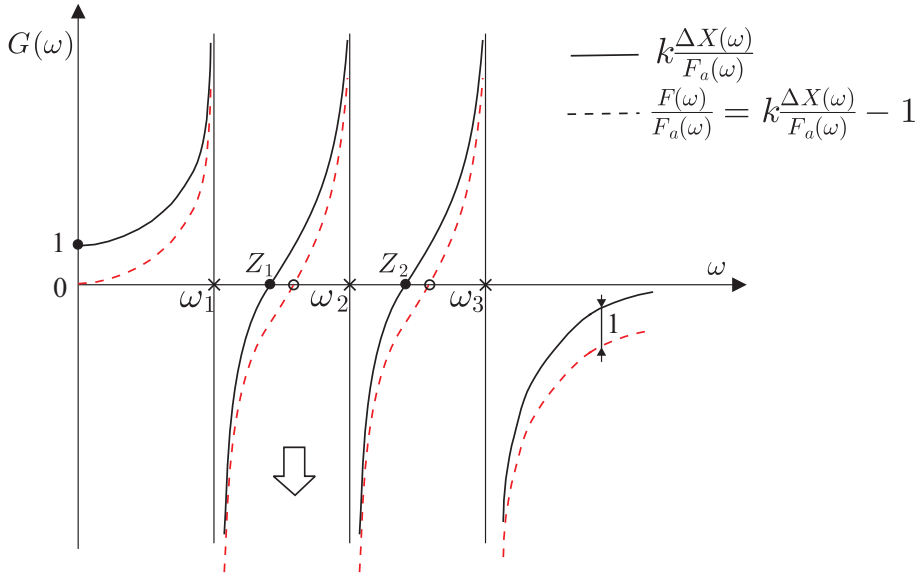

Fig. 8.11. FRFs of the single-axis oscillator connecting two arbitrary flexible structures. The full line corresponds to $k\Delta X/F_a$ and the dotted line to F/F_a; it is obtained by vertical translation of the full line by -1.

vertical translation bringing the amplitude to 0 at $\omega = 0$ (from the full line to the dotted line). This changes the locations of the zeros Z_i but the continuity of the FRF curve between two resonances guarantees that there is a zero between two consecutive poles (natural frequencies):

$$\omega_i < Z_i < \omega_{i+1} \tag{8.33}$$

8.4 Flexible body

When the payload is flexible, the behavior of the acceleration feedback and the force feedback are no longer the same, due to different poles/zeros configurations of the two control strategies. In fact, different sensor configurations correspond to different locations of the zeros in the s-plane. To analyze this situation, consider the payload with a flexible appendage of Fig.8.12; the nominal numerical values used in the calculations are $m = 1.1kg$, $M = 1.7kg$, $k = k_1 = 12000N/m$, $c_1 = 0$; the mass m_1 of the flexible appendage is taken as a parameter to analyze the interaction between the flexible appendage and the isolation system. When m_1 is small, the flexible appendage is much more rigid than the isolation system and

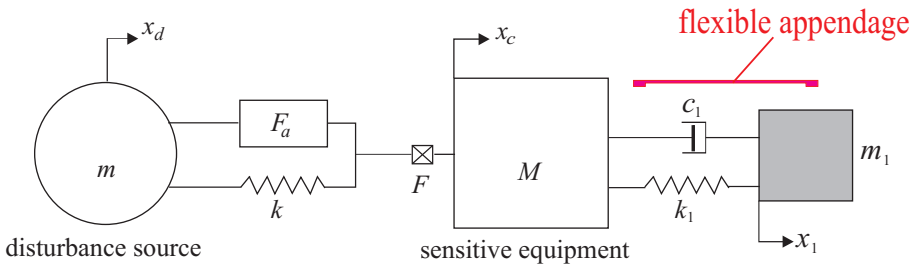

Fig. 8.12. Payload with a flexible appendage.

the situation is not much different from that of a rigid body. Figure 8.13 shows the root locus plots for $m_1 = 0.5kg$; the acceleration feedback and the force feedback have similar root locus plots, with a new pole/zero pair appearing higher on the imaginary axis; the poles and zeros still alternate on the imaginary axis and the only difference between the two plots is the distance between the pole and the zero which is larger for the acceleration feedback; as a result, the acceleration feedback produces a larger damping of the higher mode.

By contrast, when m_1 is large, the root locus plots are reorganized as shown in Fig.8.14 for $m_1 = 3.5kg$. For force feedback, the poles and zeros still alternate on the imaginary axis, leading to a stable root locus; this property is lost for the acceleration feedback, leading to an unstable loop for the lower mode. In practice, however, this loop is moved slightly to the left by the structural damping, and the control system can still operate with small gains (conditionally stable).

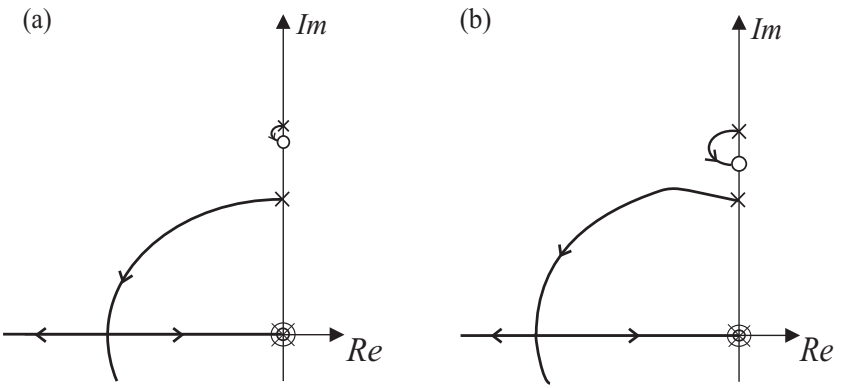

Fig. 8.13. Root locus of the isolation system with a light flexible appendage ($m_1 = 0.5kg$). (a) Force feedback. (b) Acceleration feedback.

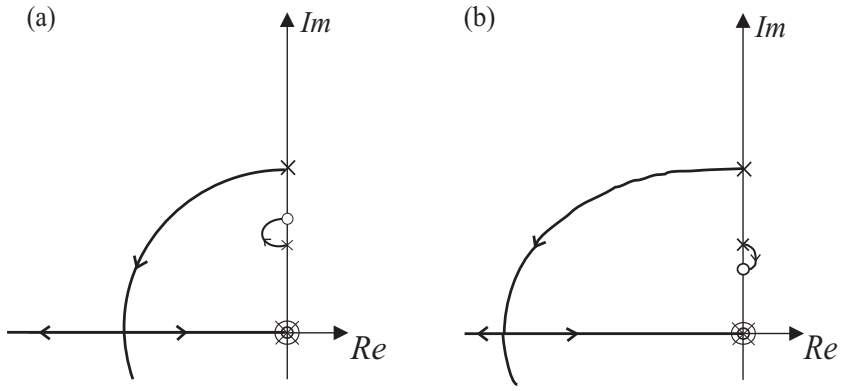

Fig. 8.14. Root locus of the isolation system with a heavy flexible appendage ($m_1 = 3.5kg$). (a) Force feedback. (b) Acceleration feedback.

8.4.1 Free-free beam with isolator

To analyze a little further the situation when the payload is flexible, consider the vertical isolation of a free-free continuous beam from the disturbance of a body of mass m, Fig.8.15.a. This situation is representative of a large space structure with its attitude control system attached to m (the disturbance is created by the unbalance of the rotating wheels). Note that the rigid body modes are uncontrollable from the internal force F_a. In the numerical example described below, the length of the beam is $l = 5m$, the mass per unit length is $\varrho = 2kg/m$, the stiffness of the isolator is $k = 1N/m$ and the mass where the disturbance is applied is $m = 1kg$; the stiffness EI of the beam is taken as a parameter.

Let Ω_i be the natural frequencies of the flexible modes of the free-free beam alone, Fig.8.15.b and Z_i be the transmission zeros corresponding to a force excitation and a collocated displacement sensor (or equivalently acceleration). According to what we have seen in the previous chapters, Z_i are the natural frequencies of the system with an additional restraint at the connecting degree of freedom of the isolator. Because of the collocation, the poles and zeros are alternating on the imaginary axis, so that Ω_i and Z_i satisfy

$$Z_i < \Omega_i < Z_{i+1} \tag{8.34}$$

Next, consider the complete system (beam + mass m) and let ω_i be its natural frequencies (flexible mode only, because the rigid body modes are not controllable from the internal force F_a). If the control system uses a force sensor, Fig.8.15.d, the transmission zeros, obtained by enforcing a

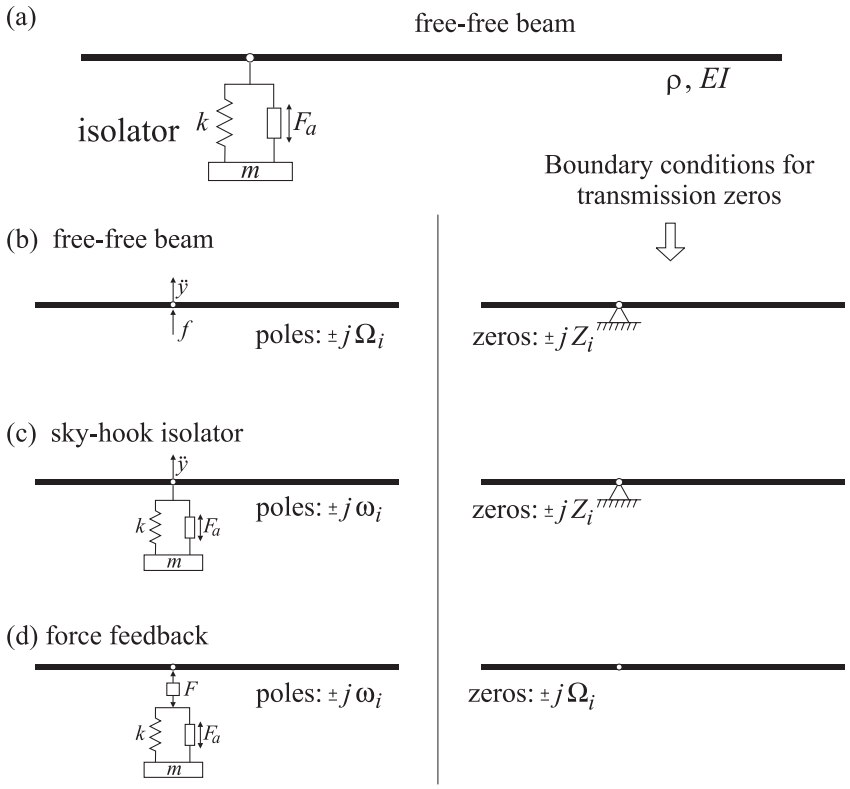

Fig. 8.15. (a) Free-free beam and single axis isolator. The other figures illustrate the various situations and the boundary conditions corresponding to the transmission zeros. (b) Free-free beam with displacement sensor and point force actuator. (c) Free-free beam and sky-hook isolator. (d) Free-free beam and isolator with force feedback.

zero force at the connecting d.o.f., are identical to the natural frequencies of the system when the isolator is disconnected from the beam; which are identical to the natural frequencies Ω_i of the free-free beam. The configuration is exactly that of Fig.8.10 and, accordingly, the open-loop FRF has alternating poles and zeros and the following relation holds:

$$\omega_i < \Omega_i < \omega_{i+1} \tag{8.35}$$

This condition guarantees the stability of the closed-loop system when a force feedback is used.

With an acceleration feedback (sky-hook damper, Fig.8.15.c, the poles are still $\pm j\omega_i$ while the zeros, obtained by enforcing a zero acceleration at

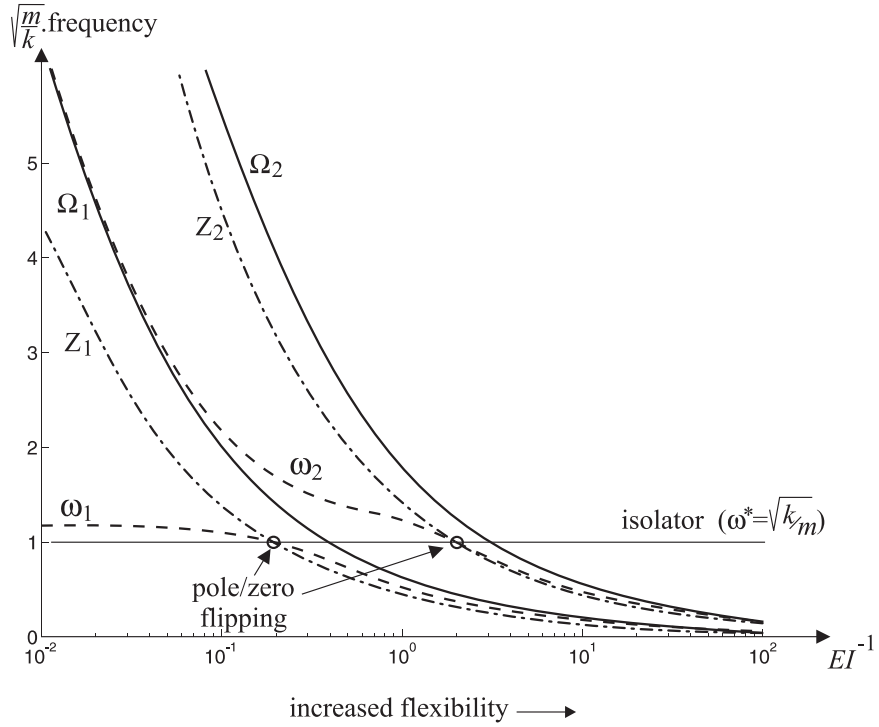

Fig. 8.16. Flexible beam with an isolator; evolution of ω_i,Z_i and ω_i with the flexibility of the beam.

the connecting d.o.f. are $\pm jZ_i$, as for the free-free beam of Fig.8.15.b. This actuator/sensor configuration is no longer collocated, so that no condition similar to (8.34) or (8.35) holds between ω_i and Z_i. When the beam is stiff, the interlacing property $\omega_i < Z_i < \omega_{i+1}$ is satisfied and the stability is guaranteed, but as the beam becomes more flexible, the values of ω_i and Z_i decrease at different rates and a pole/zero flipping occurs when they both become equal to the natural frequency of the isolator ($\omega^* = \sqrt{k/m}$), Fig.8.16. As a result, the system is no longer unconditionally stable when the flexibility is such that $\omega_1 = Z_1 = \omega^* = \sqrt{k/m}$, and above.

As a conclusion to this section, it seems that the sky-hook damper implementation (acceleration feedback) is preferable when the payload is fairly stiff as compared to the isolator corner frequency (e.g. car suspension), to benefit from the better active damping properties of the flexible modes (Fig.8.13). On the contrary, the force feedback implementation is preferable when the payload is very flexible (e.g. space structure), to ben-

efit from the interlacing of the poles and zeros, leading to guaranteed stability.

8.5 Payload isolation in spacecrafts

Space telescopes and precision payloads are subject to jitter due to the unbalanced masses of the attitude control reaction wheels or gyros. The performance of the instruments may be improved by inserting one or several isolators in the transmission path between the disturbance source and the payload. If the isolator is designed in such a way that its transmissibility exhibits a decay rate of $-40dB/decade$, the jitter can be reduced by a factor 100 by selecting the isolator corner frequency, f_0, one decade lower than the first flexible mode of the payload, f_n (Fig.8.17). Extremely sensitive payloads may even involve several isolation layers. [2]

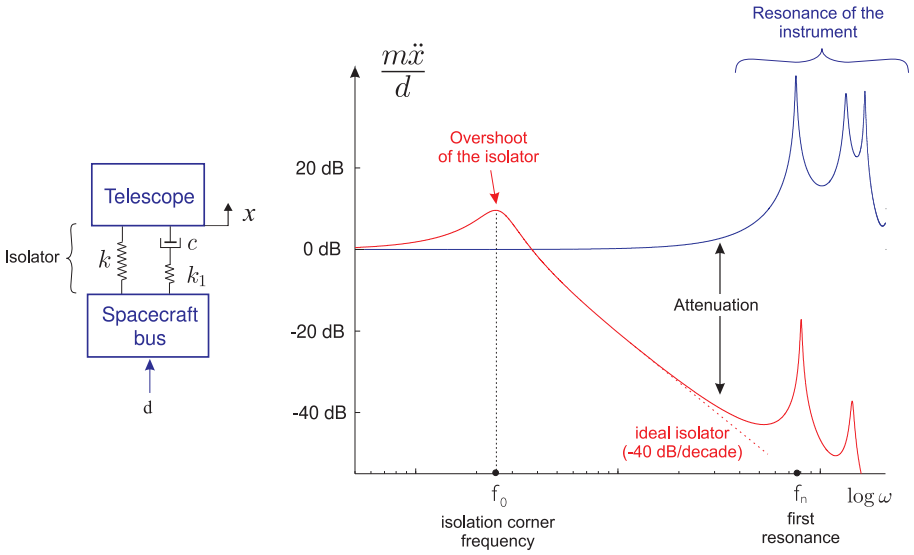

Fig. 8.17. Effect of the isolator on the transmissibility between the spacecraft bus and the telescope.

[2] The future James Webb Space Telescope, JWST will involve two isolation layers, *(i)* the wheel isolator supporting six reaction wheels, with corner frequencies at 7 Hz for rocking and 12 Hz for translation and *(ii)* a 1 Hz passive isolator at the interface between the telescope deployment tower and the spacecraft bus (Bronowicki).

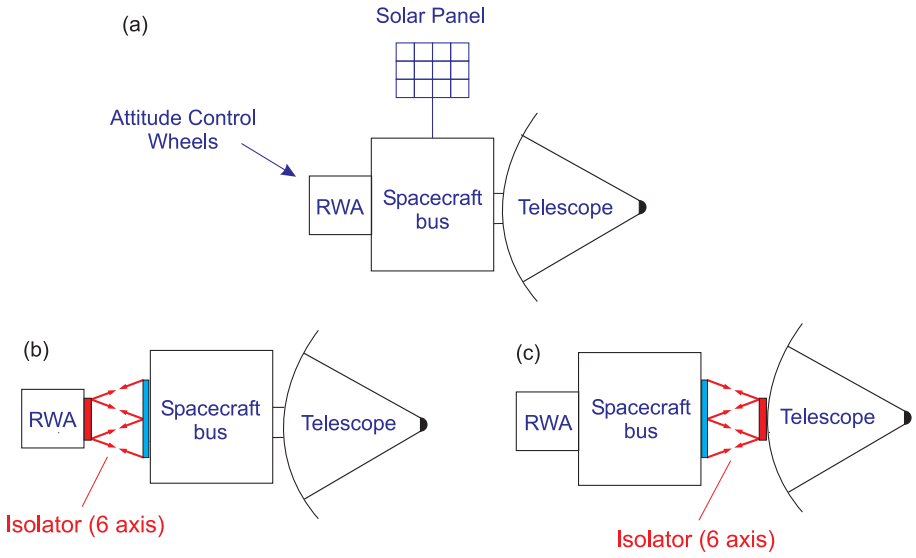

Fig. 8.18. Spacecraft architecture. (a) Without isolator. (b) Isolator placed between the Reaction Wheel Assembly (RWA) and and the spacecraft bus. (c) Isolator between the spacecraft bus and the telescope.

8.5.1 Interaction isolator/attitude control

There are several possible locations for the isolator, depending on the spacecraft architecture (Fig.8.18). If the attitude control wheels are packed in a single assembly (RWA), the isolator may be placed between the RWA and the spacecraft bus, Fig.8.18.b. Another option consists in placing the isolator between the spacecraft bus and the instrument, Fig.8.18.c; in this alternative, the rotating wheels are rigidly attached to the spacecraft bus. The additional compliance introduced by the vibration isolator has a major impact on the low frequency dynamics of the system and its interaction with the attitude control system must be taken into account. The most favorable situation is that where the attitude control actuators and the attitude sensors (star trackers) are both rigidly attached to the spacecraft bus (collocated). For non-collocated situations, the stability of the control system requires that the corner frequency f_0 of the isolator be one decade above the attitude control bandwidth, f_c; altogether,

$$f_c \sim 0.1 f_0 \sim 0.01 f_n \tag{8.36}$$

8.5.2 Gough-Stewart platform

To fully isolate two rigid bodies with respect to each other, six single-axis isolators judiciously placed are needed. For a number of space applications, generic multi-purpose isolators have been developed with a standard Gough-Stewart platform architecture, in which every leg of the platform consists of a single-axis active isolator, connected to the base plates by spherical joints. In the cubic architecture (Fig.8.19), the legs are mutually orthogonal, which minimizes the cross coupling between them. This configuration is particularly attractive, because it also has uniform stiffness properties and uniform control capability, and it has been adopted in most of the projects.

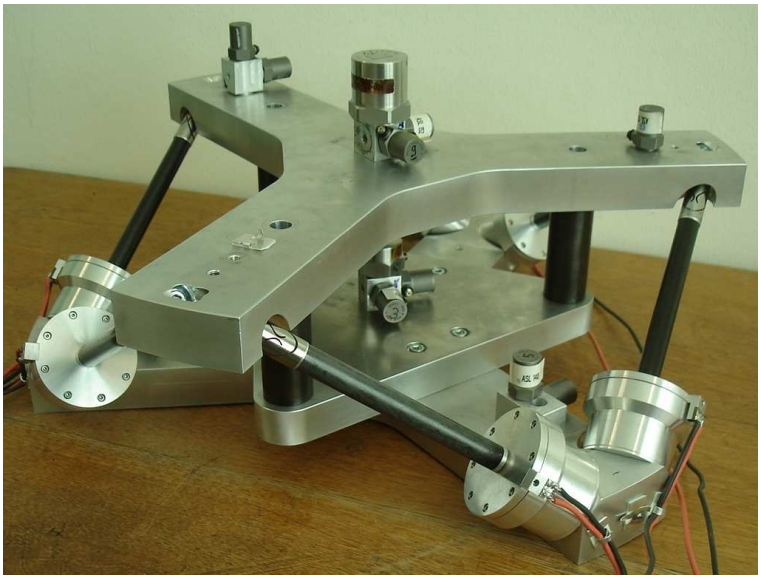

Fig. 8.19. Multi-purpose soft isolator based on a Gough-Stewart platform with cubic architecture (ULB).

8.6 Six-axis isolator

Let us consider a payload isolated by six identical isolators (Fig.8.20); if the isolators consist of simple springs of stiffness k, the six suspension modes are solution of an eigenvalue problem

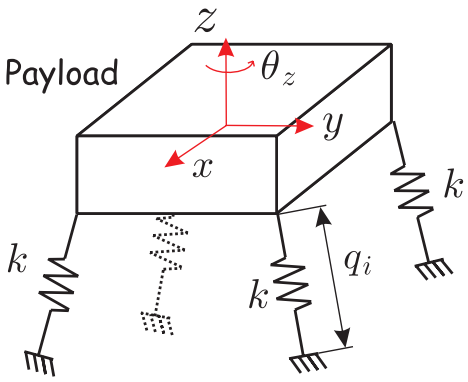

Fig. 8.20. Six-axis isolator (only four legs are represented). The connection between the leg and the support as well as the payload is done with spherical joints. The coordinates of the payload $x = (x, y, z, \theta_x, \theta_y, \theta_z)^T$ and the leg extensions $q = (q_1, \ldots, q_6)^T$ are related by $q = Jx$ where J is the Jacobian of the isolator.

$$(Ms^2 + K)x = 0 \tag{8.37}$$

where x is a vector of 6 coordinates describing the position of the payload, e.g. $x = (x, y, z, \theta_x, \theta_y, \theta_z)^T$. The mass matrix M can be obtained by writing the kinetic energy in terms of $\dot{x}$. Similarly, the stiffness matrix is obtained by writing the strain energy in terms of x. The strain energy in the system is $V = \frac{1}{2}k\, q^T q$, where $q = (q_1, \ldots, q_6)^T$ is the vector of the spring extensions in the isolator and k is the stiffness common to all springs. If J is the Jacobian matrix connecting the spring extensions q to the coordinates x (J depends on the topology of the isolator),

$$q = Jx \tag{8.38}$$

one gets that

$$V = \frac{1}{2}k\; q^T q = \frac{1}{2}k\; x^T J^T J x \tag{8.39}$$

which means that the stiffness matrix is

$$K = kJ^T J \tag{8.40}$$

8.6.1 Relaxation isolator

If the linear spring is replaced by a relaxation isolator, the common stiffness k must be replaced by the appropriate relationship between the spring force F and the spring extension $x - x_0$. From the constitutive

equations of the isolator, Equ.(8.9), one finds that the dynamic stiffness of the relaxation isolator is (Problem 8.5):

$$\frac{F}{x - x_0} = k(s) = k[1 + \frac{k_1 cs}{k(k_1 + cs)}] \tag{8.41}$$

(the stiffness is k at low frequency and k_1 at high frequency). Thus, the (frequency-dependent) stiffness matrix of the six-axis relaxation isolator reads

$$K(s) = J^T J \; k[1 + \frac{k_1 cs}{k(k_1 + cs)}] = K[1 + \frac{k_1 cs}{k(k_1 + cs)}] \tag{8.42}$$

and the eigenvalue problem (8.37) becomes

$$\{Ms^2 + K[1 + \frac{k_1 cs}{k(k_1 + cs)}]\}x = 0 \tag{8.43}$$

If ω_i and $\Phi = (\phi_1, \ldots, \phi_6)$ are the solution of the eigenvalue problem (8.37), normalized according to $\Phi^T M \Phi = I$, one can transform (8.43) into modal coordinates, $x = \Phi z$; using the orthogonality conditions, one finds a set of decoupled equations

$$s^2 + \omega_i^2[1 + \frac{k_1 cs}{k(k_1 + cs)}] = 0 \tag{8.44}$$

Upon introducing

$$\Omega_i^2 = \omega_i^2(1 + \frac{k_1}{k}) \tag{8.45}$$

the previous equation may be rewritten

$$\frac{k_1}{c}(s^2 + \omega_i^2) + s(s^2 + \Omega_i^2) = 0$$

or

$$1 + \frac{k_1}{c}\frac{s^2 + \omega_i^2}{s(s^2 + \Omega_i^2)} = 0 \tag{8.46}$$

which is identical to (8.11). Thus, according to the foregoing equation, the six suspension modes follow independent root-loci connecting ω_i and Ω_i (Fig.8.5). However, k_1/c being a single scalar parameter, the optimal damping cannot be reached simultaneously in the six modes, because of the modal spread ($\omega_1 < \omega_6$).

8.6.2 Integral Force Feedback

If the linear springs are substituted with identical active isolators such as in Fig.8.10, the dynamics of the isolator is governed by

$$M\ddot{x} + Kx = Bu \tag{8.47}$$

where the right hand side is the projection of the six actuator forces, $u = (u_1, \ldots, u_6)^T$ in the global coordinate system attached to the payload. The control forces u_i act in the direction where the leg extension q_i is measured; from the principle of virtual work,

$$(Bu)^T \delta x = u^T \delta q \qquad \longrightarrow \qquad u^T B^T \delta x = u^T J \delta x$$

which implies

$$B = J^T \qquad \text{and} \qquad K = kBB^T \tag{8.48}$$

The force sensor equation is the same as (8.31):

$$y = kq - u \tag{8.49}$$

where $y = (y_1, \ldots, y_6)^T$ is the output vector of the six force sensors; the IFF feedback law is

$$u = \frac{g}{s}\, y \tag{8.50}$$

where an equal gain is assumed for the six independent loops. Combining Equ.(8.47), (8.49) et (8.50), one gets the closed-loop equation

$$(Ms^2 + K)x = \frac{g}{s+g} kBB^T x$$

or

$$(Ms^2 + K\frac{s}{s+g})x = 0 \tag{8.51}$$

If we transform into modal coordinates, $x = \Phi z$, and take into account the orthogonality relationships, the characteristic equation is reduced to a set of uncoupled equations

$$(s^2 + \Omega_i^2 \frac{s}{s+g}) z_i = 0 \tag{8.52}$$

Thus, every mode follows the characteristic equation

$$s^2 + \Omega_i^2 \frac{s}{s+g} = 0$$

or

$$1 + g\frac{s}{s^2 + \Omega_i^2} = 0 \tag{8.53}$$

where Ω_i are the natural frequencies of the six suspension modes. The corresponding root locus is shown in Fig.8.21.a. It is identical to Fig.8.8 for a single-axis isolator; however, unless the 6 natural frequencies are identical, a given value of the gain g will lead to different pole locations for the various modes and it will not be possible to achieve the same damping for all modes. This is why it is recommended to locate the payload in such a way that the spread of the modal frequencies is minimized.

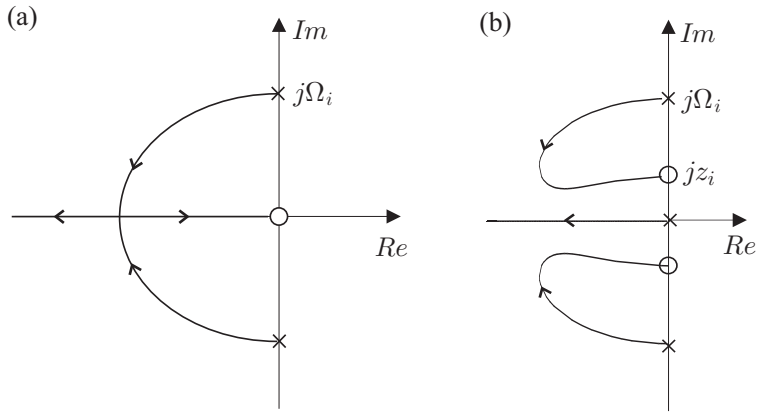

Fig. 8.21. Six-axis active isolator with independent IFF loops: root locus of individual modes. (a) with perfect spherical joints. (b) with flexible joints.

8.6.3 Spherical joints, modal spread

The foregoing results have been obtained with the assumptions that the connections are made by perfect spherical joints, so that the only contribution to the stiffness matrix come from the axial stiffness of the legs, $K = kBB^T$. However perfect spherical joints do not exist and they have friction and backlash. Backlash is not acceptable in precision engineering and the spherical joints are replaced by flexible connections with large longitudinal and shear stiffness and low bending stiffness, such as the one shown in Fig.8.22. This is responsible for an additional contribution K_e to the stiffness matrix. The global stiffness matrix is $kBB^T + K_e$ and the closed-loop equation of the suspension with the IFF controller becomes

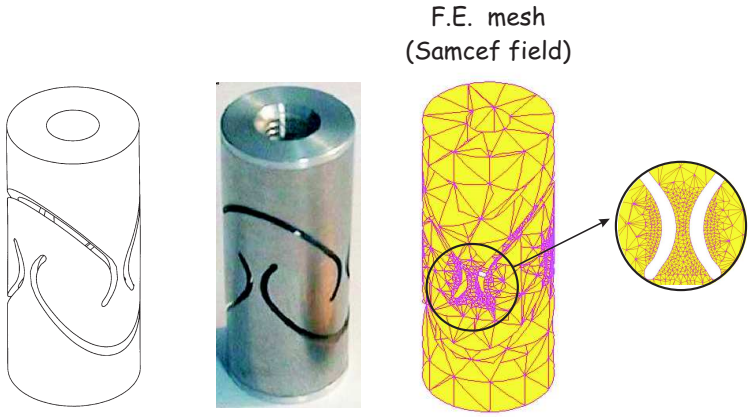

Fig. 8.22. Typical flexible joint for the connections of a six-axis isolator. Its behavior is close to a universal joint, with low bending stiffness while the other d.o.f. are rather stiff.

$$(Ms^2 + K_e + kBB^T \frac{s}{s+g})x = 0 \tag{8.54}$$

According to this equation, the transmission zeros, which are the asymptotic solutions as $g \to \infty$, are no longer at the origin ($s = 0$), but are solutions of the eigenvalue problem

$$[Ms^2 + K_e]x = 0 \tag{8.55}$$

It follows that the zeros are shifted along the imaginary axis, leading to the root locus of Fig.8.21.b, which reduces the performance of the suspension system.

As mentioned before, the six suspension modes have different natural frequencies and the decentralized IFF controller has a single gain g which has to be adjusted to achieve a good compromise in the suspension performance for the six modes. The best performance is achieved if the suspension is designed in such a way that the *modal spread*, Ω_6/Ω_1, is minimized. The combined effect of the modal spread and the joint stiffness is illustrated in Fig.8.23; there are only 4 different curves because of the symmetry of the system. The bullets correspond to the closed-loop poles for a fixed value of g; they illustrate the fact that the various loops are travelled at different speeds as g increases. How this impacts the transmissibility is examined below.

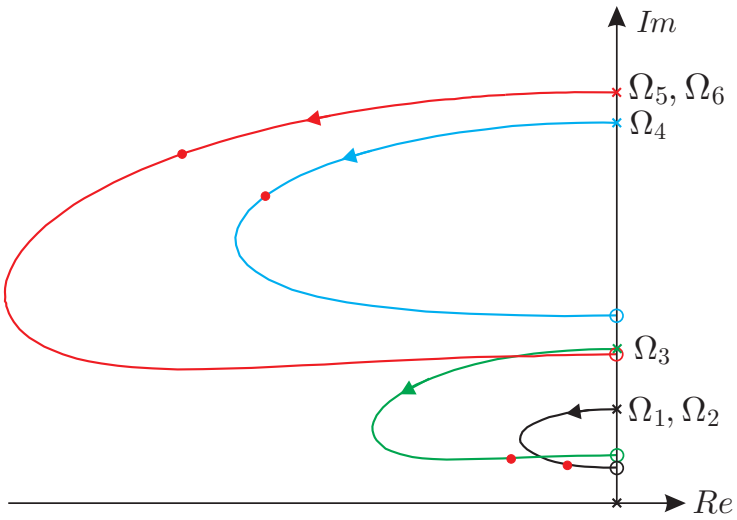

Fig. 8.23. Typical root locus of a complete isolation system with real joints. The bullets indicate the location of the closed-loop poles for the adopted value of the gain g (from Preumont et al., 2007).

8.7 Active vs. passive

Figure 8.24 compares the components involved in the passive relaxation isolator and the active one. The active isolation requires conditioning electronics for the force sensor and power electronics for the voice coil actuator. The relaxation isolator requires only a passive RL circuit but

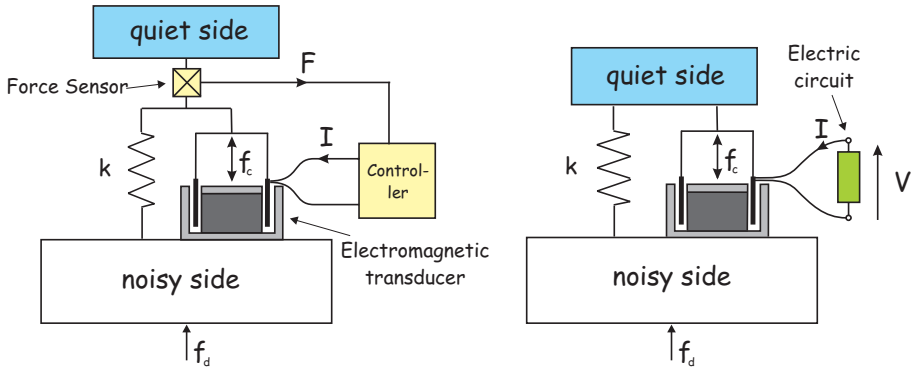

Fig. 8.24. Comparison of the active isolator (left) with the passive isolator (right); if a RL electrical circuit is used, the passive isolator is a relaxation isolator; a purely resistive circuit produces a linear viscous isolator.

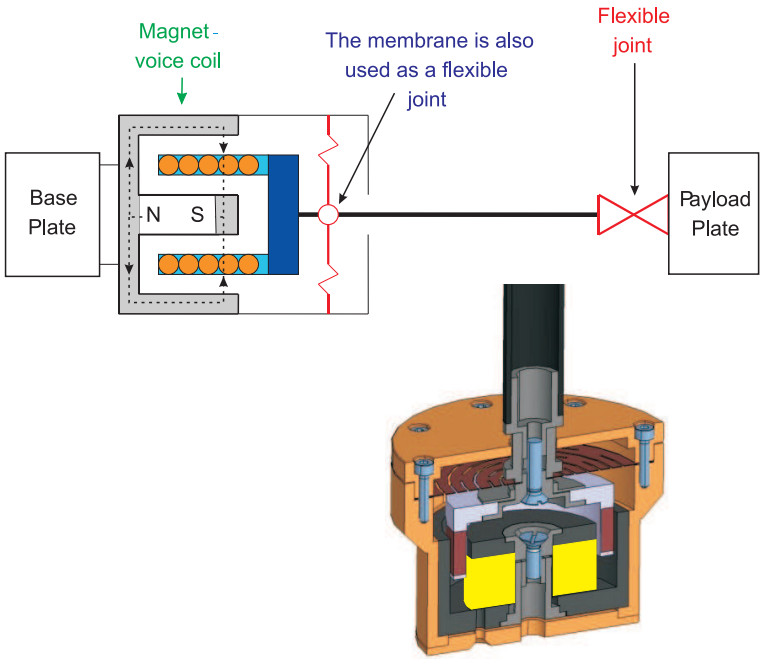

Fig. 8.25. Leg of a passive relaxation isolator; conceptual design and exploded view of the transducer showing the membrane, the magnetic circuit, the voice coil and its connection with the stinger.

also requires a bigger transducer (with a larger transducer constant T). Also, it does not have a force sensor, which makes it lighter. In fact, the legs have their own local dynamics which interfere with that of the isolator and impact significantly the transmissibility in the vicinity of the resonance frequency of the local modes and beyond. Maximizing the natural frequency of the local modes of the legs is a major challenge in the design of a six-axis isolator with broadband isolation capability. This is achieved through careful design of all the components of the isolator. Figure 8.25 shows the leg of a passive relaxation isolator; the exploded view of the transducer shows the membrane which acts as an axial spring and also plays the role of spherical joint, the magnetic circuit and the voice coil, and its connection to the stinger, made of CFRP to minimize its weight.

From the comparison of the root locus plots, of Fig.8.5 and 8.21.b, one would expect that the active isolator would have less overshoot near the resonance frequencies of the suspension. On the other hand, the passive isolator does not need a force sensor, which makes the leg a little lighter

and improves the high frequency behavior of the isolator. Fig.8.26 compares the transmissibility of the active (IFF) and the passive (relaxation) isolator. The dotted line refer to the transmissibility of the passive isolator when the RL circuit is open. As expected, the overshoot of the active one is a little lower; both have a decay rate of -40 $dB/decade$ in the intermediate frequency range, and the high frequency behavior is dominated by the local modes; the passive isolator behaves better in high frequency, because the local modes have higher frequencies.

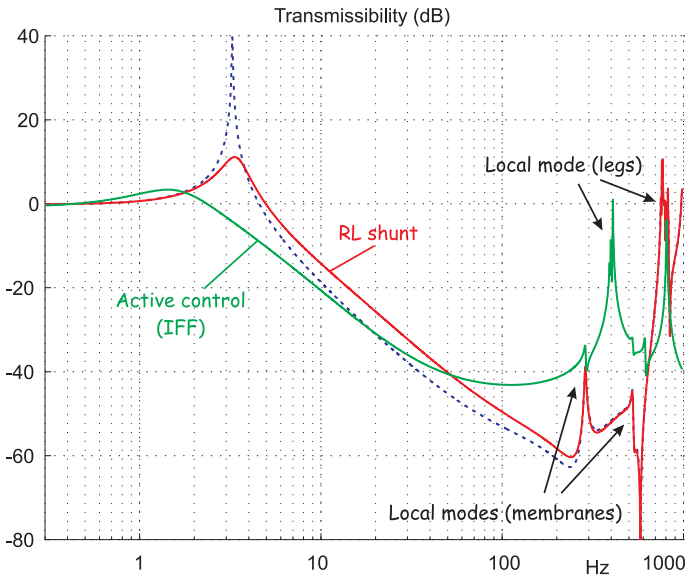

Fig. 8.26. Vertical transmissibility of a six-axis isolator: comparison of the Open-loop (dotted line), closed-loop (IFF) active isolator and passive relaxation isolator with a RL shunt (from de Marneffe et al.).

8.8 Car suspension

Ride comfort requires good vibration isolation; it is usually measured by the car body acceleration, or sometimes its derivative called *jerk*. Vehicle handling requires good road holding, which is measured by the tyre deflection. In addition to the car body acceleration and the tyre deflection, there are design constraints on the suspension travel, that is the relative displacement between the car body and the wheel.

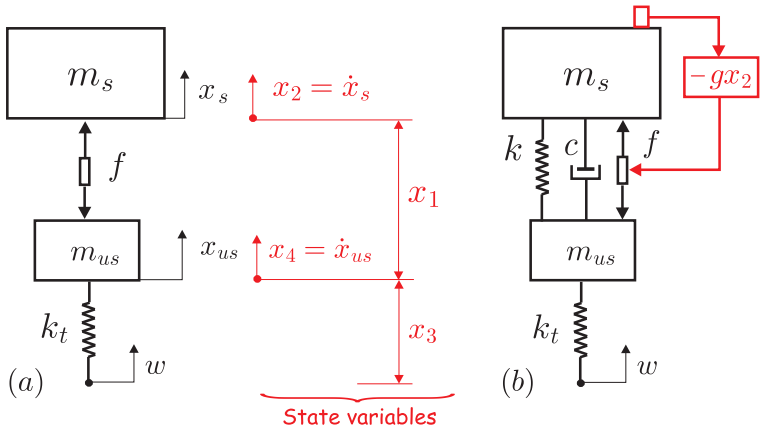

Fig. 8.27. Quarter-car, two-d.o.f. models. (a) Fully active suspension. (b) Passive suspension with an added sky-hook active control.

Figure 8.27 shows a quarter-car model of a vehicle equipped with a fully active suspension (Fig.8.27.a) or a passive suspension with an active, sky-hook damper (Fig.8.27.b); m_s refers to the sprung mass, equal to a quarter of the car body mass, and m_{us} is the unsprung mass (wheel); k_t is the stiffness of the tyre; k and c are the stiffness and damping of the passive suspension. The figure also shows the definition of the state variables used to model the systems: $x_1 = x_s - x_{us}$ is the relative displacement of the sprung mass with respect to the wheel (suspension travel), $x_2 = \dot{x}_s$ is the absolute velocity of the car body, $x_3 = x_{us} - w$ is the tyre deflection, and $x_4 = \dot{x}_{us}$ is the absolute wheel velocity. With this definition of the state variables, the dynamics of the fully active suspension (Fig.8.27.a) reads

$$m_s \dot{x}_2 = f$$

$$m_{us} \dot{x}_4 = -f - k_t x_3$$

$$\dot{x}_1 = x_2 - x_4$$

$$\dot{x}_3 = x_4 - v$$

where $v = \dot{w}$ is the road velocity. Defining the force per unit sprung mass $u = f/m_s$, the unsprung mass ratio $\mu = m_{us}/m_s$ and the tyre frequency $\omega_t = (k_t/m_{us})^{1/2}$, this system is rewritten in matrix form,

$$\begin{pmatrix} \dot{x}_1 \\ \dot{x}_2 \\ \dot{x}_3 \\ \dot{x}_4 \end{pmatrix} = \begin{bmatrix} 0 & 1 & 0 & -1 \\ 0 & 0 & 0 & 0 \\ 0 & 0 & 0 & 1 \\ 0 & 0 & -\omega_t^2 & 0 \end{bmatrix} \begin{pmatrix} x_1 \\ x_2 \\ x_3 \\ x_4 \end{pmatrix} + \begin{pmatrix} 0 \\ 1 \\ 0 \\ -1/\mu \end{pmatrix} u + \begin{pmatrix} 0 \\ 0 \\ -1 \\ 0 \end{pmatrix} v \qquad (8.56)$$

With the same state-variables, the dynamics of the system of Fig.8.27.b (without control) is governed by

$$m_s\,\dot{x}_2 = f - kx_1 + c(x_4 - x_2)$$

$$m_{us}\,\dot{x}_4 = -f - k_t x_3 + kx_1 + c(x_2 - x_4)$$

$$\dot{x}_1 = x_2 - x_4$$

$$\dot{x}_3 = x_4 - v$$

and, upon defining $\omega_n^2 = k/m_s$ (ω_n is the body resonance), $c/m_s = 2\xi\omega_n$, they are rewritten in matrix form

$$\begin{pmatrix} \dot{x}_1 \\ \dot{x}_2 \\ \dot{x}_3 \\ \dot{x}_4 \end{pmatrix} = \begin{bmatrix} 0 & 1 & 0 & -1 \\ -\omega_n^2 & -2\xi\omega_n & 0 & 2\xi\omega_n \\ 0 & 0 & 0 & 1 \\ \frac{\omega_n^2}{\mu} & \frac{2\xi\omega_n}{\mu} & -\omega_t^2 & \frac{-2\xi\omega_n}{\mu} \end{bmatrix} \begin{pmatrix} x_1 \\ x_2 \\ x_3 \\ x_4 \end{pmatrix} + \begin{pmatrix} 0 \\ 1 \\ 0 \\ -1/\mu \end{pmatrix} u + \begin{pmatrix} 0 \\ 0 \\ -v \\ 0 \end{pmatrix} \tag{8.57}$$

Passive suspension

The trade-off in the design of a passive suspension can be illustrated with the following example taken from Chalasani: The nominal values of the passive suspension are $k_t = 160000\,N/m$ (tyre stiffness), $k = 16000\,N/m$ (suspension spring stiffness), $m_s = 240\,kg$ (car body), $m_{us} = 36\,kg$ (wheel). Figure 8.28.a shows the transmissibility $T_{\ddot{x}_s v}$ between the road velocity $v = \dot{w}$ and the body absolute acceleration $\dot{x}_2 = \ddot{x}_s$ for three values of the damping constant, $c = 200$ *Ns/m*, 980 *Ns/m*, 4000 *Ns/m*. For the smallest value of c, one sees clearly the two peaks associated with the body resonance (sprung mass) and the tyre resonance (unsprung mass); the body resonance is at 7.8 *rad/s* and the tyre resonance is at 69.5 *rad/s*, respectively very close to $\omega_n = \sqrt{k/m_s} = 8.16$ *rad/s* and $\omega_t = \sqrt{k_t/m_{us}} = 66.7$ *rad/s*. As the damping increases, the amplitude of the two peaks is reduced; one sees clearly that the passive damping cannot control the body resonance without deteriorating the isolation at higher frequency. The cumulative RMS value of the body acceleration is defined by the integral

$$\sigma_{\ddot{x}_s}(\omega) = [\int_0^{\omega} |T_{\ddot{x}_s v}|^2 d\nu]^{1/2} \tag{8.58}$$

it is represented in Fig.8.28.b; since the road velocity is approximately a white noise, $\sigma_{\ddot{x}_s}$ describes how the various frequencies contribute to the

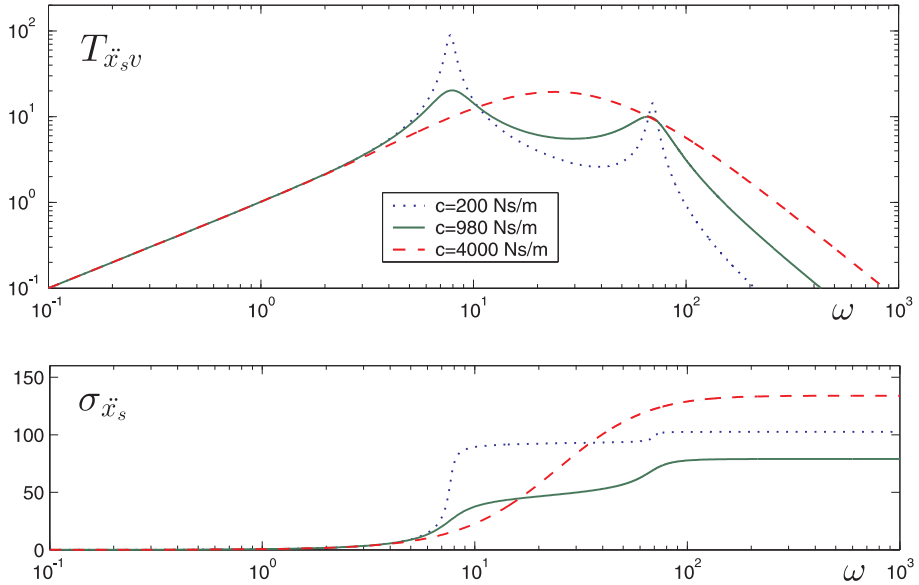

Fig. 8.28. Behavior of the passive suspension for various values of the damping constant: $c = 200$ *Ns/m*, 980 *Ns/m*, 4000 *Ns/m*: (a) Transmissibility $T_{\ddot{x}_s v}$ between the road velocity $v = \dot{w}$ and the body absolute acceleration $\dot{x}_2 = \ddot{x}_s$. (b) Cumulative RMS value of the sprung mass acceleration $\sigma_{\ddot{x}_s}$.

RMS of the body acceleration (in relative terms). When the damping increases, the RMS body acceleration initially decreases, and increases again for larger values of c.

Active suspension

A partial state feedback is added to the passive suspension; it consists of a sky-hook damper, $f = -g\dot{x}_s$ as shown in Fig.8.27.b. Figure 8.29.a shows the impact of the control gain on the transmissibility $T_{\ddot{x}_s v}$ between the road velocity $v = \dot{w}$ and the body absolute acceleration $\ddot{x}_s$; the cumulative RMS value of the sprung mass acceleration $\sigma_{\ddot{x}_s}$ is shown in Fig.8.29.b. One can see that the active control acts very effectively on the body resonance and that the attenuation is achieved without deteriorating the high frequency isolation. However, the active control is unable to reduce the wheel resonance. The active control produces a significant reduction of the RMS sprung mass acceleration but the control system fails to reduce the wheel resonance, Fig.8.29.c. The RMS tyre deflection is dominated by the wheel resonance and is not much reduced by the sky-hook control, Fig.8.29.d.

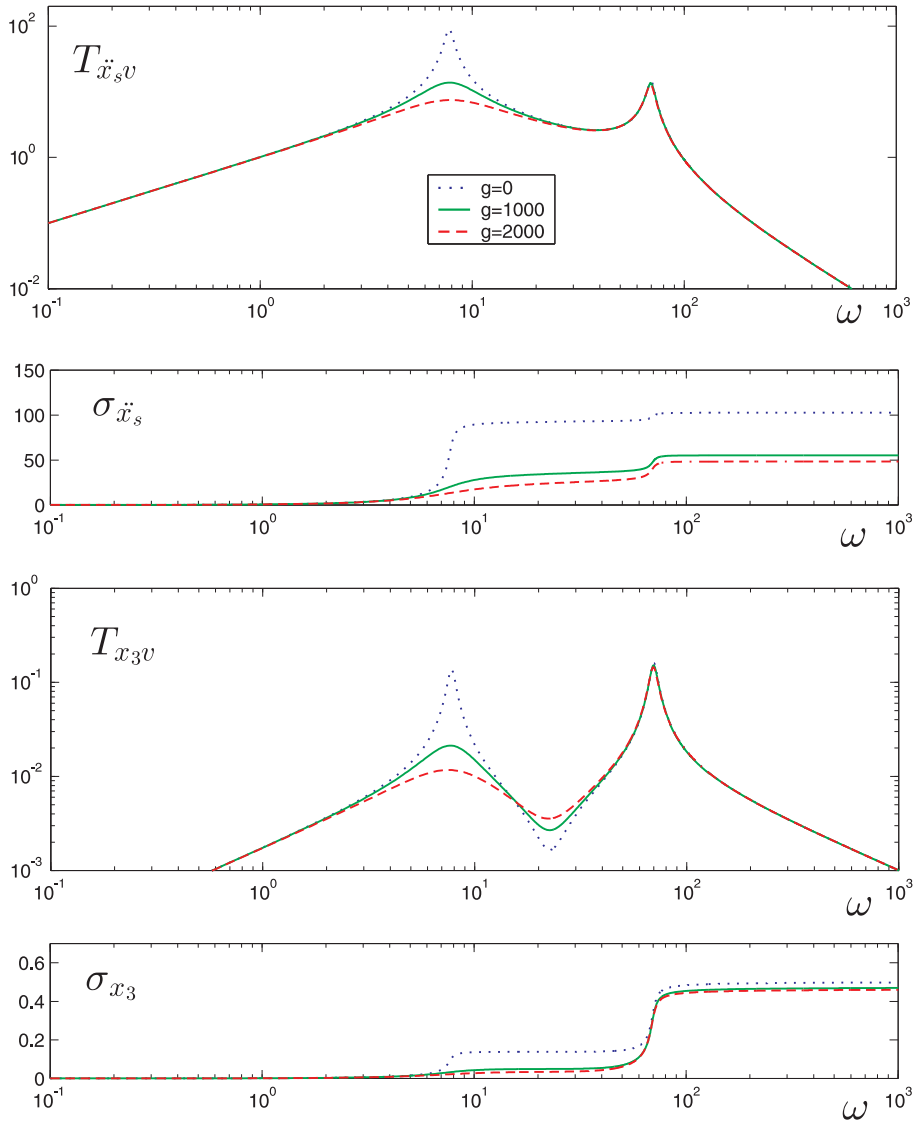

Fig. 8.29. Active suspension for various values of the control gain, $g = 0$, 1000 and 2000. The damping of the shock absorber is $c = 200$ Ns/m: (a) and (b) Sprung mass acceleration (c) and (d) Tyre deflection.

8.9 References

ABU-HANIEH, A. *Active Isolation and Damping of Vibrations via Stewart Platform*, PhD Thesis, Université Libre de Bruxelles, Active Structures Laboratory, 2003.

BOURCIER de CARBON, Ch. Perfectionnement à la suspension des véhicules routiers. Amortisseur relaxation. Comptes Rendus de l'Académie des Sciences de Paris, Vol.225, pp. 722-724, Juillet-Déc. 1947.

BRONOWICKI, A.J. Vibration Isolator for Large Space Telescopes, *AIAA J. of Spacecraft and Rockets*, vol.43, No 1, 45-53, January-February 2006.

CHALASANI, R.M. Ride Performance Potential of Active Suspension Systems, Part 1: Simplified Analysis based on a Quarter-Car Model, ASME Symposium on Simulation and Control of Ground Vehicles and Transportation Systems, Anaheim, CA, Dec. 1984.

COBB, R.G., SULLIVAN, J.M., DAS, A., DAVIS, L.P., HYDE, T.T., DAVIS, T., RAHMAN, Z.H., SPANOS, J.T. Vibration isolation and suppression system for precision payloads in space, *Smart Mater. Struct.* vol.8, 798-812, 1999.

COLLINS, S.A., von FLOTOW, A.H. Active vibration isolation for spacecraft, 42^{nd} *IAF Congress*, paper No IAF-91-289, Montreal, Oct.1991.

de MARNEFFE, B. *Active and Passive vibration isolation and damping via shunted transducers*, PhD Thesis, Université Libre de Bruxelles, Active Structures Laboratory, 2007.

de MARNEFFE, B., AVRAAM, M., DERAEMAEKER, A., HORODINCA, M. PREUMONT, A. Vibration Isolation of Precision Payloads: A Six-axis Electromagnetic Relaxation Isolator, *AIAA Journal of Guidance, Control, and Dynamics*, Vol.32, No 2, 395-401, March-April 2009.

FULLER, C.R., ELLIOTT, S.J., NELSON, P.A. *Active Control of Vibration*, Academic Press, 1996.

GENG, Z. HAYNES, L. Six degree of freedom active vibration isolation system using the Stewart platforms, *IEEE Transactions on Control Systems Technology*, Vol.2, No 1, 45-53, 1994.

HAUGE, G.S., CAMPBELL, M.E. Sensors and control of a spaced-based six-axis vibration isolation system, *J. of Sound and Vibration*, 269, 913-931, 2004.

HYDE, T.T. and ANDERSON, E.H. Actuator with built-in viscous damping for isolation and structural control, *AIAA Journal*, vol. 34(1), 129-135, 1996.

HROVAT, D. Survey of Advanced Suspension Developments and Related Optimal Control Applications, *Automatica*, Vol.33, No 10, 1781-1817, 1997.

KAPLOW, C.E., VELMAN, J.R. Active local vibration isolation applied to a flexible telescope, *AIAA J. of Guidance, Control and Dynamics*, 3, 227-233, 1980.

LASKIN, R.A., SIRLIN, S.W. Future payload isolation and pointing system technology, *AIAA J. of Guidance, Control and Dynamics*, 9, 469-477, 1986.

KARNOPP, D.C., TRIKHA, A.K. Comparative study of optimization techniques for shock and vibration isolation, *Trans. ASME, J. of Engineering for Industry, Series B*, 91, 1128-1132, 1969.

McINROY, J.E., O'BRIEN, J.F., NEAT, G.W. Precise, fault-tolerant pointing using a Stewart platform, *IEEE/ASME Transactions on Mechatronics,* Vol.4, No 1, 91-95, March 1999.

McINROY, J.E., NEAT, G.W., O'BRIEN, J.F. A robotic approach to fault-tolerant, precision pointing, *IEEE Robotics and Automation Magazine*, 24-37, Dec. 1999.

McINROY, J.E., HAMANN, J. Design and control of flexure jointed hexapods, *IEEE Transaction on Robotics,* 16(4), 372-381, August 2000.

McINROY, J.E. Modelling and design of flexure jointed Stewart platforms for control purposes, *IEEE/ASME Transaction on Mechatronics,* 7(1), March 2002.

PREUMONT, A., FRANCOIS, A., BOSSENS, F., ABU-HANIEH, A. Force feedback versus acceleration feedback in active vibration isolation, *J. of Sound and Vibration*, 257(4), 605-613, 2002.

PREUMONT, A., HORODINCA, M., ROMANESCU, I., de MARNEFFE, B., AVRAAM, M., DERAEMAEKER, A., BOSSENS, F., ABU-HANIEH, A. A six-axis single stage active vibration isolator based on Stewart platform, *Journal of Sound and Vibration*, 300 : 644-661, 2007.

PREUMONT, A. & SETO, K. *Active Control of Structures*, Wiley, 2008.

RAHMAN, Z.H, SPANOS, J.T, LASKIN, R.A. Multi-axis vibration isolation, suppression and steering system for space observational applications, *SPIE* Symposium on Astronomical Telescopes and Instrumentation, Kona-Hawaii, March 1998.

RIVIN, E.I. *Passive Vibration Isolation*, *ASME* Press, N-Y, 2003.

SPANOS, J., RAHMAN, Z., BLACKWOOD, G. A soft 6-axis active vibration isolator, Proc. of the *IEEE* American Control Conference, 412-416, 1995.

STEWART, D. A platform with six degrees of freedom, *Pro. Instn. Mech. Engrs.*, 180(15), 371-386, 1965-66.
THAYER, D., VAGNERS, J., von FLOTOW, A., HARDMAN, C., SCRIBNER, K. Six-axis vibration isolation system using soft actuators and multiple sensors; *AAS 98-064*, 497-506, 1998.
THAYER, D., CAMPBELL, M., VAGNERS J., von FLOTOW, A. Six-Axis vibration isolation system using soft actuators and multiple sensors, *J. of Spacecraft and Rockets*, Vol.39, No 2, 206-212, March-April 2002.

8.10 Problems

P.8.1 *Consider the passive isolator of Fig.8.1.b. Find the transmissibility $X_c(s)/X_d(s)$ of the isolation system.*
P.8.2 *Consider the active isolator of Fig.8.7.a with a sky-hook controller. Analyze the effect of the passive damping on the transmissibility. Is the damping beneficial or detrimental ?*
P.8.3 *Write the differential equations governing the system of Fig.8.12 in state variable form. Using the following values of the parameters: $m = 1.1kg, M = 1.7kg, k = k_1 = 1.2\ 10^4 N/m, m_1 = 0.5kg, c_1 = 0Ns/m$. Write the open-loop frequency response for the acceleration feedback ($\ddot{x}_c$) and force feedback (f) configurations and draw the corresponding poles/zeros pattern. In both cases draw the root locus for an integral controller. Do the same for $m_1 = 3.5kg$; investigate the effect of structural damping in the flexible appendage.*
P.8.4 *Consider the modal expansion of the open-loop FRF (F/F_a) of the system of Fig.8.15.d. Show that the residues are all positive and that this results in alternating poles and zeros.*
P.8.5 *Show that the dynamic stiffness of the relaxation isolator (Fig.8.3.a) is given by*

$$\frac{F}{x - x_0} = k(s) = k[1 + \frac{k_1 cs}{k(k_1 + cs)}]$$

P.8.6 *Consider the Gough-Stewart platform with cubic architecture of Fig.8.30 (Spanos et al.); the basic frame $\{x_b, y_b, z_b\}$ has its origin at node 0; the reference (or payload) frame $\{x_r, y_r, z_r\}$ has its origin at the geometrical center of the hexapod, noted as node 8, and $\vec{z}_r$ is perpendicular to the payload plate; the orientation of $\vec{x}_r$ and $\vec{y}_r$ is shown in the figure. The small displacements of the system are described by the coordinates $x = (x_r, y_r, z_r, \theta_x, \theta_y, \theta_z)^T$*

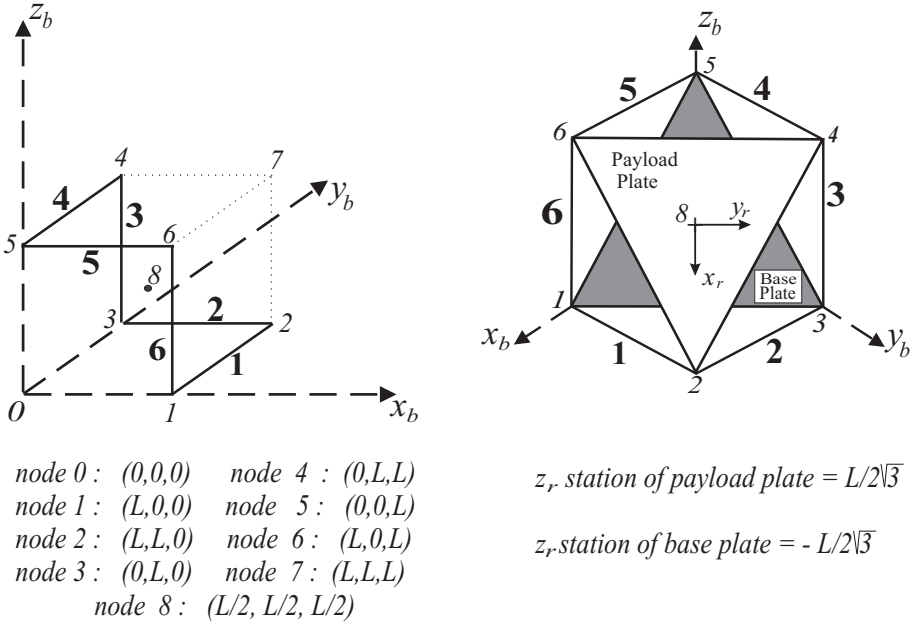

Fig. 8.30. Geometry and coordinate systems for the cubic hexapod isolator. Numbers in bold indicate the active struts.

(a) Show that the control influence matrix appearing in Equ.(8.47) reads

$$B = \frac{1}{\sqrt{6}} \begin{pmatrix} 1 & 1 & -2 & 1 & 1 & -2 \\ \sqrt{3} & -\sqrt{3} & 0 & \sqrt{3} & -\sqrt{3} & 0 \\ \sqrt{2} & \sqrt{2} & \sqrt{2} & \sqrt{2} & \sqrt{2} & \sqrt{2} \\ -L/2 & L/2 & L & L/2 & -L/2 & -L \\ -L\sqrt{3}/2 & -L\sqrt{3}/2 & 0 & L\sqrt{3}/2 & L\sqrt{3}/2 & 0 \\ L\sqrt{2} & -L\sqrt{2} & L\sqrt{2} & -L\sqrt{2} & L\sqrt{2} & -L\sqrt{2} \end{pmatrix}$$

(b) If the base is fixed and the payload is an axisymmetrical rigid body of mass m with the principal axes of inertia aligned with $\{x_r, y_r, z_r\}$, principal moment of inertia $I_x = I_y = mR_x^2$, $I_z = mR_z^2$, and with the center of mass located at an offset distance Z_c from the geometrical center, along the vertical axis z_r, show that the mass and stiffness matrices are respectively

$$M = m \begin{pmatrix} 1 & 0 & 0 & 0 & Z_c & 0 \\ 0 & 1 & 0 & -Z_c & 0 & 0 \\ 0 & 0 & 1 & 0 & 0 & 0 \\ 0 & -Z_c & 0 & (R_x^2 + Z_c^2) & 0 & 0 \\ Z_c & 0 & 0 & 0 & (R_x^2 + Z_c^2) & 0 \\ 0 & 0 & 0 & 0 & 0 & R_z^2 \end{pmatrix}$$

$$K = kBB^T = k\ diag(2, 2, 2, 0.5L^2, 0.5L^2, 2L^2)$$

where k is the stiffness of one strut. Observe that the translational stiffness is uniform in all directions and that the two bending stiffnesses are identical.

(c) Consider the natural frequencies of the isolator, solutions of the eigenvalue problem (8.37). Show that the the z-translation or "bounce" mode and the z-rotation or "torsional" mode are decoupled, with natural frequencies given by

$$\Omega_3 = \sqrt{2}\ \Omega_0 \qquad\qquad \Omega_6 = \frac{\sqrt{2}}{\rho_z}\Omega_0$$

where $\Omega_0 = \sqrt{k/m}$ and $\rho_z = R_z/L$ is the z-axis radius of gyration normalized to the strut length (for most cases, $\rho_z < 1$ and $\Omega_6 > \Omega_3$). Show that the remaining four modes are lateral bending coupled with shear; their natural frequencies occur in two identical pairs, solutions of the characteristic equation

$$\left(2 - \frac{\Omega^2}{\Omega_0^2}\right)\left(\frac{1}{2} - \rho_x^2\frac{\Omega^2}{\Omega_0^2}\right) - 2\rho_c^2\frac{\Omega^2}{\Omega_0^2} = 0$$

where $\rho_x = R_x/L$ is the x-axis radius of gyration normalized to the strut length and $\rho_c = Z_c/L$ is the center of mass offset normalized to the strut length. Show that if the center of mass is at the geometric center ($\rho_c = 0$) and if $\rho_x = \frac{1}{2}$ and $\rho_z = 1$, the hexapod will have 6 identical natural frequencies, all equal to Ω_3.

P.8.7 *Consider the fully active suspension of Fig.8.27.a where $v = \dot{w}$ is assumed to be a white noise process.*

Find the Linear Quadratic Regulator (LQR) minimizing the performance index

$$J = E[\varrho_1 x_1^2 + \varrho_2 x_2^2 + u^2]$$

and

$$J = E[\varrho_1 x_1^2 + \varrho_2 x_2^2 + \varrho_3 x_3^2 + u^2]$$

Discuss the meaning of the various terms in the performance index (The solution of this problem requires a prior reading of Chapters 9 an 11).

P.8.8 *Consider the active suspension of Figure 8.27.b with* $k_t = 160000\,N/m$ *(tyre stiffness),* $k = 16000\,N/m$ *(suspension spring stiffness),* $m_s = 240\,kg$ *(car body),* $m_{us} = 36\,kg$ *(wheel). For the three values of the control gain,* $g = 0$*, 1000 and 2000, plot the transmissibility between the road velocity* v *and the body absolute velocity* $\dot{x}_s$ *and between the road velocity and the force in the dash-pot* c*. Compare their frequency content.*